Transport and thermodynamic properties of rare earth compounds and alloys

by

Aiman Kamal Hamed Bashir

Thesis presented in the fulfilment of the requirements for the degree of ***PhD of Science*** *at The University of The Western Cape*

Departement of Physics,
University of The Western Cape,
South Africa.

Supervisor: Prof. Moise Bertin Tchoula Tchokonté

January 2017

Declaration

I declare that this thesis is my own independently researched work conducted in the Physics Department of the University of the Western cape, South Africa. It is being submitted for the degree of Doctor of Philosophy in Science, and is the first time this work is being submitted for this degree.

_____

Aiman Kamal Hamed Bashir

_____ day of _____ 2017

List of publications

1- Low-temperature transport and thermodynamic properties of dense Kondo alloys $Ce_8Pd_{24}(Al_{1-x}Sn_x)$, M.B. Tchoula Tchokonté, **A.K.H. Bashir**, A.M. Strydom, T. Doyle, D. Kaczorowski. Journal of Alloys and Compounds, 717, 2017(333-340).

2-Interplay of antiferromagnetism and Kondo effect in $(Ce_{1-x}La_x)_8Pd_{24}Al$, **A.K.H. Bashir**, M.B. Tchoula Tchokonté, D. Britiz, A.M. Strydom, D. Kaczorowski. Journal of Physics and chemistry of Solids, 106, 2017(44-51).

3-Magnetic and thermal properties of NdAuGa, **A.K.H. Bashir**, M.B. Tchoula Tchokonté, B. M. Sondezi, A.M. Strydom, D. Kaczorowski. Journal of Alloys and Compounds, 699 2017 (7-10).

4-Electrical and thermal transport properties of $RECu_4Au$ compounds, RE = Nd, Gd, **A.K.H.Bashir**, M.B. Tchoula Tchokonté, A.M. Strydom. Journal of Magnetism and Magnetic Materials. 414, 2016(69-73)

5-Crystal structure and thermodynamic properties of $NdCu_4Au$ compound. M. B. Tchoula Tchokonté, **A. K. H. Bashir**, A. M. Strydom. Journal of Physics and chemistry of Solids. 90, 2016, (59-64).

6-Magnetic and thermodynamic properties of $GdCu_4Au$. **A. K. H. Bashir**, M. B. Tchoula Tchokonté, D. Britz, B. M. Sondezi and A. M. Strydom . Journal of Physics: Conference Series 592 (2015) 012050.

7-Electrical and thermal properties of the alloy system $Ce_{1-x}La_xCu_4In$. **A. K. H. Bashir**, M. B. Tchoula Tchokonté, D. Britiz, B. M. Sondezi, A. M. Strydom and D.Kaczorowski . Journal of Physics: Conference Series 592 (2015) 012004.

8-Antiferromagnetic ordering in NdAuGe. **A. K. H. Bashir**, M. B. Tchoula Tchokonté,

J. L. Snyman, B. M. Sondezi and A. M. Strydom. Journal of Applied Physics 115,117 E134 (2014).

Acknowledgements

First of all, I thank Allah who made this work possible.

I would like to convey my deepest gratitude to my supervisor, Professor M.B.Tchoula Tchokonté for offering me this great opportunity to commence my doctoral study at the University of the Western Cape (UWC). My sincere gratitude extends to Professor M.B.Tchoula Tchokonté for his valuable suggestions, guidance, discussions, advice and encouragements which he has given to me during the course of my PhD. Moreover, I sincerely thank Professor M.B.Tchoula Tchokonté for spending most of his valuable time on assisting me to learn the research techniques of my work, data analysis and interpretation of results. On the other hand, I express my thank to Professor M.B.Tchoula Tchokonté for arranging me financial support from National Research Foundation (NRF).
I would like to thank Prof A.M Strydom at University of Johannesburg(UJ) for giving me the chance to perform some of my experiments in his laboratory, especially, electrical and thermal transport properties. Also, my sincere thanks to Prof A.M Strydom for his valuable discussions and opinions that helped me to interpret some of my results. My deepest gratitude goes to Drs. D. Britiz, B. M. Sondezi, and J. L. Snyman at UJ, for their kind patience to perform the measurements using PPMS.
I would like to express my sincere gratitude to Prof D. Kaczorowski and his team at the Institute of Low Temperature and Structure Research, Polish Academy of Sciences, for facilitating the magnetic measurements of my samples in their laboratory. Also, my deepest gratitude to Prof D. Kaczorowski for sharing valuable discussions regarding some of my work.
Also I wish to convey my warm gratitude to the staff and colleagues at University of the Western Cape, for their kind support and continuous encouragement.
My sincere thanks goes to Sudan University of Science and Technology for granting study leave to pursue my PhD study at the University of the Western Cape.
I would like to express my deepest gratitude to my family and colleagues in Sudan, for their continuous contact, encouragement and support they provided me while away from home.

Abstract

Rare-earth (RE) elements possess an incompletely filled $4f$ shell, which is very small compared to typical interatomic distances. As a result of this, RE elements and compounds exhibit characteristic properties, which deviate significantly from those of other systems containing for instance the $3d$ transition elements with expanded $3d$ shells. As a result of a small radius of the $4f$ shell, the $4f$ electron does not participate in chemical bounding. Instead, the $4f$ electron together with the nucleus act virtually as an effective nucleus. From chemical point of view all RE behave similarly. The overlap of the neighbouring f shells is extremely small. The magnetic moments associated with the $4f$ shell may be treated as well localized moments in contrast to the $3d$ which are itinerant.

The hybridization of the $4f$ electrons with the conduction bands lead to a diversity of unusual physical properties such as heavy-fermion, Kondo effect, magnetic order, superconductivity, intermediate valence properties, Fermi and non-Fermi liquid behaviour and semiconductor behaviour. For the Kondo lattice, the physics is governed by two main interactions. These are:

- The single-ion Kondo interaction caused by the antiferromagnetic exchange interaction J between the conduction electrons and a small amount of magnetic impurities (e.g. $4f$ or $3d$ ions). This interaction is characterized by a temperature scale calling the Kondo temperature T_K which favors a nonmagnetic ground state.

- The indirect Rudermann-Kittel-Kasuya-Yosida (RKKY) interaction between the magnetic $4f$ moments via the conduction electrons. In this case the $4f$ moment induces a partially oscillating spin polarization of the conduction electrons, which in turn affects the orientation of neighbouring $4f$ moment. This interaction is characterized by a temperature scale T_{RKKY} which favours a magnetic ordering of the $4f$ moments at low temperatures.

Both characteristic temperatures depend on the strength of the exchange interaction. A magnetically ordered ground state is an intuitive consequence of local magnetic moments prevalent in RE compounds but magnetic instabilities are caused by competing exchange interactions in the form of Kondo interaction versus the RKKY interaction. Admixed together with the crystal- electric field (CEF) effect are known to produce a wealth of exotic phenomena in $4f$-spin hybridized Ce and Yb compounds.

The structure of this thesis is arranged as follows:
Chapter 1 presents a brief overview of the heavy-fermion and Kondo systems.
Chapter 2: A brief summary of theoretical concepts and the physical properties of RE intermetallic compounds is presented. Kondo effect is discussed with a focus on multi-channel Kondo, disordered Kondo lattice and quantum criticality phase. The Kondo and RKKY interactions, the Landau Fermi liquid theory as well as the non-Fermi liquid behaviour are discussed. A brief overview of the transport and thermodynamics properties of RE intermetallic compounds are presented.
Chapter 3 presents the experimental techniques used in this study. Sample synthesis and characterization, transport and thermodynamic properties measurement are discussed. This is followed by chapters 4 to 7 which present the experimental results and discussions.
Chapter 4 discusses the physical properties of two RE compounds: $RECu_4Au$ with RE = Nd and Gd. The physical properties studied in this chapter are: the electrical resistivity, thermoelectric power, thermal conductivity, the Lorentz number, magnetic susceptibility, magnetization and heat capacity. The results obtained for the two cubic $RECu_4Au$ series of compounds indicate antiferromagnetic (AFM) ground state with the magnetic phase transition temperature of T_N = 3.5 K and 10.8 K for $NdCu_4Au$ and $GdCu_4Au$ respectively. A Schottky-type anomaly associated with (CEF) effect is in seen $NdCu_4Au$.
Chapter 5 presents the transport and thermodynamic properties of two RE compounds: NdAuX where (X = Ge and Ga). The physical properties studied in this chapter are: the electrical resistivity, magnetic susceptibility, magnetization, heat capacity and magnetocaloric effect. The results obtained in this chapter indicate AFM ground state with the magnetic phase transition temperature of T_N = 8.9 K and 3.5 K for NdAuGa and NdAuGe respectively. Spin-reorientation transition below the T_N at 3.6 K is seen for the NdAuGa. A small isothermal magnetic entropy is seen for the NdAuGa while CEF is seen in NdAuGe around 16.5 K.
Chapter 6 discusses the effect of La dilution on the polycrystalline Kondo lattice compound $CeCu_4In$. The results of electrical resistivity indicate an evolution from coherence Kondo lattice behaviour to incoherent single-ion scattering with increasing La content. The value of the Kondo temperature T_K obtained from the magnetoresistivity results as

well as the values of T_{max} obtained from the resistivity are interpreted in terms of the compressible Kondo lattice model. Results of the thermoelectric power are interpreted in terms of the phenomenological resonance model.

Chapter 7: The effect of La dilution and ligand substitution on the AFM Kondo lattice compound $Ce_8Pd_{24}Al$ is presented. The interplay of AFM and Kondo effect in $Ce_8Pd_{24}Al$ with the dilution of Ce with La is discussed through measurements of transport properties while the magnetic behaviour is discussed through measurements of magnetic properties. The results obtained from magnetic measurements indicate AFM order up to 20% Al substitution. On the other hand the combined Kondo and CEF effect in $Ce_8Pd_{24}Al$ with ligand substitution Al with Sn are discussed through measurement of transport properties. The results obtained from the transport measurements indicate the combined effects of Kondo and CEF up to 70% Al substitution and CEF only above 80% Al substitution. Magnetic measurements of $Ce_8Pd_{24}(Al_{1-x}Sn_x)$ indicate AFM order for all compositions.

Chapter 8: gives a summary of all results obtained in this thesis and the proposed future work.

Contents

List of Figures

List of Tables

Chapter 1

Introduction

Intermetallic compounds containing rare earth elements exhibit a large variety of interesting ground state properties, such as Kondo effect, heavy-fermion(HF) behaviour, intermediate valence, superconductivity, single and multiple magnetic transitions, spin glass, metamagnetism and large magnetocaloric effect (MEC). These unusual low-temperature properties are ascribed to the interaction of the localized $4f$ moments of rare earth elements with the conduction electrons.

The magnetic ground state properties of these intermetallic compounds are a matter of interest for two reasons: Firstly, their study helps to elucidate some of the fundamental principles of magnetism (RKKY interaction, crystal electric field, magnetoelastic properties, coexistence of superconductivity and long range magnetic order). Secondly, through an application point of view, they are of technical interest in the development of new magnetic refrigeration technology, based upon the MCE. They have brought an alternative to the conventional gas compression technique. As a result of this, many new materials with large MCE have been discovered and a very good understanding of this magnetothermal property has been achieved [1]. Among the intermetallic compounds, rare earth (RE) intermetallics compounds, in particular the RE-transition metals (RETX) series exhibiting large MCE and giant magnetoresistance have received the attention of many researchers in the past and still attract as much interest. Also, it has been found that several of these compounds have quite exceptional properties with respect to reversible absorption of hydrogen gas at room temperature and near atmospheric pressure [2]. RE intermetallic compounds generally have low magnetic transition temperatures and these transition temperatures can further be shifted to 0 K by the variation of an external control parameter such as: hydrostatic pressure, applied magnetic field or compositional concentration. This zero temperature phase transition between the magnetically ordered (generally antiferromagnetic) and a paramagnetic state as a function of an external pa-

rameter is referred to as the quantum phase transition (QPT). On the other hand and apart from magnetic properties, some intermetallic compounds containing Ce, Eu or Yb exhibit complicated behaviours resulting from strong hybridization between $4f$-electrons of these elements and the conduction electrons, such as Kondo effect, heavy fermion and intermediate valence behaviour. An exception for these compounds containing these elements is that, the proximity of the $4f$ level to the Fermi energy leads to instabilities of the charge configuration (valence) and / or of the magnetic moment.

Kondo effect is the physics by which the local moments disappear or quench at low temperatures closely analogous to the physics of quark confinement [3]. The Kondo effect has a wide range of manifestation in condensed matter physics, not only does it govern the quenching of magnetic moments, but it is also responsible for the formation of heavy fermion materials. The heavy fermion materials, which are also sometimes referred to as heavy electron systems, include binary and ternary compounds and alloys with cerium (Ce) or ytterbium (Yb) based rare earth elements [4]. The heavy fermion materials fall within a class of materials known as strongly correlated electron systems (SCES). In this class of materials, the electron interaction energy dominates the electron kinetic energies, becoming so large that they qualitatively transform the physics of the medium [5]. For the heavy fermion systems, the localized magnetic moments formed by rare earth or actinide ions transform the metal in which they are immersed, generating quasiparticles with masses in excess of 1000 bare electron masses [6].

The intense interest in heavy fermion systems started with the discovery of superconductivity in the heavy fermion $CeCu_2Si_2$ [7]. The large effective masses observed in heavy fermion materials are mainly estimated from the electronic specific heat coefficient (γ). Therefore, a generally accepted definition of heavy fermion are those systems which have $\gamma > 400$ mJ/mole.K^2 [8]. Another property of heavy Fermion systems includes an enhanced Pauli susceptibility ($\chi(0)$), indicating a large effective mass at low temperature, while obeying Curie-Weiss law at high temperature. $CeAl_3$ was the first heavy fermion system discovered by Anders *et al* [9]. It was found that the electronic specific heat and Pauli susceptibility of $CeAl_3$ below 0.2 K have enormous magnitudes $\gamma = 1600$ mJ/mol.K^2 and $\chi(0) = 4.52\times\ 10^{-7}$ m^3.mole^{-1} [9], respectively. These values are considered to be large, compared to the normal metals, such as copper (Cu) with values $\gamma = 0.7$ mJ/mole.K^2 and $\chi(0) = 12.6\times\ 10^{-11}$ m^3.mole^{-1} [10]. Generally, the heavy fermion systems lie in the range of magnetic instability. At present, many heavy fermion systems have been discovered and there is no uniformity in their properties. Some heavy fermions exhibit Fermi liquid behaviour with no magnetic phase transition while others show non-Fermi liquid behaviour. Both magnetic and superconducting quantum critical points have been

observed in some of these systems.

The physics of Kondo systems are predominantly governed by two main interactions. These are: the Rudermann-Kittel-Kasuya-Yoshida (RKKY) interaction which is characterized by the intersite interaction with a temperature scale T_{RKKY}, and the on-site Kondo interaction characterized by the Kondo temperature T_K. Both characteristic temperatures depend on the magnetic exchange integral J_{sf} between the $4f$ local moments and the conduction electrons and the density of state (DOS) at the Fermi level ($N(E_F)$). The indirect RKKY interaction promotes magnetic ordering of the moments at low temperatures, whereas the Kondo interaction induces a screening of the local $4f$ moments by the conduction electrons and thus favours a non-magnetic ground state. Generally, the low temperature properties of the rare earth compounds depend sensitively on the position of the undistributed $4f$ states with respect to the Fermi level E_F. Depending on the strength of J_{sf} related to the proximity of the $4f$ energy to the Fermi energy, a competition between RKKY interaction and Kondo effect is observed leading to different ground states varying from heavy fermion, antiferromagnetic to intermediate valence states [11]. In the case of the rare earth intermetallic compounds, the $4f$ levels are far below the Fermi level and hence $T_{RKKY} >> T_K$, as a result of this, a magnetic phase transition occurs and the localized magnetic moment does not contribute to the Kondo spin-flip scattering process. In the case of anomalous rare earth intermetallic compounds, the anomalous proximity of the $4f$ and the Fermi levels results in a strong J_{sf} enhancement. From the different dependencies of T_K and T_{RKKY} with respect to J_{sf}, we may have a non-magnetic concentrated Kondo system or intermediate valence system in the case $T_K >> T_{RKKY}$ or a magnetic concentrated Kondo system in the case $T_K > T_{RKKY}$. Studies of this particular feature of Kondo lattice were initiated by Doniach [11].

Measurements of thermodynamic and transport properties are essential to understand the diverse physical properties of the rare earth intermetallic compounds. Detailed studies of the magnetization, as functions of applied magnetic field and temperature, elucidate the nature of the interactions between the magnetic moments, as well as between the local moments and surrounding atoms. Specific heat measurements, and subsequent determinations of the change in entropy, provide insight into phase transitions, the crystalline electric field, and details of the electrons and phonons. Measurements of electrical and thermal transport properties provide us with information about the underlying excitations and dominant scattering mechanisms. For instance, electrical resistivity can be used to analyze scattering mechanisms and study the Kondo effect. The logarithmic increase in electrical resistivity of some intermetallic compounds is usually a characteristic of Kondo behaviour. At very low temperatures, the electrical resistivity can be a very useful tool in

determining the Fermi liquid and spin wave behaviours in some rare earth intermetallic compounds.

The application of magnetic field to electrical resistivity (magnetoresistivity) of Kondo systems influences details of density of states (DOS) in the proximity of the Fermi energy, and hence properties depending on DOS are modified [12]. Thermal conductivity probes the scattering of all particles, quasi-particles or energy excitations that contribute to the heat transport within a material, while the thermoelectric power is sensitive to changes in the electronic DOS at the Fermi level. In fact, thermoelectric phenomena arise from the entanglement of thermal and electrical transport processes due to two reasons: first of all heat transport by charge carriers and secondly scattering processes between charge carriers and the other heat carrying quasiparticles such as phonons. Therefore, a flow heat or charge generally induces both a temperature gradient and an electric field. A major part of physical properties studied in this thesis relied on the thermoelectric transport of rare earth compounds containing Ce and Nd. In rare-earth compounds, Kondo interaction and CEF excitations usually give rise to large anomalies (peaks) in thermoelectric power. Therefore, thermoelectric power investigations are suited excellently for studying the Kondo and CEF energy scales in these materials.

Chapter 2

Theoretical concepts and physical properties of rare earth intermetallics

2.1 Electronic structure and magnetism of Rare-earth elements

Rare earth elements are the fifteen elements that extend from lanthanum La (atomic number 57) to lutetium Lu (atomic number 71), which are referred to the lanthanides in the periodic table. Moreover, the two elements scandium Sc (atomic number 21) and Ytterbium (atomic number 39) are considered to be within the rare earth elements group. The lanthanides (which will denote in the remainder of the thesis as rare earths (RE)) are chemically very similar, and therefore it is difficult to separate them from one another or to obtain them in pure states. The purity (%) for most of the RE varies between 99.99 and 99.95. However, the number of electrons in the inner $4f$ shell of the RE is gradually filled when moving from La with no f electrons, to Lu with a filled shell of 14 electrons.

In the free RE atoms, the electronic configuration is described by $4f^n5s^25p^65d^16s^2$ (n=0-14). Thus, the electronic structure of each RE element consists of a partially filled $4f$ subshell, and outer $5S^2$ and $5P^6$ subshell. With increasing nuclear charge, electrons enter into the underlying $4f$ subshell rather than the external $5d$ subshell. Since the filled $5S$ and $5P$ subshells screen the $4f$ electrons, the RE have very similar chemical properties. Thus, RE ions are usually trivalent both in their atomic state and in solid state. An interesting expectation occurs for Ce, Eu and Yb in the solid state. For instance, the element Ce can exist as either in trivalent Ce^{3+} or tetravalent Ce^{4+}. The trivalent Ce^{3+} has a magnetic moment while the tetravalent Ce^{4+} is non-magnetic. The element Yb displays similar behaviour and can exist as either in trivalent Yb^{3+} or divalent Yb^{2+}. The valence

instabilities observed for Ce and Yb compounds are ascribed to the fact that the $4f$ shell for these elements is not well shielded. As a result, their $4f$ electrons can hybridize with the conduction band leading to phenomena like intermediate valence [13], kondo effect [3] and HF behaviour [14]. Also, a characteristic feature of (RE) is the regular decrease in the atomic volume or radius when one goes from La to Lu. This feature is known as the lanthanide contraction. Furthermore, the heavy RE crystallise in a hexagonal closed-packed (hcp), while double hexagonal closed-packed (dhcp) predominates among the lighter RE-elements [14, 15]. An exception occurs for Ce which exhibits many phases in the metallic state, Eu which has a cubic (bbc) structure and Sm, which is rhombohedral at room temperature. The list of the trivalent rare RE with some of their basic electronic properties are shown in Table 2.1.

Table 2.1: The rare earth elements and some of their properties[15].

Element	Atomic No.(Z)	$4f^n$	Crystal form at room Temp	Atomic radius. S(a.u)	S	L	J	Effect magnetic moment μ_{eff} in μ_B
Sc	21		h.c.p					
Y	39		h.c.p					
La	57	0	dhcp	3.92	0	0	0	0
Ce	58	1	f.c.c and dhcp	3.83	3	1/2	5/2	2.54
Pr	59	2	dhcp	3.82	5	1	4	3.58
Nd	60	3	dhcp	3.80	6	3/2	9/2	3.62
Pm	61	4	-	3.78	6	2	4	3.68
Sm	62	5	rhomb	3.77	5	5/2	5/2	0.85
Eu	63	6	b.b.c	4.26	3	3	0	0.00
Gd	64	7	h.c.p	3.76	0	7/2	7/2	7.94
Tb	65	8	h.c.p	3.72	3	3	6	9.70
Dy	66	9	h.c.p	3.70	5	5/2	15/2	10.6
H_0	67	10	h.p.c	3.69	6	2	8	10.6
Er	68	11	h.c.p	3.67	6	3/2	15/2	9.6
Tm	69	12	h.c.p	3.65	5	1	6	7.6
Yb	70	13	f.c.c	4.05	3	1/2	8/7	4.53
Lu	71	14	h.c.p	3.62	0	0	0	0

The magnetic properties of RE elements are determined by the localized electron spins of the partially filled $4f$-electrons orbits, which especially in the case of heavy RE elements (Gd to Tm) are largely unaffected by their neighbouring ions in the crystal. Therefore, the crystal electric field resulting from the neighbouring ions does not quench the magnetic moments of most RE elements. However, the population of the $4f$-electrons and the available states of the local atomic orbitals is defined by the Hund's rules. Accordingly, the electrons are arranged to maximize their spin angular momentum S and orbital angular momentum L. The spin S and orbital angular momentum L are then strongly coupled in the Russell-Saunders coupling scheme to give a total angular momentum $J = |L \pm S|$ depending upon whether the $4f$-electron orbit is more than half filled (Gd to Yb) or less than half filled (Ce to Eu), respectively. The values of quantum numbers S, L, and J as well as the values of effective magnetic moment μ_{eff} are also given in Table 2.1. The theoretical values of μ_{eff} gathered in Table 2.1 are obtained from Hund's rule in Bohr magneton as it will be explained in section 2.3.2.

2.2 Theoretical background

2.2.1 Kondo effect

The Kondo effect, as evidenced from the appearance of the resistivity minimum at temperatures where normal $\rho(T) \sim T^5$ metallic behaviour was expected was proved to originate from magnetic impurity diluted in the metal. The temperature dependence $\rho(T)$ of such dilute magnetic impurities alloys follows a $-ln(T)$ increase below the temperature of $\rho(T)$ minimum T_{min}. Originally, the occurrence of a resistivity minimum was thought to be a departure from Matthiessen's rule, in accordance to which the total resistivity is the sum of different scattering processes include residual and phonon terms, and the $-lnT$ behaviour was unexplainable with the formula of the scattering mechanisms understood at that time.

Kondo proposed a model based on the $s - d$ exchange interaction to explain the $\rho(T)$ in dilute magnetic impurities alloys. This model showed that the logarithmic increase below T_{min} results from the conduction-electron spin-flip scattering by the localized magnetic moments of the $3d$ or $4f$. In this theory, Kondo considered the problem of a single magnetic impurity, where the interaction between the conduction electrons and the $4f$-electrons of magnetic impurities can be described by the so-called $s - d$ exchange Hamiltonian,

$$H = -J\vec{S}.\vec{s}, \tag{2.1}$$

where $\vec{S}$ is the impurity ion spin and $\vec{s}$ is the conduction electron spin and J the exchange coupling constant. Starting from the exchange Hamiltonian with a negative value of the exchange coupling constant J, and using the third-order perturbation based on Born approximation, Kondo obtained an expression of the resistivity of the magnetic impurities [3]:

$$\rho_{imp} \propto J^2 S(S+1)\left[1 - 4JN(E_F)ln\left(\frac{k_B T}{D}\right)\right], \tag{2.2}$$

where $N(E_F)$ is the electron density of states (DOS) at the Fermi level E_F, and D is a cut-off energy that roughly corresponds to the conduction electron bandwidth. The resistivity minimum results from the combined effect of phonon contribution arising from scattering of conduction electrons from lattice excitations, which decreases monotonously with decreasing temperature, and the impurity contribution $\rho_{imp}(T)$, which increases with decreasing temperature due to enhanced scattering of conduction electrons by the $4f$ local magnetic moments. However, Kondo model breaks down below a characteristic temperature known as Kondo temperature [16]:

$$T_K \backsim T_F exp\left[\frac{-1}{N(E_F)|J|}\right], \tag{2.3}$$

where $T_F = E_F/k_B$ is the Fermi temperature. At temperatures $T \geqslant T_K$, the magnetic $4f$-ions behave as free magnetic moments, therefore a Curie-Weiss behaviour of the magnetic susceptibility χ is observed with a negative Curie-Weiss temperature θ_p. At very low temperature $T \leqslant T_K$ the resistivity saturates to a constant value, due to a complete screening of $4f$-localized moments by conduction electrons as $T \to 0$, where the nonmagnetic singlet is fully established. Consequently, the Kondo temperature, T_K set the dividing line between the local moment behaviour, where the spin is free, and the low temperature limit, where the spin becomes highly correlated with the surrounding conduction electrons. Experimentally, this temperature marks the low temperature limit of a Curie susceptibility. The physics by which the local moment disappears or "quenches" at

low temperature is closely analogous to the physics of quark confinement and it is named the "Kondo effect" after the Japanese physicist Jun Kondo .

An important step in solving the magnetic single-impurity problem is provided by the Anderson model [17], which in its original form is a Hamiltonian that is used to describe magnetic impurity embedded in a metallic host. In this model, the metallic host is represented by a band with energy E_k and a momentum k. The localized $4f$ electron have an energy E_k, an angular momentum j and a quantum number M. The significant feature of this model is the hybridization matrix element V_{kf}, which determines the degree of mixing of the localized $4f$ and the conduction bands. This leads to a broadening of the $4f$ level with a width Δ given by:

$$\Delta = \pi |V_{kf}|^2 N(E_F), \tag{2.4}$$

where $|V_{kf}|$ is the average of hybridization strength. Another model which describes the single impurity problem is known as the Coqblin-Schrieffer model [18]. In their model, Coqblin and Schrieffer consider the Anderson model and derive the effective exchange interaction between the conduction electron and the impurity moment, taking into account combined spin and orbit exchange scattering. Schrieffer and Wolff [19] using a concail transformation have shown that, in the limit of small mixing of the localized $4f$-electron and the conduction bands, the Anderson Hamiltonian leads to an energy-dependent antiferromagnetic exchange interaction $J_{kk'}$ given as:

$$J_{kk'} = -\frac{|V_{kf}|^2}{E_{4f}}, \tag{2.5}$$

where E_{4f} represents the energy difference between $4f$-level and Fermi level. The hybridization between the local $4f$ states and the conduction-electron states gives rise to a strong enhancement of the DOS near the Fermi level with a width of the order of $k_B T_k$, which is called the Abrikosov-Suhl or Kondo resonance.

The single impurity problems described by the Kondo, Anderson and Coqblin-Schrieffer models can be solved using different methods. One of these methods is based on the Wilson's [20] numerical renormalization group. Properties such as magnetic susceptibility

$\chi(T)$ [20, 21] and specific heat $C(T)$ [22] have been calculated for the whole temperature range. Several workers [23–25] proposed an exact method using the Bethe-ansatz diagonalization method [26] to find solution for the Anderson and Coqblin-Schrieffer models. The Bethe-ansatz calculations of the Coqblin-Schrieffer model formulated by Schlottmann [27] provide exact solutions of magnetic field dependence of resistivity (magnetoresistance) of the single-ion Kondo systems.

2.2.2 Kondo lattice and Rudermann-Kittel-Kasuya-Yoshida interaction

The single-ion Kondo effect is caused by the antiferromagnetic exchange interaction J between the conduction electrons and a small amount of magnetic impurities such as $4f$ or $3d$ ions. The situation changes qualitatively in the case of Kondo Lattice, where the magnetic ions actually obey the translational symmetry of the crystal lattice. Above T_K, the results for the lattice are qualitatively similar to those obtained for the single-ion Kondo system. Below T_K, the magnetic impurities form a regular sublattice within the crystal lattice, and therefore coherence effects due to the formation of extended Bloch states may arise. This alters, in particular, the transport properties such as the resistivity $\rho(T)$. With decreasing temperature the resistivity $\rho(T)$ exhibits a pronounced maximum near the characteristic temperature T_{coh}, and then followed by a rapid drop towards the lowest temperatures. Furthermore, below T_{coh} (well below T_K), the resistivity $\rho(T)$ follows a T^2 power-law behaviour characteristic of a Fermi liquid behaviour.

Although the distance between neighbouring magnetic moments in a Kondo lattice system is relatively small compared to dilute Kondo systems, the direct interaction between the $4f$ local magnetic moment is still small. Interaction between them can only be possible via polarized conduction electrons. This indirect interaction is known as Ruderman-Kittel-Kasuya-Yosida (RKKY), and leads to a magnetic ordering of $4f$ moments at low temperatures. The coupling between two spins S_i and S_j at distance r_{ij} is given by [28]:

$$J^{ij}_{RKKY} = 6\pi J^2 Z N(E_F)\left[\frac{sin(2k_F r_{ij})}{(2k_F r_{ij})^4} - \frac{cos(2k_F r_{ij})}{(2k_F r_{ij})^3}\right], \tag{2.6}$$

where J^{ij}_{RKKY} represents the strength of the magnetic exchange interaction. Z is the number of conduction electrons per atom and k_F the Fermi momentum. The RKKY interaction leads to either antiferromagnetic, ferromagnetic order, depending on the magnitude of r_{ij}. The energy scale associated with RKKY interaction is given by:

$$k_B T_{RKKY} \backsim J^2 N(E_F). \tag{2.7}$$

The competition between the Kondo interaction and the RKKY interaction gives rise to a large variety of low-temperature behaviours in Kondo-lattice compounds. Doniach [11] proposed a phase diagram to illustrate the different ground states in a Kondo lattice system, depending on the strength of the exchange coupling constant J, depend only on J and the density of states $N(E_F)$. Fig 2.1 shows the Doniach phase diagram in a slightly modified form [29]. The characteristic temperatures of the Kondo and RKKY interaction T_K and T_{RKKY}, as well as the magnetic ordering temperature T_{mag} are shown against the antiferromagnetic exchange interaction J. In the upper part, there are four main areas with different characteristic behaviours which appear within this framework:

- (M)-*Magnetic materials*: For a small exchange integral J between the local moments and the conduction electrons, the Kondo type spin-flip scattering can be neglected, leading to a magnetically ordered ground state (mediated by the RKKY interaction).

- (KM)-*Kondo Magnetics*: With increasing J and at high temperature regime, the Kondo characteristics start to manifest itself within the system as a logarithmic increase in the resistivity with decreasing temperature in the high temperature free-ion regime. However, at low temperatures magnetic ordering is observed due to the stronger RKKY interaction.

- (HF)-*Heavy Fermions*: In this region with increasing J, magnetic ordering is suppressed due to the dominance of the spin fluctuations caused by the Kondo effect. There is a large increase in the density of states (DOS) due to the Abbikosov-Suhl resonance (ASR) which creates quasi-particles. At a critical value of J, ordering occurs in the zero-temperature limit, this is commonly known as a quantum phase transition, where unconventional or non-Fermi liquid behaviour may be observed.

- (IV)-*valence fluctuating or intermediate valence compounds*: With further increasing J, real excitations between neighbouring valence states generate a non-integer valence. In this case, a non-integer occupancy of the $4f$ level is found. At the same time, the high DOS and in consequence the HF behaviour is destroyed.

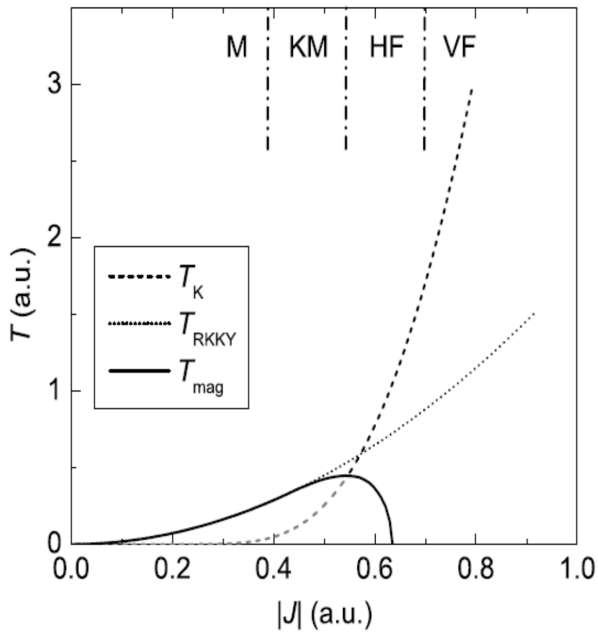

Figure 2.1: Doniach phase diagram [29]. T_K and T_{RKKY} are the characteristic temperatures of the Kondo and the RKKY interaction, respectively. In the upper part, the regions with different behaviour are marked :M - magnetic materials, KM-Kondo magnetics, HF-heavy fermions, and VF-valence fluctuating or intermediate-valence compounds.

2.2.3 Landau Fermi-liquid Theory

The electric properties of most metals can be well understood from the free electron model [30], where the electrons are treated as non-interacting. This model describes the electrons in the outermost shell of the atoms. In a crystal, these electrons are rather free to move around among the atoms, and can thus be described as an electron gas. The deviation from ideal gas behaviour can in many cases be captured by the concept of Fermi liquid which was first introduced by the Russian physicist Lev Landau [31]. However, Landau-Fermi liquid (LFL) theory which is based on the concept of quasiparticles [31–34] assumes a one-to-one corresponding of excitations (quasiparticles) of an interacting system with those of a non-interacting one (free electron gas), where the interactions are replaced by a constant effective potential. At low enough temperatures, the energy uncertainty associated with the finite life time of the quasiparticles is lower than the thermal energy k_BT. In this case, the properties of the system of interacting fermions are similar to those of the Fermi gas, which however will differ from those in the non-interacting gas. The electron-electron interactions mainly cause a renormalization of the particle mass, hence the free-electron mass is replaced by the effective mass m^*. LFL theory thus predicts that the low temperature properties of a Fermi system obey the same laws as the Fermi gas with a renormalized effective mass m^*. In particular, the specific heat, susceptibility and resistivity contribution of a Landau Fermi liquid behave as [35]:

$$\frac{C(T)}{T} = \gamma_{FL} = \left(\frac{m^*}{m_e}\right)\gamma_0, \qquad \text{where} \qquad \gamma_0 = \left(\frac{\pi^2 k_B^2}{3}\right)\eta(\epsilon_F), \tag{2.8}$$

$$\chi(T)_{FL} = \left(\frac{m^*}{m_e}\right)\frac{\chi_0}{1+F_\alpha^0}, \qquad \text{where} \qquad \chi_0 = \mu_B^2\eta(\epsilon_F), \tag{2.9}$$

$$\rho = \rho_0 + AT^2, \tag{2.10}$$

where m_e is the free electron mass, F_0^a is a Landau parameter, ρ_0 is the residual resistivity, and A is a scattering coefficient proportional to $(m^*)^2$. The linear temperature dependence of the electronic specific heat and the constant Pauli susceptibility χ_0, which are predicted as in the case of noninteracting electrons, are actually detected in nonmagnetic metals. In HF the hybridization of the $4f$ electron states with the conduction-electron states gives rise to very large effective masses of (100 to 1000) m_0. Despite the strong interactions, a large number of these systems still behave like a LFL at low T. Due to the large effective masses, they exhibit a strongly enhanced Pauli susceptibility χ_{FL} , a large γ_{FL} coefficient, and a ρ_{FL} contribution to the resistivity at low T. Comparing Eq 2.8 and 2.9 it is evident that the quantites χ_{FL} and γ_{FL} are similarly enhanced by a factor m^*/m_0 compared to the free-electron values. This is expressed by the dimensionless Sommerfeld-Wilson ratio RSW [20], which relates χ_{FL} and γ_{FL} as:

$$R_{SW} = \frac{\pi^2 k_B^2}{3\mu_0\mu_{eff}^2}\frac{\chi}{\gamma}. \tag{2.11}$$

For noninteracting electrons $R_{SW} = 1$, while it typically takes values between 2 and 5 for HF systems.

2.2.4 Non-Fermi liquid behaviour

After it had been established that most of the heavy-fermion systems obey Fermi liquid behaviour at low temperatures due to strong interactions, some of them have recently appeared not to follow this behaviour and are characterized by Non-Fermi liquid (NFL). Non-Fermi liquid (NFL) behaviour manifests itself in the power-law of physical quantities,

with exponents different from those of a Fermi liquid [34]. At low temperatures (10 K) physical properties are found to be as such:

$$C(T)/T \propto -[(1/T_0)ln(T/T_0)], \tag{2.12}$$

$$C(T)/T \propto -[1-(T/T_0)^{1/2}] \qquad \text{or} \qquad -ln(T/T_0), \tag{2.13}$$

$$\rho(T) \propto [1-a(T/T_0)^2], \tag{2.14}$$

where the energy scale parameter T_0 is related to spin fluctuation energies in ω and q [36], and a is a prefactor. However, current theories to explain NFL behaviour have played an important role in experimental efforts. These theories can be divided into three general categories: multichannel Kondo models, models based on nearness to a magnetic transition that has an ordering temperature near 0 K (the quantum critical point), and models based on a disorder that can induce a spread of Kondo temperatures T_K.

2.2.4.1 Multichannel Kondo model

The ordinary single channel Kondo model, as it was described above, consists of one or more spin 1/2 local moments interacting antiferromagnetically with conduction electrons in a metal. The simplest extension of this ordinary Kondo model in metals which yields non-Fermi liquid physics is the multichannel Kondo impurities in which the conduction electrons are given an extra quantum label known as the channel [37]. In other words, the local moment interacts with different channels of conduction electrons. The independent screening by more than one channel produces an overcompensation regime of the local moment [38], and therefore, non-Fermi liquid is possible. Usually, the M-channel Kondo model is described by a Hamiltonian that shows the interaction between the conduction electrons in M identical bands or channels with an arbitrary localized spin $\vec{S_I}$[37]. However, the ground state of this model with impurity S_I but different M can fall into three different cases for antiferromagnetic coupling $J > 0$ summarized as [36, 37]:

- *Compensated* ($M = S_I$): the number of conduction-electron channels is just sufficient to compensate the impurity spin into a singlet. This gives rise to normal Fermi-liquid behaviour.

- *Undercompensated* ($M < S_I$): the impurity spin is not fully compensated since there are not enough conduction-electron degrees of freedom to yield a singlet ground state.

- *Overcompensated* ($M > S_I$): the impurity spin is overcompensated and the critical behaviour (divergence in J in which the spin affects the conduction electrons, power law, or logarithmic behaviour in measured quantities like magnetization, resistivity or specific heat) sets in as the temperature and external field $\rightarrow 0$.

Let us now focus to the case $S_I = 1/2$ and discuss the physical properties at low temperatures. In the case of $M = 1$, the ordinary Kondo problem, C/T tends to a constant value proportional to $1/T_K$. In the two-channel Kondo effect($M = 2$), the Sommerfeld coefficient γ and the magnetic susceptibility $\chi(T)$ show $-lnT$ divergence and the electrical resistivity obeys $\rho(T) \propto \text{constant} \pm \sqrt{T}$ in the limit $T \rightarrow 0$ with the residual entropy $S(T \rightarrow 0) = ln\sqrt{2}$ [39]. Finally, when $M \geq 2$ which is the case of overcompensated, NFL behaviour with temperature dependence of $\rho(T) \propto T^{2/(2+M)}$ for the electrical resistivity and $C(T)/T \propto T^{[(2-M)/(2+M)]}$ for the electronic specific heat is expected [37].

2.2.4.2 Disordered Kondo Lattice

As was discussed above, the Kondo temperature T_K is a characteristic temperature in the single-channel Kondo problem below which an impurity $S = 1/2$ magnetic spin is compensated by the surrounding conduction electrons. This T_K value may be considered as a crossover temperature below which Fermi-liquid behaviour occurs. Generally, in a random diluted solution of impurities, the microscopic parameters J (strength of hybridization) and $N(E_F)$ (density of state at Fermi level) which determine the coupling between magnetic impurity and conduction electrons, acquire well defined values yielding a unique Kondo temperature for the system under consideration. However, in disordered systems, a distribution of Kondo temperatures may arise from statistically fluctuating J and/or $N(E_F)$. This situation arises in disordered heavy-fermion systems, where the competition of Kondo screening and interaction of magnetic moments takes place in a disordered environment, often leading to non Fermi-liquid behaviour [36]. Recently, in the work by Castro Neto *et al.* [40], non-Fermi-liquid behaviour in disordered systems is described as arising from disorder and the competition between the RKKY spin interaction and the Kondo moment-compensation effect leading to Griffiths-phase (rare strongly coupled magnetic clusters) behaviour [41]. The model of Castro Neto *et al.* predicts that the low temperature magnetic susceptibility and electronic specific heat are characterized by the power-law $\chi \propto C(T)/T \propto T^{\lambda+1}$ with an exponent $\lambda \sim 0.7 - 0.8$. In addition, the

low temperature electrical resistivity can be described by $\rho(T) - \rho_0 \propto T^n$, where in many cases $n \approx 1$ rather than $n = 2$ except for Fermi liquid behaviour.

2.2.4.3 Quantum Criticality phase

Usually, Quantum Criticality phase (QCP) manifests itself in magnetic materials when their magnetic transition phase is suppressed to 0 K by pressure, magnetic field or chemical substitution. The quantum phase transition occurring at 0 K can not happen from thermal fluctuations, and hence the quantum fluctuations are responsible for this kind of phase transition [34, 36, 42]. In this case, NFL behaviour observed in such materials might be attributed to the quantum fluctuations of the order parameter at low temperatures near $T = 0$. Quantum critical phenomena have been investigated using renormalization-group theory by a number of workers [43–45]. However, the QCP models predict that the thermodynamic properties will diverge as power-laws, where many Non-Fermi liquid (NFL) systems exhibit logarithmic divergences (i.e.$-lnT$). In the vicinity of the zero temperature QCP and according to a model by Millis and Hertz [36], in the case of antiferromagnetism, $C/T = \gamma_0 - a\sqrt{T}$, $\chi \backsim T^{3/2}$, and $\rho = \rho_0 + cT^{3/2}$ and in the case of ferromagnetism $C/T = a \log (T_0/T)$ and $\rho = \rho_0 + cT$ are observed.

2.3 Thermodynamic properties of rare earth intermetallic compounds

2.3.1 Specific heat

The specific heat capacity is one of the most important physical quantities which can assist in determining the magnetic properties of solids. The specific heat is the amount of heat necessary to raise the temperature of a material by a unit amount. Depending on whether the pressure or the volume is kept constant, the specific heat is shown by C_P or C_v respectively. At high temperatures (near room temperature), the specific heat of materials is explained by the classical concept of degrees of freedom. Dulong and Petit predicted a constant specific heat value of 24.9 mJ/(mole.K) for most solids at room temperature. This can be explained by the equipartition theorem; each atom can be considered as an independent oscillator with average kinetic energy $\frac{3}{2}k_BT$ and average potential energy $\frac{3}{2}k_BT$. The average total energy is thus $3N_Ak_BT$ where N_A is the Avegadro's number . Therefore the classical heat capacity follows:

$$C_v = \frac{dU}{dT} = 3N_Ak_B = 3R, \tag{2.15}$$

where $R = N_A K_B$ is the ideal gas constant. This equation is often used to examine whether the sample structure and the number of atoms per formula units is consistent with the measured and classical limits of heat capacity. However, at low temperatures the heat capacity varies and goes to zero as the temperature goes to zero. This cannot be explained according to the classical concept of degrees of freedom. This only can be explained by quantum mechanics mechanisms.

The specific heat capacity originates from different types of contributions: the lattice or phonon contribution C_{ph}, the electric contribution C_e, the magnetic contribution C_{mag} and the nuclei contribution C_{nucl}. Therefore, the resulting total specific is the sum of these contributions and can be written as:

$$C_{tot}(T) = C_{ph}(T) + C_e(T) + C_{mag}(T) + C_{nucl}(T). \tag{2.16}$$

The low temperatures phonon contribution to the specific heat can be successfully explained in terms of the Debye model [46]. The fundamental assumption in the Debye model is that the solid can be treated as isotropic elastic continuum for all possible vibrational modes. This assumption leads to the Debye phonon heat capacity given in the form:

$$C_v(T) = 9NR(\frac{T}{\theta_D})^3 \int_0^{x_D} \frac{x^4 e^x}{(e^x - 1)^2}, \tag{2.17}$$

with $x = \dfrac{h\omega}{k_B T}$, N is the number of atoms per formula unit. For the case $T \leqslant \theta_D$

$$C_v(T) = \frac{12\pi^4}{5}(\frac{NR}{\theta_D^3})T^3 = \beta T^3, \tag{2.18}$$

where $\beta = (\dfrac{1943.7N}{\theta_D^3})$ J/mol.K^4 with θ_D the Debye temperature in K. Eq 2.18 is well-known as the Debye T^3-law which can serve in calculating the value of θ_D after extracting the value of β from the heat capacity data. Experimentally, the results of phonon heat

capacity of rare earth based compounds are obtained from their La, Y or Lu non-magnetic based counterparts.

Although the electronic heat capacity is very small at room temperature, it is very important at low temperature for classifying whether the compound is in the heavy fermion state or not. In a metal, only those electrons close to the Fermi level, within the approximate range k_BT of the Fermi energy, contribute to the specific heat. Therefore, the electronic coefficient γ is proportional to the density of states at the Fermi level $N(E_F)$ which in turn is related to the effective mass m^* of the conduction electrons in the form [47]:

$$\gamma = \frac{2}{3}\pi^2 k_B^2 N(E_F), \tag{2.19}$$

with

$$N(E_F) = \frac{m^* k_F}{2\pi^2 \hbar^3}. \tag{2.20}$$

At low temperatures and in most cases, the phonon or lattice vibration must be considered. Thus the total heat capacity can be expressed as:

$$C_v(T) = \gamma T + \beta T^3. \tag{2.21}$$

It is observed that the coefficient γ of typical heavy fermion materials is temperature dependent and becomes more enhanced with a decrease in temperature. Thus the large value of γ has become a distinguishing feature of this class of materials. For instance, the archetypal compounds within this class of materials are $CeAl_3$ and $CeCu_6$ with γ=1600 mJ.mole^{-1}.K^{-2} [8] and 1670 mJ.mole^{-1}.K^{-2} [48] respectively compared to that of a normal metal such as copper Cu with γ=0.7 mJ.mole^{-1}.K^{-2} [10]. The large values of γ for such compounds originates from the fact the $4f$-levels in these compounds lie close to the Fermi levels, resulting in a strong interaction between the conduction electrons and the $4f$ electrons. The interaction between these being antiferromagnetic, the conduction electrons gradually compensate the localised $4f$ moments as the temperature is lowered below the characteristic temperature T^*. Subsequently, this interaction leads to a sharp resonance peak in the density of states at the Fermi level and hence to a large γ value. The temperature dependence of γ observed in these $4f$ compounds is a consequence of

the gradual compensation process of the $4f$-moment by the conduction electrons. For this reason γ is commonly defined as $\gamma = C/T$ for the heavy-fermion compounds [46]. The specific heat and the occurrence of high γ values have been studied for many heavy fermion and Kondo systems.

In addition to lattice and electronic contributions, the various magnetic excitations can also contribute to the total specific heat capacity. Specifically, the thermal excitation of spin waves results in such magnetic heat capacity contribution. Quantized spin waves are called magnons. According to the magnetic order there are two main types of magnons: ferromagnetic (FM) and antiferromagnetic (AFM) magnons. Hence, for ferromagnetic materials at low temperature the magnon contribution can be given as:

$$C_M(T) = S_f \left(\frac{k_B T}{2JS} \right)^{3/2}, \tag{2.22}$$

where S_f is a quantity that depends on the type of lattice parameter under consideration, J is the exchange term, S is the spin angular momentum. A number of magnetic rare earths possess a strong anisotropy resulting from the interaction between the non-spherical charge distribution of the ions with the crystal electric field (CEF). This leads to a formulation of an energy gap, E_g, in the spin wave dispersion. This energy gap causes an exponential term to appear in the magnon specific heat, i.e:

$$C_M(T) \sim T^{3/2} exp^{-E_g/k_B T}. \tag{2.23}$$

Ignoring the energy gap, the total low-temperature specific heat of a metallic ferromagnet may be written as:

$$C_v(T) = \gamma T + \beta T^3 + \delta T^{3/2}. \tag{2.24}$$

In the case of antiferromagnetic materials, the magnons specific heat is proportional to T^3 and is given as:

$$C_M(T) = S_{af} R \left(\frac{k_B T}{2J'S} \right)^3. \tag{2.25}$$

The constant S_{af} in the Eq 2.25 depends on the crystal structure and has been calculated for several types of lattices [49, 50]. For antiferromagnets too, when there is an energy gap in the magnon dispersion relation, Eq 2.25 contains an exponential term:

$$C_M(T) \sim T^3 exp(-E_g/k_B T). \tag{2.26}$$

Similar to ferromagnetic case, ignoring the energy gap, the total low-temperature specific heat may be written as:

$$C_v(T) = \gamma T + \beta T^3 + \delta T^3. \tag{2.27}$$

One of the most important quantities that is associated with magnetic heat capacity is the magnetic entropy (S_{mag}). The magnetic entropy provides an idea about the degeneracy of the system. The magnetic entropy is usually given by integrating the magnetic specific heat as:

$$S_{mag}(T) = \int \frac{C_M}{T} dT. \tag{2.28}$$

Because of the weakly-interacting local magnetic moment between rare-earth atoms, each ion has an intrinsic total angular momentum J, and the ground state will be $(2J+1)$ fold degenerate. The temperatures increasing stimulates all these states to be populated, and hence the magnetic entropy should saturate to:

$$S_{mag} = Rln(2J+1). \tag{2.29}$$

The temperature at which the entropy saturates provides information about crystalline electric fields(CEF). The crystalline electric fields lead to the splitting of the ground states into different discrete energy levels. The occupation of these different discrete energy levels, gives rise to an additional contribution to the total specific heat, known as the Schottky term. In this case, the internal energy is changed, leading to a hump which clearly appears in the magnetic specific heat curve Fig 2.2. This hump cannot be noticed in the total specific heat curve, because it is superimposed on the lattice and other contribution [51]. For the simple case of two energy levels ε_0 and ε_1 and with degeneracies g_0 and g_1, respectively,the Schottky term can be written as:

$$C_{sch}(T) = R\left(\frac{\Delta}{T}\right)^2 \frac{(g_0/g_1)exp(\Delta/T)}{[1+(g_0/g_1)exp(\Delta/T)]^2}. \tag{2.30}$$

In the case of heavy fermion and Kondo systems, an exact solution for the spin 1/2 Kondo [25] and Anderson models [52] for the thermodynamic equation was obtained in the scope of the Bethe-*ansatz* solution of the Coqblin-Schrieffer model. The resulting solutions show the crossover from the local-moment regime to Fermi-liquid behaviour for the spin 1/2 problem, at a characteristic temperature T_K. Oliveira and Wilkins [21] using the renormalization group theory, obtained the impurity specific heat over a large temperature range. The resulting specific heat in this model shows a maximum at $0.67T_K$ and in the zero temperature limit was found to be:

$$\lim_{T\to 0}\frac{C_{imp}(T)}{T} = \gamma(0) = \frac{2\pi^2}{3}\frac{0.103R}{T_K}. \tag{2.31}$$

An exact solution to the Coqblin-Schrieffer model for the heat capacity was also obtained using the Bethe-*ansatz* method. Rajan [53] proposed thermodynamic equations of Coqblin-Schrieffer model for extended values of j (j>1/2). The resulting specific heat for the case $j = 1/2$ shows a peak at $0.45T_K$ and in the zero-temperature limit can be written in the form:

$$\lim_{T\to 0}\frac{C_{imp}(T)}{T} = \gamma(0) = \frac{(N-1)\pi R}{6T_0}, \tag{2.32}$$

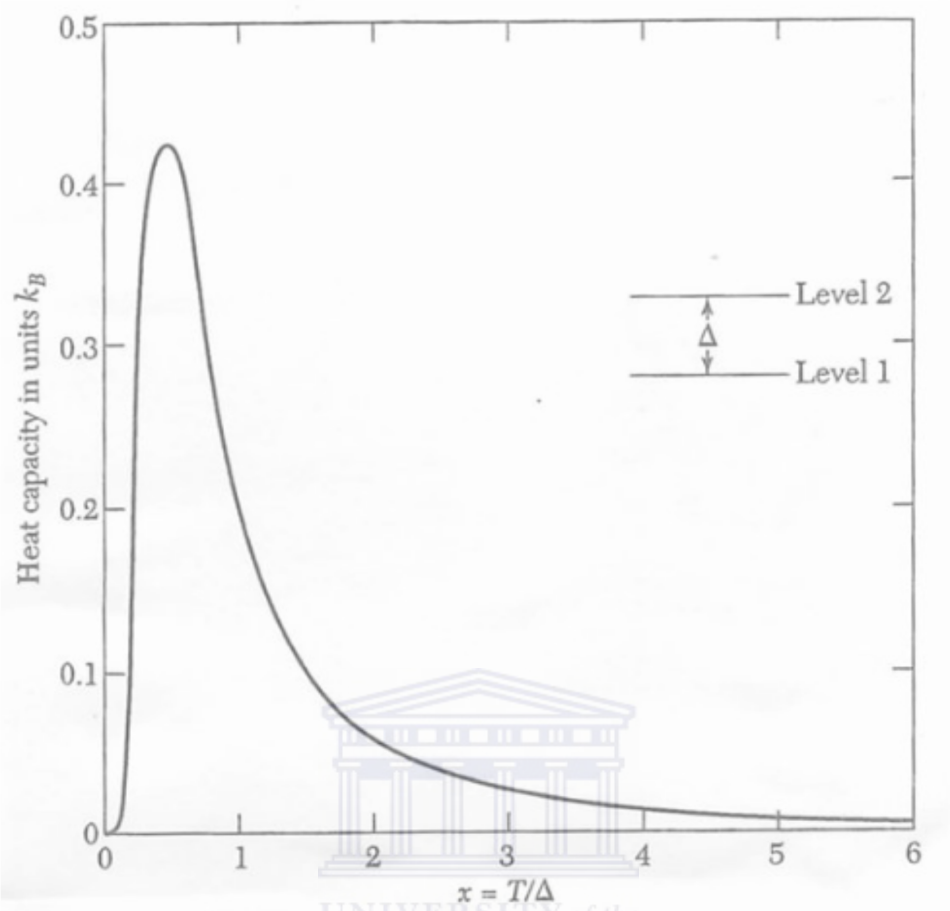

Figure 2.2: The Schottky heat capacity of a two level system [46].

where $N = 2j + 1$ is the multiplet and T_0 is a characteristic temperature related to T_K through Wilson number $W = T_K/T_0$, with $\frac{W}{4\Pi} = 0.102676$ [54].

2.3.2 Magnetic properties

2.3.2.1 Basics concepts

The magnetism of materials originates from the magnetic moment of an atom or ion, generated by the motion and intrinsic spin of electrons around the nucleus. This magnetic moment which can either be localized or itinerant in the metal is a fundamental quantity in magnetism, and can be defined as:

$$\mu = \gamma J. \tag{2.33}$$

The constant γ is defined as the ratio of the magnetic moment to the angular momentum, called the gyromagnetic ratio. J is the total angular momentum given by:

$$\vec{J} = \vec{L} \pm \vec{S}, \tag{2.34}$$

where $\vec{L}$ and $\vec{S}$ are orbital and spin angular momenta. For a free atom g is called the g_J-factor given by Lande' equation :

$$g_J = 1 + \frac{J(J+1)S(S+1) - L(L+1)}{2J(J+1)}, \tag{2.35}$$

μ_B is the Bohr magneton defined as:

$$\mu_B = e\hbar/2m. \tag{2.36}$$

Where e is the free electron charge, $\hbar$ is the reduced Planck constant and m is the electron mass. According to the Hund's rules, the value of J is $L - S$ if the electron shell is less than half full and $L + S$ if it is more than half full. Since the Hund's rules predict the ground state magnetic configuration, the magnetic moment of an ion can be estimated assuming that only this ground state is populated. Therefore, at high temperatures in the paramagnetic region the effective magnetic moment is given as [10]:

$$\mu_{eff} = g_J\sqrt{J(J+1)}\mu_B \tag{2.37}$$

2.3.2.2 Curie-Weiss Law

The magnetic moment per unit volume is defined as magnetization (M). The magnetization is usually measured as a function of temperature (T) and magnetic field (H). To determine the temperature dependence of the magnetization it is useful to analyse a

system of N states with energies E_n, and hence the magnetization is given by [10]:

$$M = -\frac{N}{V}\frac{\partial E_n(H)}{\partial H} = \frac{N}{V} g_J \mu_B J B_J(\beta g_J \mu_B J H) \tag{2.38}$$

where B_J is the Brillouin function defined as:

$$B_J(x) = \frac{2J+1}{2J}\coth\left(\frac{2J+1}{2J}x\right) - \frac{1}{2J}\coth\left(\frac{1}{2J}x\right). \tag{2.39}$$

At high temperatures the Brillouin function may be approximated as:

$$B_J(x) \approx \frac{J+1}{3J}x + O(x^3). \tag{2.40}$$

Therefore, the susceptibility as a function of temperature is given by:

$$\chi = \frac{M}{H} = \frac{n\mu_0\mu_{eff}^2}{3k_B T} = \frac{C}{T}, \tag{2.41}$$

where C is the Curie constant. The Eq 2.41 is known as the Curie's law, which in fact illustrates that the high temperature magnetic susceptibility is inversely proportional to temperature. However, for materials with magnetic ordering, there is some spontaneous interaction between the neighbouring unpaired electrons at low temperature. In this case, the Curie's law is modified by incorporating an additional parameter θ (Weiss temperature), and becomes the Curie-Weiss's law which is written as:

$$\chi = \frac{C}{T-\theta}. \tag{2.42}$$

2.3.2.3 Magnetic ordering types

Materials which are magnetized, more or less, in a magnetic field are called magnetic materials. There can be various types of magnetism such as diamagnetism, paramagnetism, ferrmagnetism. But in this section we will be concern with some of the types, which are relevant to the work in this thesis. However, depending on the sign and the value of θ of the Curie-Weiss's law, magnetic materials are divided into three types. If $\theta = 0$ the material is classified as an ideal paramagnet, if $\theta > 0$ the material may be classified as an enhanced paramagnet or could be for ferromagnetic for much larger θ, if $\theta < 0$ the material is antiferromagnetic or ferromagnetic.

In most cases, paramagnetic materials contain magnetic atoms or ions whose spins are isolated from their magnetic environment and can more or less freely change their directions. At finite temperatures, the spins are thermally agitated and take random orientations. During the application of a magnetic field, the average orientation of spins are slightly changed so as to produce a weak induced magnetization parallel to the applied magnetic field. The susceptibility in this case is inversely proportional to the absolute temperature (the Curie law). Conduction electrons which form an energy band in metallic crystals also exhibit paramagnetism. Since, in this case, the excitation of minus spins to the plus spin band is opposed by an increase of kinetic energy of electrons irrespective of temperature, the susceptibility is independent of temperature which is known as Pauli paramagnetism [10, 55].

Antiferromagnetism is a weak magnetism which is similar to paramagnetism in the sense that it exhibits a small positive susceptibility. The temperature dependence of susceptibility of this kind of magnetism, however, characterized by the occurrence of a kink in the $\chi - T$ curve at the so-called Neél temperature. The reason for this, is that below this temperature antiparallel spins completely cancels each other. In such an antiferromagnetic arrangement of spin, the tendency to be magnetized by the external field is opposed by a strong negative interaction acting between plus and minus spins. Above the Neél point, the spin arrangement becomes random, so that susceptibility now decreases with an increase in the temperature.

In the case of ferromagnetism, the spins are aligned parallel to one another as a result of strong positive interaction between the neighbouring spins. As the temperature increases, the arrangement of spins is disturbed by thermal agitation, thus resulting in a temperature dependence of spontaneous magnetization. Above the Curie point, the susceptibility obeys the Curie-Weiss law, which states that the inverse susceptibility $1/\chi$

rises from zero at the Curie point and increases linearly with temperature. In ferromagnetic materials, θ is positive [56] and typically close to the Curie temperature T_C.

other types of magnetic ordering which appear at some places in this thesis are metamagnetism and spin glasse. Metamagnetism is the name given by Becquerel and van den Handel [57] to the phenomenon which is interpreted as a transition from antiferromagnetism to ferromagnetism and vice versa, caused by the application of a strong field or by a change in temperature. This phenomenon is clearly visible in the field dependence of magnetization measurements. In this case, the magnetization initially increases with the field slowly, while above a certain field it increases suddenly.

Spin glass may be defined as a random, mixed interacting magnetic system characterized by a random freezing of spin at a well-defined temperature T_f below which a high irreversible, metastable frozen state occurs without the usual long-range spatial magnetic order [58]. The two important prerequisites of spin glass are firstly the randomness in either position of spin, or the signs of the neighbouring coupling: ferro ($\uparrow\uparrow$) or antiferromagnetic ($\downarrow\uparrow$). There must be disorder, site or bond in order to create a spin glass, otherwise the magnetic transition will be of the standard ferromagnetic or antiferromagnetic type of long-range order.

2.3.2.4 Magnetic susceptibility of Kondo systems

Similar to the specific heat, an exact solution for spin $-1/2$ Kondo model, for susceptibility was obtained. Wilson [20], using renormalization group theory, found an exact solution for the Kondo ground state. A singlet (non-magnetic) in which the spins of the magnetic ions were fully compensated for by the conduction electrons. Above T_K the single-ion contribution to the magnetic susceptibility ($\chi_{singleion}(T)$) showed a quasi-free behaviour similar to that predicted by Curie-Weiss law, while below T_K the single ion contribution to the magnetic susceptibility showed a Fermi liquid behaviour. In the latter behaviour, a singlet ground state is formed and hence the effective magnetic moment of the magnetic ion is fully quenched. The zero temperature limit of the resulting susceptibility achieves a constant value given as [20]:

$$\chi(T \to 0) = \frac{0.103(g_J \mu_B)^2}{T_K}. \tag{2.43}$$

The susceptibility of the single impurity system which is based on the Bethe-ansatz so-

lution for $s = j = 1/2$ case shows a Curie-Weiss behaviour at higher temperatures and a Pauli-like behaviour at the lowest temperatures. Rajan [53], extended the theory to higher values of j using the Bethe-*ansatz* solution of the Coqblin-Schrieffer Hamiltonian. At Zero temperature and field with total angular momenta j= 1/2,...,7/2, the susceptibility is obtained analytically and expressed in the form:

$$\chi(T \to 0) = \frac{N(N^2-1)g_J^2\mu_B^2}{24\pi k_B T_0} \tag{2.44}$$

where $N = 2j + 1$ is the degeneracy of the system, and T_0 is related to T_K through the Wilson number (W=1.2901): $W = T_K/T_0$ [59]. The result for the case $j = 1/2$ is consistent with that obtained by Wilson within the renormalization group method below T_K [20]. The finite temperature behaviour of the susceptibility for all higher values of j shows a maximum at a critical temperature T_0, which increases with increasing j. The crossover of the susceptibility from temperature-independent Pauli behaviour to temperature-dependent Curie-Weiss behaviour depends on the temperature regions. At zero temperature and for all values of j, the susceptibility saturates and follows Pauli-type behaviour. At higher temperature ranges well above T_K, the susceptibility shows Curie-Weiss behaviour.

2.3.2.5 Crystalline electric field

In most compounds, the magnetic ions that form part of a crystalline lattice, experience a crystalline electric field produced by surrounding ions and valence electrons. The surrounding ions, modelled as point charges, produce the crystal electric field (CEF) which is yet another mode of interaction between a magnetic moment and its environment in the metal [60]. Although the exchange interaction may be anisotropy, the crystal electric field can also be considered as a primary origin of anisotropies observed in the magnetic properties of rare earth intermetallic compounds. Thus, the magnetization in the normal state is found to have a strong magnetic anisotropy due to CEF, splitting a $2J+1$ degenerate ground state of the rare earth ions where J is the total angular momentum [61, 62]. Moreover, the CEF will partially lift the maximum degeneracy allowed by the J-multiplet. The number of resulting multiplets is determined by the local crystal symmetry. Their relative energetic positions depend on the exact form and magnitude of the CEF. For ions with an odd number of $4f$ electrons, such as Ce^{3+}, the CEF leaves at least a twofold degeneracy of each level, in accordance with Kramer's rule. The energy splitting of an excited CEF level is simply given as:

$$\Delta_{CEF} = k_B T_{CEF}, \tag{2.45}$$

where Δ_{CEF} is the energy splitting between the ground state and an excited CEF state, and T_{CEF} is the temperature corresponding to a CEF splitting of Δ_{CEF}.

The CEF splitting affects many physical properties. For a system with a first excited level at $k_B T_{CEF}$ above the ground state, only the lowest lying multiplet has a significant probability of occupancy for $T \ll T_{CEF}$. Consequently, the properties of the system are determined by the ground-state multiplet. With increasing temperature higher CEF levels become populated. The corresponding increase of entropy shows up as an extra contribution to the specific heat of the system in the region of T_{CEF}, in the form of a Schottky anomaly. The transport properties reflect the enhanced scattering on CEF excitations around T_{CEF}. The change of the effective moment with increasing occupancy of higher lying multiplets becomes apparent in the magnetic susceptibility. At low temperatures ($T \ll T_{CEF}$) the effective magnetic moment is determined by the ground-state multiplet. A Curie-Weiss behavior of the susceptibility with the free-ion magnetic moment is observed only at temperatures well above the excitation temperature of the highest multiplet.

A much simpler method to calculate the effect of the CEF potential is to introduce the Stevens equivalent operators [63]. It has been shown that the matrix elements of the crystal field Hamiltonian are proportional to a set of operators containing components of the total angular momentum, J. The Hamiltonian in this representation then becomes:

$$H_{CEF} = \sum_n \sum_{m=0}^{n} B_n^m O_n^m, \tag{2.46}$$

where the O_n^m are the elements of the Stevens operator which depends on J, and the terms B_n^m are numerical coefficients known as crystal field parameters. The sign and magnitude of the coefficients B_n^m are very important in determining the relative CEF energies. One of the ways to determine B_n^m is approximately through the point charge calculations while the other way is through experimental means by measuring susceptibility or heat capacity using neutron diffraction. Since point charge calculations are poor approximations, nowadays the sophisticated computational tools are used to perform these calculations.

If the crystal field Hamiltonian is applied onto the wave function of the $4f$ ion, one obtains the energies of the eigenstates created by the crystal field splitting as:

$$H_{CEF}|\psi\rangle = E|\psi\rangle. \tag{2.47}$$

The appropriate crystal field Hamiltonian for a cubic point group symmetry is given by :

$$H_{CEF} = B_4^0(O_4^0 + 5O_4^4) + B_6^0(O_4^0 - 21O_6^6). \tag{2.48}$$

where the crystal field is fully determined by the two parameters B_4^0 and B_6^0. The corresponding eigenstates are Γ_7-doublet and Γ_8-quartet :

$$|\Gamma_7\rangle = a|\mp 5/2\rangle - b|\mp 3/2\rangle. \tag{2.49}$$

$$|\Gamma_8\rangle = |\mp 1/2\rangle. \tag{2.50}$$

$$|\Gamma_8\rangle = b|\mp 5/2\rangle + a|\mp 3/2\rangle. \tag{2.51}$$

For the hexagonal symmetry, the crystal field Hamiltonian is written as:

$$H_{CEF}^{hex} = B_2^0O_2^0 + B_4^0O_4^0 + B_6^0O_6^0 \tag{2.52}$$

In the case of Cerium systems the 6th order term vanishes; then the Hamiltonian becomes:

$$^{Ce}H_{CEF}^{hex} = B_2^0O_2^0 + B_4^0O_4^0. \tag{2.53}$$

The crystal field in hexagonal symmetry yields pure eigenstates, determined from J_z, and the ground state multiplet split into three Kramer's doublets:

$$|\Gamma_7\rangle = |\mp 1/2\rangle, \tag{2.54}$$

$$|\Gamma_8\rangle = |\mp 5/2\rangle, \tag{2.55}$$

$$|\Gamma_9\rangle = |\mp 3/2\rangle. \tag{2.56}$$

2.3.3 Magnetocaloric effect

Magnetocaloric effect (MCE) is the change in isothermal magnetic entropy (ΔS_m) and adiabatic temperature (ΔT_{ad}) that accompany magnetic transitions in materials during the application or the removal of magnetic field under adiabatic conditions. The physics of MCE effect gets enriched by correlated spin-lattice degrees of freedom. The MCE arises due to the presence of two energy reservoirs in magnetic materials: one with phonon and the other with magnon excitations. These two reservoirs are coupled by spin-lattice interaction. An external magnetic field affects the spin degrees of freedom resulting in heating or cooling of magnetic materials. This description of MCE indicate that the highest change in temperature is expected from strongly magnetostrictive magnetic materials. The MCE increases with an increase of the applied magnetic field and with the change of magnetization $M(T, H)$ during application of magnetic field. This implied that the effect reached its maximum in the vicinity of magnetic transition temperatures. Experimentally MCE can be measured in terms of: (i) isothermal magnetic entropy change and (ii) adiabatic temperature change. Other associated measures is the figure-of-merit (ZT) parameter and the relative cooling power (RCP).

2.3.3.1 MCE from magnetization

The change in isothermal magnetic entropy is calculated by using the isothermal magnetization data $M(T, H)$ measured at different temperatures near the magnetic transition temperature (T_C / T_N, of a ferromagnet / ferrimagnet / antiferromagnet). ΔS_m is often computed by numerically integrating the thermodynamic Maxwell relation [64, 65]

$$\Delta S_m(T, H) = S_m(T, H) - S_m(T, 0) = \int_0^H \left(\frac{\partial M}{\partial T}\right)_H dH. \tag{2.57}$$

Since $\frac{\partial M}{\partial T}$ has its maximum at the transition temperature, a large MCE is expected near the transition temperature. It is exceedingly high ("giant" or "colossal") for the first order phase transition. The upper limit for the molar magnetic entropy variation is given by the magnetic contribution [64, 66]

$$S_M^{max} = Rln(2J+1), \tag{2.58}$$

where R is the gas constant and J is the total angular momentum quantum number.

2.3.3.2 MCE from heat capacity data

The change in isothermal magnetic entropy can also be obtained from heat capacity data $C(T)$ measured in zero magnetic field and in applied magnetic field using the following relation [64, 65]:

$$\Delta S_m(T,H) = \int_0^T \frac{C(T,H) - C(T,0)}{T} dT, \tag{2.59}$$

where $C(T,0)$ and $C(T,H)$ are the heat capacities of the magnetic materials measured at temperature T in zero magnetic field and in an applied field H.

The adiabatic temperature change $\Delta T_{ad}(T,H)$ can be determined using the experimentally measured heat capacity $C(T,H)$ [64, 65]:

$$\Delta T_{ad}(T,H) = \int_0^H \left(\frac{\partial M}{\partial T}\right)_H \frac{T}{C(T,H')} dH'. \tag{2.60}$$

The relative cooling power RCP of a refrigerator is defined as the amount of heat transfer between the hot and the cold reservoir during the complete refrigeration cycle and is used as a key parameter to quantify the efficiency of the refrigerator. RCP is calculated as the area under ΔS_m versus. T curve [66] using the formula:

$$RCP = \Delta S_m^{Max} \times \Delta T_{FWHM}, \tag{2.61}$$

where $\Delta T_{FWHM} = T_{hot} - T_{cold}$. Here T_{hot} and T_{cold} are the temperature below and above T_C or T_N at 50% of the maximum magnetic entropy change, S_M^{max}.

2.4 Electrical transport properties

2.4.1 Boltzman's equation

Classical transport phenomena are controlled by two contrary mechanisms: driving forces induce a directive motion of the particles, while scattering retards it. Thus, transport properties in metals arise from electron scattering when a breakdown of the perfect periodic potential occurs in real crystals. This breakdown occurs from a variety of different scattering processes. A description for these scattering processes is given by the linearized Boltzmann equation. Under certain assumptions this theory may be used to describe charge and heat transport in solids. The requirement is that the charge or heat carriers can be described as classical particles with momentum $\hbar\vec{k}$ and position $\vec{r}$. At equilibrium the time-dependent distribution function $f(\vec{r,k},t)$ must satisfy the equation [47]:

$$\vec{k}.\nabla_k f + \vec{v}_k.\nabla_r f = \left(\frac{\partial f}{\partial t}\right)_c. \tag{2.62}$$

Here, $f(\vec{r,k},t)$ is a measure for the density of carriers with wave vector $\vec{k}$ at position $\vec{r}$ and time t. The velocity $\vec{v}$ is the group velocity of a wave packet of charge or heat carriers. Eq 2.62 when linearized leads to an integral equation, known as *Bloch equation* [47]. In general, a solution to this equation cannot be obtained in close form. The most powerful method of the solution involves the use of a variational principle first advanced by Kohler [67]. The application of this procedure requires first the selection of a suitable trial function containing parameters which are then adjusted in accordance with the variational principle. The transport coefficients (electrical conductivity, thermal conductivity, and thermoelectric power), in this variational method, appear as a ratio of determinants of infinite dimensionality. The other, and most direct, avenue leading to a solution of the Bloch equation, depends on the use of a relaxation time approximation given by:

$$\left(\frac{\partial f}{\partial t}\right)_c = -\frac{f - f_0}{\tau}. \tag{2.63}$$

The distribution function f_0 is given by the Fermi-Dirac or Bose-Einstein statistic in the case of fermion or bosons. The relaxation time τ is determined by the different effective scattering processes. If independent scattering processes with relaxation time τ_i are considered, the effective total relaxation time is generally calculated as the inverse of a sum of the inverse τ_i:

$$\frac{1}{\tau} = \sum_i \frac{1}{\tau_i}. \tag{2.64}$$

The solution of the linearized Boltzman's equation using the relaxation time approximation provides a basis for many theoretical calculations of thermal transport processes.

2.4.2 Electrical resistivity

Measurements of electrical resistivity properties are essential to understand the diverse physical properties of the rare earth intermetallic compounds. Usually these measurements may be used to determine the sample quality, scattering mechanisms, magnetic ordering temperature and to study the Kondo effect. For instance, the determination of Curie temperature of ferromagnetic materials is generally difficult from the temperature-dependent magnetization, since this feature is typically very broad. This is often not the case in measurements of the resistivity, where the resistivity sharply decreases below the Curie temperature, corresponding to a loss of disorder scattering from the magnetic moments. Also, these measurements may reveal properties that are not readily visible in the magnetization or specific heat, such as the appearance of gaps in the Fermi surface due to the charge or spin density waves.

The electric resistivity of metals and alloys originates from various types of scattering processes that conduction electrons experience along their motion in the crystals. These scattering processes can be due to:

• The presence of impurities either accidental or deliberate in the samples, and imperfections in crystals such as grain boundaries.

• The temporal displacement of ions from their fixed positions due to thermally excited lattice vibrations. This effect increases largely as the temperature rises.
• Deviation from perfect magnetic order caused by spin disorder in magnetic materials as the temperature is increased towards their ordering temperatures. This scattering attains its maximum value in the paramagnetic region.
• The localized magnetic moments of $4f$ or $5f$ atoms in dilute systems, especially, concentrated Kondo systems, HF materials, group IV and spin fluctuation systems.
• Electrons also scatter from each other but for normal metals this effect is very small. At higher temperature this effect is negligible due to the dominance of electron-phonon scattering [10].

Since the electron-electron scattering in a normal metal is often negligible at higher temperatures, the other types of scattering can be described in terms of a unique relaxation time. It should be noted that the relaxation time is an important parameter that is responsible for the magnitude of the electrical resistivity. The scattering processes mentioned above are based on the assumption that they are taken independently from each other as stated by Matthiessen's rule [68]. Accordingly, the resulting relaxation time takes the form:

$$\frac{1}{\tau} = \sum \frac{1}{\tau_i} = \frac{1}{\tau_0} + \frac{1}{\tau_{ph}} + \frac{1}{\tau_{mag}}, \tag{2.65}$$

where τ_0 and τ_{ph} are relaxation times for impurity and phonon scattering, respectively, and τ_{mag} is the relaxation time for spin fluctuations. Assuming the validity of Matthiessen's rule, the total resistivity $\rho(T)$ of a magnetic material may be expressed as:

$$\rho(T) = \rho_0 + \rho_{ph}(T) + \rho_{mag}(T). \tag{2.66}$$

The first term ρ_0 represents the contribution due to defects and imperfections to the total resistivity, which is dominant at the lowest temperatures and known as the residual resistivity. Since these defects or imperfections are temperature-independent, ρ_0 is also temperature-independent and exhibits a constant value when the temperature is lowered towards absolute zero. Furthermore, it should be noted that ρ_0 is a sensitive measure of the degree of perfection of a sample that is determined by a quantity known as a resid-

ual resistivity ratio RRR. This RRR of a sample is generally defined as a ratio of its resistivity at room-temperature to that extrapolated to 0 K as $RRR = \rho_{300K}/\rho_{0K}$. In this regard, the highest value of this ratio indicates the highest quality of the sample. In general, residual resistivity is affected by imperfections which modify some parameters in the samples such as band structure, the Fermi energy, the density of state and the effective mass. These parameters determine the magnitude of the RRR for a sample [47]. In order to lessen the RRR value, some techniques may be used during the sample synthesis such as remelting for several times and annealing at sufficiently high temperature.

The second term ρ_{ph} describes the temperature-dependence of resistivity due to the scattering of electrons from phonons which is called phonon-electron scattering. This scattering mechanism is dominant at higher temperature where the thermal vibrations of ions around their equilibrium positions, break down the regularity of ideal crystals that will produce displacements of the ions from their equilibrium positions. According to the Debye model [68], the term phonon is assigned to the thermal vibrations of ions. In this model, the highest phonon frequency in the Brillouin zone ω_{max} can be estimated roughly from the relation $\hbar\ \omega_{max} \approx k\theta_D$, where θ_D is the Debye temperature as deduced from heat capacity measurements. The temperature variation of electric resistivity due to the phonon contribution, $\rho(T)$, can be expressed by Bloch-Grüneissen Law [68]:

$$\rho_{ph}(T) = \frac{4\kappa}{\theta_R}\left(\frac{T}{\theta_R}\right)^5 \int_0^{\theta_R/T} \frac{x^5 dx}{(e^x - 1)(1 - e^x)}, \tag{2.67}$$

where κ is the electron-phonon coupling constant. θ_D is the characteristic temperature for the lattice resistivity and takes on a numerical value. The lattice specific heat-derived Debye temperature θ_D is often used instead of θ_R because their values are nearly alike [47]. At high temperatures ($T \geq \theta_R/2$), the number of phonons that are created is proportional to the temperature and hence $\rho_{ph} \propto T$ is obtained in this region [30]. At sufficiently low temperatures, electron-phonon scattering is nearly elastic [30] and the scattering probability reaches a T^5-dependence so that $\rho_{ph} \propto T^5$. However, in some cases in alloys containing d-transition metals, T^3-dependence is expected instead of a T^5-dependence due to $s - d$ interband scattering [69]. Also a deviation from the linear behaviour at high temperatures occurs in alloys of d-transition metals, in which interband $s - d$ scattering into filled d-band is responsible for an additional term called the Mott's term in the resistivity which is proportional to T^3 [70]. In such cases the Bloch-Grüneissen expression is replaced by the Bloch-Grüneissen-Mott expression expression in the form:

$$\rho_{ph}(T) = \frac{4\kappa}{\theta_R}\left(\frac{T}{\Theta_R}\right)^5 \int_0^{\theta_R/T} \frac{x^5 dx}{(e^x-1)(1-e^x)} - \alpha T^3. \tag{2.68}$$

The third term $\rho_m(T)$ in Eq 2.66 which is also symbolized as $\rho_{4f}(T)$ represents the magnetic contribution to the total electrical resistivity. This magnetic contribution originally results from the scattering of conduction electrons in the host metals, from magnetic $4f$-ions of the rare earth elements. These magnetic $4f$-ions which are also known as local moments, usually influence the resistivity of both magnetically ordered and Kondo systems. In the case of magnetically ordered materials a spin-disorder scattering occurs which increases with increasing temperature, and it reaches its maximum value in the paramagnetic region above the ordering temperature. However, the expression for electrical resistivity corresponding to spin disorder scattering is temperature independent and is given in the Born approximation [71] as:

$$\rho_{4f}(T > T_{ord}) = \frac{3\pi N m^*}{2\hbar e^2 E_F}|\Gamma|^2(g_J-1)^2 J(J+1), \tag{2.69}$$

where m^* is the effective electron mass, e is the electron charge, E_F is the Fermi energy, Γ is the coupling constant of the exchange interaction between $4f$ spins and the conduction electrons spins, N is the density of states per atom per spin of the host metal and J is the total angular momentum of $4f$ moments. Eq 2.69 predicts that ρ_{4f} is proportional to the de Gennes factor $(g-1)^2 J(J+1)$ [72]. In the case of Kondo materials, the $4f$ resistivity follows a logarithmic increase with decreasing temperature below a minimum in the total resistivity. This behaviour was explained by Kondo [73], who in the framework of the $s-d$ model showed that in the third order of perturbation theory in Γ, the scattering amplitude of the conduction electrons diverges as $T \to 0$. Based on this explanation and taking the density of states to be constant in the conduction electron bandwidth interval $-D < E_F < D$ and zero elsewhere, the $4f$ resistivity can be written as:

$$\rho_{4f} = \frac{2\pi N(E_F) n_f m^*}{n_c^h N_c \hbar e^2}\Gamma^2 J(J+1)\left[1 + 4\Gamma N(E_F) ln\left(\frac{k_B T}{D}\right)\right]. \tag{2.70}$$

Here n_f is the concentration of magnetic impurities, n_c^h is the number of conduction electrons per host atom and N_c is number of atoms in the host metal. Eq 2.70 describes the logarithmic increase towards low temperature only if Γ is negative. This negative

value of Γ in the Kondo effect suggest AFM coupling between the local moment and the conduction electrons.

Finally, other types of scattering may affect the total resistivity of metals such as electron-electron scattering and spin wave scattering. The contribution of electrons scattering with themselves to the total resistivity is given as [30]:

$$\rho_{e-e} = k_B T^2 \left[\frac{\pi^2 \hbar^2}{m k_F}\right]^2. \tag{2.71}$$

At room temperature, the contribution of electron-electron scattering to the total resistivity is approximately 10^4 times smaller than other components. Furthermore, at lower temperatures, the total resistivity decreases as T^2 allowing this contribution to be neglected within the temperature region of interest. Correspondingly, the spin wave scattering describes the scattering of conduction electrons by magnons (quantized spins). This usually occurs at low temperatures below ordering temperatures for magnetic materials. In the case of antiferromagnetic magnons the dispersion relation is given as:

$$\omega^2 = \Delta_{AFM}^2 + Dk^2, \tag{2.72}$$

whereas for the ferromagnetic magnons is given by:

$$\omega = \Delta_{FM} + Dk^2, \tag{2.73}$$

where Δ is the energy gap in spin wave spectrum and D is the spin wave stiffness. Accordingly, the total resistivity of an antiferromagnetic material below the ordering temperature may be expressed by [74]:

$$\rho(T) = \rho(0) + A_{\rho,AFM}\Delta_{\rho,AFM}^{3/2} T^{1/2} exp(-\Delta_{\rho,AFM}/T).\left[1 + \frac{2}{3}\frac{T}{\Delta_\rho} + \frac{2}{5}\left(\frac{T}{\Delta_\rho}\right)^2\right], \tag{2.74}$$

where $A_{\rho,AFM}$ is a prefactor.

2.4.3 Magnetoresistivity

Magnetoresistivity MR is the phenomenon where the resistivity of the material changes with applied magnetic field H. Classically, MR depends on both the strength of the magnetic field and the relative direction of the magnetic field with respect to the current. The MR is usually expressed in the form:

$$\frac{\Delta\rho}{\rho} = \frac{\rho(H,T) - \rho(0,T)}{\rho(0,T)}, \tag{2.75}$$

where $\rho(0,T)$ is the zero-field resistivity and $\rho(H,T)$ is the resistivity in a field. In general, the influence of applying a magnetic field increases the resistivity in most ordinary metals and alloys, resulting in a positive MR. For a number of ferromagnetic materials, a negative character of magnetoresistivity due to the electron-spin scattering arises as follows: The magnetic field increases the effective field acting on the localized spins and suppresses the fluctuation of spins in space and time, which leads to the decrease of the resistivity [75]. The negative magnetoresistivity is also shown in dilute alloys with paramagnetic impurities. Yoshida [76] first explained the negative magnetoresistivity of the magnetic alloys. He showed in the molecular field approximation that when impurity spins formed antiferromagnetic ordering the negative magnetoresistivity arises from the cross term due to the magnetic and non-magnetic impurity scattering. Recently Williams[77] has also calculated the negative magnetoresistivity of ferromagnetic dilute alloys in the spin wave approximation. In the case of a number of Heavy-fermion materials the magnetoresistivity takes positive values due to a shift in the residual resistivity and a change in the T^2 coefficient of $\rho(T)$ [78]. In the case of a Kondo system and in the coherent state, the magnetoresistivity is thought to be positive [79]. The effect of applying a magnetic field on a system exhibiting the conventional $-lnT$ in the resistivity at zero field, is to suppress the spin-flip. This leads to the formation of a resistivity maximum, which shifts to higher temperatures with increasing field. This behaviour suggests the development of phase coherence between semi-screened magnetic moments at lower temperatures causing a negative magnetoresistivity in this temperature region. For systems with independent Kondo impurities, i.e a low density of RE atom (incoherent Kondo scattering or Kondo hole alloys) a negative magnetoresistivity is observed [80]. This behaviour is due to the

suppression of the incoherent Kondo scattering in a magnetic field and corresponding increase of the lifetime τ of the conduction electrons [81].

The result of the Bethe ansatz calculations of the Coqblin-Schrieffer model given by Andrei [82] and Schlottmann [27], yields an exact solution of the MR for the spin-1/2 case:

$$\frac{\rho(B)}{\rho(0)} = \Big[\frac{1}{2J+1} sin^2(\frac{\pi n_f}{2J+1}) \sum_{l=0}^{2J} sin^{-2}(\pi n_l)\Big]^{-1}. \tag{2.76}$$

where n_f is the $4f$ electron occupation number. The integer valence limit of the Coqblin-Schrieffer approach to the degenerate Anderson model ($n_f \longrightarrow 1$) is obtained by suppressing charge fluctuations. This constrains the level occupation used and splits the $(2J+1)$ multiplet in a magnetic field as:

$$\sum_{l=0}^{2J} n_l = n_f = 1. \tag{2.77}$$

Exact solutions for $J = 1/2$ in the Schlottmann's formalism is completely determined by a single parameter known as the characteristic field $B^*(T)$. According to Batlogg *etal.*[83], for finite temperature, B^* depends linearly on temperature as follows:

$$B^*(T) = B^*(0) + \frac{k_B T}{g\mu_K} = \frac{k_B(T_K + T)}{g\mu_K}, \tag{2.78}$$

where μ_K is the effective magnetic moment of the Kondo ion. The relation of B^* and T_K indicates that the physics of Kondo impurity is entirely dominates by one energy scale T_K.

2.5 Thermal transport properties

2.5.1 Thermoelectrical power

The thermoelectric power (TEP) is a powerful technique which may reveal the electronic features of materials since it is a sensitive probe of energies near the Fermi surface. In

general the TEP of magnetic ordered materials is given by [84]:

$$S(T) = S_d(T) + S_g(T) + S_m(T). \tag{2.79}$$

Here $S_d(T)$, $S_g(T)$ and $S_m(T)$ are the contributions to the thermoelectric power due to electron diffusion, phonon-drag and magnon-drag, respectively. The latter two terms are usually neglected at higher temperatures because it is believed that these two contributions decrease rapidly with increasing temperature [85, 86]. However, at low temperature, the phonon-drag contribution to the total thermoelectric power is directly proportional to T^3, whilst at higher temperatures is inversely proportional to T. The electron diffusion term S_d can be calculated from the linearized Boltzmann equation in the degenerate limit ($k_B T \leqslant E_F$) as:

$$S_d = \frac{\pi^2}{3}\frac{k_B^2 T}{q_e}\left(\frac{\partial ln\sigma(E)}{\partial E}\right)_{E_F}, \tag{2.80}$$

where σ is the dc electrical resistivity. Generally, the diffusion TEP, S_d is associated with a system of electrons that interact with a random distribution of scattering centres that are assumed to exist in thermal equibrium at the local temperature T. More precisely, this term describes the diffusion of the conduction electrons due to the temperature gradient. Thus, in moving along with the temperature gradient the conduction electrons undergo scattering processes: the electron-impurity scattering, the electron- phonon scattering and spin-dependent scattering processes.

Assuming a spherical Fermi surface and isotropic relaxation time τ, the electric conductivity and thermoelectric power can be written as:

$$\sigma = \frac{2}{3}e^2 N(E)v^2(E)\tau(E) \tag{2.81}$$

$$S_d = \frac{\pi^2}{3}\frac{k_B^2 T}{q_e}\left(\frac{\partial lnN(E)}{\partial E} + \frac{\partial lnv^2(E)}{\partial E} + \frac{\partial ln\tau(E)}{\partial(E)}\right)_{E_F}. \tag{2.82}$$

For a metal with light charge carriers, the first term in Eq 2.82 generally dominates significantly and therefore:

$$S_d = \frac{\pi^2}{3}\frac{k_B^2 T}{q_e}\left(\frac{\partial lnN(E)}{\partial E}\right)_{E_F}. \tag{2.83}$$

At very low temperatures, where the relaxation time τ is limited by scattering from impurities, the thermoelectric power calculated in the free-electron approximation is linear in temperature:

$$S_d = \frac{\pi^2 k_B^2 T}{3 q_e E_F}. \tag{2.84}$$

The thermoelectric power of heavy-fermion compounds, in general, show large values. This is due to the enhancement of the DOS near the Fermi level as a result of the hybridization between the local $4f$ states and the conduction electron states. The enhancement of the DOS near the Fermi level also known as the Abrikosov-Suhl resonance has a narrow half width (1-100 K). As a result of that, the energy derivative of $N(E)$ at E_F which is proportional to S_d may take on large values more than 10 to 100 times with respect to typical S_d values of normal metals. In the case of Ce and Yb-based Kondo systems, both Kondo interaction and CEF excitations may generate large anomalies in thermoelectric TEP. The thermoelectric power of these compounds typically exhibits a maximum for Ce-based compounds, and a minimum for Yb-based compounds [87, 88]. Additionally, for a CEF level at $T_{\Delta CEF} \geqslant T_K$ theoretical calculation predict a large positive (Ce) or negative (Yb) contribution with a peak positioned at (0.3 to 0.6)$\times T_{\Delta CEF}$[4]. Thermoelectric power investigations may then be used for the determination of the Kondo and CEF energy scales. A recent theoretical treatment of the TEP of most Ce and Yb-based heavy-fermion and Kondo compounds was put forward using the phenomenological resonance model[89]. In this model, the dominant contribution to the TEP is caused by the scattering of conduction electrons from the wide s-band into a narrow f-band approximate by a Lorentzian shape. $S(T)$ can then be written:

$$S(T) = \frac{2}{3}\pi^2 \frac{k_B}{|e|}\frac{TE_f}{(\pi^2/3)T^2 + E_f^2 + \Gamma_f^2} \tag{2.85}$$

where E_f and W_f are the position of the f-band peak relative to the Fermi level E_F and its width, respectively, both in unit of temperature (Kelvins). Eq 2.85 satisfactorily describes the temperature dependences of TEP of the majority of systems with intermediate valence (IV) of Ce. But it can be valid to describe Kondo systems by using the known relationship between the parameters E_f, Γ_f and T_K ($E_f = T_K$, $\Gamma_f = \pi T_K/N_f$)[90], where N_f is the orbital degenercy $2J+1$. For moderate heavy-fermions with low T_K values, Eq 2.85 describes a scattering of conduction electrons on an ensemble of incoherent impurities than on a narrow f-band [88]. Therefore in case of energy scale dominated by CEF, W_f in Eq 2.85 is related mainly to the temperature of the CEF (T_{CEF}), which means that the relaxation time depends on the energy, for that $W_f = \dfrac{\pi T_{CEF}}{N_f}$ is used for $T > T_K$ and finally the TEP can be expressed as:

$$S(T) = \frac{2}{3}\pi^2 \frac{k_B}{|e|} \frac{T.T_K}{(\pi^2/3)T^2 + T_K^2 + (\pi^2/N_f^2)T_{CEF}^2}. \tag{2.86}$$

2.5.2 Thermal conductivity

Thermal conductivity $\lambda(T)$ of metals originates from different types of contributions, which primarily represent the heat carriers in these metals. In normal metals, electrons and thermal vibrations of the lattice (phonons) act as heat carriers, whereas in magnetic materials heat can also be carried by magnons[91]. Therefore, thermal conductivity is simply defined as the measurement of the ability of a material to transport heat. In this section only the heat transport by phonons λ_{ph} and electrons λ_e is discussed. The total thermal conductivity can be calculated as the sum of the contributions resulting from different types of heat carriers:

$$\lambda_{tot}(T) = \lambda_{ph}(T) + \lambda_e(T). \tag{2.87}$$

The electronic contribution λ_e to the total thermal conductivity λ_{tot} can be calculated from the linearized Boltzmann equation within the relaxation time approximation. For a

spherical Fermi surface and that the relaxation time τ only depends on the energy of the heat carriers, λ_e for a free electron gas is given by:

$$\lambda_e = \frac{\pi^2}{3}\left(\frac{k_B}{e}\right)^2 T\sigma. \tag{2.88}$$

Eq 2.88 leads directly to the Wiedemann-Franz law, which states that the ratio of electronic thermal conductivity to electrical conductivity is linear in temperature:

$$\frac{\lambda_e}{\sigma} = \frac{\pi^2}{3}\left(\frac{k_B}{e}\right)^2 T = L_0 T, \tag{2.89}$$

where $L_0 = 2.45 \times 10^{-8} W\Omega/K^2$ is the Lorentz number. The Wiedemann-Franz law holds even if the constant-energy surfaces are not spherical. It is strictly valid for elastic scattering processes, e.g. scattering from stationary imperfections and impurities at low temperature. At elevated temperatures (10 K to several 100 K) inelastic scattering dominates and deviations from the Wiedemann-Franz law is observed. At higher temperatures the energy loss due to inelastic scattering is small compared to $k_B T$, therefore the Wiedemann-Franz law is valid again.

On the other hand, the phonic contribution λ_{ph} to λ_{tot} is limited due to a large number of different scattering processes with relaxation times τ_i, including for example scattering on sample or grain boundaries τ_B, scattering from imperfections τ_D, phonon-electron scattering (τ_{ph-e}),...etc. Thus, in this case, the combined relaxation time τ_{Ph} can be calculated according to Eq 2.64. However, the phonon contribution to the total thermal conductivity can be obtained using the Debye approximation for phonon dispersion relation as [92]:

$$\lambda_{ph} = \frac{k_B}{2\pi^2 \upsilon_{ph}}\left(\frac{k_B}{\hbar}\right)^3 T^3 \int_0^{\Theta_D/T} \frac{x^4 e^x \tau_{ph}}{(e^x - 1)^2} dx, \tag{2.90}$$

where υ_{ph} is the velocity of sound in the lattice and given by:

$$\upsilon_{ph} = \frac{k_B \theta_D}{\hbar}(6\pi^2 N)^{-1/3}. \tag{2.91}$$

Here N is the number of atoms per unit cell.

Chapter 3

Experimental Techniques

3.1 Sample Preparation

The polycrystalline samples studied in this work are: $(Ce_{1-x}La_x)Cu_4In$, $(Ce_{1-x}La_x)_8Pd_{24}Al$, $Ce_8Pd_{24}(Al_{1-x}Sn_x)$, $RECu_4Au$ (RE = Nd, Gd) and NdAuX (X = Ga, Ge). All the starting elements were brought from Alfa Aesar company with the following purity in $wt\%$: La: 99.99; Ce: 99.98; Nd:99.99 ; Gd:99.99; Lu:99.99; Cu: 99.99; Au: 99.95; Pd: 99.97; In: 99.998 ; Ge: 99.999; Ga: 99.999 Sn:99.995;and Al: 99.999. All the compounds of the alloys systems under study, along with their nonmagnetic counterparts were prepared from their starting elements weighted to an accuracy of 0.01 mg using a microbalance (OHAUS crop. Pine Brook, NJ USA). The powder element of Sn was compressed using pellet dye in a laboratory hydraulic press below the maximum pressure recommended for the particular dye. The polycrystalline samples of these systems were prepared by arc-melting the constituent elements on a water-cooled copper hearth in a titanium gathered Argon atmosphere (50 kPa below atmospheric pressure) at the Department of Physics, University of the Western Cape using an arc-furnace melting chamber Fig 3.1 and 3.2. Polycrystalline samples of all the compounds and alloys were prepared by arc-melting the constituent elements on a water-cooled copper hearth in a titanium guttered ultra-high purity argon atmosphere. Ingots were turned over and remelted several times to ensure good homogeneity of the samples. Weight losses after final melting were always less than 1% for all prepared samples. Electrical and thermal transport as well as thermodynamic measurements were performed on as-cast samples, except for NdAuGa. The ingot sample of NdAuGa was wrapped in a tantalum foil (purity of 99.99 wt-%) and sealed off in an evacuated quartz tube for heat treatment at 850 ^{0}C for two weeks. The samples for resistivity, susceptibility, magnetization, specific heat, thermoelectric power and thermal conductivity measurements were cut from the as-cast ingot using a Micracut 125 low speed precision cutter with a diamond coated blade of thickness 0.381 mm in Fig 3.3.

Figure 3.1: Arc-melting furnace chamber at the University of the Western Cape (Physics Department).

The samples for resistivity measurements were cut in the form of a parallelepiped rectangle with typical dimension $1 \times 1 \times 6$ mm^3, while for thermoelectric power and thermal conductivity measurements the dimensions were $1 \times 2 \times 8$ mm^3. These dimensions were measured using a travelling microscope to an accuracy of ± 5 μm with a geometrical uncertainty of $\frac{A}{l} \pm 2\%$ where A is the cross-sectional area of the sample and l is the length. Samples for magnetic susceptibility, magnetization and specific heat were cut in the form of a cube with a typical dimensions of $1 \times 1 \times 1$ mm^3. All these parts were cut out of the centre of the ingot in order to avoid the bottom surface and the top layer where the stress in the material as evidenced by hairline cracks was sometimes found. Parts of the as-cast ingot as well as the annealed were used for X-ray diffraction (XRD) measurement for structural, and SEM and EDS analysis as discussed in the following sections.

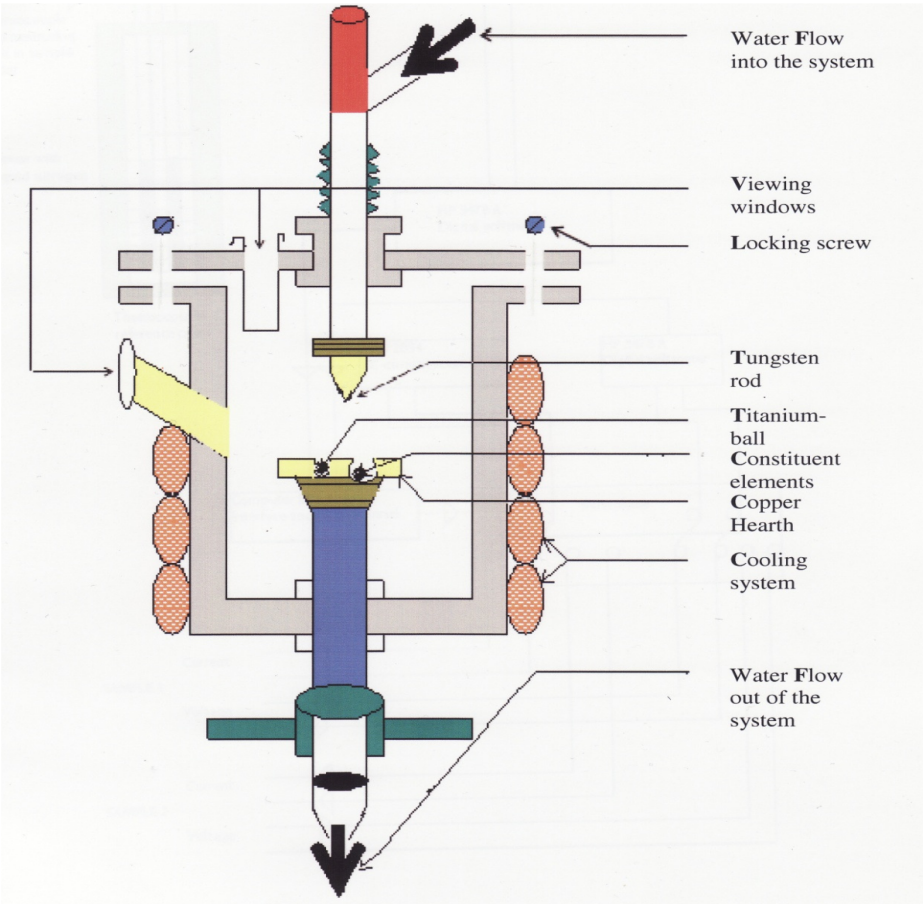

Figure 3.2: Schematic diagram of the arc-furnace melting chamber.

Figure 3.3: Micracut 125 low speed cutter at the University of the Western Cape (Physics Department).

3.2 Samples characterization

3.2.1 Powder X-ray Diffraction

All the samples thus prepared for investigation in this work were characterized by X-ray powder diffraction using a Bruker D8 Advance diffractometer with Cu K_α radiation (λ = 1.540598 Å) located at iThemba LABS, Cape Town shown in Fig 3.4. One part of the ingot of each prepared sample was finely ground in an agate mortar and subsequently spread out on a hollow rectangular sample holder. A potential difference of 40 kV was applied across the filament and the anode target. The data collection was made using a computer supplied with EVA software from BRUKER, equipped with the diffractometer. The output data were collected in 2θ diffraction range with a step increment of approximately $\Delta 2\theta = 0.034^0$. The diffraction patterns were measured in the range $20^0 \leqslant 2\theta \leqslant 90^0$, which correspond to the range where reflections are expected for the majority of d-spacing found in intermetallic compounds. In order to obtain perfect XRD patterns of the samples, the background intensity produced in these patterns were subtracted.

Figure 3.4: Bruker D8 Advance powder diffractometer.

Qualitative analysis of the room temperature X-ray diffraction patterns were made using the Pawley Cell and Intensity Least (CAIL) fit method, while the quantitative analysis was performed with a full-profile Rietveld refinement method, both from TOPAS ACADEMIC programme. No evidence of parasitic phases or unreacted elements was found in the X-ray diffraction patterns of all prepared compositions. Individual peak positions, lattice parameters, unit-cell volume, crystal structure, Wyckoff symmetry sites and occupation factors were determined using Pawley Cell and Intensity Least (CAIL) square fit and Rietveld refinement from TOPAS ACADEMIC program. The theoretical initial parameters were loaded onto these software to initialize the refinement.

3.2.2 Electron Micro-probe

For further characterization, electron micro-probe analysis was performed on some of our samples. The most important type of micro-probe instrument involves the use of the electron beam because of the vast information that can be obtained from the interaction of an electron beam with the sample. This helps for characterizing the micro-structure and micro-composition of materials.

In this study, AURIGA Field Emission High Resolution Scanning Electron Microscopy integrated system (SEM), equipped with a camera was used for elemental microanalysis and for obtaining topological information of the samples. The electron micro-probe was performed with the option of electron dispersive spectroscopy (EDS). In order to obtain an accurate analysis, the samples were well polished using a diamond disc embedded in an electronic polishing machine under running coolant. The polished samples were then amounted to carbon tabs placed on Aluminum stubs. Carbon tabs help the samples to stick well to the stubs. They also prevent the sample from charging up and reducing the effective electron energy thus enhancing the secondary electron yield during the analysis. The SEM images were taking by either backscattered electron (BSE) or secondary electron (SE) modes for different zooming scales with probe accelerating voltage 15 kev and in a Gun vacuum of 7.7 $\times 10^{-10}$ mbar.

3.3 Physical properties measurements

Electrical resistivity, magneto-resistivity, heat capacity, thermoelectric power and thermal conductivity measurements were performed using a commercial device Quantum Design Physical Property Measurement System (QD PPMS), San Diego (USA) shown in Fig 3.5. The measured temperature and magnetic field ranges are 1.9 K to 400 K and 0 T to 9 T. Magnetic susceptibility and magnetization measurements were performed by means of

Figure 3.5: A commercial Quantum Design Physical Property Measurement system (QD PPMS), University of Johannesburg, Department of Physics.

Figure 3.6: A Superconducting Quantum Interference Device (SQUID) magnetometer in a Quantum Design Magnetic Property Measurement System (QD MPMS-5).

a Superconducting Quantum Interference Device (SQUID) magnetometer in a Quantum Design Magnetic Property Measurement System (QD MPMS-5), San Diego (USA) (Fig 3.6), with sample temperature between 1.7 and 400 K and magnetic fields up to 7 T.

3.3.1 Magnetic properties

Magnetic susceptibility χ and magnetization isotherm M measurements were performed on a single piece of sample with mass ($\approx$ 15 mg) of each polycrystalline sample in the temperature range 1.7-300 K and in fields up to 7 T using a Quantum Design Magnetic Properties Measurement System (MPMS-5). A regular plastic straw was used as a sample holder because it has a low mass and less diamagnetic background signal. The sample was cut into an elongated piece to minimize the demagnetizing fields, and put into a small plastic bag, inserted into the straw. The plastic bag signal was subtracted using the known mass once the measurement was done. The pick-up coil of the SQUID (Fig 3.7), produces a current which is proportional to the gradient of the external field, rather than the field itself. The overall measurement is performed by moving the sample with a stepper motor through the pick-up coils. During the sample movement, its magnetic moment couples inductively with the coils, and produces a current variation in the superconducting circuit which is proportional to the sum of the fluxes across the coils. The same current is then coupled to the SQUID loop and produces a final voltage output that is recorded using a lock-in technique. The output voltage versus the position curve is measured as an average of different scans of the sample position to reduce the noise, and extracts the value of the magnetic moment.

In this work, magnetic susceptibility (magnetic moment as a function of temperature) measurements were carried out under field-cooled (FC) condition on DC option with a static magnetic field ($\leqslant$ 1000 Oe). Furthermore, low temperature susceptibility measurements were also conducted under Zero-field-cooled (ZFC) condition for some selected compounds. These measurements were performed at different cooling rates. Magnetization isotherm (magnetic moment as a function of temperature) measurements were performed at fixing sample temperatures and scans the applied field up to 7 T.

3.3.2 Electrical resistivity

DC electrical resistivity measurements were performed using the PPMS, by a standard four probe method over the temperature range from 1.9 to 300 K, on a bar shaped specimen of a typical dimension of $1 \times 1 \times 6$ mm^3. The resistivity puck has space for three samples (Fig 3.8). Kapton tape was placed on the sample puck surface to prevent the electric contact between samples and the puck surface. The samples were attached to the

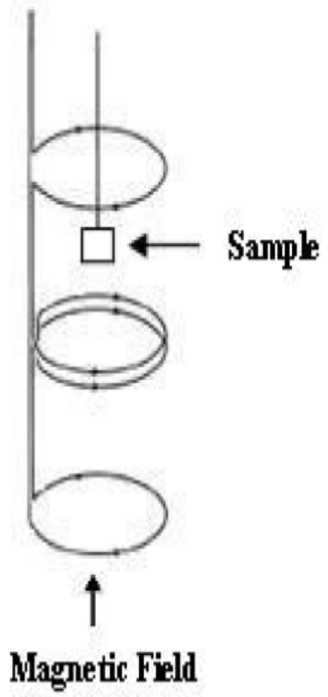

Figure 3.7: A schematic of the pick up coil used in the SQUID. The bottom arrow shows the direction of the current induced by the magnetic moment of the sample.

capton tape by G.E varnish Glue (C5-101 from Oxford instrument). The G.E vanish glue was used because of its excellent adhesive properties below helium temperature and its good thermal conductivity and electrical insulating properties. The four contact leads in Fig 3.9 were made from 50 μm gold wire and were attached to the samples with electrically conductive silver paste from Dupont (4922N single component epoxy which is 70% elemental silver) for brittle samples or spot welded.

In general, PPMS eliminates the thermoelectric effect that arises from the current and voltage leads by using a fast current reversal technique in which the current polarity in the sample continuously flips, and measuring the resistivity as the average of two readings of positive and negative currents. The measurement of the voltage drop (ΔV) across the sample has two contributions: the contact voltage due to circuitry ($\Delta V_{contact}$) and sample voltage due to resistivity (ΔV_{sample}). Since ($\Delta V_{contact}$) is independent of the direction, (ΔV_{sample}) can be easily obtained using a current reversal technique which is described as follows: when the current flows from I^+ to I^-, the voltage is taken as ΔV_1, then when the current is reversed and flows from I^- to I^+, the voltage is taken as ΔV_2. This leads to:

$$\Delta V_1 = V_{contact} + V_{sample},$$
$$-\Delta V_2 = V_{contact} - V_{sample},$$
$$\Delta V_{sample} = (\Delta V_1 + \Delta V_2)/2.$$

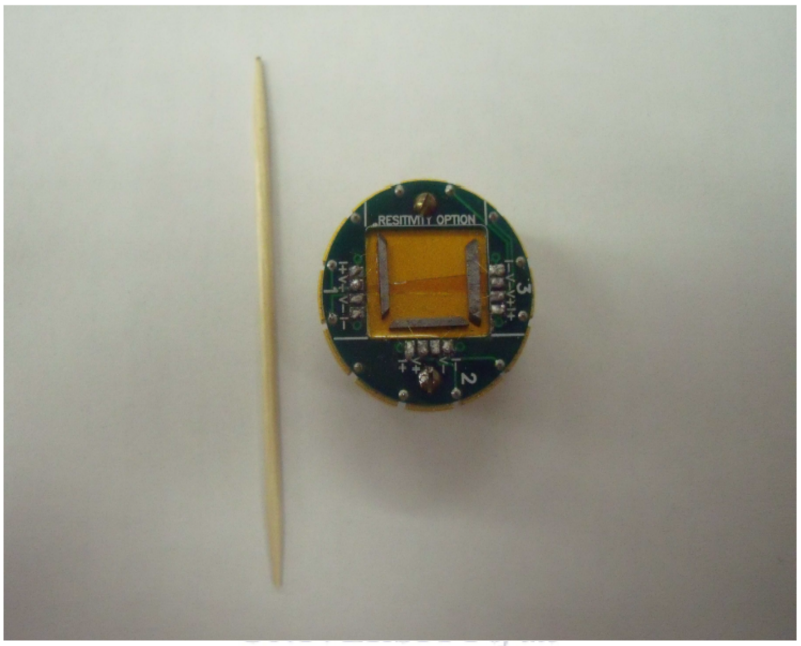

Figure 3.8: The resistivity sample puck with 3 samples mounted.

The PPMS measures electrical resistance $R(T)$ of the sample and then calculates the resistivity $\rho(T)$ using a cross sectional area of the sample, and voltage leads separation length (l). The value of the input current and the sample geometry during measurement were set to $I = 4500\mu$A, cross sectional area A =1 mm^2 and the length between voltage leads l = 1 mm. The PPMS software used: $\Delta V_{sample} = RI$ and $\Delta V_{sample} = \dfrac{LI\rho}{A}$ to compute the resistance and resistivity of the sample. The real value of the resistivity of the sample is calculated manually using the measured cross section area of the sample and the voltage contact length that are taken before loading the sample into PPMS. Magnetoresistance measurements were conducted to some selected samples of $Ce_{1-x}La_xCu_4In$ and $(Ce_{1-x}La_x)_8Pd_{24}Al$ systems. These measurements were performed in the form of magnetic field dependence of resistivity for fixed sample temperatures and field values up to 9 T.

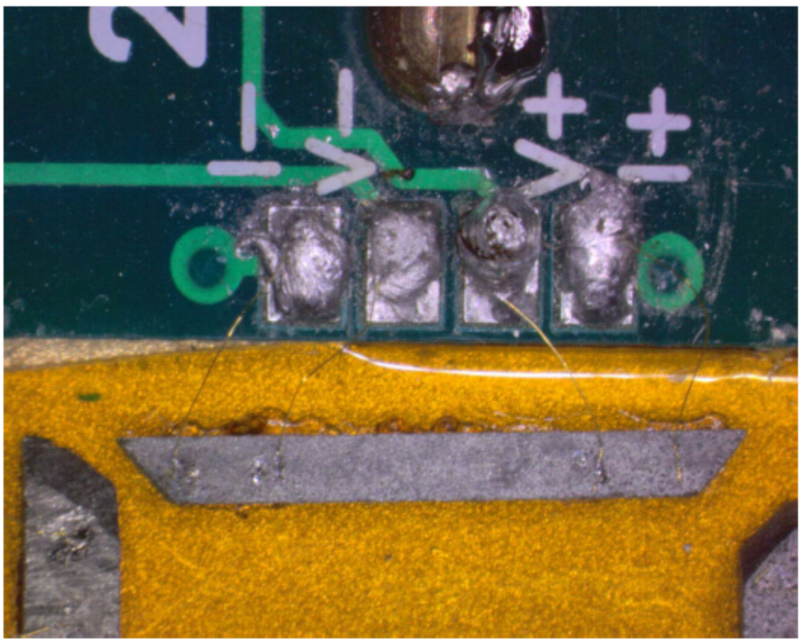

Figure 3.9: Magnification of a single sample in Fig 3.8 showing the spot-welded contacts on the resistivity sample puck in the 4-probe configuration.

3.3.3 Specific heat

The PPMS uses a relaxation-time method to measure the specific heat in the temperature range from 1.8 K to 400 K. On the specific heat measurement puck, a heater and thermometer are attached to the bottom of a sample platform shown in Fig 3.10. Small wires provide the electrical connection to the heater and thermometer and also provide the thermal connection and mechanical support to the sample platform. The sample platform accommodates small samples weighing approximately 100 mg or less. The sample has to be finely polished and shaped to the platform dimensions to make a better thermal contact. The samples were fixed with grease Apiezon N on the sapphire platform of the sample holder in Fig.3.10. The contribution of the grease and platform to the total heat capacity was determined in a separate measurement before mounting the sample, and subsequently subtracted from the total specific heat to obtain the sample specific heat. During a measurement, a known amount of heat is supplied by a heater at constant power for a fixed time t, and then this heating period is followed by a cooling of the same period. After each measurement cycle, the data obtained fits the entire temperature response of the sample platform to the two-τ model from Quantum Design to determine the heat capacity. This model accounts for both the thermal relaxation of the sample platform to the bath temperature and the relaxation between the sample platform and the sample itself [93]. The PPMS chooses the result of the model from best fits. Finally, PPMS software computes the heat capacity in units of mJ/mole.K by multiplying the specific

heat of the sample by the molar mass of the sample and divided by the mass of the sample.

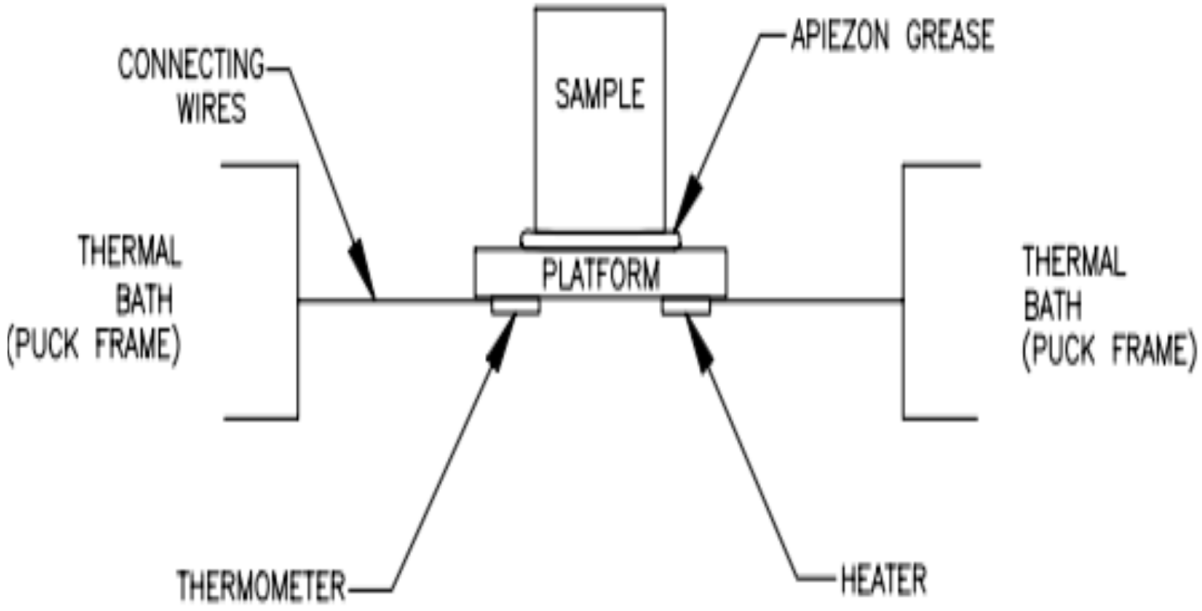

Figure 3.10: A schematic diagram of the PPMS heat capacity calorimeter puck.

3.3.4 Thermal Transport

Thermoelectric power and thermal conductivity are measured simultaneously in the temperature range between 1.9 K and 400 K, by the four-probe longitude semi-adiabatic steady-state technique using QD PPMS Thermal Transport option (TTO). The samples used for TTO measurements were cut into bar shapes of typical dimensions of $8 \times 2 \times 1$ mm^3. As shown in Fig 3.11, the sample was attached to the Cernox thermometers and heater shoes by four gold-coated copper contacts. Usually, mounting is done using silver-filled, electrically conductive epoxy (H20E from Epoxy Technology), which creates robust contacts. Samples were protected from excessive radiation loss by a copper isothermal radiation shield. The heat pulse is applied by a resistance-chip heater fixed on a gold-plated copper shoe. The Cernox thermometers to the shoe assemblies measure the corresponding temperatures across the sample and voltages. However, the TTO determines the thermoelectric power by creating a specified temperature difference between the hot and cold

thermometers, as it does for thermal conductivity. The TTO measures the thermoelectric power by means of thermoelectric voltage drop created between the thermometer shoes in response to the corresponding temperature difference across the sample in units of μV/K.

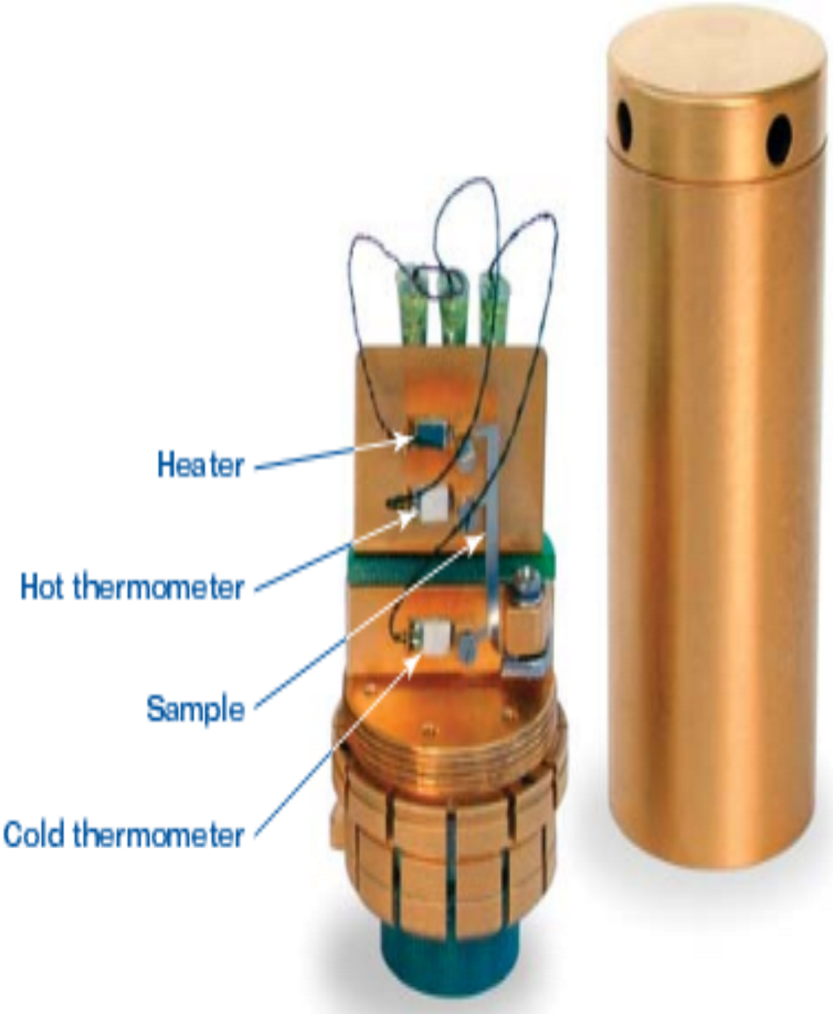

Figure 3.11: TTO puck with the resistance chip heater and the two Cernox thermometers on the side.

Chapter 4

Electrical, thermal transport and thermodynamics properties of $RECu_4Au$ compounds (RE = Nd and Gd)

4.1 Introduction

The studies of binary intermetallic compounds $RECu_5$ (RE = earth elements), indicate that these compounds exhibit interesting crystallographic features depending on the RE ion [94, 95]. These compounds crystallize either in the hexagonal $CaCu_5$-type structure with space group $P6/mmm$ for light RE elements (RE = La-Sm) or the cubic $AuBe_5$-type structure for heavy RE elements [96–98]. For the RE elements in the intermediate region (RE = Gd, Tb, Dy) or Y, the crystallographic structure is that of the cubic or hexagonal structure depending on the heat treatment given to the samples [99, 100].

Several investigations were devoted to the effect of substitution of one Cu with M atoms, $RECu_4M$ (M = Ag, Au, Pd, Al, In) on the crystallographic, magnetic and electrical properties and these lead to phases crystallizing in the cubic $MgCu_4Sn$-type structure with space group $F\overline{4}3m$ (a ternary variant of $AuBe_5$) [101–108]. For instance, $RECu_4Au$ and $RECu_4Pd$ are isotructural with $RECu_4Ag$ which adopts the cubic $MgCu_4Sn$-type structure and the Au or Pd are situated at the (1/4, 1/4, 1/4) positions of the unit cell [107].

The effect of replacement of one Cu atom with M atom such as Ag or Pd in $RECu_5$ compounds, considerably affects their conduction electron-mediated RKKY exchange interaction, and this may lead to a different ground state in the resulting compounds. The

transport and magnetic properties studies of the $RECu_4M$ compounds have been reported in the literature. These studies indicate interesting features, particularly for those crystallizing in the hexagonal $CaCu_5$-type structure [109–112]. For instance semi-metallic-like behaviour was observed in YCu_4In and $GdCu_4In$ analogues and exchange frustrated antiferromagnetism (AFM) in $GdCu_4In$ [113–115]. While $GdCu_5$ orders AFM at 12.5 K [100], $GdCu_4Pd$ orders ferromagnetically (FM) with a Curie temperature $T_c = 110$ K [99]. Ferromagnetic ordering was also observed in other compounds with light RE elements such as $PrCu_4Pd$ ($T_C = 5$ K), $NdCu_4Pd$ ($T_C = 12$ K), $SmCu_4Pd$ ($T_C = 28$ K) and $EuCu_4Pd$ ($T_C = 24.5$ K) [99]. The first-order valence transition in $YbCu_4In$ has been reported in the literature as well as the studies of $YbCu_4M$ (M = In, Ni, Pd, Cd, Mg, Tl, Au and Ag) [116, 117]. A complex inhomogeneous magnetic state arising from Cu-Mn disorder, $3d-3d$ and $3d-4f$ interaction has been reported in $RECu_4Mn$ compounds (RE = La-Sm and Gd) which have the hexagonal crystal symmetry of the parent compound $RECu_5$ [118].

The study of magnetic properties of the Cubic $GdCu_5$ and the hexagonal $NdCu_5$, in particular, are reported in the literature [100, 119, 120]. $GdCu_5$ is found to order antiferromagnetically at $T_N = 12.5$ K, while $NdCu_5$ intermetallic compound orders ferromagnetically below $T_c = 14.5$ K and spin reorientation transition of the Nd^+ magnetic moment occurs at $T_R = 5.7$ K [119]. Neutron diffraction experiments at short wavelength where the absorption cross section of Gd is not high, indicates that below T_N, $GdCu_5$ orders in an incommensurate triangular structure associated with a propagation vector $Q = 1/3$, 1/3, 0.223 [112]. This incommensurate magnetic structure arises from the weak negative interaction between Gd nearest neighbours. Furthermore, the usual magnetic properties and the behaviour of low temperature resistivity seem to be related to the incommensurate magnetic structure in compounds without magnetocrystalline anisotropy [112].

The effects of substituting one Cu with Be or Ag in $NdCu_5$ were investigated in [121–125]. For $NdCu_4Be$, the magnetic properties have been investigated through measurements of electrical resistivity, magnetization and heat capacity down to 1.8 K [124]. It was observed that, the substitution of Be for Cu retains the crystal structure, the metallic nature as well as the nature of the magnetic ordering of the parent binary compound $NdCu_5$. The ferromagnetic transition temperature shifts to higher temperature at $T_C = 24$ K for $NdCu_4Be$ compound. This substitution most likely alters the band characteristic due to the different valencies of Cu and Be. Therefore, the magnetic coupling between the Nd ions, which depends upon a number of factors such as the Nd-Nd bond lengths, Fermi energy and the average number of conduction electrons per atom, changes and adopts a ferromagnetic nature in $NdCu_4Be$ [124]. In the case of $NdCu_4Ag$ compound, the substitution of Ag for Cu changes the crystallographic structure as well as the nature of the magnetic ordering

and the transition temperatures, the transition being AFM in contrast to the FM ground state encountered in the binary $NdCu_5$. The studies of the magnetic properties of the single crystal $NdCu_4Ag$ indicate an AFM phase transition at $T_N = 7$ K [101], 4.3 K [124] or 4.2 K [121] and Curie-Weiss behaviour above 10 K, with a Weiss constant temperature θ_P = -12 K, and an effective magnetic moment of 3.60 μ_B [121]. The magnetic entropy derived from the specific heat reaches to $S \approx Rln4$ at T_N= 4.2 K and to $S \approx Rln10$ around 50 K [121]. The results of this magnetic entropy suggest a CEF ground state of $NdCu_4Ag$ compound to be a quartet state $\Gamma_8^{(1)}$ $\Gamma_8^{(2)}$ since in a cubic CEF, the tenfold degenerate ground state multiplet $^4I_{9/2}$ of the Nd^{3+}-ion splits into three states: a Γ_6 doublet and two quartets of $\Gamma_8^{(1)}$ $\Gamma_8^{(2)}$. The high field magnetization studies up to 27 T of the single crystal of $NdCu_4Ag$ at 1.7 K and 0.6 K indicate two metamagnetic transitions in the field range 5 and 15 T for the three cubic field directions [100], [110] and [111] Refs[122, 123].

4.2 Sample preparation and characterization

The polycrystalline samples of $NdCu_4Au$, $GdCu_4Au$ and $LuCu_4Au$ were prepared by arc-melting using same procedure described in section 3.1. Metals of the following purity in wt% were used: Nd, Gd, Lu and Au: 99.99; Cu: 99.995. Losses in weight after melting were smaller than 1% for all prepared samples. Samples thus prepared were characterized by X-ray powder diffraction using a Bruker D8 Advance diffractometer with a CuKα radiation (λ = 1.540598 Å). The diffraction patterns were analyzed using the Rietveld and CAILS-Pawley (cell and intensity least-squares) method.

4.3 Results and Discussions

4.3.1 Crystallography

X-ray diffraction patterns showed that the three compounds are single phase as their diffraction peaks could be indexed to appropriate crystal symmetries, although for $LuCu_4Au$ there remains a weak impurity peak (the intensity is at most less than 8.6% of the most intense major-phase peak). X-ray diffractograms obtained for $NdCu_4Au$ and $GdCu_4Au$ compounds together with the Rietveld full-profile least-squares (LSQ) and the CAILS-Pawley refinement fits to the data are shown in Figs 4.1 and 4.2. The space group setting used in the refinement was $F\overline{4}3m$ of the cubic $MgCu_4Sn$ structure, where RE atoms occupy the crystallographic $4a$ sites, Cu atoms occupy the $16e$ sites and Au atoms occupy the $4c$ sites. The resulting cubic crystal structure is depicted in Fig 4.3 and the atomic

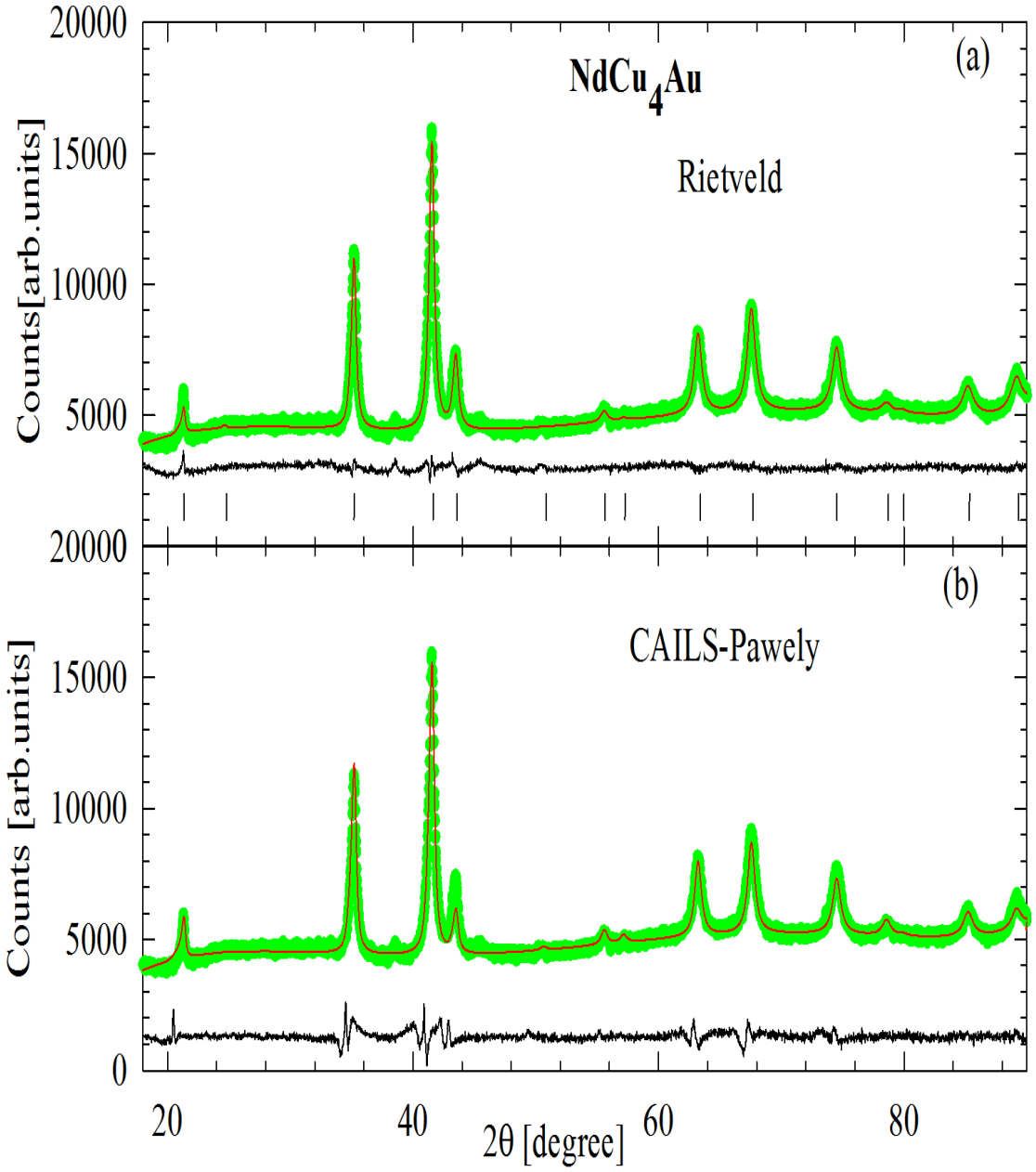

Figure 4.1: Rietveld and CAILS-Pawley analysed diffraction patterns for $NdCu_4Au$. The observed data are shown by green symbols and the solid black lines through the data represent the results of the structure Rietveld and CAILS-Pawley refinements. The lower red curves are the difference curve between the experimental data and the calculated curve and the vertical black lines in (a) are the Bragg positions.

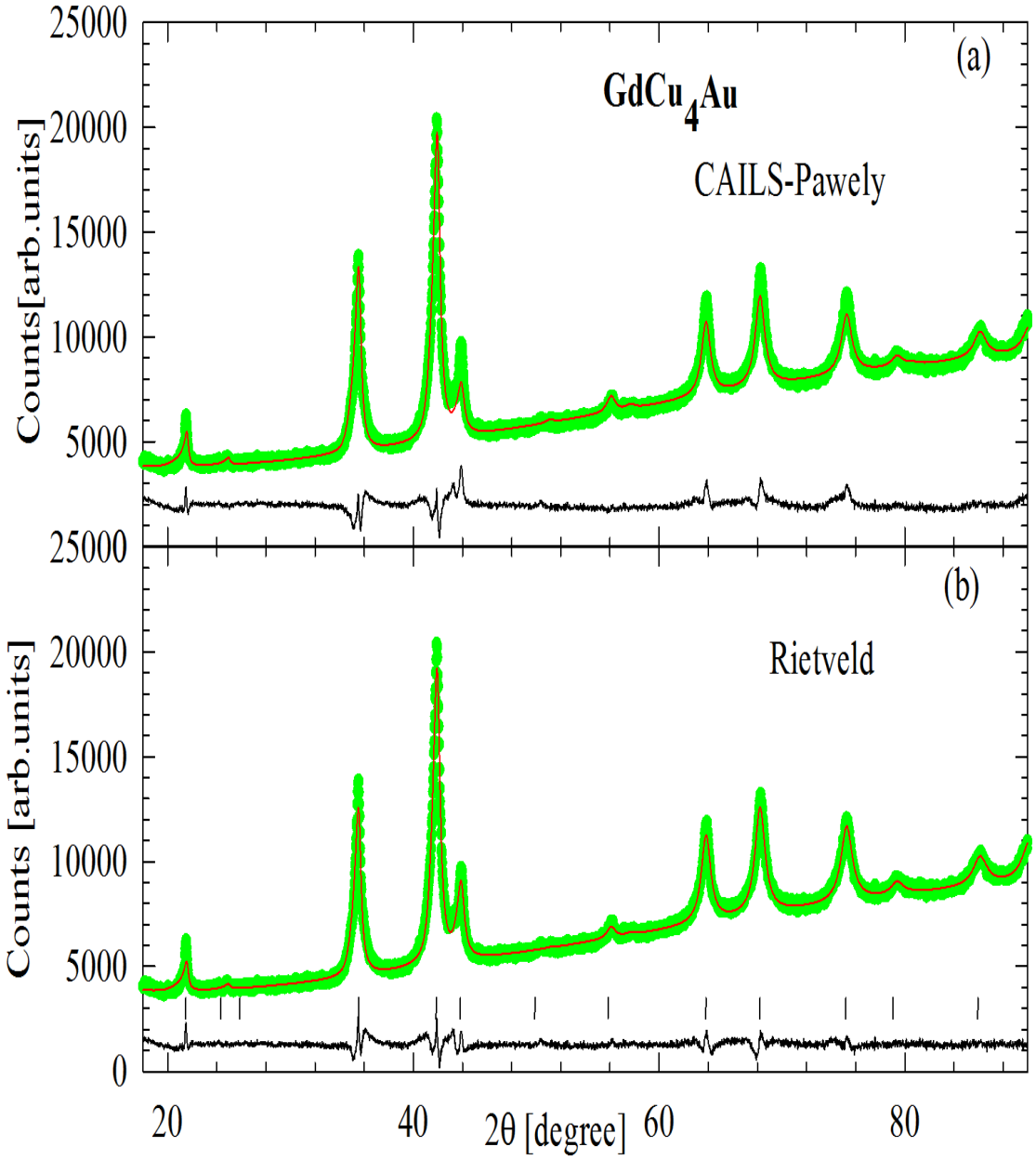

Figure 4.2: Rietveld and CAILS-Pawley analysed diffraction patterns for $GdCu_4Au$. The observed data are shown by green symbols and the solid black lines through the data represent the results of the structure Rietveld and CAILS-Pawley refinements. The lower red curves are the difference curve between the experimental data and the calculated curve and the vertical black lines in (b) are the Bragg positions.

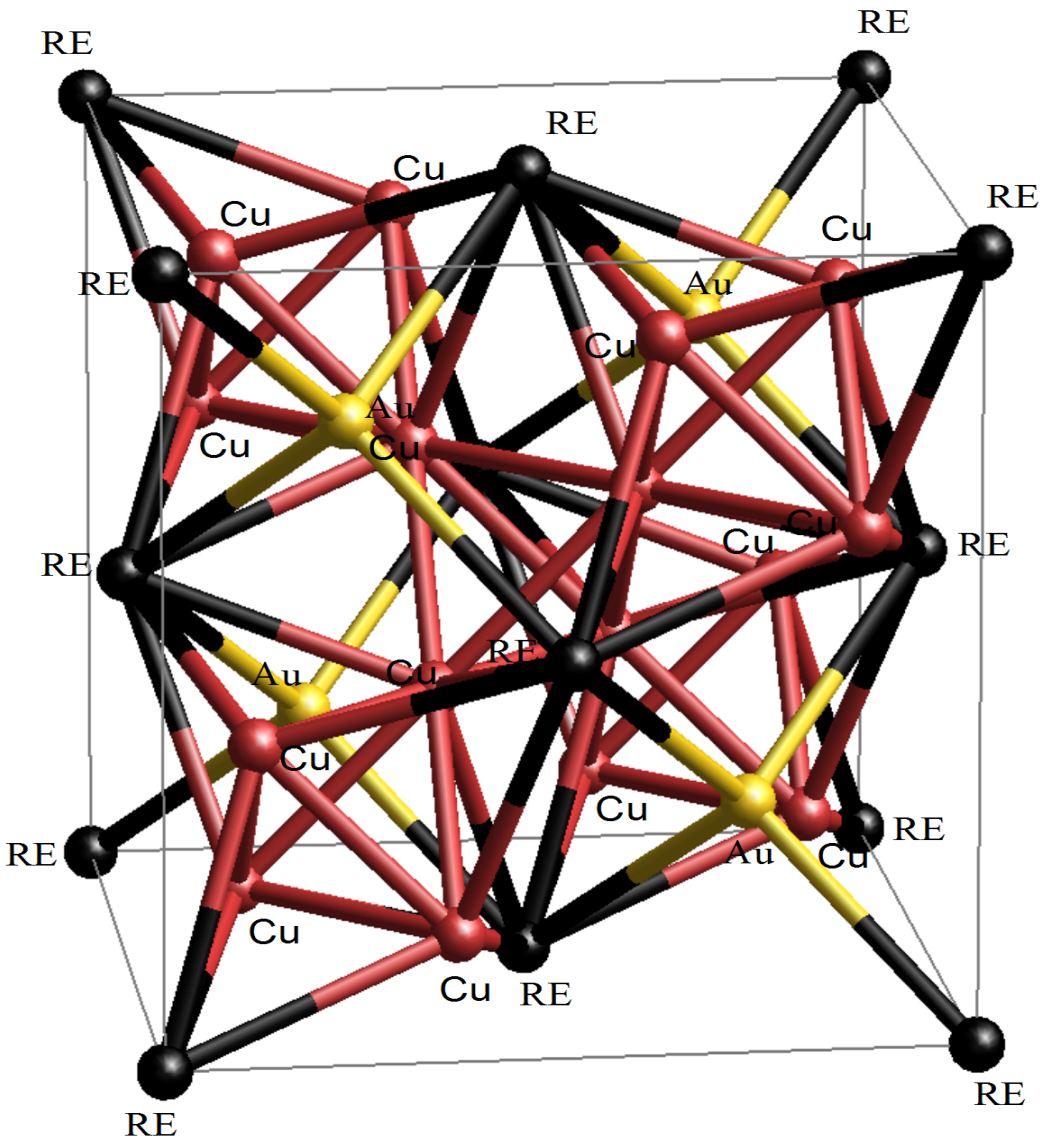

Figure 4.3: The cubic crystal structure of $RECu_4Au$ (RE = Nd, Gd and Lu). The black spheres represent the RE atom, the red spheres represent the Cu atom and the yellow spheres represent the Au atom.

coordinates in $NdCu_4Au$, $GdCu_4Au$ and $LuCu_4Au$ compounds are listed in Table 4.1. In the refinement process, the occupancy fraction as well as the isotropic displacement parameter (B_{iso}) of all the atoms were kept fixed (fully occupied). The resulting phase density amounts to 10.60(2)cg/cm^3, 11.11(5) g/cm^3 and 11.57(9) g/cm^3 for $NdCu_4Au$, $GdCu_4Au$ and $LuCu_4Au$, respectively. It is observed that the biggest value of phase density is for the Lu compound analogous to the Gd and Nd compounds, which may be attributed to the increase of atom mass.

Table 4.1: Atomic coordinates, site occupancy (S.O.) and the isotropic displacement parameter (B_{iso}) for $NdCu_4Au$, $GdCu_4Au$ and $LuCu_4Au$ obtained from the full-structure Rietveld refinement method, as well as, lattice parameters and the unit cell volumes for these compounds. The S.O. and the beq of all atoms were kept fixed.

Compound	Atoms	Wyckoff site	x	y	z	S.O	B_{iso}	a (Å)	volume (Å^3)
$NdCu_4Au$	Nd	4a	0	0	0	1	1	7.1961(5)	372.6(8)
	Cu	16e	0.627(1)	x	x	1	1		
	Au	4c	1/4	1/4	1/4	1	1		
$GdCu_4Au$	Gd	4a	0	0	0	1	1	7.143(3)	364.5(5)
	Cu	16e	0.623(1)	x	x				
	Au	4c	1/4	1/4	1/4				
$LuCu_4Au$	Lu	4a	0	0	0	1	1	7.051(2)	350.5(3)
	Cu	16e	0.627(6)	x	x				
	Au	4c	1/4	1/4	1/4				

The room temperature lattice parameter and the unit cell volume for our compounds are also presented in Table 4.1. It should be noted that the bigger value of V for the Nd compound compared to the Gd and Lu compounds is a consequence of the bigger ionic radius for Nd than Gd and Lu. Compared to the $NdCu_4Ag$ compound with a large unit cell volume [121] than $NdCu_4Au$ compound, this is a consequence of bigger covalent radius of Ag than Au. The interatomic distances calculated from the Rietveld refinement for all the compounds under study are given in Table 4.2. For all the three compounds the shortest distances (2.507 Å for $NdCu_4Au$, 2.498 Å for $GdCu_4Au$ and 2.456 Å for $LuCu_4Au$) were obtained for Cu-Cu with bond angle 60^0, compared to the sum of their covalent radii (2.76 Å). Such a small distance between the Cu atoms indicates a strong overlap between $4d$ electrons of Cu, which may be responsible for the change of the RE-RE bond lengths as well as the substitution of Cu with Au and hence the change in the nature of magnetic ordering and the transition temperature of $RECu_4Au$ compared to $RECu_5$. The refined agreement indices for the three compounds are: R_p (an indicator of the goodness of fit: GOF), R_{wp} (a measure of the GOF calculated point by point and weighted by the standard deviation of the data), R_{exp} (an expected value of R_{wp}, $\chi^2 = R_{wp}/R_{exp}$ (GOF based

Table 4.2: Interatomic distance of $NdCu_4Au$, $GdCu_4Au$ and $LuCu_4Au$ compounds. Only distances less than 4 Å are shown.

	(Nd, Gd)	d(Å)	Cu	d(Å)	Au	d(Å)
$NdCu_4Au$	12Cu:	2.9803	3Cu:	2.507	12Cu:	2.9882
	4Au:	3.11686	3Cu:	2.582	4Nd:	3.11686
			3Nd:	2.9803		
			2Au:	2.9882		
$GdCu_4Au$	12Cu:	2.9563	3Cu:	2.498	12Cu:	2.9616
	4Au:	3.0905	3Cu:	2.548	4Gd:	3.0905
			3Gd:	2.9563		
			2Au:	2.9616		
$LuCu_4Au$	12Cu:	2.9153	3Cu:	2.456	12Cu:	2.9224
	4Au:	3.0486	3Cu:	2.9153	4Gd:	3.0486
			3Gd:	2.9224		
			2Au:	3.0486		

on statistic), R_B (Bragg or intensity factor, a measure of the quality of the structural model related to the peak shape and not the area and DW (Durbin-Watson parameter: a measure of the quality of the fit model) are listed in Table 4.3 and they are defined as [126]:

$$R_p = \left[\frac{\sum \mid Y_{0,m} - Y_{c,m} \mid}{\sum Y_{0,m}}\right]^{1/2} \tag{4.1}$$

$$R_{wp} = \left[\frac{\sum w_m (Y_{0,m} - Y_{c,m})^2}{\sum w_m Y_{0,m}^2}\right]^{1/2} \tag{4.2}$$

$$R_{exp} = \left[\frac{\sum (M - P)}{\sum w_m Y_{0,m}^2}\right]^{1/2} \tag{4.3}$$

$$\chi^2 = \left[\frac{\sum w_m (Y_{0,m} - Y_{c,m})^2}{\sum (M - P)}\right]^{1/2} \tag{4.4}$$

$$DW = \frac{\sum_{m=2}^{M} (\Delta Y_m - \Delta Y_{m-1})}{\sum_{m=1}^{M} (\Delta Y_m)^2}; \Delta Y_m = Y_{0,m} - Y_{c,m}. \tag{4.5}$$

It is noted that though the quality of the fit is reasonably good (Figs 4.1 and 4.2), the observed values of χ^2 and the R-factors obtained from the Rietveld refinement are relatively good as indicate in Table 4.3. On the other hand the values of R_B listed in Table 4.3 indicate that the structural model is probably correct. In order to investigate the quality of the Rietveld refinement fit, further refinement of the XRD pattern was performed on the basis of the CAILS-Pawley refinement method using the $F\overline{4}3m$ space group (Figs 4.1 and 4.2). It should be noted that the CAILS refinement method is different from the traditional Rietveld refinement technique in the sense that only cell parameters, peak width parameters and integrated intensities are refined. CAILS refinement is independent of the atomic position parameters (or structural model) and only depends on the space group symmetry. Furthermore, in the CAILS method the intensities of all peaks vary independently. The values of χ^2 and the R-factors obtained from the CAILS refinement are also listed in Table 4.3. It is observed that these values are comparable to the values obtained from the full-structure Rietveld refinement discussed above. This observation reveals that the values of χ^2 and the R-factors are not due to an incorrect structural model. Detailed analysis of the refined profile in both methods reveals that the observed peak shape is different from the peak shape calculated using three phase peak type functions for classical analytical full pattern fitting. These are: the Pseudo-Voigt (PV-peak-type), the Thompson-Cox-Hasting Pseudo-Voigt (TCHZ-peak-type) and the macro-Pearson VII (PVII-peak-type) functions. The best fit was obtained using the PVII-peak-type function (see difference curves in Figs 4.1 and 4.2). However, the peak shapes are still not captured perfectly, which may be due to strain or chemical inhomogeneity or high defect density in the sample. The overall diffraction patterns show that the sample is largely single phase with small amount impurity in the case of $LuCu_4Au$ compound.

Table 4.3: The refined agreement indices of the full-structure Rietveld and CAILS refinement method (for comparison only).

Compounds	$NdCu_4Au$		$GdCu_4Au$		$LuCu_4Au$	
Parameters	Rietveld	CAILS	Rietveld	CAILS	Rietveld	CAILS
R_p%	4.087	2.877	2.349	1.654	4.411	5.080
R_{wp}%	5.649	4.328	3.384	2.343	6.315	7.07
R_{exp}%	1.381	1.377	1.183	1.180	1.165	1.164
χ^2	4.092	3.144	2.86	1.986	4.419	5.082
R_B%	3.21		3.08		3.14	
DW%	0.138	0.229	0.265	0.547	0.111	0.084

Figs 4.4 and 4.5 show micrographs of $NdCu_4Au$ and $GdCu_4Au$ taken from scanning electron microscope (SEM) under approximately 1 × magnification. These micrograph images show a single phase, with the slight discolouration attributed to the polycrystalline nature

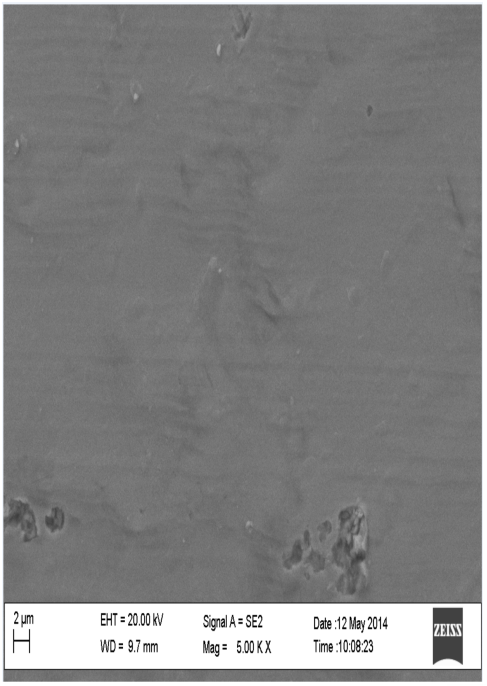

Figure 4.4: SEM micrograph of $NdCu_4Au$ taken at 5 × magnification.

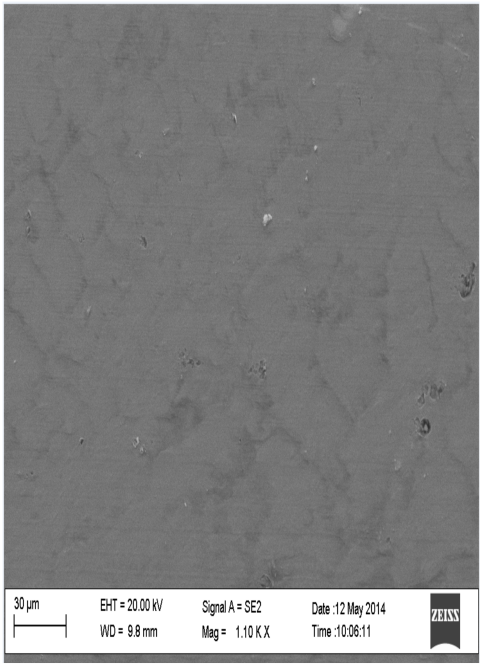

Figure 4.5: SEM micrograph of $GdCu_4Au$ taken at 1.10 × magnification.

of the samples. Also, they are characterized by smooth surfaces, a further verification of homogeneity of the compounds. There are also cracks or scratches visible from polishing of the surface prior to the scanning process. Energy dispersive spectroscopy (EDS) analyses of our compounds $NdCu_4Au$, $GdCu_4Au$ and $LuCu_4Au$ indicate the sample elemental composition normalized to the Nd, Gd and Lu content to be $NdCu_{4.117}Au_{0.730}$, $GdCu_{4.152}Au_{0.847}$ and $LuCu_{4.064}Au_{0.832}$, which are roughly in the 1-4-1 composition.

4.3.2 Electrical resistivity

The main panel of Fig 4.6 shows the temperature variation of $\rho(T)$ of $NdCu_4Au$ and $GdCu_4Au$ compounds. It is observed that, at low temperature, $\rho(T)$ data shows a sudden drop due to the suppression of the magnetic scattering associated with AFM anomalies at T_N=3.8 K and 10.9 K for $NdCu_4Au$ and $GdCu_4Au$ compounds, respectively as indicated by arrows in the insets of Fig 4.6. These values of T_N corroborate with the values obtained from the susceptibility $\chi(T)$ and heat capacity $C_p(T)$ studies which are shown in the coming sections. Electrical resistivity,$\rho(T)$, of most rare earth compounds at high temperatures usually deviate from linearity expected from the electron-phonon interaction. This deviation from linearity is sometimes associated with the presence of the $s-d$ scattering or crystal-electric field (CEF) effect. Accordingly, the high temperatures,

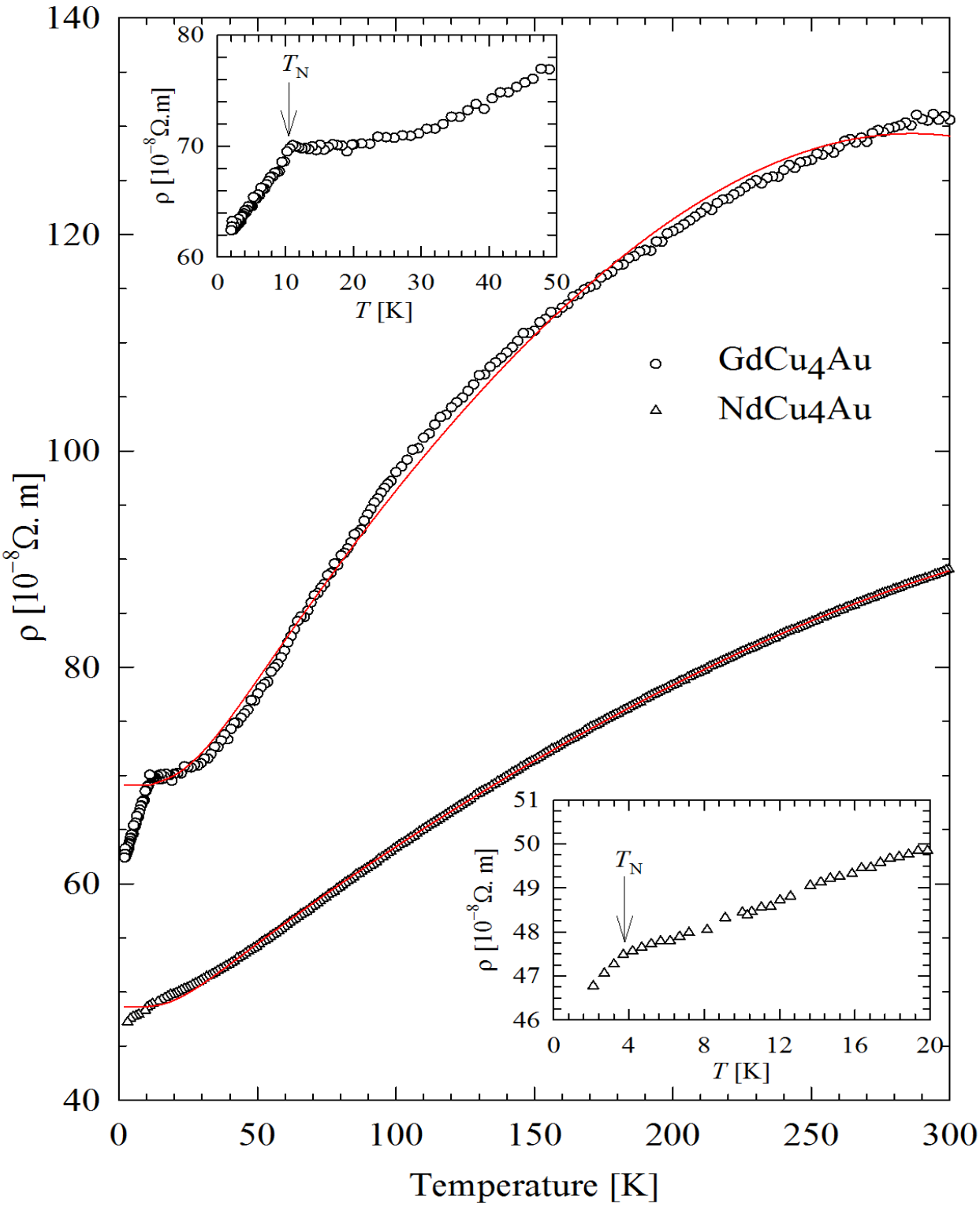

Figure 4.6: Temperature dependence of the electrical resistivity, $\rho(T)$, of $NdCu_4Au$ and $GdCu_4Au$ compounds. The red solid curves are the Bloch-Grüneissen-Mott fits (Eq 4.6). The insets are the low temperatures $\rho(T)$ data of both compounds with the arrows indicating the magnetic phase transition temperature at T_N.

Table 4.4: Resistivity parameters of $NdCu_4Au$ and $GdCu_4Au$ above their respective T_N values. These parameters were obtained from a least-squares fit of the measured $\rho(T)$ data to Eq 4.6 .

Parameters	$NdCu_4Au$	$GdCu_4Au$
$(\rho_0 + \rho_0^\infty)[10^{-8}\Omega.m]$	48.6	68.7
$\kappa[10^{-8}\Omega.m/K]$	0.1653(2)	0.324(2)
Θ_D[K]	127(1)	170(3)
$\alpha[10^{-14}\Omega.m/K^3]$	0.326(3)	1.35(3)

$\rho(T)$ behaviour of $NdCu_4Au$ and $GdCu_4Au$ compounds are characteristic of the electron-phonon scattering in the presence of the $s-d$ interband scattering and can be described according to the Bloch-Grüneisen-Mott (BGM) formula:

$$\rho(T) = \left(\rho_0 + \rho_0^\infty\right) + 4\kappa T\left(\frac{T}{\Theta_D}\right)^4 \int_0^{\Theta_R/T} \frac{x^5 dx}{(e^x - 1)(1 - e^x)} - \alpha T^3, \tag{4.6}$$

where $\left(\rho_0 + \rho_0^\infty\right)$ is the sum of the residual resistivity due to impurities and imperfections in the crystal and the spin-disorder resistivity due to the presence of disordered magnetic moments. The second term described the scattering of conduction electrons by phonons (θ_D being the Debye temperature and κ is the electron-phonon coupling constant) and the third term described the $s-d$ interband scattering known as the Mott's term. In the case of $NdCu_4Au$ compound, deviation from linearity of $\rho(T)$ may also originate from the presence of CEF effect observed from the heat capacity results. Least square (LSQ)fits of the measured $\rho(T)$ data to Eq 4.6 (solid red lines Fig 4.6) yield the resistivity parameters gathered in Table 4.4.

In the ordering region ($T \leq T_N$), the magnetic properties of both compounds are similar, where $\rho(T)$ is a linear function of temperature. This linear behaviour is more evident for the $GdCu_4Au$ compound as seen in Fig 4.7. $\rho(T)$ below T_N can be expressed in the form: $\rho(T) = \rho_0 + AT$. The linear fit of $\rho(T)$ data below T_N gives values of ρ_0 and A gathered in Table 4.5. The resulting spin-disorder resistivity for the Gd compound is also gathered in Table 4.5. The linear T-dependence below T_N may originate from the combination of

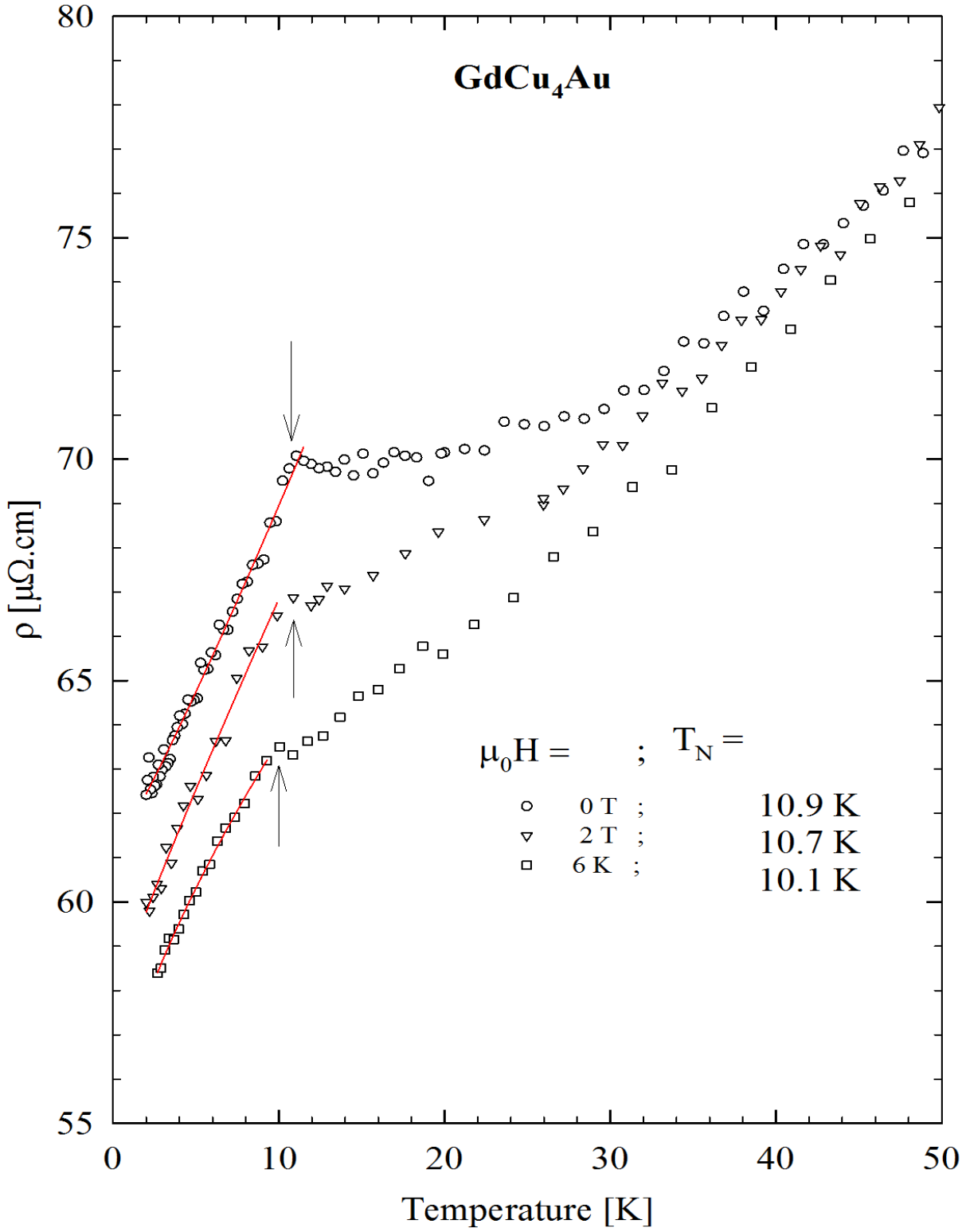

Figure 4.7: Low temperature electrical resistivity $\rho(T)$ of $GdCu_4Au$ in applied field of 0, 2 and 6 T. The arrows indicate the sudden drop of $\rho(T)$ data at a temperature associated with T_N. The red solid lines represent the linear fits of $\rho(T)$ below T_N.

magnetic and phononic plus possible Fermi liquid contributions. Application of a magnetic field slightly suppress T_N value from 10.9 K to 10.1 K in fields up to 6 T as well as the residual resistivity, while the coefficient A and ρ_0^∞ increases with applied magnetic field as indicated in Table 4.5.

Table 4.5: Linear fits parameters of the low temperatures $\rho(T)$ data of $GdCu_4Au$, as measured in different fields.

$\mu_0 H$ [T]	0	2	6
$\rho_0[10^{-8}\Omega.m]$	61.2(3)	58(1)	54.8(8)
$A[10^{-8}\Omega.m/K]$	0.6(1)	1.1(6)	1.9(6)
T_N[K]	10.9(7)	10.6(2)	10.1(1)
$\rho_0^\infty[10^{-8}\Omega.m]$	4.5(3)	10.7(1)	13.9(8)

4.3.3 Magnetic susceptibility and magnetization

The temperature variation of the inverse magnetic susceptibility,$\chi^{-1}(T)$, measured in applied field of 0.05 T in the temperature range 1.8-300 K is shown in Figs 4.8 and 4.9 for the $NdCu_4Au$ and $GdCu_4Au$ compounds, respectively. For $NdCu_4Au$, the modified Curie-Weiss behaviour is observed at higher temperature and a deviation occurs below 10 K. It is most likely just connected with an approach to magnetic ordering. LSQ fits of the modified Curie-Weiss relationship can be expressed:

$$\chi(T) = \chi(0) + \frac{N_A \mu_{eff}^2}{3K_B(\theta_P + T)}. \tag{4.7}$$

Above 10 K the values of the susceptibility parameters are listed in Table 4.6. The obtained μ_{eff} value is close to the free Nd^{3+} Hund's rule expectation value, $g_J = [J(J+1)]^{1/2} = 3.56\mu_B$. In order to investigate the magnetic state of $NdCu_4Au$ at low temperature, the low temperature field-cooled (FC) and zero-field-cooled(ZFC),$\chi(T)$ data are plotted in the inset of Fig 4.8. It is observed that both FC and ZFC $\chi(T)$ data coincide into a single curve which suggest a homogeneous magnetic spin state and no sign of short-range order. Both curves rise into an anomaly at $T_N = 3.9$ K which is attributed to an AFM-like phase transition for this compound. This value of T_N obtained for our $NdCu_4Au$ compound may be compared to the value of 4.2 K [121] or 4.3 K [125] for the single-crystal $NdCu_4Ag$ compound. This similarity of T_N values may be attributed to

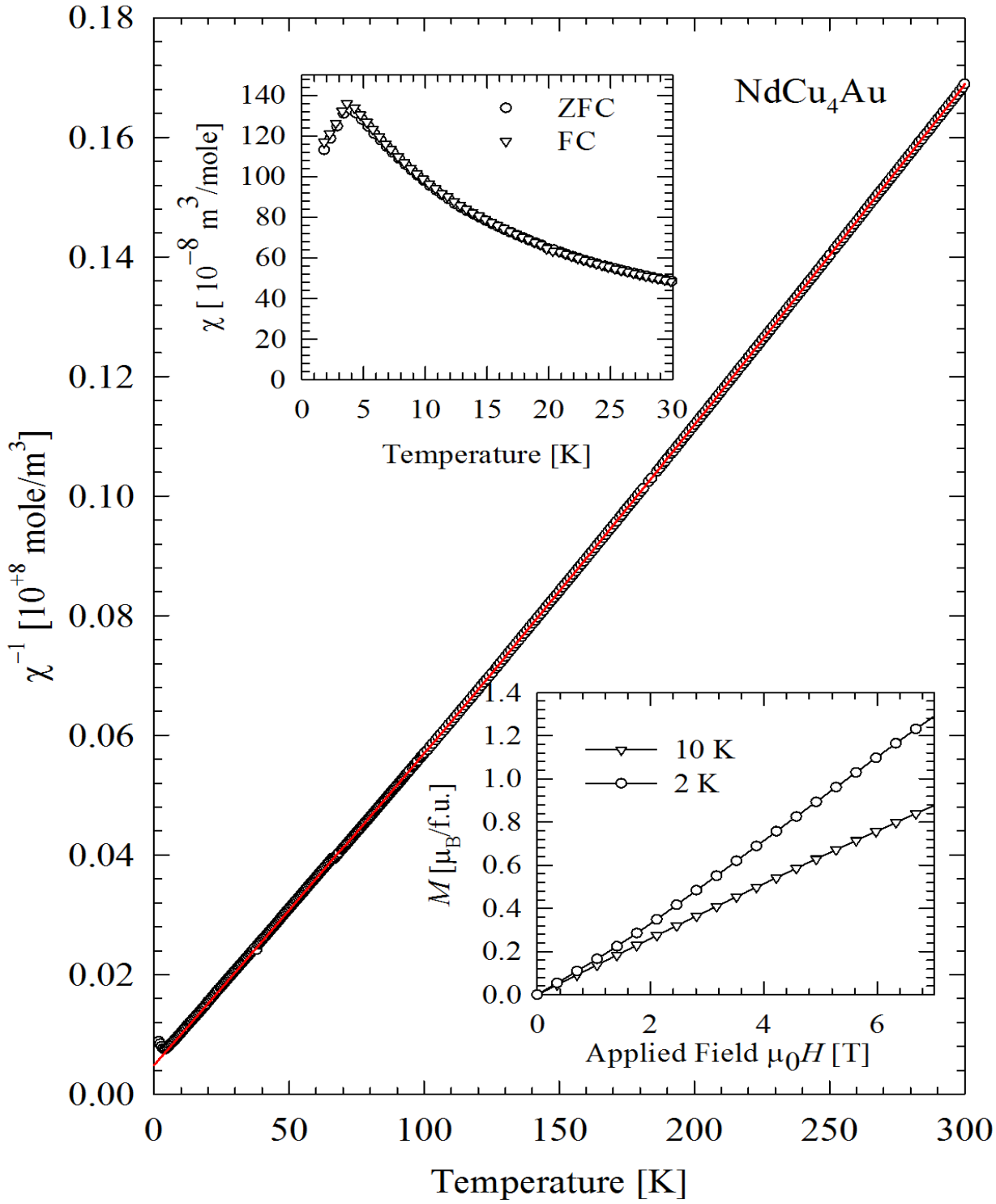

Figure 4.8: The temperature dependence of the inverse magnetic susceptibility, $\chi^{-1}(T)$ for $NdCu_4Au$. The red solid line is LSQ fits of the modified Curie-Weiss relation (Eq 4.7) above 10 K. The upper inset shows the low temperature $\chi(T)$ data measured in zero-field-cooled (ZFC) and in field-cooled (FC) run. The lower inset shows the field dependence magnetization $M(\mu_0 H)$ measured at 2 K and 10 K in field up to 7 T.

the iso-electronic nature of the Au and Ag atom and suggests that conduction electron-mediated RKKY interaction in $NdCu_4Ag$ is not affected by replacing Ag with Au atom in contrast to $NdCu_5$ compound with the substitution of one Cu with Ag or Au atom. Similar to the substitution of Ag for Cu in $NdCu_5$, the substitution of Au for Cu drastically changes the crystallographic structure as well as the nature of the magnetic ordering and the transition temperature, the transition being FM for $NdCu_5$ to AFM for $NdCu_4Au$. The magnetization,$M(\mu_0 H)$, for $NdCu_4Au$ as measured below and above T_N(at 2 K and 10 K) in fields up to 7 T is shown in lower inset of Fig 4.8. It is observed that the isothermal curves show no anomaly associated with metamagnetic transition observed in $NdCu_4Ag$ [122, 123], and increase almost linearly with field up to 7 T. For both isotherms, $(M\mu_0 H)$ reaches the value of 1.33 μ_B and 0.91 μ_B at 7 T in the ordering and paramagnetic regions respectively. These values of at 7 T for both isotherms are considerably reduced compared to the full magnetic moment value of the free Nd^{3+} Hund's rule expectation value 3.62 μ_B.

For the $GdCu_4Au$ compound, it is observed that $\chi(T)$ data (Fig 4.8) obey the Curie-Weiss magnetic behaviour above T_N, leading to the susceptiblity parameters shown in Table 4.6, when fitted to the CW law:

$$\chi^{-1}(T) = 3k_B(\theta - T)/N_A\mu_{eff}^2. \tag{4.8}$$

The obtained μ_{eff} value listed in Table 4.6 is close to the free-ion Gd^{3+} Hund's rule expectation value, $g_J = [J(J+1)]^{1/2} = 7.94\ \mu_B$. Deviation of the CW behaviour below T_N may be attributed to magnetic ordering or crystal-electric field effect. To further explore the low temperature magnetic state of $GdCu_4Au$, the low temperature field-cooled (FC) and zero-field-cooled $\chi(T)$ data are depicted in upper inset of Fig 4.9. Both FC and ZFC $\chi(T)$ data rise into an anomaly at T_N =10.8 K which is attributed to a putative AFM-like phase transition for this compound.

Table 4.6: Magnetic susceptibility fit parameters of $NdCu_4Au$ and $GdCu_4Au$ compounds.

Compound	$\mu_{eff}[\mu_B]$	$-\theta_P$[K]	$\chi(0)$ [$\times 10^{-8} m^3$/mole]
$NdCu_4Au$	3.54	10.19	193.5
$GdCu_4Au$	7.44	15.01	–

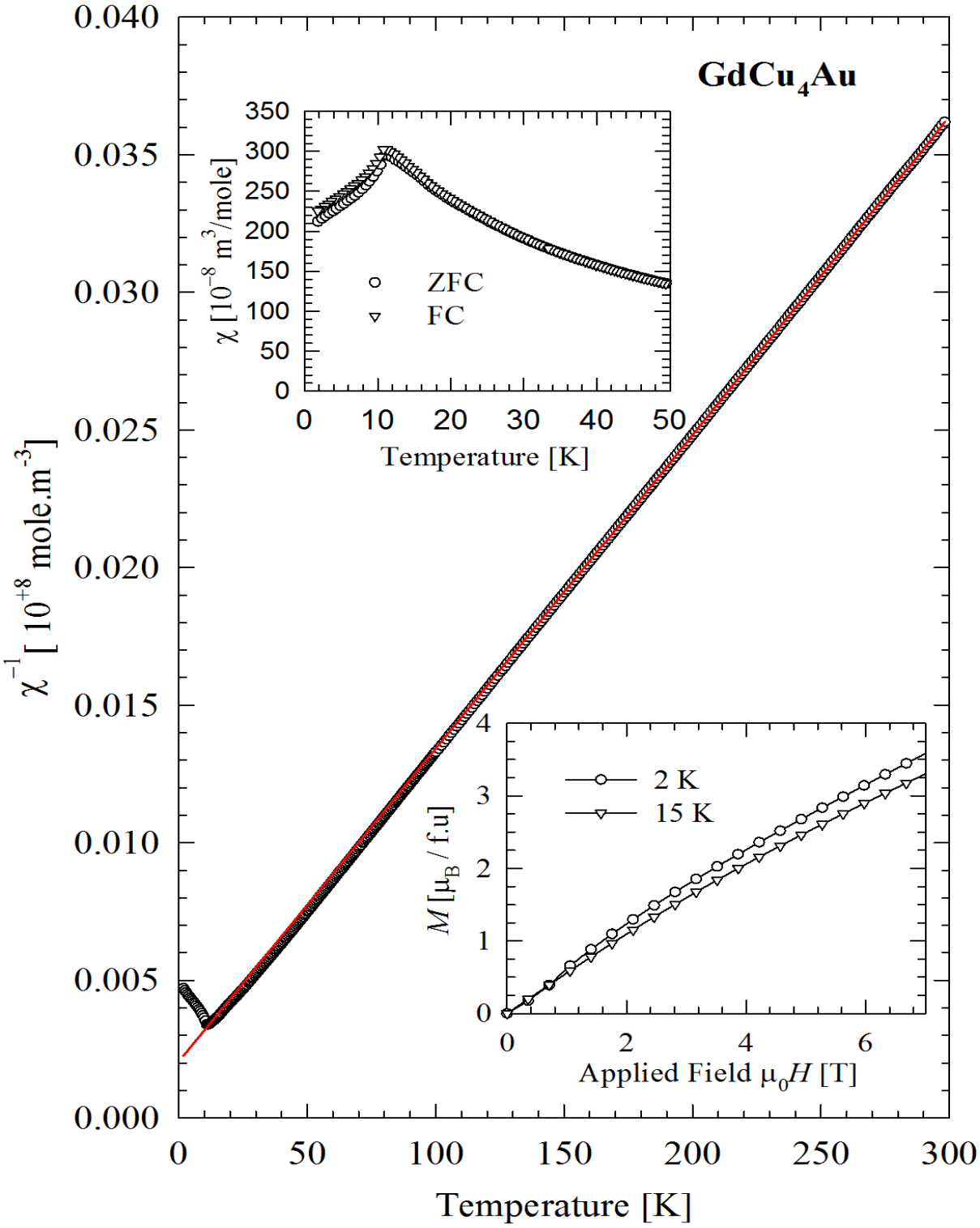

Figure 4.9: Temperature dependence of inverse magnetic susceptibility, $\chi^{-1}(T)$ data for the $GdCu_4Au$. The red solid line is LSQ fits of the Curie-Weiss relation (Eq 4.8) above 10 K. The upper inset shows the low temperature $\chi(T)$ data measured in zero-field-cooled (ZFC) and in field-cooled (FC) run. The lower inset shows the field variations of the magnetization $M(\mu_0 H)$ measured at 2 K and 15 K in field up to 7 T.

Furthermore, it is observed that the FC and ZFC $\chi(T)$ data split into two branches above T_N at a freezing temperature $T_f = 15$ K. Such a bifurcation may originate from an inhomogeneous magnetic ground state in this compound, as a result a spin-glass-like state may form that causes the bifurcation or from an accidental magnetic history of the sample. It should be noted that the observed thermomagnetic irreversibility of $GdCu_4Au$ is very small compared to other RE compounds such as $RENi_4Si$ [127]. It was pointed out that the large thermomagnetic irreversibility observed in $RENi_4Si$ arise from the anisotropy due to RE-ion except for the Gd compound. However, the small thermomagnetic anisotropy for the Gd compound is due to the fact that Gd-ion is characterized by the orbital momentum L= 0 implying a negligible magnetic anisotropy also observed in our sample. Our value of T_N= 10.8 K obtained for $GdCu_4Au$ may be compared to the values of T_N= 10 K and 12.5 K reported in the literature for the parent compound $GdCu_5$ [100, 128]. This similarity of $T_N$values of $GdCu_4Au$ and $GdCu_5$, suggest that conduction electron-mediated RKKY exchange interaction in $GdCu_5$ is not affected by substitution of Au for Cu in contrast for $TbCu_5$ compound with the substitution of Pd for Cu [129]. Finally, $M(\mu_0 H)$ for $GdCu_4Au$ as measured below and above T_N (2 K and 15 K) in field up to 7 T is depicted in the lower inset of Fig 4.9. It is observed that $M(\mu_0 H)$, for both isotherms, increase linearly with field up to 0.7 T, and exhibit a slight upward curvature above this field which may be attributed to metamagnetic transition for $T = 2$ K and a downward curvature for $T = 15$ K.

4.3.4 Specific heat

4.3.4.1 $NdCu_4Au$

The temperature dependence of specific heat, $C_p(T)$, of $NdCu_4Au$ and the non-magnetic reference compound $LuCu_4Au$ as measured in the temperature range 1.8-300 K are displayed in Fig 4.10. It is observed that $C_p(T)$ curve of this non-magnetic reference compound varies monotonically with no anomaly down to 1.8 K, and approaches the classical value of $3NR = 149.7$ J/K of the Dulong-Petit law around 180 K due to the vibrational mode of N= 6 atoms per formula unit. At higher temperatures range, C_P of $LuCu_4Au$ may be expressed by the standard Debye formula:

$$C_p(T) = \gamma T + 9NR(\frac{T}{\theta_D})^3 \int_0^{x_D} \frac{x^4 e^x}{(e^x - 1)^2}, \tag{4.9}$$

where the first term represents the electronic contribution and the second term is the Debye formula contribution. N is the number of atoms per formula unit. LSQ fit of the experimental data points of $LuCu_4Au$ to Eq 4.9 (red solid line in Fig 4.10) yields the

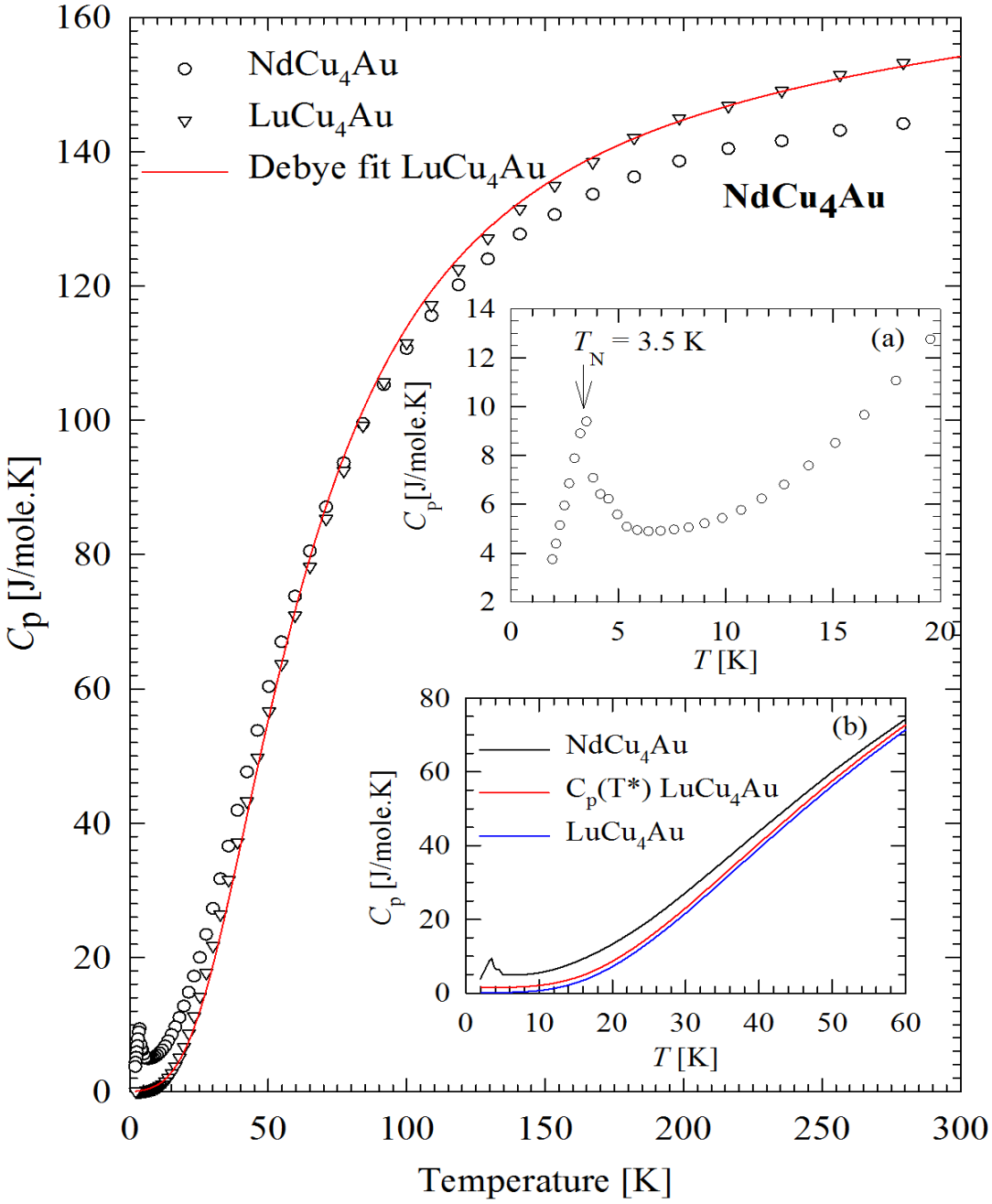

Figure 4.10: The specific heat $C_p(T)$ data of $NdCu_4Au$ (open circle)and $LuCu_4Au$ (open triangle). The red solid line in the main panel represents LSQ fit of $C_p(T)$ of $LuCu_4Au$ data to Eq 4.9. The inset (a) shows the low temperature $C_p(T)$ data of $NdCu_4Au$ with the arrow at the magnetic phase transition taken at the sharp peak. The inset (b) shows $C_p(T)$ data of $NdCu_4Au$ (black line), $LuCu_4Au$ (blue line) and mass corrected $C_p(T)$ data of $LuCu_4Au$ according to Eq 4.10 (red line).

values of $\gamma = 0.033$ J/mol.K and $\theta_D = 254(1)$ K for the electronic heat capacity coefficient and the Debye temperature, respectively. For the magnetic compound $NdCu_4Au$, a sharp peak on the $C_p(T)$ data of 9.39 J/mol.K is found at 3.5 K (as indicated by an arrow in the inset(a) of Fig 4.10) that corresponds to the phase transition from the paramagnetic state to the AFM one. This value of T_N=3.5 K is very close to the value of 3.9 K observed in the $\chi(T)$ data. No evidence of charge or spin-density wave was observed on the C_p data of $NdCu_4Au$ compound below T_N, since $C_p(T)$ below T_N varies almost linearly with temperature down to 1.8 K. To obtain the magnetic $4f$ electronic contribution to the total heat capacity of $NdCu_4Au$, the mass-corrected lattice contribution $C_p(T)$ of the isomorphous nonmagnetic $LuCu_4Au$ compound was used. This is because of the significant difference in molar masses between $NdCu_4Au$ and $LuCu_4Au$. Similar to ref [130], the mass-corrected lattice contribution was obtained by changing the temperature scale of the measured $C_p(T)$ to T^*, given in the form:

$$C_P(T^*) = T\left[\frac{M_{LuCu_4Au}}{M_{NdCu_4Au}}\right]^{1/2} \times \left[\frac{M_{LuCu_4Au}}{M_{NdCu_4Au}}\right]^{3/2}, \tag{4.10}$$

where M_{NdCu_4Au}, M_{NdCu_4Au}, V_{LuCu_4Au} and V_{NdCu_4Au} are the molar masses and unit cell volumes of $LuCu_4Au$ and $NdCu_4Au$, respectively, and T being the measured temperature of $LuCu_4Au$ compound. The inset b) of Fig 4.10 shows the mass-corrected $C_p(T^*)$ as calculated from Eq 4.10 (red solid line), as well as the measured $C_p(T)$ (black solid line) for $LuCu_4Au$. The magnetic contribution $C_{4f}(T)$ of $NdCu_4Au$ is then obtained by subtracting $C_p(T^*)$ lattice contribution of $LuCu_4Au$ from the measured data of $NdCu_4Au$. Fig 4.11 exhibits the temperature dependence of the $4f$ specific heat $C_{4f}(T)$ of $NdCu_4Au$. It should be noted that C_{4f} has entropy contributions coming from magnetic ordering at T_N as well as from splitting of the ground multiplet under the presence of a crystal field. In a cubic CEF, the tenfold degenerate ground-state multiplet $^4I_{9/2}$ of the Nd ion splits the 4_f level into three states: a I_6 doublet and two quartet of $I_8^{(1)}$ and $I_8^{(2)}$ with the two higher states at energy separation Δ_1 and Δ_2 from the ground state ($\Delta_0 = 0$). It is observed that C_{4f} above T_N exhibits a broad maximum centred around 20 K characteristic of a Schottky-type anomaly. This thermal dependence of the Schottky-type anomaly due to CEF effect can be described by the expression [131],

$$C_{4f}(T) = R\left[g_0 g_1\left(\frac{\Delta_1}{T}\right)^2 e^{(-\Delta_1/T)} + g_0 g_2\left(\frac{\Delta_2}{T}\right)^2 e^{(-\Delta_2/T)} + g_1 g_2\left(\frac{\Delta_1 - \Delta_2}{T}\right)^2 e^{(-(\Delta_1-\Delta_2)/T)}\right]$$
$$\times\left[\frac{1}{g_0 + g_1 e^{-\Delta_1/T} + g_2 e^{-\Delta_2/T}}\right]. \tag{4.11}$$

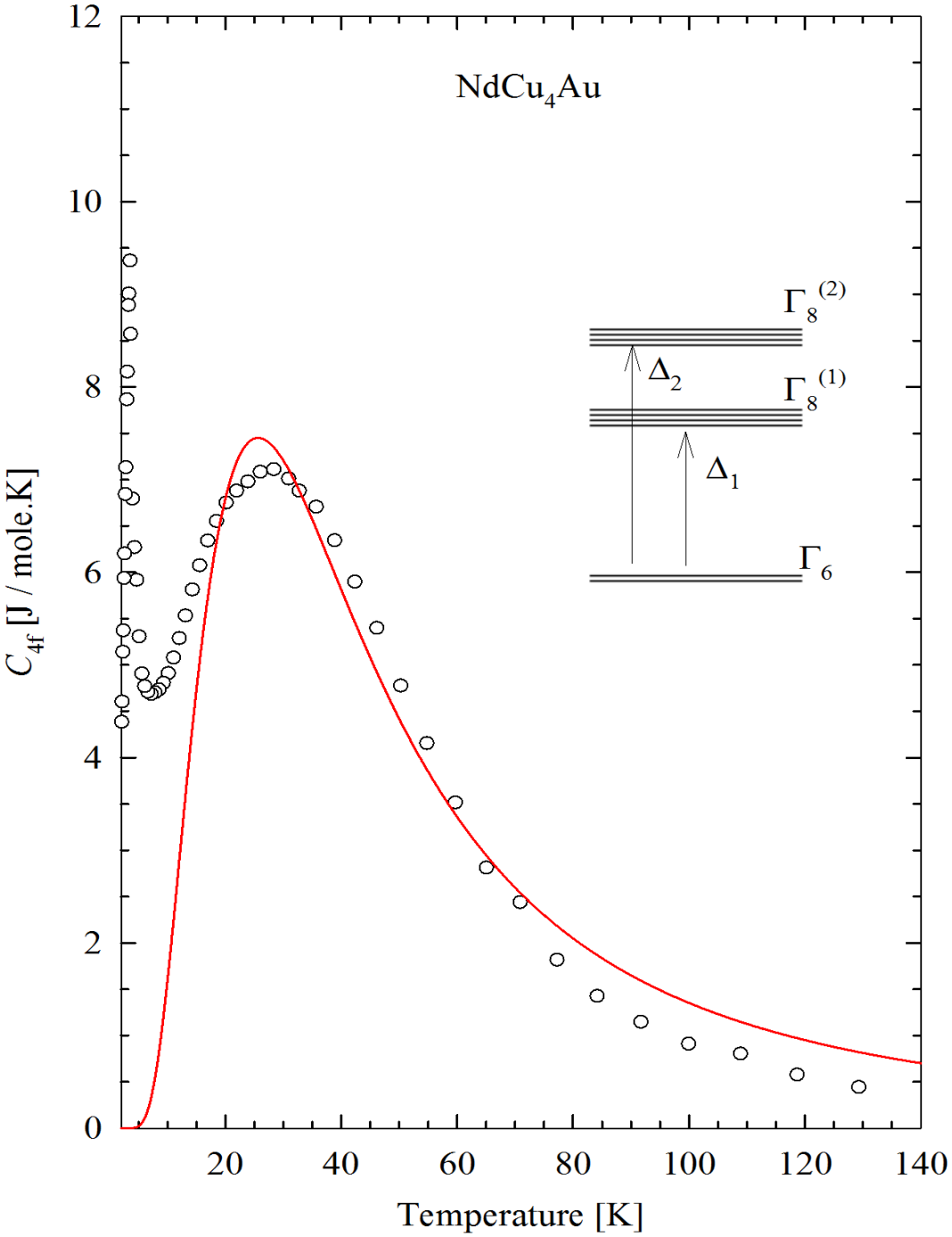

Figure 4.11: The temperature dependence of the $4f$-electron contribution to the specific heat C_{4f} of $NdCu_4Au$ obtained by subtracting the $C_p(T^*)$ data of $LuCu_4Au$(red solid line in the inset(b) of Fig 4.10). The solid red curve is the CEF-derived Schottky anomaly using Eq 4.11. The inset shows Schottky model based on the CEF energy scheme.

Δ_1 and Δ_2 represent the successive energy levels of the CEF and degeneracies $g_1$and g_2. The analysis of the Schottky peak in $C_{4f}(T)$ above the transition temperature T_N based on Eq 4.11 is displayed in Fig 4.11 (by red solid line) using a degeneracy $g_0 = 2$, $g_1 = 4$ and $g_2 = 4$ of the ground state doublet Γ_6, the first excited state quartet Γ_8^1, and the second excited state quartet Γ_8^2 of Nd^{3+}-ion respectively. The calculated energy separations are $\Delta_1 = 62(5)$ K for the first excited state and $\Delta_2 = 109(9)$ K for the second excited state. For further investigation of the ground state doublet of N^{3+}-ion, the $4f$ entropy of $NdCu_4Au$ was calculated by using the formula:

$$S_{4f} = \int_T^0 \frac{C_{4f}}{T} dT. \tag{4.12}$$

It is observed that at T_N, the magnetic entropy $S_{4f}(T)$ reaches the value of $Rln2$ at 4.2 K close to the value of T_N as expected for the two-level ground states Fig 4.12. Compared to $NdCu_4Ag$ (T_N=4.2 K) [121], $SmCu_4Ag$ ($T_N = 5.5K$) and $SmCu_4Au$ ($T_N = 3.6K$) [132], it was reported that, $S_{4f}(T)$ reach the value $Rln4$, $Rln3.2$ and $Rln1.8$ respectively at their magnetic phase transition temperature T_N. From this behaviour of $S_{4f}(T)$ at T_N, it was suggested that the ground state CEF of $NdCu_4Ag$ and $SmCu_4Ag$ might be Γ_8 quartet and that of $SmCu_4Au$ might be Γ_7 doublet. Accordingly, the ground state CEF of our $NdCu_4Au$ compound can likely be considered a doublet Γ_6 and the first and second excited states are one of the two Γ_8, in spite of the fact that we cannot distinguish the two quartets from the present specific heat experiment.

4.3.4.2 $GdCu_4Au$

The temperature dependence of specific heat $C_p(T)$ of $GdCu_4Au$ is displayed in Fig 4.13. It is noted that $C_P(T)$ varies monotonically with a sharp peak at the magnetic phase transition temperature $T_N = 10.4$ K (see inset of Fig 4.13). This value is close to that observed in the susceptibility data. At higher temperature, $C_P(T)$ curve reaches the classical value of the Dulong-Petit law around 180 K. No evidence of charge or spin density wave was observed on the $C_P(T)$ data of $GdCu_4Au$ compound below T_N. The magnetic contribution to the specific heat C_{4f} as well as the magnetic entropy S_{4f} are shown in Fig 4.14. C_{4f} was calculated by subtracting the mass-corrected $C_P(T^*)$ of $LuCu_4Au$ from the $C_P(T)$ of $GdCu_4Au$. It should be noted that the mass-corrected $C_P(T^*)$ was calculated using the Eq 4.10. The maximum observed in C_{4f} curve, may still originate from the large difference in the lattice vibrational spectra of the two compounds as a consequence of the bigger atomic mass for Lu than for Gd. It could also originate for the fact that

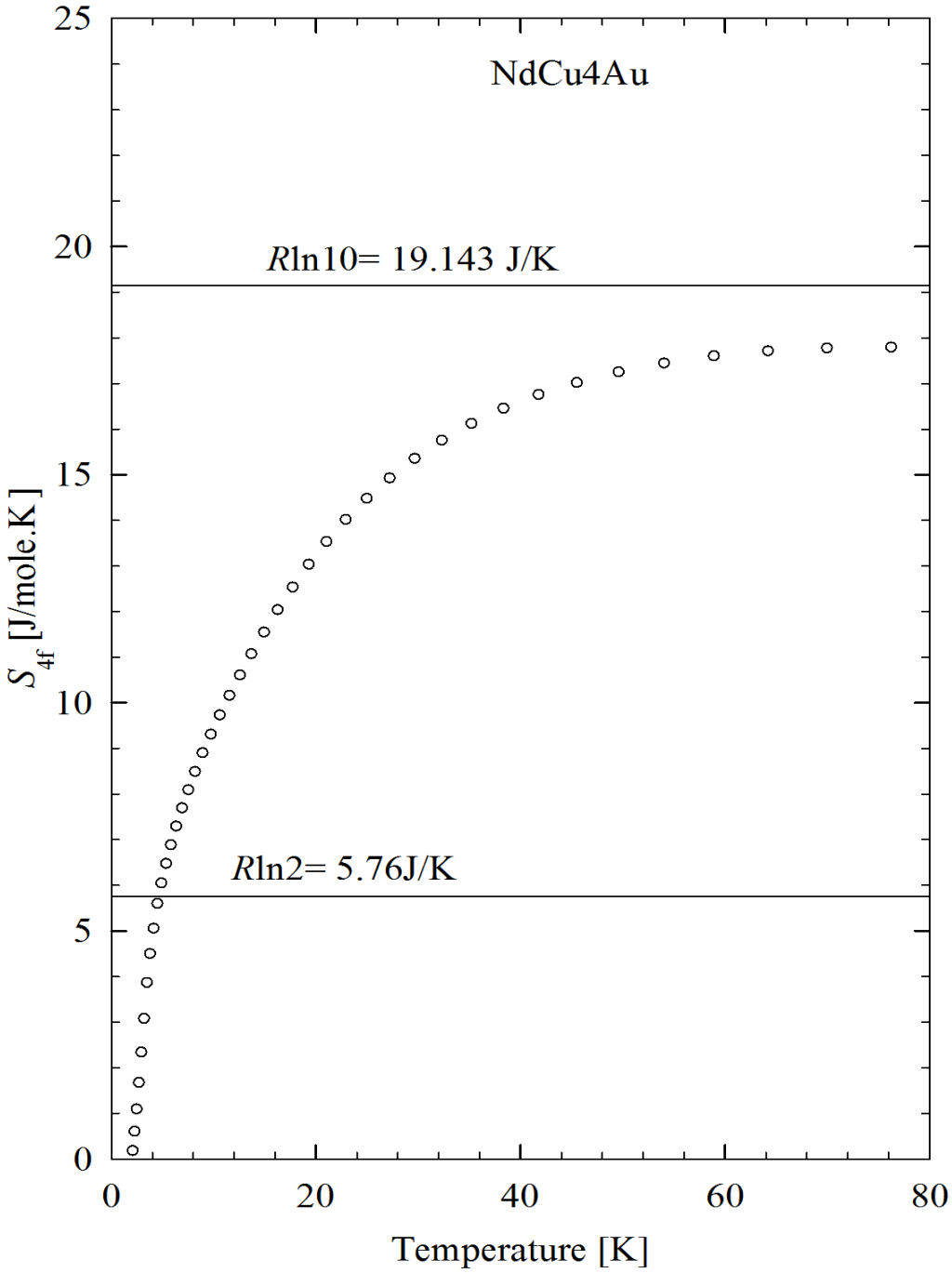

Figure 4.12: The temperature dependence of the $4f$-electron magnetic entropy $S_{4f}(T)$ of $NdCu_4Au$. The bottom and top horizontal lines are the constant values of $Rln2$ and $Rln10$ expected for the two-level ground state and the full multiplet.

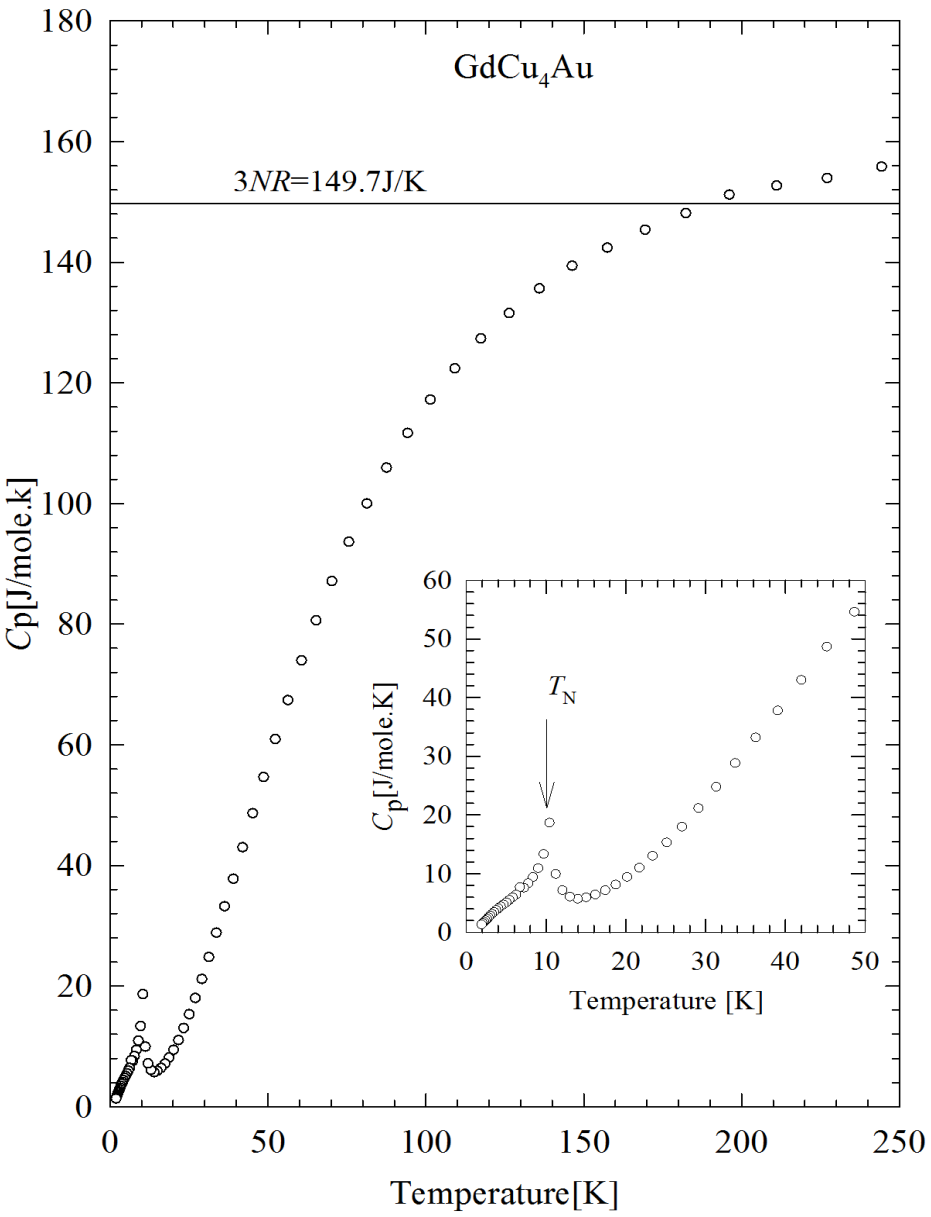

Figure 4.13: Temperature dependence of the specific heat $C_P(T)$ of $GdCu_4Au$. The inset shows the low temperature $C_P(T)$ with the arrow indicating the magnetic phase transition. The top horizontal lines are the classical value of of the Dulong-Petit law due to the vibrational mode of $N = 6$ atoms per formula unit.

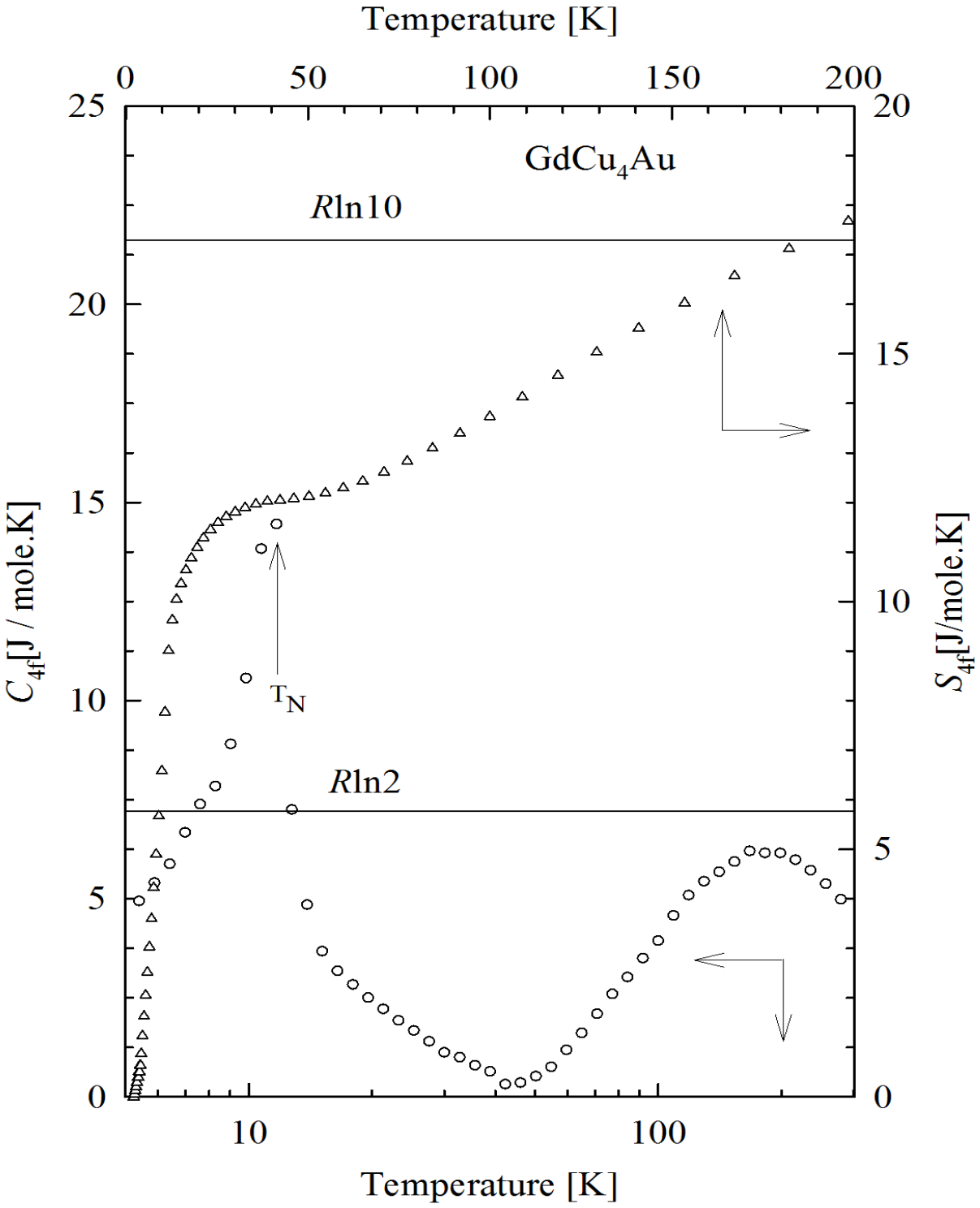

Figure 4.14: The temperature dependence of the $4f$-electron specific heat $C_{4f}(T)$ and the $4f$-electron entropy $S_{4f}(T)$ for $GdCu_4Au$.

Gd ion is characterized by a total angular momentum L=0 and J=S. It should be noted that, the impurity observed in the non-magnetic counterpart may have an impact on the specific heat measurements, leading to a considerable uncertainty in the estimation of C_{4f}. Therefore, we cannot attribute the observed maximum at high temperature to a Schottky anomaly being a result of crystal electric field splitting of the ground state level. The magnetic entropy S_{4f} was calculated from the magnetic part C_{4f} of $GdCu_4Au$ using Eq 4.12. At T_N, S_{4f} reaches nearly 25% more of the value of $Rln(2)$ as expected for the two level ground states and 15% more of the value of $Rln(2J+1) = Rln(8)$ at room temperature.

4.3.5 Thermoelectric power

The temperature dependence of $S(T)$ of the sample $NdCu_4Au$ and is displayed in Fig 4.15. It is seen that $S(T)$ data of $NdCu_4Au$ is positive for the whole temperature range studied, which may be ascribed to the domination of holes in heat transport process in this compound. The overall behaviour of $S(T)$ data of $NdCu_4Au$ compound is dominated by a gradual decrease upon cooling from room temperature and reaching values in the local minimum of 0.05μ V/K at temperature T_N = 3.5 K (see inset Fig 4.15). The observed values of T_N in $S(T)$ data may be compared to the temperature of the magnetic phase transition observed in $\rho(T)$ results as well as to the values reported in the studies of $\chi(T)$ and $C_P(T)$. $S(T)$ data for the $NdCu_4Au$ was analyzed similarly to many f-electron systems using the phenomenological resonance model [89]. In this model, the dominant contribution to $S(T)$ is caused by the scattering between electrons of a broad s-band and a $4f$-narrow derived quasiparticles band of a Lorentzian shape with a wide W_f located at E_f in respect to the Fermi level E_F. The temperature dependence of $S(T)$ for the $NdCu_4Au$ compound can be written as follows with W_f and E_f expressed in Kelvin:

$$S(T) = \frac{2}{3}\pi^2 \frac{k_B}{|e|} \frac{T.E_f}{(\pi^2/3)T^2 + E_f^2 + (\pi^2/N_f^2)W_f^2} + S_d(T). \tag{4.13}$$

where $S_d(T)$ represents the Mott's term, which is related to the density of states of the $4f$-band $N(E_f)$ given by:

$$S_d(T) = \frac{\pi^2 k_B^2 T}{3q_e} \left| \frac{\partial N(E_f)}{\partial E_f} \right|_{E_f}. \tag{4.14}$$

In the free-electron model approximation, Eq 4.14 is reduced to:

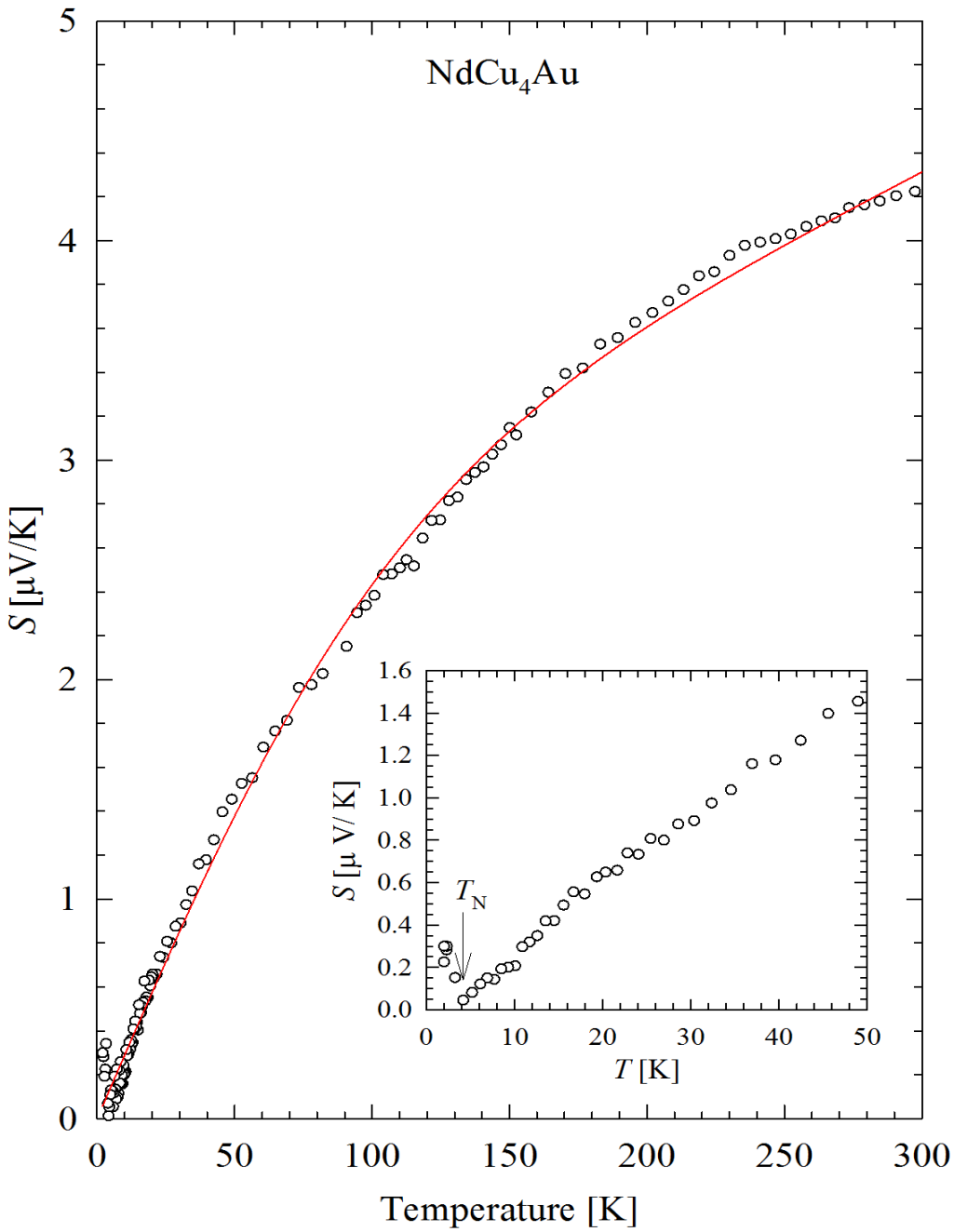

Figure 4.15: Temperature dependence of the thermoelectric power $S(T)$ of $NdCu_4Au$. The solid curves is the fit of $S(T)$ data to the phenomenological resonance model Eq 4.13. The inset is the low temperature $S(T)$ data with an arrow indicating the position of the minimum at a temperature associated with T_N.

$$S_d(T) = \frac{\pi^2 k_B^2 T}{3q_e E_F} = aT. \tag{4.15}$$

The Mott's term therefore can be used to estimate the Fermi energy E_F. LSQ fits of the measured $S(T)$ data points to Eq 4.13 for $NdCu_4Au$ compounds (solid curves Fig 4.15) yield the thermoelectric power parameters listed in Table 4.7.

On the other hand, thermoelectric power $S(T)$ of $GdCu_4Au$ is shown as a function of temperature in Fig 4.16. It is seen that $S(T)$ data of $GdCu_4Au$ take both positive and negative values, which may be attributed to the balance between electrons and holes contributions in heat transport process. The behaviour of $S(T)$ data of $GdCu_4Au$ below 100 K shows a gradual decrease upon cooling the sample and attaining a minimum value of $-0.3\mu V/K$ at temperature $T_N = 11.1$ K. This minimum seen at T_N (inset of Fig 4.16) is connected with AFM transition which is also confirmed in the susceptibility and heat capacity data for this compound. At higher temperatures, $S(T)$ data of $GdCu_4Au$ is dominated by a broad maximum centred at around 100 K. Above this maximum $S(T)$ data exhibit a linear decreasing with increasing temperatures and a sign change from positive to negative around 200 K. The linear temperature dependence of $S(T)$ at higher temperature indicate a diffusion mechanism. In contrast to many Ce compounds, the observed maximum in $S(T)$ data of the Gd compound is not related to coherent-related maximum nor CEF, since for Gd the ground multiplet $L = 0$, but may be attributed to phonon drag which depend on the relaxation time for electron magnon scattering. This effect is washed out at higher temperatures because the electron phonon scattering becomes increasingly important [85]. In this case $S(T)$ of $GdCu_4Au$ compound is also described in terms of the phenomenological resonance model taking into account Mott's diffusion and the phonon drag terms ($S_{ph}(T) = \beta/T$), which finally can be expressed as:

$$S(T) = \frac{2}{3}\pi^2 \frac{k_B}{|e|} \frac{T.E_f}{(\pi^2/3)T^2 + E_f^2 + (\pi^2/N_f^2)W_f^2} + S_d(T) + S_{ph}(T). \tag{4.16}$$

The results obtained from LSQ fits of the measured $S(T)$ data to Eq 4.16 for $GdCu_4Au$ are also presented in Table 4.7. The values of the Fermi energy E_F for both Nd and Gd compound are calculated using Eq 4.15. The analysis of the parameters shown in Table 4.7 indicates that the values of the Fermi energy obtained for both compounds are typical for normal metals. Furthermore, the absolute values of the diffusion term aT which is related to the electronic structure near the Fermi level for both compounds are largely different and relatively larger compared to many Ce heavy-fermion compounds and Kondo systems [88, 133, 134]. Similarly, the values of the width of $4f$-band (W_f) are of the same order

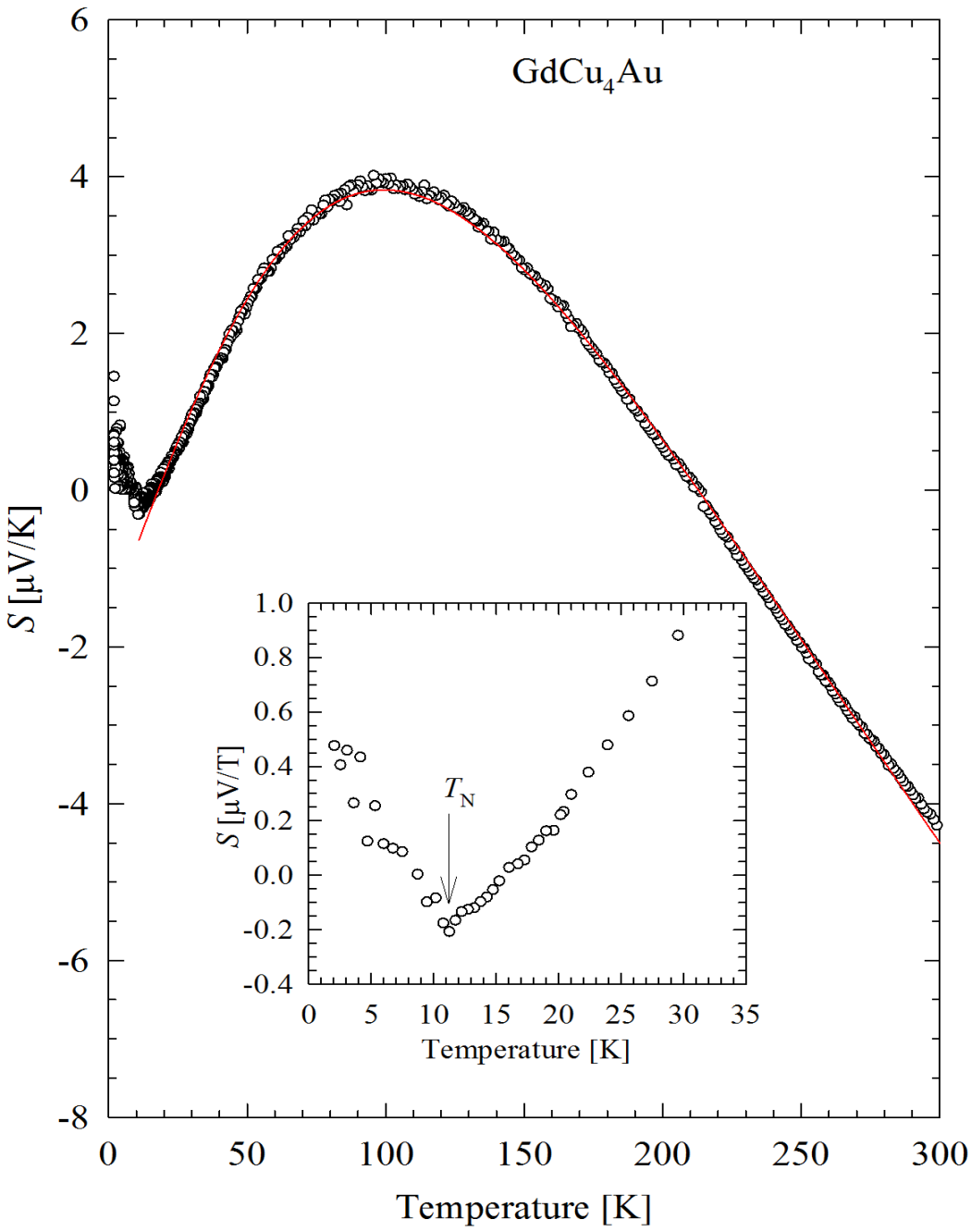

Figure 4.16: Temperature variation of the thermoelectric power $S(T)$ of $GdCu_4Au$. The red solid line through the data points is the fit of $S(T)$ data to the phenomenological resonance model Eq 4.16. The inset is the low temperatures $S(T)$ data with an arrow indicating the position of the minimum at a temperature which associated with T_N.

Table 4.7: LSQ fits parameters of $S(T)$ data to Eqs 4.13 and 4.16 for the $NdCu_4Au$ and $GdCu_4Au$ compounds, respectively.

Parameters	$NdCu_4Au$	$GdCu_4Au$
E_f [K]	3.81(6)	18.2(4)
E_f [meV]	0.328(4)	1.56(3)
W_f[K]	329(58)	306(5)
W_f[meV]	28.3(5)	26.4(4)
$a[\mu V/K^2]$	0.0090(5)	-0.0414(8)
E_F[eV]	2.7	0.6
β [μV]		-0.22(7)

of magnitude for both compounds and roughly 7 times larger in magnitude compared to that of CeT_4M (M =Cu, Ni; M =In, Ga) [88], $CeCu_4Ag$ [133] and $Ce_{1-x}La_xCu_4Al$ [134].

4.3.6 Thermal conductivity and the Lorentz number

The temperature dependence of the thermal conductivity $\lambda(T)$ together with the separated phonon $\lambda_{ph}(T)$ and electronic $\lambda_{elec}(T)$ contributions for $NdCu_4Au$ and $GdCu_4Au$ are shown in Fig 4.17. The electronic contribution,$\lambda_{elec}(T)$ for which the conduction electrons are the carriers, originating from the scattering of these carriers by the lattice imperfections, phonons and magnetic moments. This contribution depends on both temperature and phonon density and is given by the Wiedemann-Franz law: $L = L_0T/\rho_0$ with $L_0 = 2.45 \times 10^{-8}$W Ω/K^2 being the Lorentz number and ρ_0 the residual resistivity. The phonon contribution for which the phonons are the carriers, originates from the collisions of phonon on: impurities and defects present in the lattice, conduction electrons as well as other phonon and magnetic moments [135]. The phonon contribution is obtained by subtracting the electronic contribution from the total thermal conductivity $\lambda(T)$ and assuming that, the two terms are independent of one another and that there are no other carriers of heat (such as magnons).

It is observed from Fig 4.17 that $\lambda(T)$ for both compounds decrease gradually upon cooling the samples down to 50 K, followed by a fast decrease below this temperature.

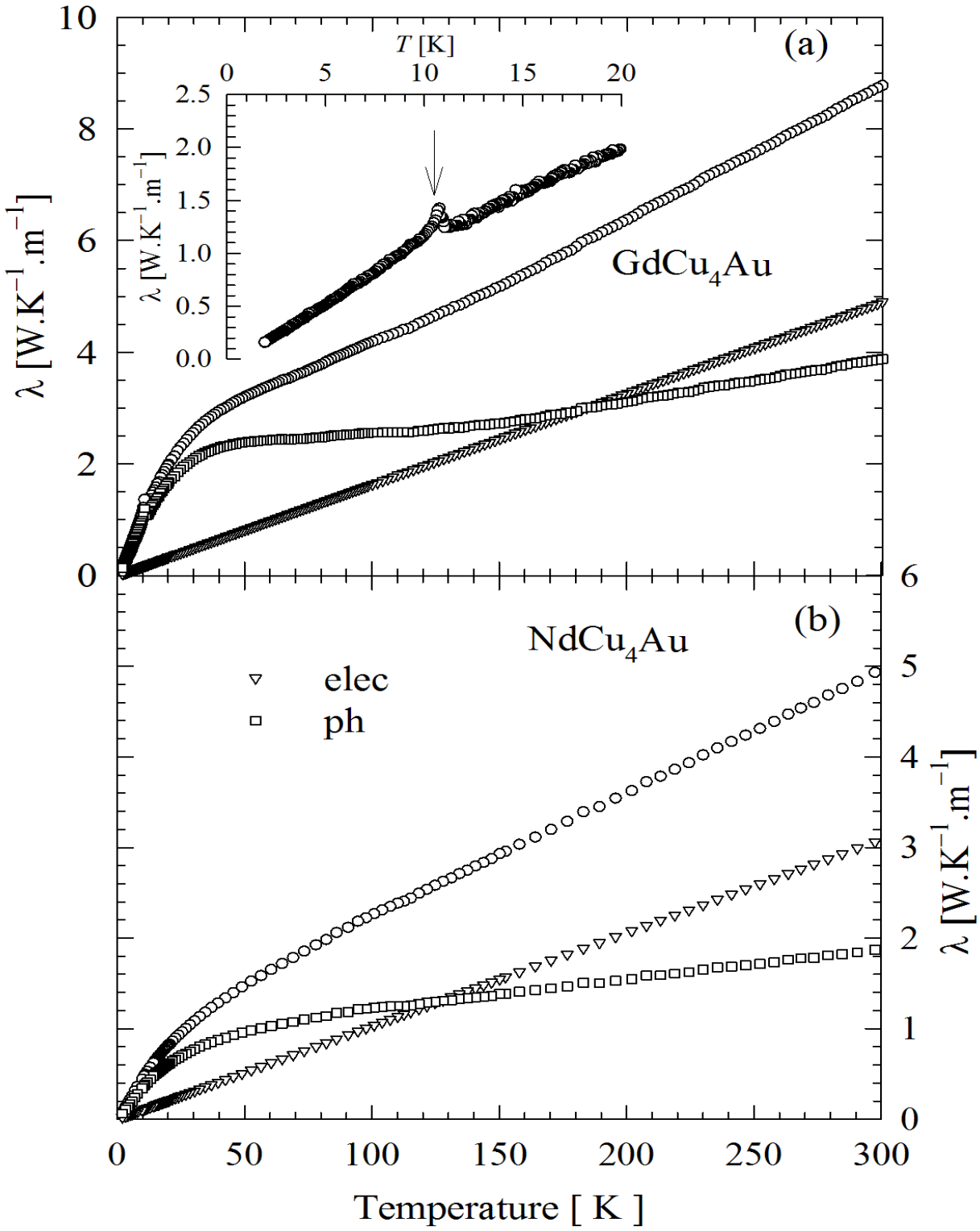

Figure 4.17: Temperature dependence of the thermal conductivity, $\lambda(T)$ in (a) $NdCu_4Au$ and (b) $GdCu_4Au$ together with the electronic λ_{elec} and phonon λ_{ph} components of $\lambda(T)$. The inset of (a) shows the low temperature $\lambda(T)$ of $GdCu_4Au$, with the arrow indicating the position of the peak at a temperature associated to T_N.

Furthermore, it appears that the phonon contribution dominates marginally that of the electronic contribution below 110 K and 160 K for the Nd and Gd compounds, respectively. This behaviour corroborates with the results of the Lorentz number shown in Fig 4.18, which shows a growth of L/L_0 with the decrease in temperature. Above 110 K and 160 K, the electronic contributions for the compounds predominate, but significantly for the Nd compound compared to the Gd compound. Similar behaviour has been observed in many other compounds [88, 135–137]. It was reported that the type and concentration of defects in a crystal play a significant role in the phonon contribution to the thermal conductivity of metals [135]. This results in the temperature dependence of dominant phonon wavelength which increases from the value comparable to the lattice parameter at high temperature to a value of the order of 100 Å at liquid helium temperature [138]. As a result, this leads to the dependence of the phonon thermal conductivity with the size and geometrical shapes of the lattice defects [135]. It should be noted that, the slope of $\lambda(T)$ above and below 50 K increases as one moves from light to heavy RE compounds (Nd to Gd). This observation may originate from the difference of the Debye temperature of Nd and Gd. Below 20 K (see the inset Fig 4.17), $\lambda(T)$ curve of the $GdCu_4Au$ shows a small peak at a temperature of 10.6 K which is close to T_N value observed in $\rho(T)$ and $S(T)$ results. This anomaly of the thermal conductivity at the transition point is interpreted as a critical scattering of phonons due to the critical fluctuation of the spin energy density which appears through the specific heat [139].

Fig 4.18(a) displays the temperature dependence of the Lorentz number $L(T) = \lambda(T)\rho(T)/T$, normalized to L_0. It is observed that, for both compounds L/L_0 are nearly temperature independent on cooling from room temperature down to 100 K. This is followed by a strong increase with further cooling, reaches a maximum at 10 K and a sharp decrease below 10 K for both compounds. Fig 4.18(b) displays the normalized Lorentz number scaled so that L/L_0=1, in order to illustrate the Wiedemann-Franz law. According to the Wiedemann-Franz law, this ratio should be aimed at one in the whole temperature range if the lattice vibrations can be neglected. Consequently, the observed strong increase in L/L_0 indicate a deviation from the Wiedemann-Franz law with an appreciable lattice vibration in both compounds. Similar behaviour was observed in many other compounds [88, 134–136]. For Ce compounds such as $CeNiAl_4$ [135] and $CeCuAl_4$ [134], it has been reported that the increase in L/L_0 may be attributed to an additional lattice thermal conductivity (phonon) or the energy dependent Kondo scattering process and the spin scattering of charge carriers does not play a significant role. It is most likely that, the increase in L/L_0 for our compounds which does not show evidence of Kondo effect, may only be attributed to the dominant lattice thermal conductivity also observed in $LaNiAl_4$ [134]. It should be noted that the observed maximum in L/L_0 curves increase in magnitude similar to the slope of $\lambda(T)$ curves as one moves from light to heavy RE

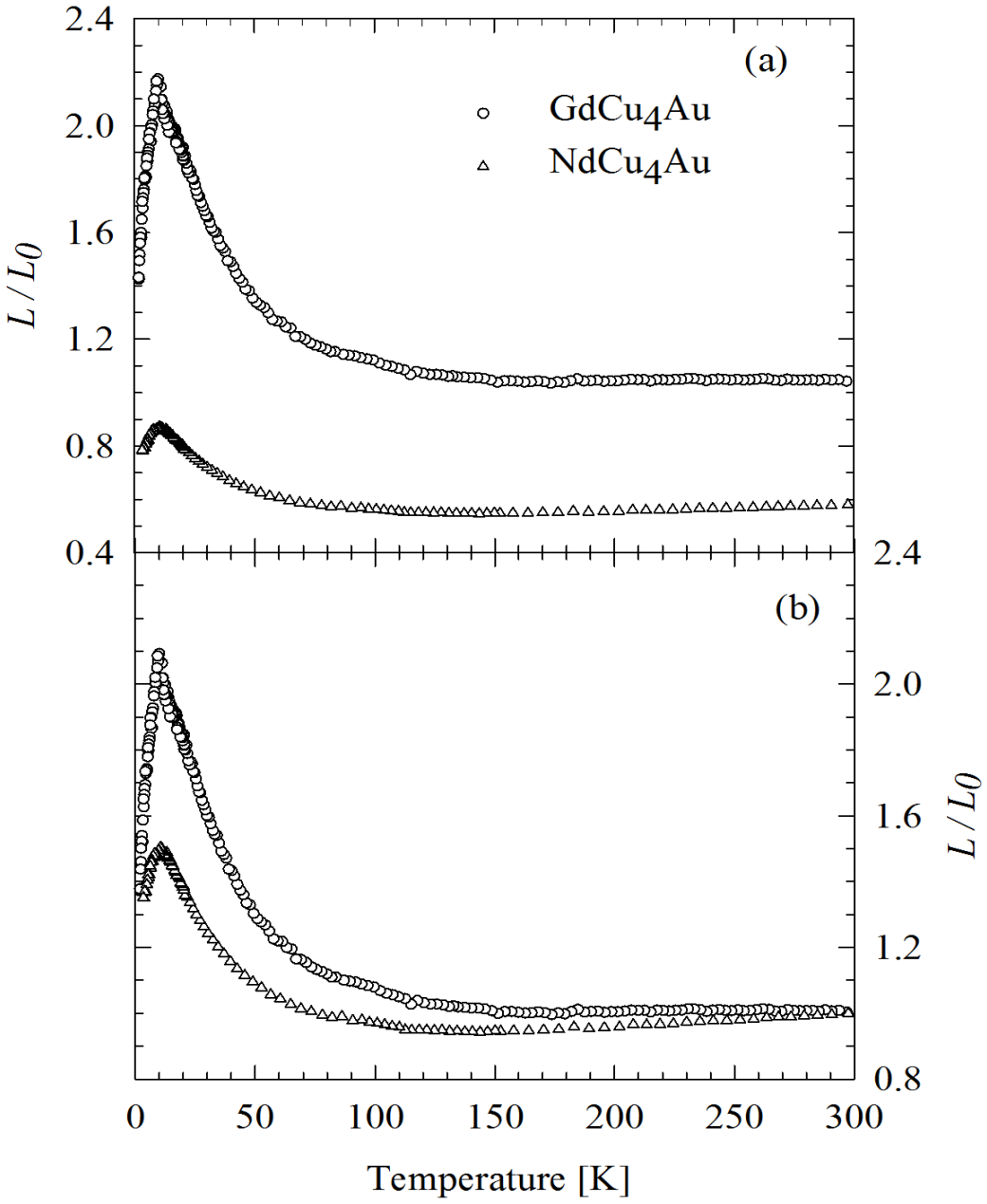

Figure 4.18: Temperature dependence of the (a) normalized Lorentz number, L/L_0 and (b) L/L_0 scaled to 1 at 300 K for $NdCu_4Au$ and $GdCu_4Au$ compounds.

compounds, which may suggest that the lattice vibrations become more important in $GdCu_4Au$ than $NdCu_4Au$ compounds, as expected from the Debye temperature of Gd which is greater than that of Nd, since the Debye temperature is an indicator of the lattice vibration in the crystal. In Fig 4.19 we present the dimensionless figure of merit, which is a measure of the efficiency of the thermoelectric materials, for comparison with the commercially used composition like Bi_2 Te_3 where $ZT \approx 1$ at room temperature [140]. ZT data of the $NdCu_4Au$ increases upon heating the sample and tends to saturation at room temperature at a value of 3.16×10^{-3}. On the other hand, ZT of $GdCu_4Au$, firstly increase upon heating, reaches a maximum value of at the same temperature of 100 K observed in the $S(T)$ result. With further heating ZT decreases to zero at a temperature of 212 K and increases strongly with further heating up to room temperature.

4.4 Conclusion

In this chapter an investigation of the novel AFM $NdCu_4Au$ compound as well as an ordinary AFM $GdCu_4Au$ compound have been presented for the first time in the frame work of crystal structure and thermodynamic properties. EDS studies indicate the 1-4-1 composition for all compounds. X-ray diffraction studies indicate the ordered cubic MgCu4Sn-type structure with space group $F\overline{4}3m$ for all compounds in contrast to the hexagonal CaCu5-type structure encountered for most binary $RECu_5$. From the magnetic susceptibility and specific heat results both $NdCu_4Au$ and $GdCu_4Au$ are found to order in an antiferromagnetic type of spin arrangement below $T_N = 3.9$ K and 10.8 K for Nd and Gd compounds, respectively. A possible spin-glass-like behaviour was observed for the Gd compound. No evidence of a matamagnetic transition is observed for Nd compound, but it is observed for the Gd compound above 0.7 T at a temperature below its T_N value. CEF splitting of $J = 9/2$ ground state of Nd^{3+} was observed at low temperature in $C_p(T)$ data, which plays an influential role in the ground state of $NdCu_4Au$ compound. The calculated CEF parameters from $C_{4f}(T)$ shows that the first order and second order excited states are 62(5) K and 109(9) K from the ground state. The $4f$-electron derived magnetic entropy for both compounds indicate long-range correlation above T_N and also suggest that the ground state of the CEF of $NdCu_4Au$ might be Γ_6 doublet and the first and second excited one of the two Γ_8 quartets. The electrical resistivity, thermoelectric power and thermal conductivity results indicate an AFM-like transition at T_N also observed in the susceptibility and heat capacity studies. $\rho(T)$ for both compounds are characteristic of electron-phonon scattering in the presence of the $s-d$ interband scattering. $S(T)$ data of $NdCu_4Au$ is positive over the whole temperature, while $S(T)$ data of $GdCu_4Au$ takes positive and negative values and is dominated by a broad maximum at 100 K. For both

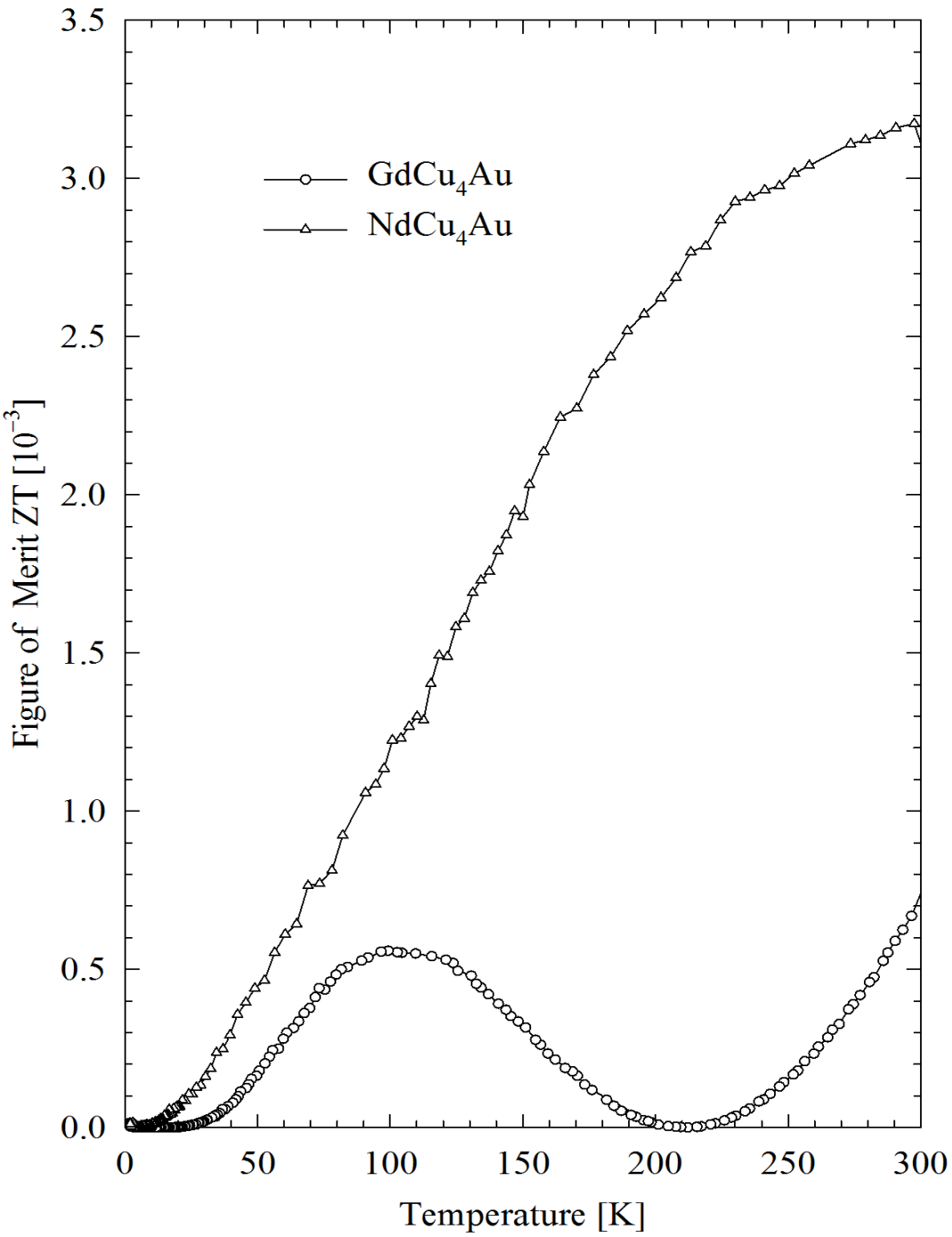

Figure 4.19: Temperature dependence of the thermoelectric figure of merit (ZT) for $NdCu_4Au$ and $GdCu_4Au$ compounds.

compounds, $S(T)$ data has been successfully interpreted in terms of the phenomenological resonance model taking into account the Mott's diffusion and the phonon drag terms. $\lambda(T)$ of $NdCu_4Au$ is lower than that of $GdCu_4Au$ and both decrease linearly upon cooling. The reduced Lorentz number L/L_0 deviates from the Wiedemann-Franz law, which can be attributed to the dominant lattice thermal conductivity.

Chapter 5

Electrical and thermodynamic properties of the ternary intermetallic compound NdAuX, where X = Ge and Ga

5.1 Introduction

Among the equiatomic ternary compounds of rare earths, a number of recent surveys have highlighted their crystallographic and magnetic properties. RETX (RE = rare earths, T =transition metals and X = p-block elements) series, in particular, is a large group of intermetallic compounds. The interesting feature of this group is that it shows a variety of physical properties such as Kondo effect, heavy fermion behaviour, spin glass state, intermediate valence, superconductivity, multiple magnetic transitions and metamagnetism. On the other hand, these compounds show interesting pressure effects on their structural and magnetic properties. Modification using hydrogen and nitrogen is also observed to alter their crystal structure and magnetic properties considerably. In general, these compounds show a variety of physical properties over a wide range of temperatures.

The compounds of RETX series show a variety of crystal structures depending on the constituents. The compounds with different RE, T, and X elements crystallize in different crystal structures. While, in most of the cases, the compound with same T and X atoms, but with different RE ions show the same crystal structure. Most of the RETX compounds are found to form in the different types of the hexagonal structure. In particular, the group of RETX with (T = Au, Cu) and (X= Ge, Si) are found to adopt different types of the hexagonal structure depending on the heat treatment [141, 142]. It has been observed that the RECuSi compounds crystallize in two different types of crystal

structures. The high temperature phase forms in the AlB_2-type structure ($P6/mmm$), while the low temperature phase adopts the Ni_2In-type structure ($P63/mmc$) [143–145]. Similar to RECuSi compounds, the type of hexagonal structure of RECuGe compounds was found to vary with annealing temperature [141, 146]. In addition to the hexagonal structure, RETX can also be formed in the other types of crystal structures. For instance, REMnAl (RE= Ce, Nd, Gd) and REPdSb (RE=Dy-Yb) series were found to exhibit the cubic structure [147–150]. Some other compounds were found to form in the tetragonal type structure such as REPtSi (RE=La-Nd, Sm, Gd) [151]. The compounds in RERhX (X = Ga, Si, Ge, and Sb), RETGa (T = Au, Pd, and Pt) and REAuAl(RE = La, Ce, Nd) series were found to crystallize in the different type orthorhombic structure, except LaRhSi which is found to form in cubic structure[152–158].

Aside from crystallographic structure, RETX compounds show remarkable magnetic and transport properties. The magnetic properties are mainly derived from bulk magnetization measurements and neutron diffraction data. It has been observed that some of these compounds are paramagnetic down to 2 K such as RENiSb (RE = Y, La, Pr) [159] and RENiAl (RE = Yb, Lu) [160]. Furthermore, some of these compounds were found to order ferromagnetically such as RECuAl (RE = Gd, Tb, Dy, Ho, Er and Tm) [161], while some others order antiferromagnetically such as RENiSn (RE = Nd-Tm)[162–165]. On the other hand, RETX compounds exhibit very interesting magneto-transport properties. Many of them show large magnetoresistance, positive or negative, in the magnetically ordered regime. For instance, all compounds in RERhGe (RE = Tb-Er) show a positive magnetoresistivity which changes its sign above the critical field [166]. The negative MR at temperature down to 10 K observed in NdAuAl confirms the FM ordering in this compound [167]. The electrical resistivity of RETX also shows interesting different behaviours. For example, the metallic behaviour was observed for REPtSb (RE = La-Sm) and RERhAl (RE = Y, Ce, Pr, Nd, Gd) [168, 169]. Compounds such as CeRhGe and CeRhBi show a double peak in resistivity data which correspond to Kondo and CEF effect [170, 171].

The magnetic and magneto-transport properties of RECuX with (X = Si , Ge) and REAuGe, in particular, display interesting features. The study of magnetic properties of CeCuSi and CeAuGe revealed that they order ferromagnetically at 15.5 K and 10 K, respectively [172–174]. Many workers have investigated the magnetization and magnetic structure of RECuSi compounds. The compounds with RE = Pr, Gd and Tb with AlB_2 type crystal structure show FM behaviour below their Curie temperatures of 14 K for PrCuSi, 49 K for GdCuSi and 47 K for TbCuSi [175]. Later, it was reported that PrCuSi and GdCuSi order antiferromagnetically at T_N= 5.1 K and 14 K, respectively [176, 177]. Neutron diffraction studies showed that TbCuSi has cosinusoidally modulated magnetic structure at 4.2 K, while RE = Dy and Ho compound do not show any magnetic ordering

down to 4.2 K [178]. DyCuSi and HoCuSi are AFM with T_N= 11 K for DyCuSi and 9 K for HoCuSi and show sine modulated structure with magnetic order in the temperature range of 1.4 K to T_N [145]. On the other side, Neutron diffraction and magnetization measurements show that the compounds of RECuGe series with RE = Pr, Nd, Gd, Tb, Dy and Er are AFM at low temperatures. The transition temperatures are 1.8 K for PrCuGe, 3.5 K for NdCuGe, 17 K for GdCuGe, 11.6 K for TbCuGe, 6 K for DyCuGe, 6.1 K for HoCuGe and 4.3 K for ErCuGe [141]. All compounds except NdCuGe show sine modulated magnetic structures. It has been observed that the direction of moments in compounds with RE = Tb and Dy is perpendicular to the c-axis while for RE = Ho and Er is parallel to c-axis [141]. In the case of ErCuGe, an additional magnetic transition was observed at 3.7 K [179]. The compounds are found to change their magnetic state from AFM to FM on the application of an external field [179].

On the other hand, among all the compounds of REAuGe, only CeAuGe shows FM ordering below a Curie temperature T_C, which is confirmed by neutron diffraction study [172, 180]. The ternary compounds REAuGe with (RE = Sc, Y and Lu) show a weak diamagnetic behaviour [181], whereas REAuGe (RE = Nd, Gd-Er) compounds show AFM ordering[172, 182]. The neutron diffraction measurements in REAuGe (RE = Pr, Nd, Tb, Dy, Ho, Er) compounds reveal that PrAuGe does not show any additional magnetic reflections at 1.6 K, while magnetic structure of NdAuGe and ErAuGe show the magnetic structure, which can be described by two propagation vectors [183]. HoAuGe show incommensurate magnetic structure below T_N, while the magnetic structure in TbAuGe was reported to be complex. The ordering temperatures obtained from neutron diffraction data are 8.8 K for NdAuGe, 7.6 K for TbCuGe, 6.1 K for DyCuGe, 7.6 K for HoCuGe and 5.7 K for ErCuGe. Later, Baran *et al.* [184] reported the neutron diffraction results in HoCuGe and ErCuGe. At low temperatures, both HoCuGe and ErCuGe show a collinear magnetic structure described by a propagation vector $K = (1/2, 0, 0)$, which transforms into transverse sine wave incommensurate magnetic structure close to their ordering temperatures [184]. However, in ErCuGe some magnetic reflections show significant broadening attributed to magnetic domain size effect [184]. Recently, Sondozi *et al.*[185] reported on the effect of La dilution on CeAuGe. Their study shows that the dilution of Ce magnetic species with La resulted in the suppression of T_C = 10 K in CeAuGe down to about 0.87 K obtained in $Ce_{0.3}La_{0.7}AuGe$. The extreme two Ce-dilute compounds, $Ce_{0.2}La_{0.8}AuGe$ and $Ce_{0.1}La_{0.9}AuGe$ appear to remain paramagnetic down to $T \rightarrow 0$.

Based on these rich properties of the RETX compounds, we undertake to investigate the electrical and thermodynamic properties of the ternary compounds NdAuGe and NdAuGa. In the first part of this chapter, the compound NdAuGe is investigated by means of XRD, electrical resistivity, $\rho(T)$, magnetic susceptibility, $\chi(T)$, magnetization

$M(\mu_0 H)$ and specific heat, $C_P(T)$. The measurements on the non-magnetic part LaCuAu is also performed in order to help in extracting the magnetic heat capacity for NdAuGe. In the second part of this chapter, NdAuGa is investigated by structural, magnetic, magnetocaloric and heat capacity measurements.

5.2 Sample preparation and characterization

Polycrystalline samples of NdAuGe, NdAuGa and LaAuGe were prepared by arc-melting procedure as explained in section 3.1. Metals of the following purity in Wt% were used Nd and La: 99.99; Au: 99.95 and Ge and Ga: 99.9999. The resulting weight loss after final melting was less than 1%. Subsequently the sample ingot of NdAuGa was wrapped with tantalum foil, encapsulated in an evacuated quartz tube, and heat treated at 850^0C for two weeks. All the prepared samples were checked by XRD at room temperature using a Bruker D8 Advance diffractometer described in section 3.2.1. The diffraction patterns were analyzed using the full profile Rietveld refinement method.

5.3 Results and discussion

5.3.1 X-ray diffraction and crystal structure

The obtained XRD patterns for NdAuGe and NdAuGa are shown in Figs 5.1 and 5.2, together with the full profile Rietveld LSQ refinement. XRD studies reveals that all the samples were single phase materials and crystallized in the hexagonal LiGaGe-type crystal structure for the NdAuGe and LaAuGe, while NdAuGa adopted the orthorhombic CeCu2-type crystal structure. The resulting room temperature lattice parameters and unit cell volumes are listed in Table 5.1. For the NdAuGe, the space group setting used in the refinement was the hexagonal $P6_3mc$ (No. 186). In this space group, the Nd / La occupy the crystallographic $2a$ site with atomic coordinate (0, 0, z), while Au and Ge occupy the crystallographic site $2b$ with atomic coordinate (1/3, 2/3, z_1) and (1/3, 1/3, z_2). In this refinement the z coordinate of the Nd / La atom was kept fixed z = 0.5042 and the site occupancy factor of all the atoms was set fixed to 100%. The resulting atomic coordinates are gathered in Table 5.1 and the final discrepancy factors of the Rietveld refinement (R_p, R_{wp}, R_{exp}, χ^2, DW, R_B and phase density) are gathered in Table 5.2. The resulting hexagonal crystal structure of the LiGaGe-type is depicted in Fig 5.3. In case of NdAuGa, the input space group setting was orthorhombic $Imma$ (No. 74) structure established before for EuAgGe . The assumed crystal structure of the CeCu2-type is depicted in Fig 5.4. In this unit cell, Nd atoms occupy the $4e$ sites with atomic coordinate (0, 1/4, z_1), while Au and Ga atoms share the $8h$ sites with

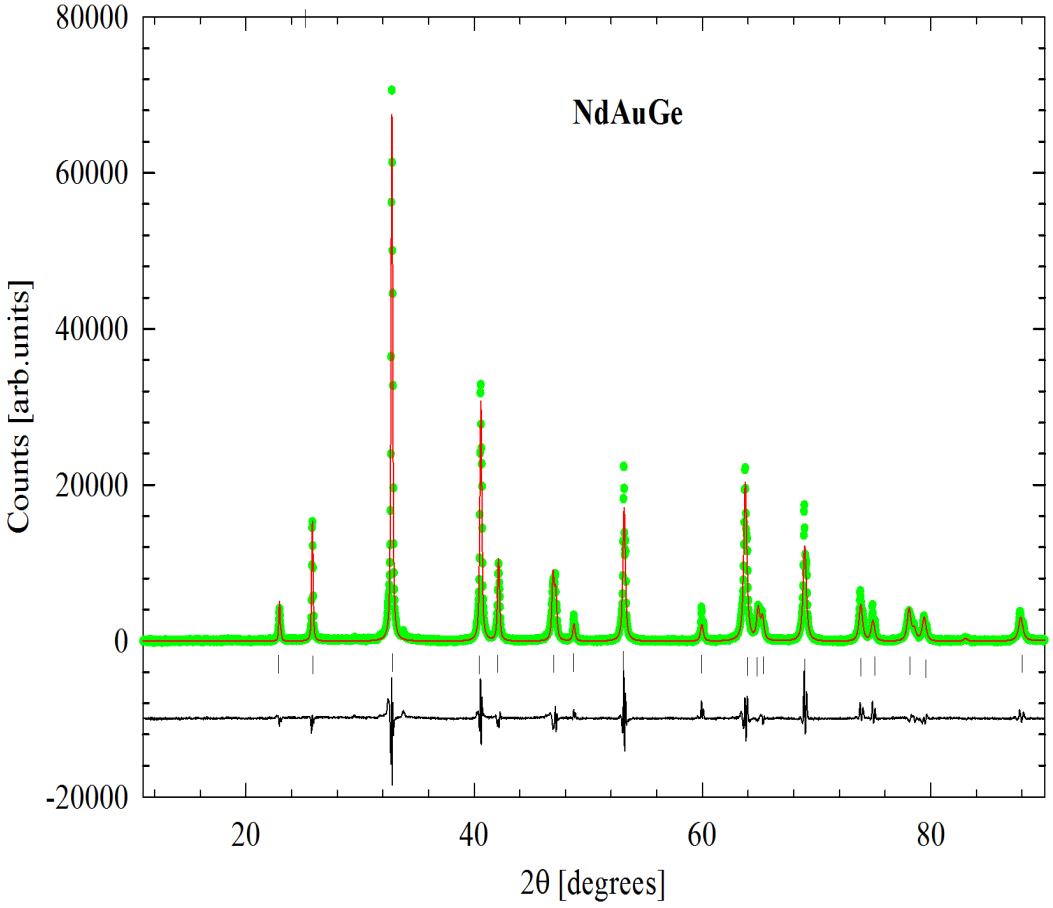

Figure 5.1: XRD diffraction patterns for NdAuGe. The observed data are represented by green symbols and the solid red line through the data represents the result of the full profile Rietveld refinement. The lower red curve is the difference curve between the experimental data and the calculated curve. The vertical lines represent the Bragg's reflection.

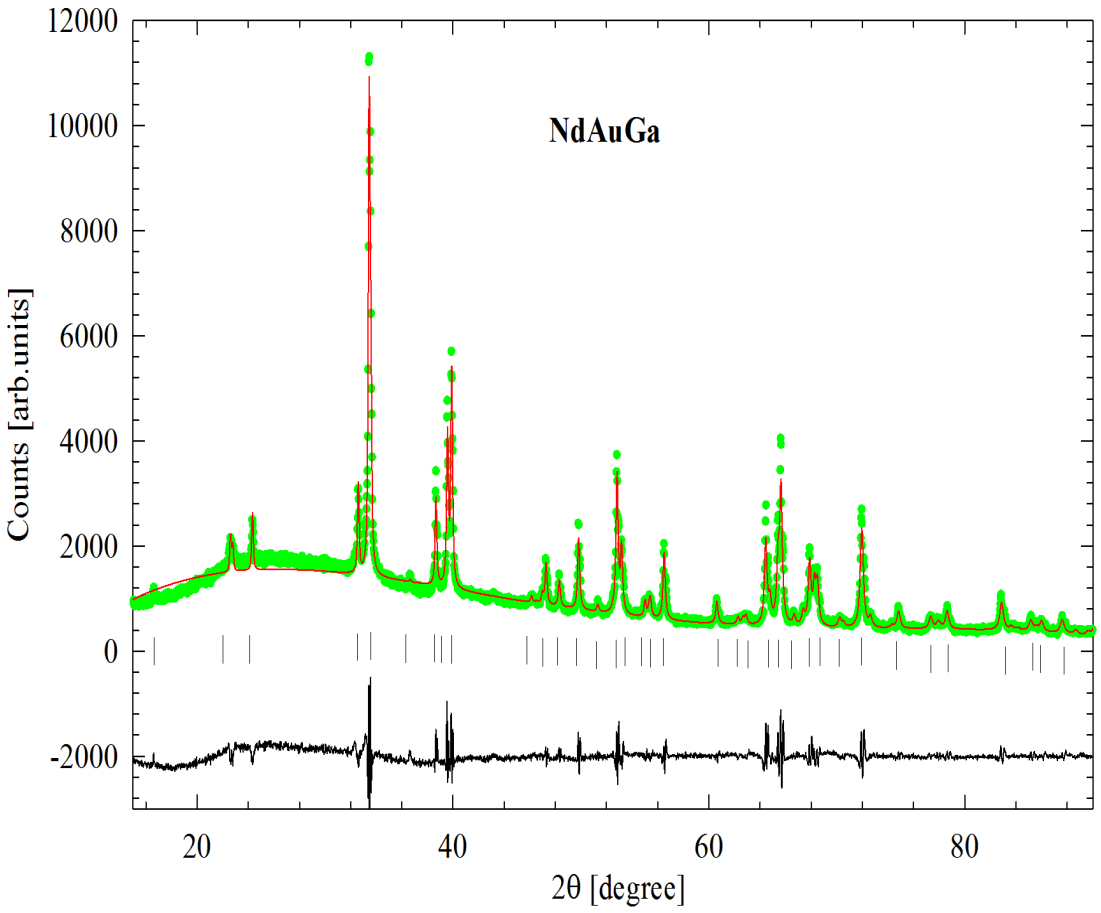

Figure 5.2: XRD pattern of NdAuGa (green symbols) and its Rietveld analysis (solid black line). The curve in the bottom is the difference curve between the experimental and calculated data. The vertical lines represent the Bragg's reflection.

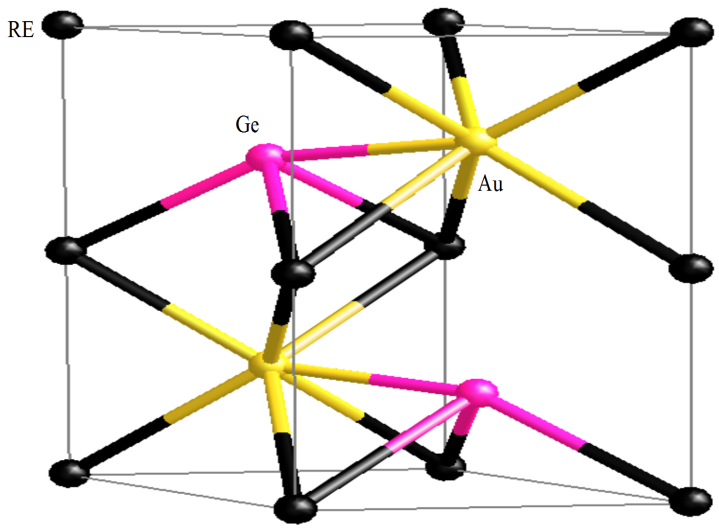

Figure 5.3: Hexagonal crystal structure of NdAuGe obtained by Rietveld refinement method. Black circles represent the RE atoms (RE= La, Nd), yellow circles represent Au atoms and pink circles represent Ge atoms.

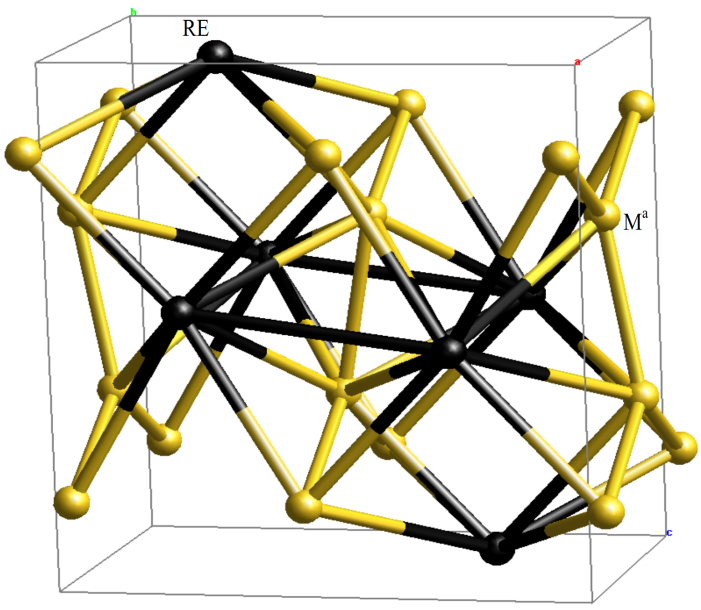

Figure 5.4: Orthorthombic crystal structure of NdAuGa obtained from Rietveld refinement method. Black circles represent the RE atoms (RE= Nd), yellow circles represent M = 4Au + 4Ga

Table 5.1: Atomic coordinates, lattice parameters and unit-cell volume V of REAuX (RE= La, Nd) and (X= Ge, Ga). M is denoted to (4Au+4Ga).

	Atoms	Wyckoff site	x	y	z	a [Å]	b [Å]	c [Å]	V [Å^3]
NdAuGe	Nd	2a	0	0	0.5042	4.4328(4)		7.724(1)	131.44(3)
	Au	2b	1/3	2/3	0.7676(5)				
	Ge	2b	1/3	2/3	0.2120(6)				
LaAuGe	La	2a	0	0	0.5042	4.4650(3)		8.142(7)	140.58(1)
	Au	2b	1/3	2/3	0.7405(6)				
	Ge	2b	1/3	2/3	0.2521(2)				
NdAuGa	Nd	4e	0	1/4	0.5352(7)	4.5541(5)	7.3167(9)	7.8051(9)	260.07(4)
	M	8h	0	0.0326(6)	0.1687(8)				

Table 5.2: The refined agreement indices and phase densities obtained from the full-structure Rietveld refinement method.

Compounds	NdAuGe	LaAuGe	NdAuGa
Parameters			
R_p(%)	7.549	10.355	9.549
R_{wp}(%)	10.271	15.542	12.234
R_{exp}(%)	1.637	1.518	3.083
χ^2	4.981	4.473	3.968
R_B(%)	8.17	10.72	8.47
Phase density [g/cm^3]	10.39	12.89	9.7

atomic coordinate (0, y, z_2). In the refinement process, the full occupancies of both 4e and 8h sites were assumed and the isotropic displacement parameters of all atoms were kept fixed, while the free atomic coordinates, z_1, y and z_2 were varied. The calculations yielded values listed in Table 5.1. The refined lattice parameters and the unit cell volume obtained for NdAuGa are in good agreement with the literature data [158]. The final discrepancy factors of the Rietveld refinement are also listed in Table 5.2. It should be noted that the bigger volume value of the unit cell volume of LaAuGe compared to NdAuGe as well as that of NdAuGa compared to NdAuGe is a consequence of the bigger atomic radius for La than Nd and Ga than Ge.

5.3.2 Scanning Electron Microscope (SEM)

SEM micrograph for NdAuGe is shown in Fig 5.5. It is characterized by a smooth surface which confirms the homogeneity of this compound. Furthermore, no discolouration is observed on the sample surface which indicates the single phase of this compound. EDS

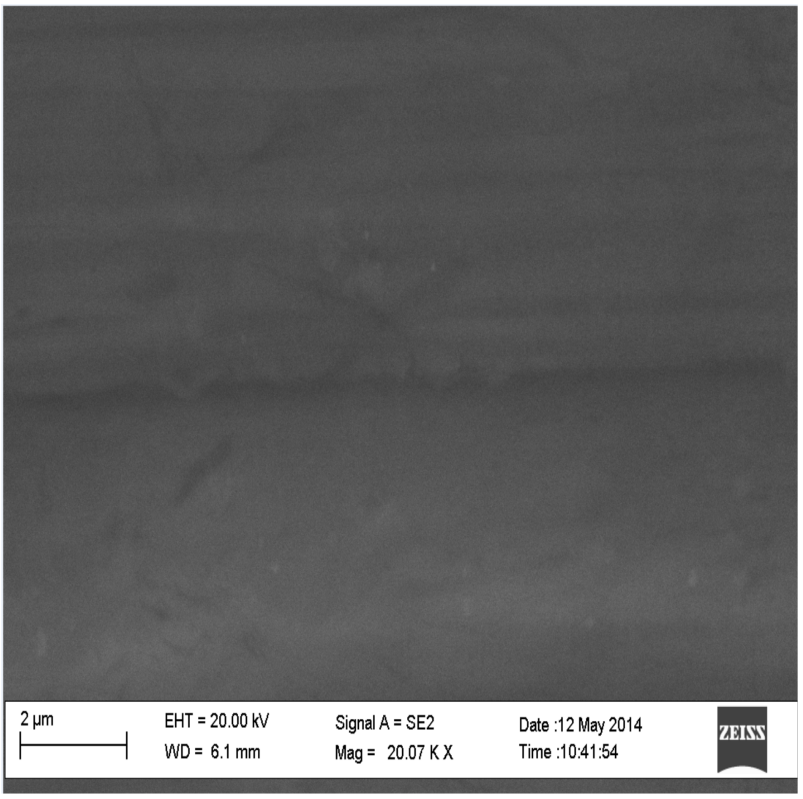

Figure 5.5: SEM micrograph of NdAuGe taken at 20.07 × magnification.

analyses of the two compounds NdAuGe and LaAuGe indicate the sample elemental composition normalized to the Nd and La content to be $NdAu_{1.121}Ge_{0.848}$ and $LaAu_{1.192}Ge_{0.899}$, which are roughly in the 1:1:1 composition.

5.3.3 Electrical and thermodynamic properties of NdAuGe compound

5.3.3.1 Electrical resistivity

The temperature dependence of the electrical resistivity $\rho(T)$ for NdAuGe is depicted in Fig 5.6. The measurement was taken in the temperature range between 1.8 K to 300 K. $\rho(T)$ curve shows a linear behaviour up to 150 K and a tendency toward saturation above room temperature. The linear behaviour below 150 K is characteristic of electron-phonon scattering and the tendency toward saturation is ascribed to the electron-phonon scattering in the presence of CEF effect. The room temperature $\rho(T)$ reaches 242 $\mu\Omega$.cm, which is relatively large but within the limit of a metallic system. This large value may be compared to the values of 260 $\mu\Omega$.cm, obtained for the NdCuGe [186], and was ascribed to a large electron-phonon interaction consistent with large phonon-drag term in the thermoelectric power results for the compound. The bottom inset of Fig 5.6 shows the

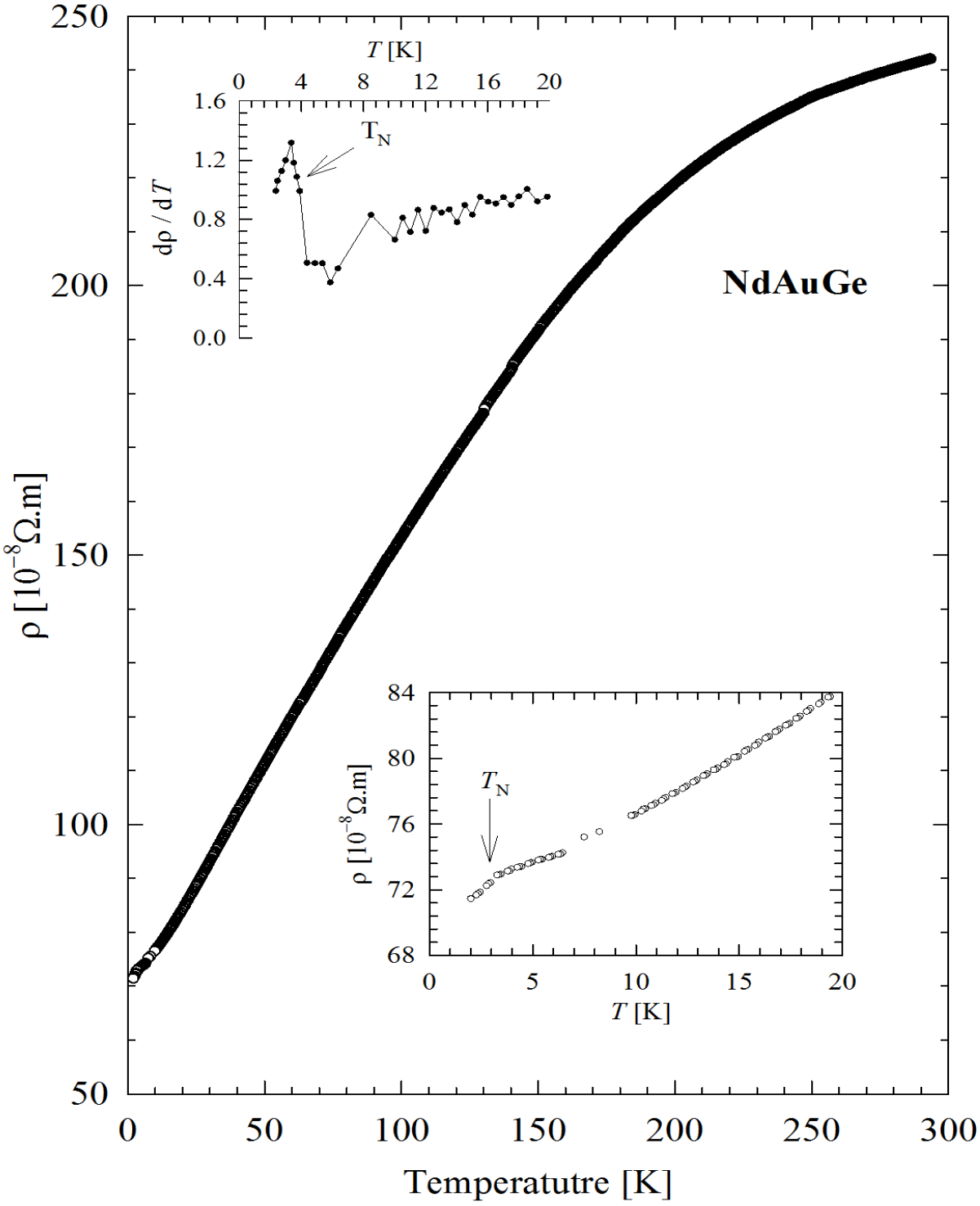

Figure 5.6: Temperature dependence of the electrical resistivity, $\rho(T)$, of NdAuGe. The top inset represents $d\rho/dT$ and the bottom inset show $\rho(T)$ below 20 K. The arrows indicate the phase transition.

low temperature $\rho(T)$ with an arrow indicating the position of the magnetic transition at $T_N = 3.8$ K. The rapid drop of $\rho(T)$ in a linear behaviour below T_N is due to the suppression of the magnetic scattering associated with AFM anomalies. The top inset of Fig 5.6 shows the derivative, $d\rho/dT$, which illustrate a phase transition at 3.8 K as indicated by the arrow. This value has been estimated in accordance with the criterion given by Sato *et al.*[187], which is at the midpoint of the anomaly produced due to a large drop in the $d\rho/dT$ curve (arrow top inset of Fig 5.6). The value of $T_N = 3.8$ K obtained from $\rho(T)$ corroborates with the values obtained from magnetic susceptibility $\chi(T)$ and specific heat $C_p(T)$ as it will be shown in the coming sections.

5.3.3.2 Magnetic susceptibility and magnetization

The temperature dependence of the inverse magnetic susceptibility χ^{-1} for NdAuGe, as measured in a field of 0.5 T is depicted in Fig 5.7. It is observed that $\chi^{-1}(T)$ data confirm a Curie-Weiss (CW) magnetic behaviour above 100 K when fitted to the Curie-Weiss law:

$$\chi^{-1}(T) = 3K_B(T - \theta_p)/N_A\mu_{eff}^2. \tag{5.1}$$

The resulting parameters obtained from the LSQ fits in the temperature range 100-300 K (solid red line in Fig 5.7) are: The effective magnetic moment μ_{eff} =3.546(4) μ_B and the paramagnetic Weiss temperature constant $\theta_p = -6.1(4)$ K. The obtained μ_{eff} is close to the free-ion Nd^{3+} Hund's rule expectation value, $g_J[J(J+1)]^{1/2} = 3.62$ μ_B. The obtained paramagnetic Weiss temperature constant θ_P can be compared to that one obtained for NdCuGe [186]. At low temperature $\chi^{-1}(T)$ curve deviates from the Curie-Weiss behaviour which may be attributed to magnetocrystalline anisotropy. In order to investigate the Crystal Electrical Field (CEF) splitting of Nd levels below 50 K, the low temperature range of χ^{-1} data (6-40 K) is fitted to Curie-Weiss (CW) magnetic behaviour (solid blue line, inset of Fig 5.7). LSQ fit yields μ_{eff}=3.31μ_B with much a reduced negative θ_p value of $-3.4(4)$ K. In the case of a ground state, CEF doublet composed of levels $-\frac{9}{2} \leq m_J \leq +\frac{9}{2}$, CEF splitting of the multiplets, reduces the total angular momentum J. This in turn lowers the μ_{eff} given in the form $\mu_{eff} = 2g_J m_J\sqrt{3/4}$. The observed $\mu_{eff} = 3.31$ μ_B with $g_J = 8/11$ gives $m_J = 2.63$ which is close to 2.5, indicating that the ground state is presumably composed of $\pm 5/2$ levels, similar to NdCuGe [186]. The low temperature zero-field-cooled (ZFC) and field-cooled (FC) magnetic susceptibility $\chi(T)$ data are depicted in Fig 5.8(a). The FC $\chi(T)$ data rises into an anomaly at 3.7 K which is attributed to AFM phase transition also observed in $\rho(T)$ data. It was observed that

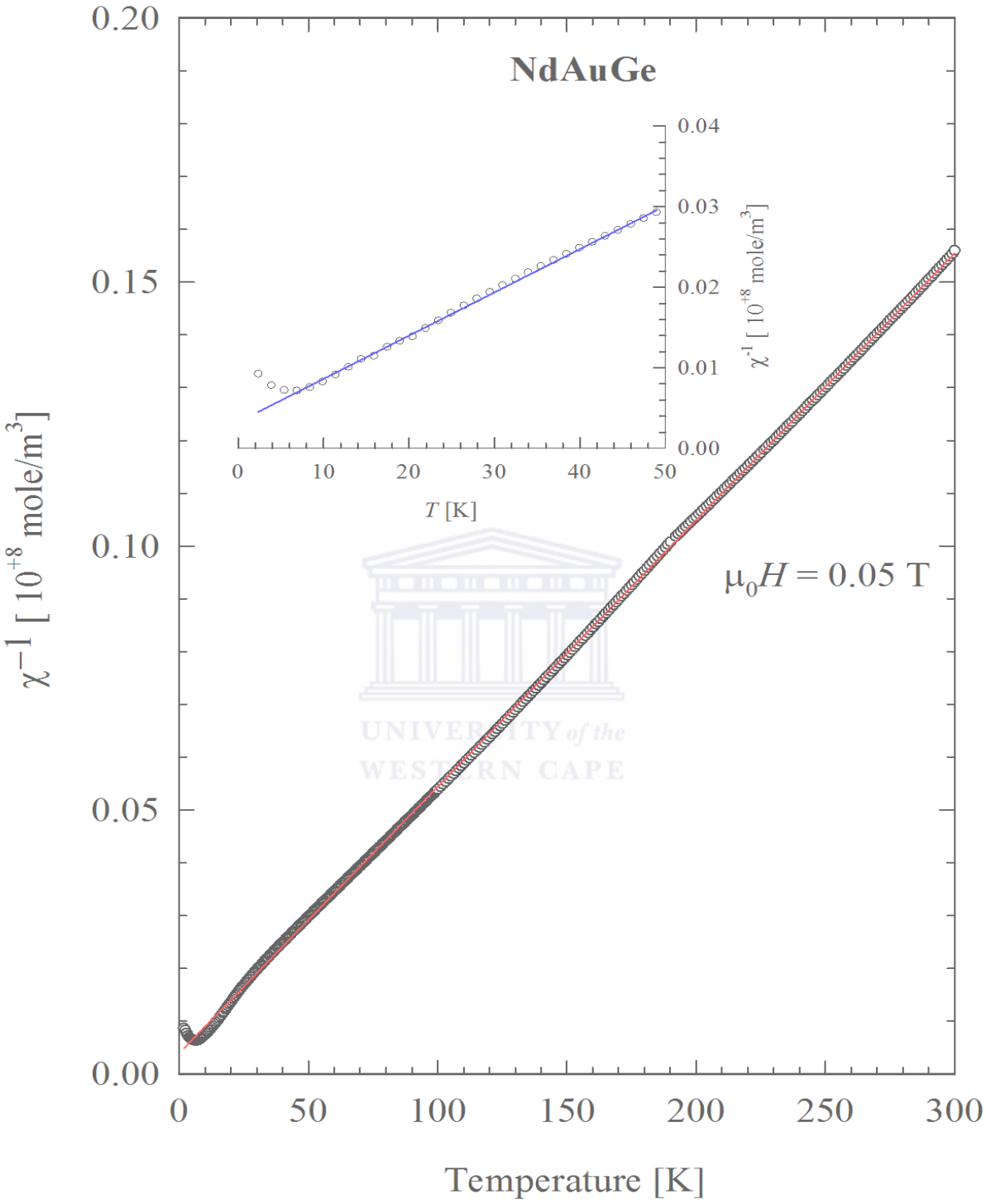

Figure 5.7: $\chi^{-1}(T)$ data with the Curie-Weiss fit (solid red line) according to the experimental data above 100 K. The inset shows the low temperature, $\chi^{-1}(T)$ data with the Curie-Weiss fit (solid blue line) according to the experimental data between 6 and 40 K.

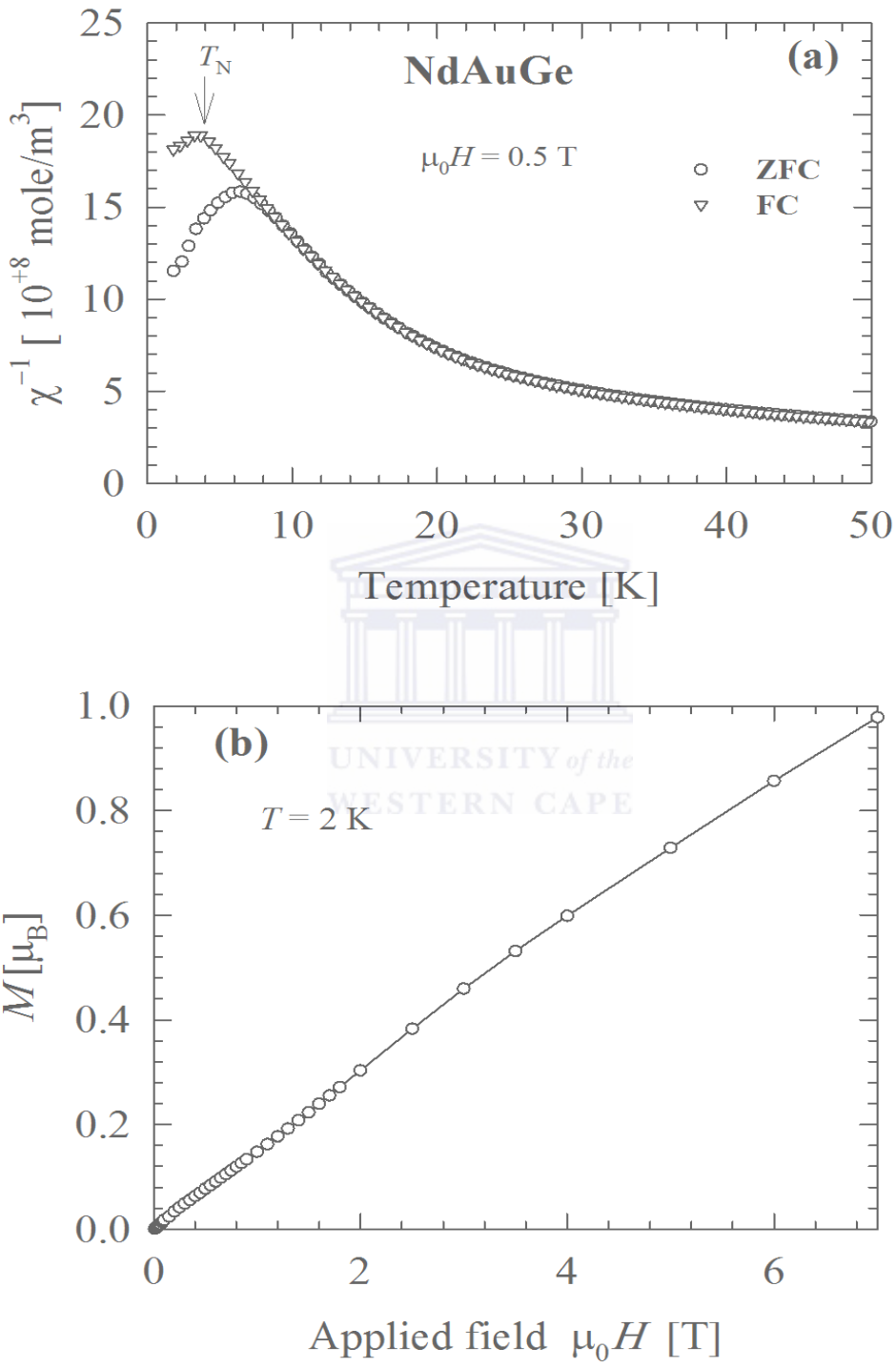

Figure 5.8: (a) Low temperature $\chi(T)$ data measured in ZFC and in FC run. (b) Field dependence of the magnetization measured at 2 K of NdAuGe.

ZFC and FC $\chi(T)$ results taken in a field of 0.5 T split into two branches well above T_N at 7.3 K. Such a bifurcation may originate from an inhomogeneous magnetic ground state in this compound, as a result a spin glass-like state may be the cause of the bifurcation. The field dependent magnetization, $M(\mu_0 H)$, measured at 2 K in field up to 7 K is presented in Fig 5.8(b). It can be seen that the $M(\mu_0 H)$ curve increases linearly with field up to 3 T and exhibits a slight upward curvature above this field. The deviation of linearity at 3 T may be attributed to the metamagnetic behaviour.

5.3.3.3 Heat capacity

Fig 5.9 shows the heat capacity $C_P(T)$ results for NdAuGe together with the non-magnetic LaAuGe. For the isomorphous non-magnetic compound, $C_P(T)$varies monotonically with no anomaly down to 1.9 K. At higher temperatures, both heat capacity curves for the two samples approach the classical value $3NR$ = 74.83 J/mole K of the Dulong-Petit law above 250 K (horizontal line in Fig 5.9) due to the vibrational mode of N=3 atoms per formula unit. The inset of Fig 5.9 shows the low temperatures $C_P(T)$ data for both compounds. For NdAuGe, a sharp anomaly is observed at the magnetic phase transition temperature T_N= 3.4 K, taken at the peak as indicated by an arrow. The difference between the NdAuGe and LaAuGe heat capacity curves at higher temperatures may be attributed to the crystalline electric field (CEF) splitting of the Nd^{3+}-ion. Fig 5.10 displays the $4f$-electron magnetic contribution to the specific heat capacity C_{4f}. C_{4f} was calculated by subtracting an interpolated LaAuGe curve from that of NdAuGe. It is observed that C_{4f} above the magnetic transition region exhibits a broad maximum centred around 16.5 K, characteristic of a Schottky-type anomaly, due to the freezing out of CEF-split magnetic levels. This maximum fits well in absolute magnitude to a three-level CEF Schottky description,

$$C_{4f}(T) = \frac{R}{T^2}\left[\frac{\sum_{i=0}^{n-1}(\frac{g_i}{g_{i+1}})\Delta_i^2 e^{-\Delta_i/T}}{\sum_{i=0}^{n-1} e^{-\Delta_i/T}} - \left(\frac{\sum_{i=0}^{n-1}(\frac{g_i}{g_{i+1}})\Delta_i e^{-\Delta_i/T}}{\sum_{i=0}^{n-1} e^{-\Delta_i/T}}\right)^2\right]. \quad (5.2)$$

The Least-square fitting to Eq 5.2 (solid curve in Fig 5.10), was achieved by using a degeneracy ratio $\frac{g_0}{g_1}$ =1 and $\frac{g_1}{g_2}$ =2 between the ground state and first excited state and between the first excited state and second excited state of Nd^{+3}-ion, respectively. The fitting in Fig 5.10 provides the estimations of the energy splitting taking the ground state Δ_0 =0; Δ_1 =25.8(4) K and Δ_2 =50.7(4) K.

The temperature dependence of magnetic entropy $S_{4f}(T)$ is displayed in Fig 5.11. $S_{4f}(T)$ was calculated from magnetic heat capacity $C_{4f}(T)$ data of NdAuGe using the relation:

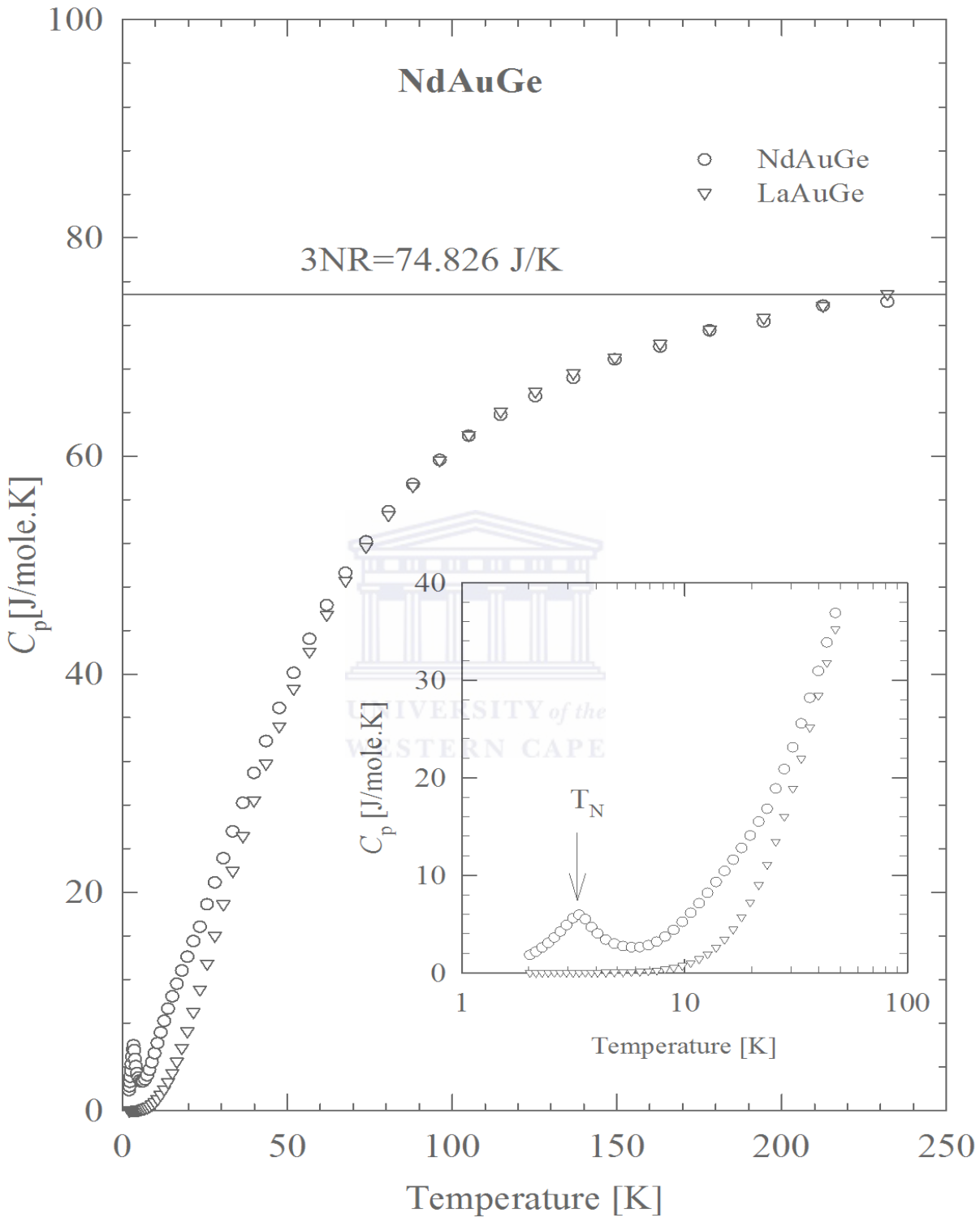

Figure 5.9: Temperature dependence of the heat capacity $C_P(T)$ of NdAuGe together with LaAuGe. The inset shows the low temperature $C_P(T)$ with an arrow at the magnetic phase transition.

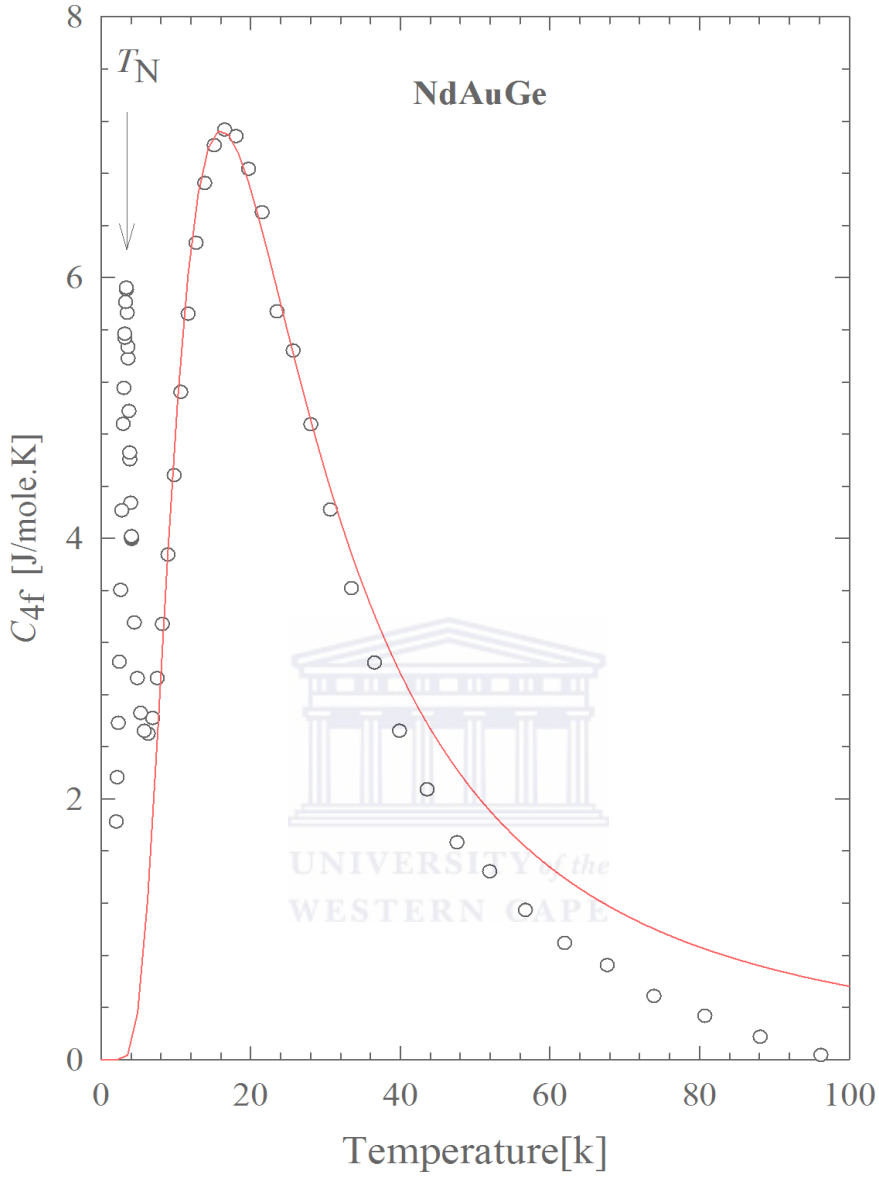

Figure 5.10: The temperature dependence of the $4f$-electron specific heat, $C_{4f}(T)$ with CEF Schottky description fit (Eq.6.4, solid red line) to the experimental data above T_N.

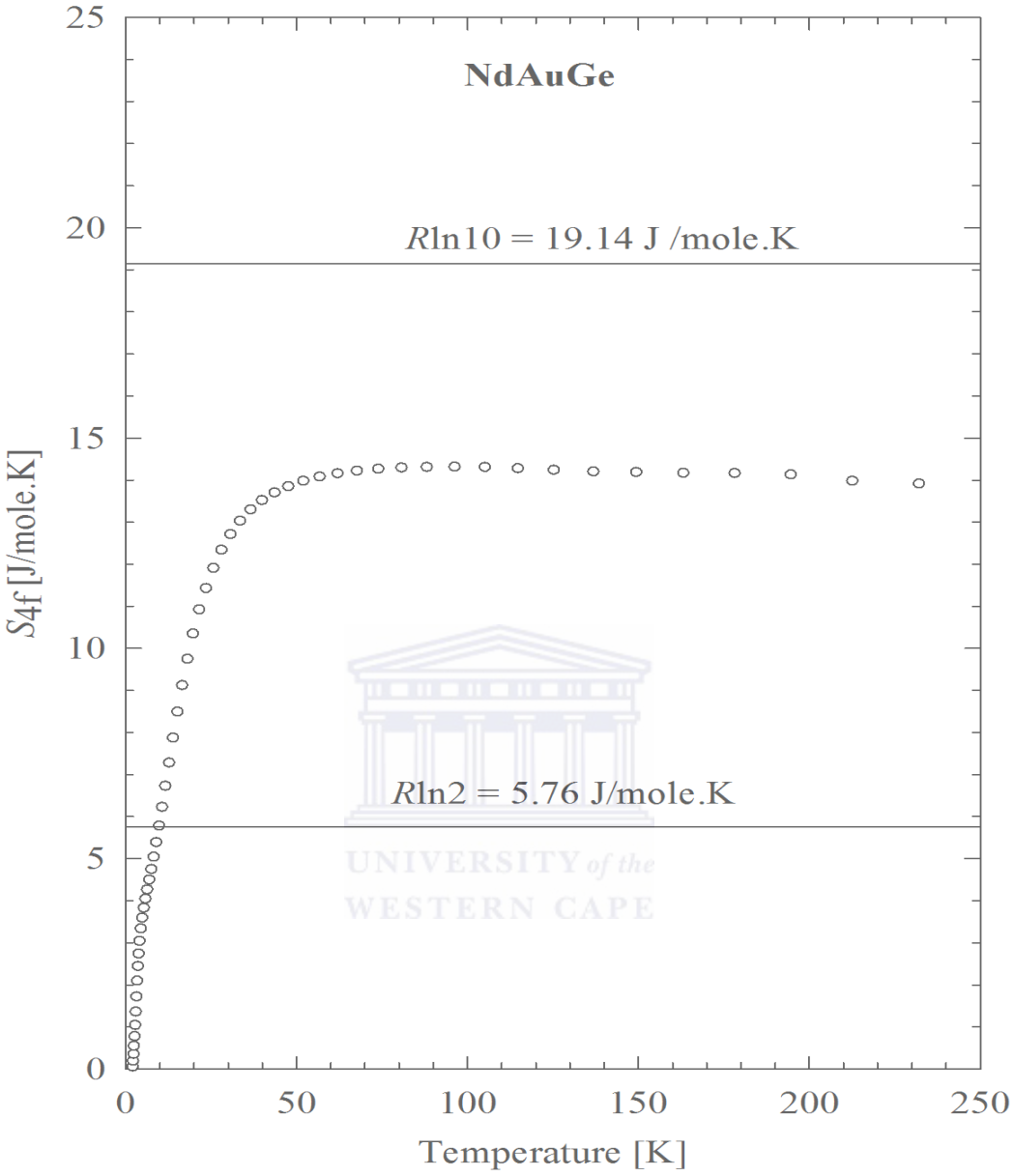

Figure 5.11: Temperature dependence of $4f$-electron entropy, $S_{4f}(T)$, of NdAuGe with two horizontal solid black lines indicating $Rln2$ and $Rln10$ associated with the two-level ground state and the full multiplet, respectively.

$S_{mag} = \int_0^{T'} [C_{4f}(T')/T']dT'$. As can be seen from Fig 5.11, $S_{4f}(T)$ has its largest drop over the temperature range corresponding to the Schottky-like peak in C_{4f} due to CEF splitting, while a further drop is observed near T_N. Also, it is observed at T_N, S_{4f} reaches nearly 36.5% of the $Rln(2)$ value expected for the two-level ground state and 75% of the value of $Rln(2J+1) = Rln(10)$ for $J = 9/2$ at room temperature. The drop in entropy of NdAuGe near T_N is close to a two-level ground state, although the theoretical value of this entropy at T_N is considerably smaller than $Rln(2) = 5.76$ J/mol.K and approaches this value around 9.7 K well above T_N. This is similar to that observed for NdCuGe [186]. Furthermore, the value of $C_{4f}(T)$ at T_N (see Fig 5.10) is roughly two times smaller than $\frac{3}{2}R = 12.47$ J/mol.K expected for the two-level ground state.

5.3.4 Thermodynamic properties of NdAuGa

5.3.4.1 Magnetic susceptibility and Magnetization

The dc magnetic susceptibility, $\chi(T)$ of NdAuGa as it was measured in a field of 0.1 T is shown in Fig 5.12. It is observed that $\chi^{-1}(T)$ data above 50 K follows the Curie Weiss law Eq 5.1, with the Weiss temperature $\theta_p = -7.6(4)$ K and the effective magnetic moment, $\mu_{eff} = 3.635(3)\mu_B$. The experimental value of of μ_{eff} is close to the free Nd^{3+} ion value $g_J[J(J+1)]^{1/2} = 3.62\ \mu_B$. The negative θ_p hints at antiferromagnetic interactions. Below 50 K, the inverse susceptibility deviates from the CW law, likely due to depopulation of CEF levels with decreasing temperature. As can be inferred from the inset to Fig 5.12, $\chi(T)$ exhibits a sharp maximum at $T_N = 8.9$ K, which is a characteristic of long-range antiferromagnetic (AFM) phase transition. Below T_N, the magnetic susceptibility steeply decreases, yet below $T_t = 3.6$ K it slightly increases. The temperature at which this upturn in $\chi(T)$ occurs coincides with the temperature at which $C_P(T)$ forms a maximum (see section.5.3.4.3). Based on both findings, a kind of magnetic order-order transition may be anticipated.

As visualized by the solid line in the inset to Fig 5.12, the $\chi(T)$ data of NdAuGa in the ordered state can be approximated by the formula:

$$\chi(T) = \chi_0' + A_\chi \sqrt{\Delta_\chi T}(\Delta_\chi T) exp(-\frac{\Delta_\chi}{T}) \tag{5.3}$$

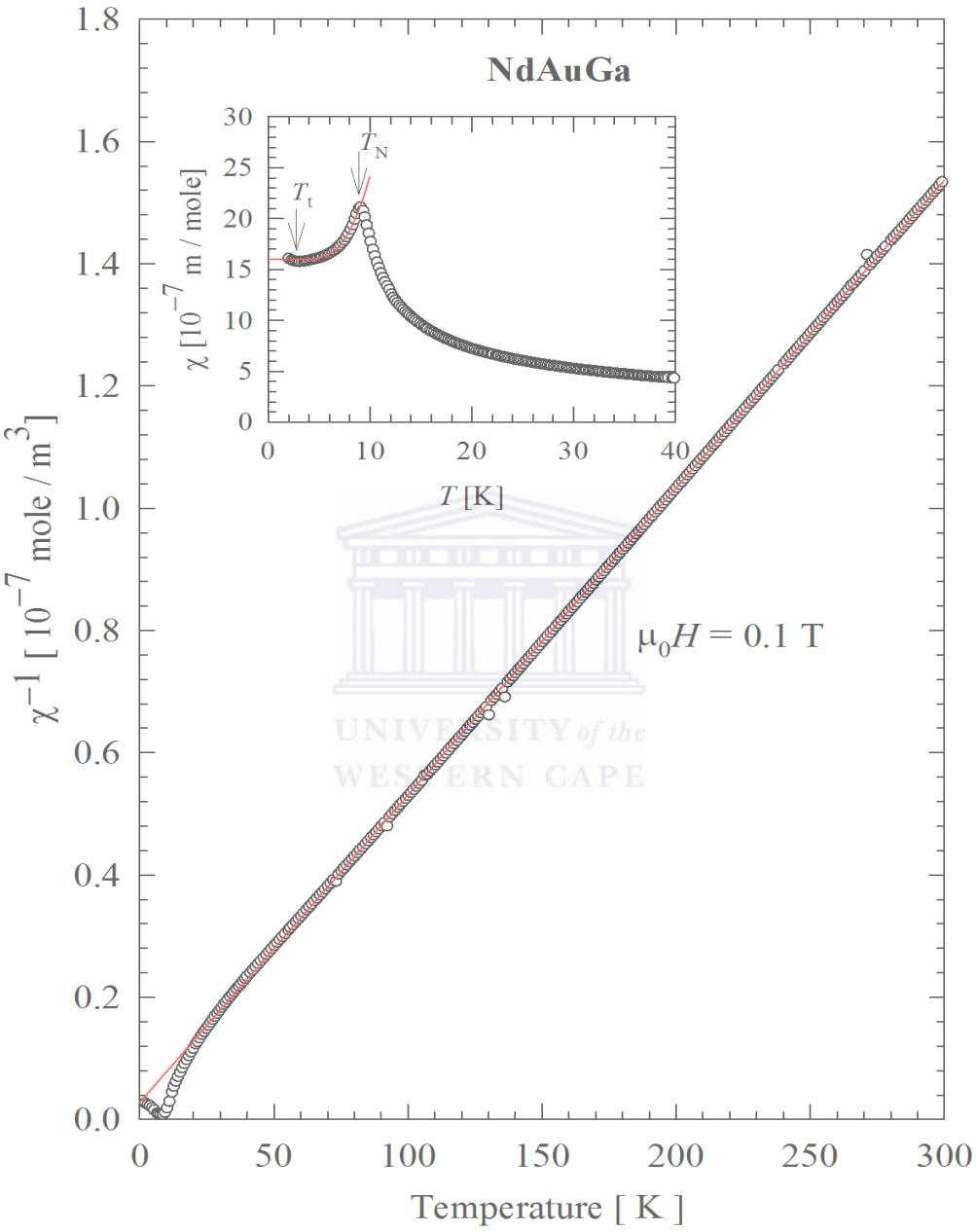

Figure 5.12: $\chi^{-1}(T)$ data of NdAuGa compound with the Curie-Weiss law fit (solid red line) according to the experimental data above 50 K. The inset show the low temperature $\chi(T)$ data with spin-wave fit (Eq 5.3, solid red line) according to the experimental data between 4 and 8 K.

appropriate for an anisotropic antiferromagnet [188]. The LSQ fit of Fig 5.3 to $\chi(T)$ data below T_N yielded the temperature independent term :$\chi_0^{'} = 16.04(2) \times 10^{-7}$ m$^3/mole$ and the prefactor $A_\chi = 18(2) \times 10^{-7}$ m$^3/mole$ and the energy gap in the spin-wave spectrum $\Delta_\chi = 40(1)$ K.

The isothermal magnetization $M(\mu_0 H, T)$ of NdAuGa was measured in magnetic fields up to 5 T at several different temperatures in the range 2 K $\leqslant T \leqslant$20 K is shown in Fig 5.14. In the ordered region, $M(\mu_0 H, T)$ initially increases linearly up to a critical field $(\mu_0 H)_{met} = 0.1$ and 0.05 T for $T = 2$ and 4 K, respectively, that can be associated with a metamagnetic-like singularity (see the inset to Fig 5.14). In high fields, the low-temperature $M(\mu_0 H)$ isotherms show some downward curvature. In the terminal field $(\mu_0 H)_{met} = 5$ T, the magnetization reaches values ranging from 1.35 μ_B to 0.26 μ_B at temperatures from 2 to 20 K. The magnitude of $M(\mu_0 H, T)$ at 2 K is less than half of the theoretical saturation moment of the free Nd^{3+} ion ($g_J J = 2.72\mu_B$). This discrepancy likely results from combined effect of CEF and magnetic anisotropy. To find out the nature of the magnetic phase transition, the Arrott-plots (M^2 versus $\mu_0 H/M$) are shown in Fig 5.15. According to Banerjee criterion [189], the positive slope of all of the Arrott plots of a compound indicates a second order magnetic phase transition, while negative slope of some of these plots indicates the first order nature. In our case, it is observed from Fig 5.15 that, the Arrott plots show positive slopes for all temperatures indicating a second order nature of the transition.

5.3.4.2 Magnetocaloric effect (MCE)

The calculation of MCE has been done from isothermal magnetization M ($\mu_0 H$, T) data. The isothermal magnetic entropy change, ΔS_M has been estimated from the Maxwell's relation:

$$\Delta S_M = \int_0^H \left(\frac{\partial M}{\partial T}\right)_H dH. \tag{5.4}$$

The temperature dependence of $-\Delta S_M$ for various field changes is depicted in Fig 5.13. Clearly, $-\Delta S_M$ rises into a sharp peak at 8.1 K, i.e. close to T_N. The magnitude of this feature increases with increasing field and reaches a maximum $-\Delta S_M = 3.1$ J/kg.K for a field change of 5 T. The latter value is close to the value of 3 J/kg.K obtained for TbCuGe, yet distinctly smaller compared to the values $-\Delta S_M = 15$, 12.3 and 12.7 J/kg.K reported for DyCuGe, H_0CuGe and ErCuGe [190], respectively. Remarkably, no sign change was observed in the temperature variations of MCE, which suggest that

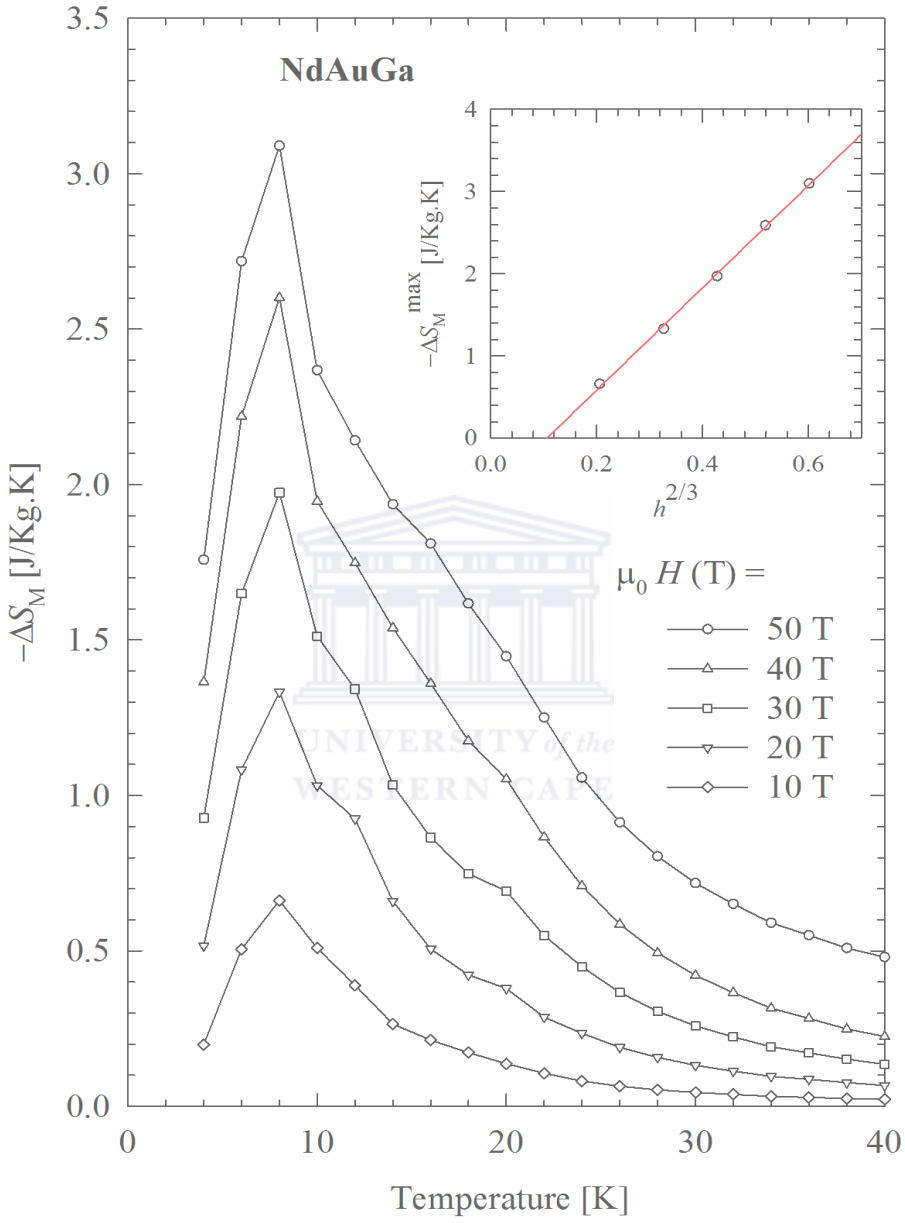

Figure 5.13: The temperature dependence of isothermal magnetic entropy change (-ΔS_M) for NdAuGa compound. The inset shows the field dependence of (-ΔS_M^{max}) with the solid line representing the fit of the data points to Eq.(6.8).

the AFM structure in NdAuGa is collinear, in contrast to the case of other RETX compounds with non-collinear AFM structures, like e.g. GdCuSi [191].

For magnetic materials with second order transition $-\Delta S_M$ follows the relation [192]:

$$-\Delta S_M = h^{2/3} S(0,1) + S(0,0), \tag{5.5}$$

where h is the reduced field ($h = \frac{\mu_0 H \mu_B}{k_B T_N}$), $S(0,1)$ is a parameter connected to the spontaneous magnetization at 0 K ($S(0,1) = kM_s(0)$, k being a constant) and $S(0,0)$ is the reference parameter. The inset of Fig 5.13 shows the plot of $-\Delta S_M^{max}$ versus $h^{2/3}$ and LQS fit of Eq 5.5 to the experimental data (solid red line in the inset of Fig 5.13). The so-obtained parameters are $S(0,0) = -0.62(8)$ and $S(0,1) = 6.2(2)$. It should be noted that the negative value of $S(0,0)$ corroborates the second order magnetic phase transition in NdAuGa, while the linear dependence of $-\Delta S_M^{max}$ versus $h^{2/3}$ indicates the strongly localized character of Nd moment [193].

5.3.4.3 Heat capacity

The specific heat as a function of temperature, $C_P(T)$, measured for NdAuGa in zero magnetic field is depicted in the main panel of Fig 5.16. Over a broad temperature range, $C_P(T)$ can be approximated by the standard Debye law:

$$C_p(T) = \gamma T + 9NR(\frac{T}{\theta_D})^3 \int_0^{x_D} \frac{x^4 e^x}{(e^x - 1)^2}, \tag{5.6}$$

where γ is the Sommerfeld coefficient, N is the number of atoms per formula unit, R is the gas constant, and θ_D stands for the Debye temperature. The LSQ fits of Eq 5.6 to the experimental data above 20 K yielded: $\gamma = 20(1)$ mJ/mole.K^2 and $\theta_D = 170(1)$ K. The obtained value of θ_D is fairly similar to those reported for other members of the RETX series [194, 195].

The inset to Fig 5.16 shows the low-temperature $C_P(T)/(T)$ data. Remarkably, two distinct maxima can be discerned, at the temperatures T_N and T_t determined from the magnetic susceptibility studies. While the former feature clearly manifests the onset of the AFM state, the latter one probably occurs because of a change in the AFM structure of NdAuGe. It is worth recalling that a very similar feature in the ordered state was

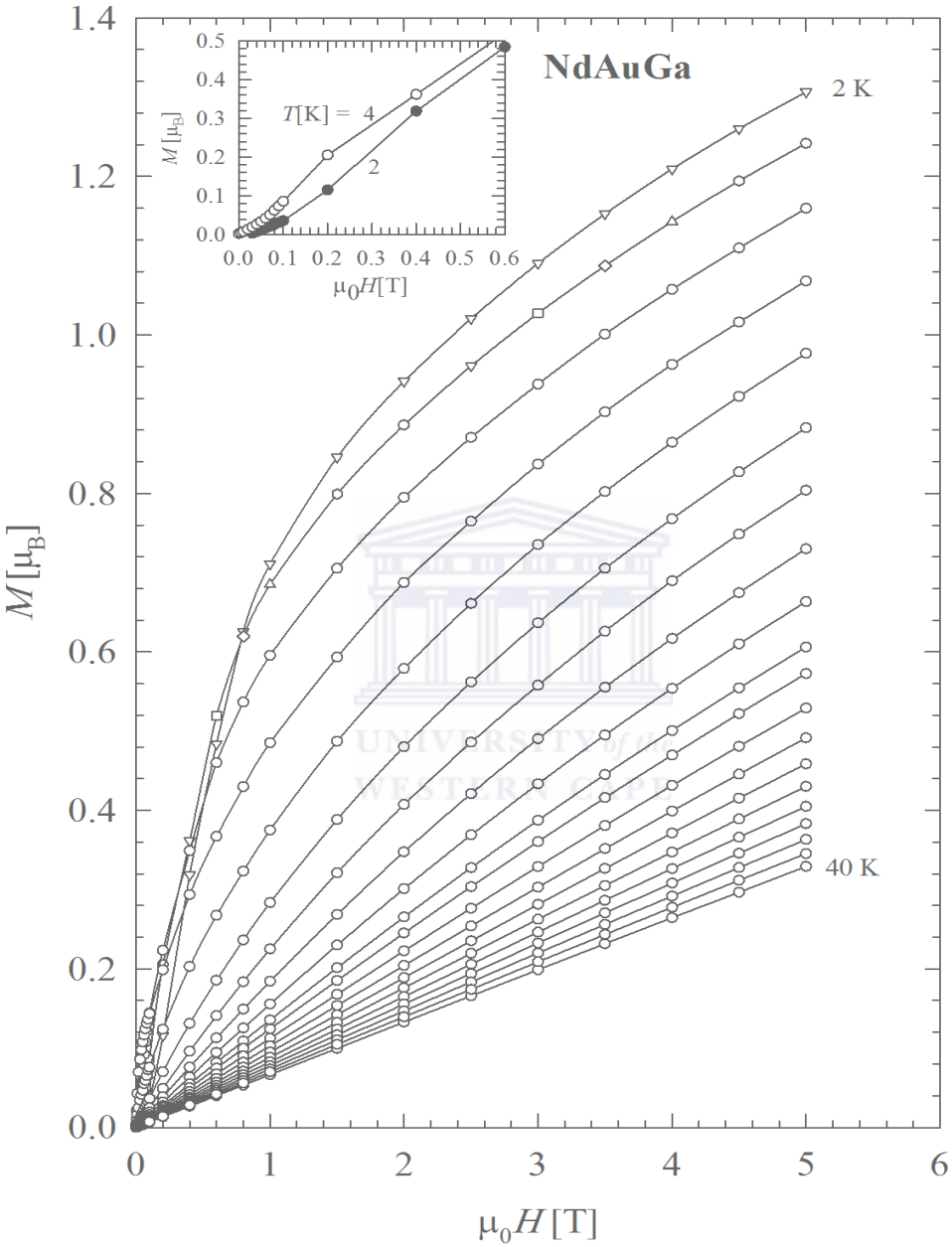

Figure 5.14: Magnetization isotherms at different temperatures between 2 and 40 K, taken in step of 2 K, for NdAuGa compound. The inset shows an expanded plot of magnetization at low field for two isotherms in the ordering region, 2 and 4 K.

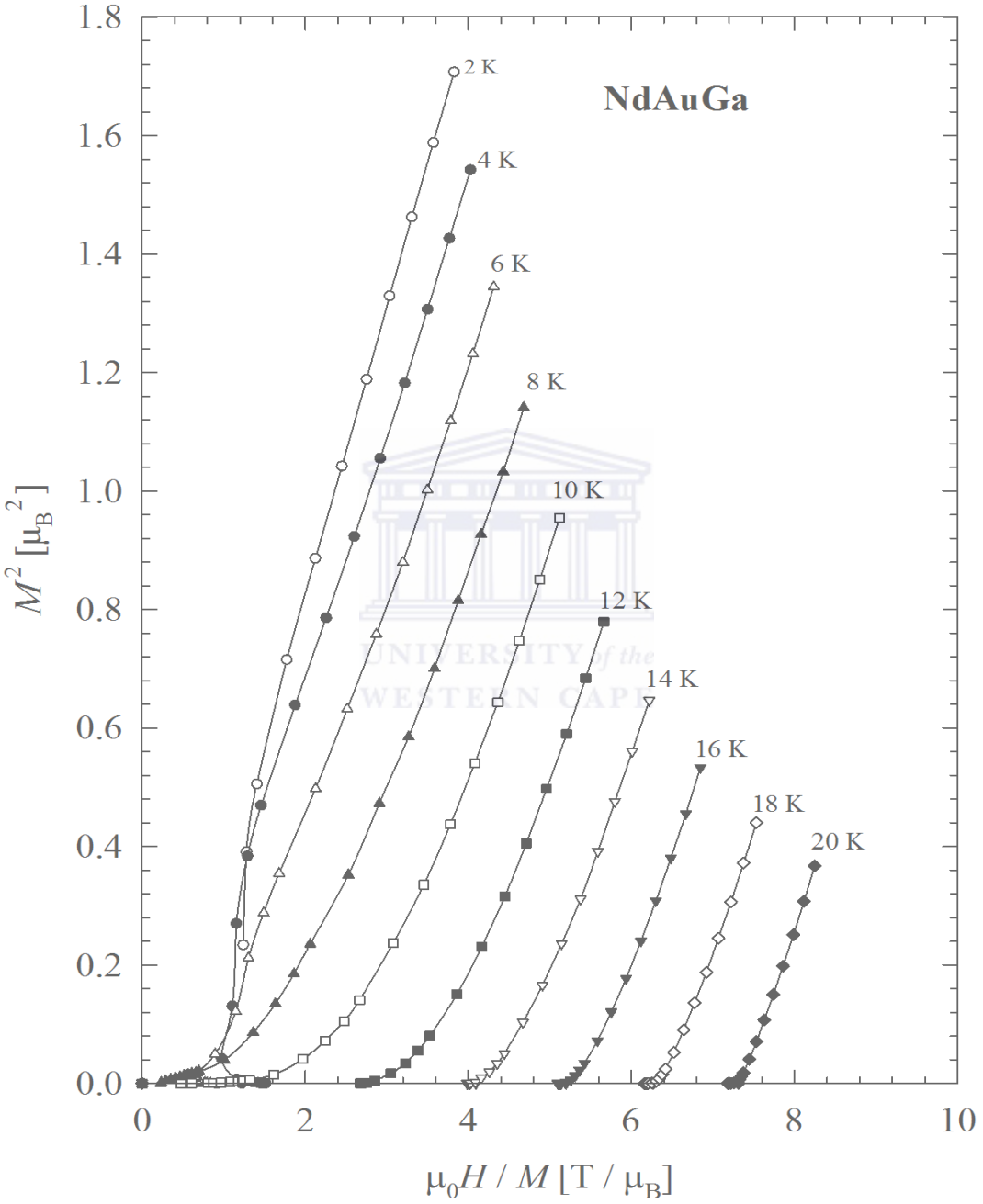

Figure 5.15: The Arrott-plots, M^2 versus $\mu_0 H/M$ in the vicinity of T_N for NdAuGa compound.

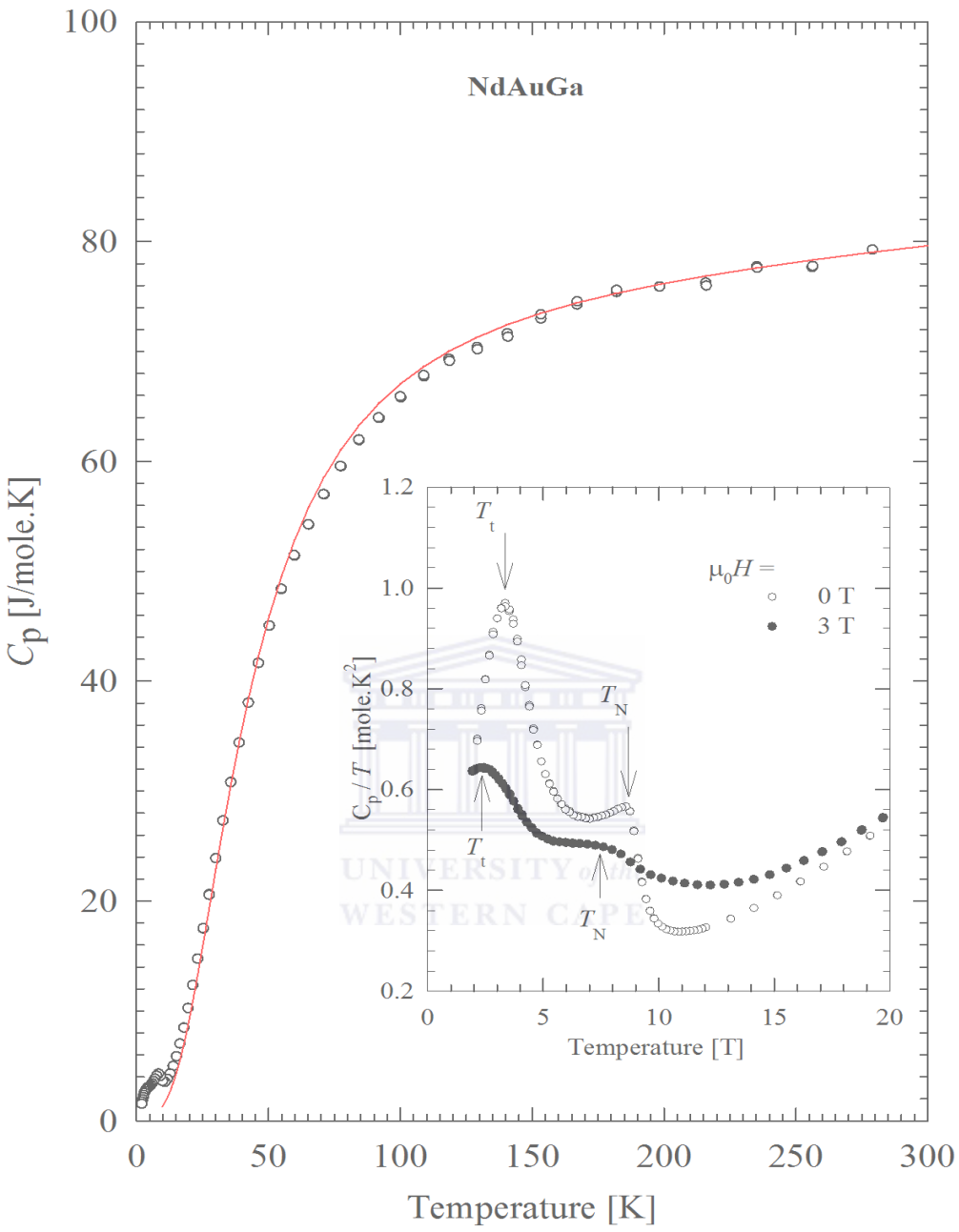

Figure 5.16: The heat capacity data of NdAuGa at 0 T together with Debye fit (Eg 5.6, solid red line through the data points). The inset shows the low temperature $C_P(T)/T$ in 0 and 3 T field. The arrows indicate the magnetic phase transitions temperature.

observed for other equiatomic rare-earth intermetallics, such as GdCuSi [191], TbCuGe [190], and attributed to spin reorientation of the rare-earth magnetic moments. Upon applying magnetic field, the two anomalies in the specific heat broaden and shift to lower temperatures (see the inset to Fig 5.16), thus indicating the AFM character of the magnetic ordering in NdAuGe in both the magnetic phases.

5.4 Conclusion

XRD and SEM studies confirm the single-phase purity of all the investigated compounds. XRD studies in particular indicates the hexagonal LiGaGe-type crystal structure with space group $P6_3mc$ (No. 186) for the NdAuGe and LaAuGe while NdAuGa adopted the orthorhombic CeCu2-type crystal structure with space group $Imma$ (No. 79). At high temperatures, $\chi(T)$ data follows the CW behaviour with an effective magnetic moment $\mu_{eff} = 3.546(4)\ \mu_B$ and $3.635(3)\mu_B$ for NdAuGe and NdAuGa respectively close to the value of $3.62\mu_B$ expected for the Nd^{3+}ion and a CW temperature constant of -6.1 K and -7.6 K respectively. The low temperature $\chi(T)$ data for the NdAuGe, in particular follow the CW behaviour in the temperature range 20 K $\leq T \leq$ 40 K, with a reduced μ_{eff} and θ_p values of 3.31 μ_B and -3.4 K, respectively. The reduced value of μ_{eff} indicates a ground state composed of $\pm 5/2$ levels. ZFC and FC $\chi(T)$ data for the NdAuGe indicate spin-glass behaviour. The low temperatures $\chi(T)$ data indicate AFM-type ordering at $T_N =$ 3.7 K and 8.9 K for NdAuGe and NdAuGa respectively. The Arrott-plot for the NdAuGa compound suggest a second order phase transition. Magnetization data measured at 2 K reveals the occurrence of metamagnetic transition at 3 T for NdAuGe compound and at 0.1 T and 0.05 T for NdAuGa compound, measure in the ordering region at 2 K and 4 K respectively. The magnetocaloric effect in NdAuGa is fairly modest, weaker than in other RETX family. The isothermal magnetic entropy change reach a maximum value of 3.1 J/kg.K for the field change of 5 T at 8.1 K. Heat capacity data for NdAuGe compound confirms the magnetic transition at $T_N = 3.4$ K, while the $4f$-electron specific heat indicates a Schottky-type anomaly around 16.5 K with energy splitting $\Delta_1 = 25.8$ K and $\Delta_1 = 50.7$ K, that are associated with the first and second excited states of the Nd^{3+}-ion respectively. For NdAuGa heat capacity studies in zero and in applied magnetic field shows long-range magnetic ordering with features across several properties that resemble AFM-type ordering at 8.9 K. A second maximum at 3.6 K in the heat capacity data indicates the rearrangement of the AFM structure.

Chapter 6

Effect of La-dilution of the Polycrystalline Kondo Lattice $CeCu_4In$

6.1 Introduction

The binary intermetallic compound $CeCu_5$ is known to be both an antiferromagnet with $T_N = 4$ K and a Kondo lattice with $T_K = 2.2$ K [110, 196]. The latter effect is evident from some facts that have been observed in its electrical transport and thermodynamic properties. For instance, electrical resistivity $\rho(T)$ exhibits negative logarithmic contributions, while a pronounced minimum in the temperature dependent thermoelectric power is observed. Also the Sommerfield coefficient γ deduced from the low temperature heat capacity measurement shows an enhanced value [197] (about 120 mJ.mole^{-1}K^{-2}), which is analogous to some values that were obtained typically for magnetically Kondo-lattice compounds such as $CeAl_2$[7, 198] and $CeCu_2$ [84, 199]. Furthermore, the $4f$-electron entropy has a value of about 2/3 of the expected value $Rln2$ at $T = T_N$. Finally, the ordered magnetic moment obtained from neutron diffraction measurements was 0.36 μ_B instead of the 0.42 μ_B expected for the spin$-1/2$ doublet ground state, and a Kondo interaction strength of $T_K \approx 2.2$ K has been assessed to clarify the variance between the experimental and theoretical values of the moments [200]. These facts indicate that some of the $4f$ moments are involved in the Kondo interaction, and the feature of magnetic ordering in the ground state is not composed by the entire ensemble of the $4f$ moments.

$CeCu_5$ has the hexagonal-$CaCu_5$ structure with space group $P6/mmm$ [110]. Similar to some other binary compounds, $CeCu_5$ is also of interest as an initial material for a group of compounds formed from the substitution of Cu by an atom M, such as (M = Pd, Ag, Al, Ga and In) [133, 201–204]. The resulting compounds with M= Pd, Al and Ga retained the hexagonal structure of $CeCu_5$ [201–203], while the compounds with M =

Ag and In form in different structures [133, 204]. The substitutions of one Cu with elements M mentioned above, increase the average conduction electron density, which screen the localized $4f$ moment states in $CeCu_5$, leading to a nonmagnetic heavy-Fermion (HF) ground state in $CeCu_4M$ [133, 202–204]. An exception has been observed for $CeCu_4Pd$ which exhibits a magnetic phase transition below 1.8 K [201]. The compound $CeCu_4Ag$ [133] was found to adopt the cubic $MgSnCu_4$-type structure with space group $F\overline{4}3m$. Its electrical resistivity exhibits a Kondo-like logarithmic increase up to a maximum at $T = 75$ K, and sharp drop below this maximum. The magnetic measurements show that $CeCu_4Ag$ is a paramagnetic with an effective magnetic moment $\mu_{eff} = 2.54\mu_B$ and a paramagnetic Curie temperature $\theta_P = -33$ K. The thermoelectric power is positive over the whole temperature range and below $T_{max} = 25$ K falls rapidly. The measured thermal conductivity of the $CeCu_4Ag$ compound increases with increasing temperature. The electronic specific heat coefficient γ of this compound was estimated from specific heat data to be 500 J.mole^{-1}.K^{-2}.

Transport, magnetic and thermodynamic properties studies of the $CeCu_4M$ with (M = Al, Ga and In) [202–204] have confirmed the HF state in these compounds. The compounds with Al and Ga retained the hexagonal-Ca_5 structure, while a change to orthorhombic-$CeCu_{4.38}In_{1.62}$ type structure with space group $Pnnm$ was observed for $CeCu_4In$ [204]. The magnetic measurements on $CeCu_4Al$ reveals the paramagnetic state with effective moment $\mu_{eff} = 2.53\ \mu_B/f.u$ and Curie temperature $\theta_P = -10$ K [202]. The temperature-dependence of electrical resistivity $\rho(T)$ of this compound shows a decrease from room temperature down to a minimum at $T = 100$ K and then an increase below this minimum up to 2.5 K. This behaviour of $\rho(T)$ is ascribed to the single-site Kondo scattering caused by the localized $4f$-electrons of the Ce^{3+} ions. The interpretation of the Ce $3d$ and $4d$ XPS spectra result indicates the localized feature of the Ce $4f$ states. The obtained electronic heat capacity $\gamma = 210$ mJ/mole K^{-2} emphasizes the heavy fermion state of the $CeCu_4Al$ compound. The Kondo temperature for $CeCu_4Al$ evaluated from the various experimental measurements is found to be between 2.5 to 5 K [202]. Several studies [205–207] were reported on the effect of La dilution on $CeCu_4Al$ specifically in relation to the electrical transport and thermodynamic properties. Recently, Falkowski *et al.* [134, 208] reported thermoelectric power and thermal conductivity of $Ce_xLa_{1-x}Cu_4Al$ alloys series. Their results show that the thermoelectric power is positive with a peak except for non-cerium $LaCu_4Al$, and the peak shifts slight from 27 K to 25 K upon La concentration. The measured thermal conductivity increases with temperature increase.

$CeCu_4Ga$ compound was found to have a nonmagnetic ground state down to 30 mK [203]. The temperature dependence of electrical resistivity $\rho(T)$ of this compound is a character-

istic of HF system. $CeCu_4Ga$ possess also an extremely enhanced electronic contribution to the specific heat which exceeds 3 J.mole^{-1}.K^{-2}. At a very low temperature (below 2 K), $C_P(T)/T$ showed a strong increase with a value of about 3.15 J.mole^{-1}.K^{-2} at 0.9 K [203]. The Kondo temperature determined from magnetic susceptibility and specific heat data of this compound is of the order of a few Kelvin. A large peak in thermoelectric power was found for $CeCu_4Ga$ at a temperature quite higher than the Kondo temperature.

The studies of magnetic and electronic properties of $CeCu_4In$ compound in particular [88, 204], indicate paramagnetic behaviour down to 2 K. $\chi(T)$ data follows the Curie-Weiss law with effective magnetic moment $2.4\mu_B$ and paramagnetic Weiss temperature $\theta_P = -27$ K. Heat capacity studies confirm the HF character for this compound with the electronic heat capacity coefficient $\gamma = 235$ J/mole.K^2. $\rho(T)$ behaviour is characteristic of a Kondo lattice compound with a well defined resistivity maximum at 25 K.

In this chapter, a study on the effect of La dilution on $CeCu_4In$ will be presented. This study aims to clarify the evolution from a coherent Kondo lattice in $CeCu_4In$ to incoherent single-ion Kondo behaviour with La doping. In this study the results of Lattice parameters, electrical resistivity, magnetoresistivity, magnetic susceptibility, magnetization, thermoelectric power and thermal conductivity measurements on polycrystalline $Ce_{1-x}La_xCu_4In$ are presented. The application of the compressible Kondo model on $Ce_{1-x}La_xCu_4In$ is also presented.

6.2 Sample preparation and Characterization

The polycrystalline samples of the alloy series $Ce_{1-x}La_xCu_4In$ with $0 \leqslant x \leqslant 1$ were prepared with the same arc-melting procedure described in section 3.1. The weight losses of all members in this series are found to be less that 0.1% of the total weight. All the samples thus prepared were characterized by X-ray powder diffraction using a Bruker D8 Advance powder diffractometer with CuK_α radiation described in chapter 3. The diffraction spectra were analysed using the CAILS-Pawley refinement method from TOPAS ACADEMIC programme. All the compositions investigate were single phase with no evidence of parasitic phase or unreacted elements.

6.3 Results and discussions

6.3.1 Lattice parameters and unit-cell volume

All the compositions in the alloy system $Ce_{1-x}La_xCu_4In$ were found to crystallize in the orthorhombic-$CeCu_{4.38}In_{1.62}$ type structure with space group *Pnnm* (No. 58). The lattice parameters and the unit cell volume obtained for the parent compound $CeCu_4In$ is in good agreement with previously reported values [204]. The X-ray pattern of the two parent compounds $CeCu_4In$ and $LaCu_4In$ as representative examples shown are in Fig 6.1. It is observed that the refined room-temperature lattice parameters and the unit cell volume Fig 6.2 increase linearly with increased La content. The observed linear increase confirms the Vegard's rule which suggests no sudden change in the Ce valence across the series.

6.3.2 Electrical resistivity

The temperature dependence of the zero-field total resistivity, $\rho(T)$ for several compositions in the series $Ce_{1-x}La_xCu_4In$ are depicted in Fig 6.3. It is observed that $\rho(T)$ data evolves from coherent Kondo scattering at low temperature for alloys in the range $0 \leqslant x \leqslant 0.3$, with a well defined Kondo peak at T_{max} as indicated in Table 6.1 to incoherent single-ion Kondo scattering for alloys with $x \geqslant 0.4$. It is observed that T_{max} which is a fair indication of the Kondo temperature T_K for dense Kondo alloys systems, shifts to lower temperature with increase La content x. Furthermore the magnitude of $\rho(T)$ decreases with La content which suggest no disorder in Ce-La in the whole concentration range. At higher temperature for all Ce containing alloys in the series, $\rho(T)$ data follows a $-ln(T)$ dependence as is to be expected for incoherent single-ion Kondo scattering (see fits of $\rho(T)$ to Eq 6.1). The observed resistivity maximum ranging from 34 K to 13.4 K reflects a coherence effect that sets in at low temperature. It should be noted that, for dense Kondo alloy, the maximum occurring in $\rho(T)$ at T_{max} is a measure of the Kondo temperature T_K. $\rho(T)$ of the non-magnetic counterpart $LaCu_4In$ depart from linearity at high temperature and is describe by the Bloch-Grüneissen-Mott formula:

$$\rho_{ph}(T) = \rho_0 + \frac{4\kappa}{\theta_R}\left(\frac{T}{\Theta_R}\right)^5 \int_0^{\Theta_R/T} \frac{x^5 dx}{(e^x - 1)(1 - e^x)} - \alpha T^3, \tag{6.1}$$

where all the parameters have their usual meaning with αT^3 being the Mott's term [209]. LSQ fits of $\rho(T)$ data of $LaCu_4In$ compound to the experimental data (solid line Fig. 6.3)

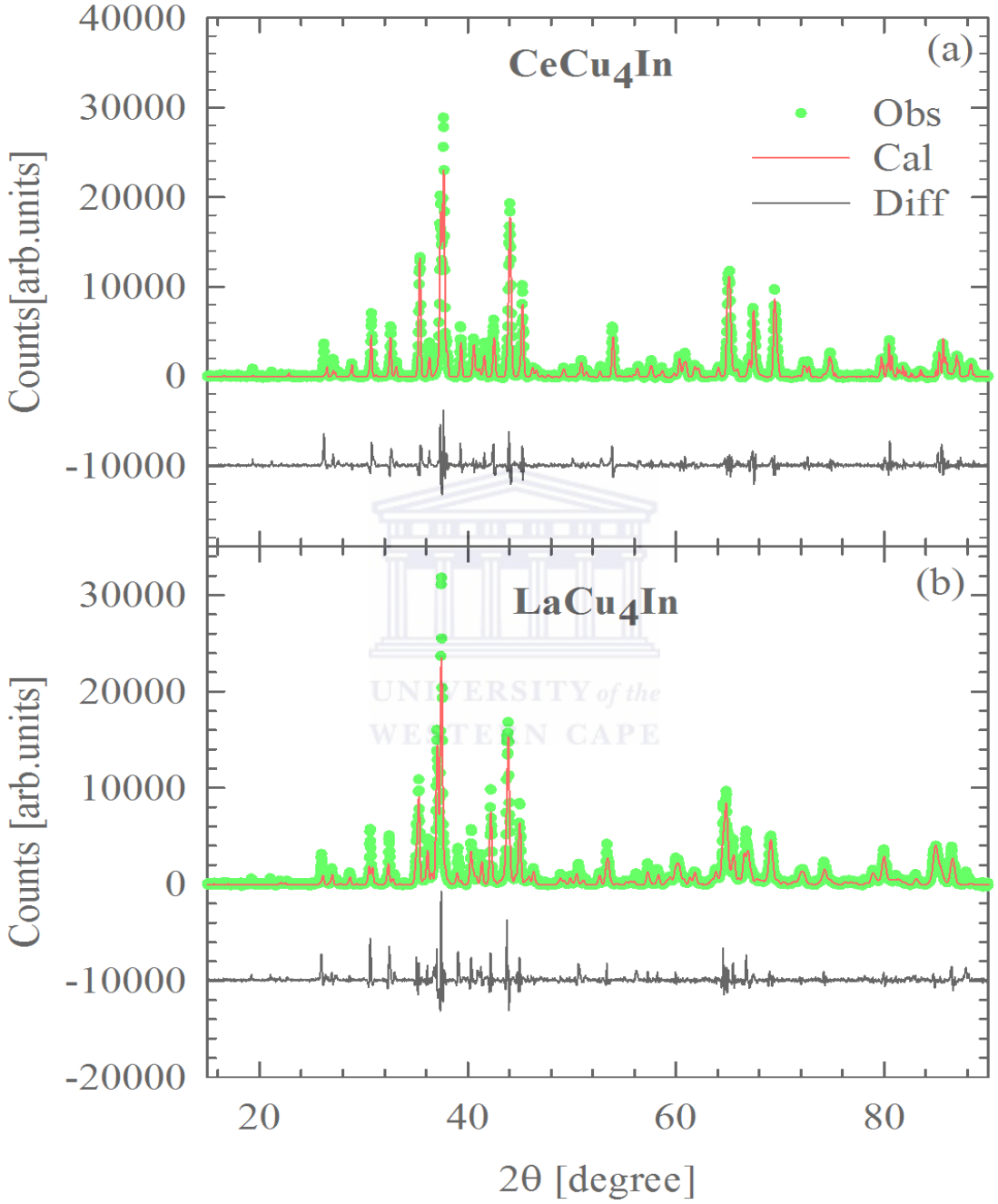

Figure 6.1: X-ray diffraction patterns for $CeCu_4In$ (a) and $LaCu_4In$ (b). The observed data are shown by green symbols and the solid red lines through the data represent the result of the CAILS Pawely refinement. The lower black curves are the difference between experimental and the calculated curves.

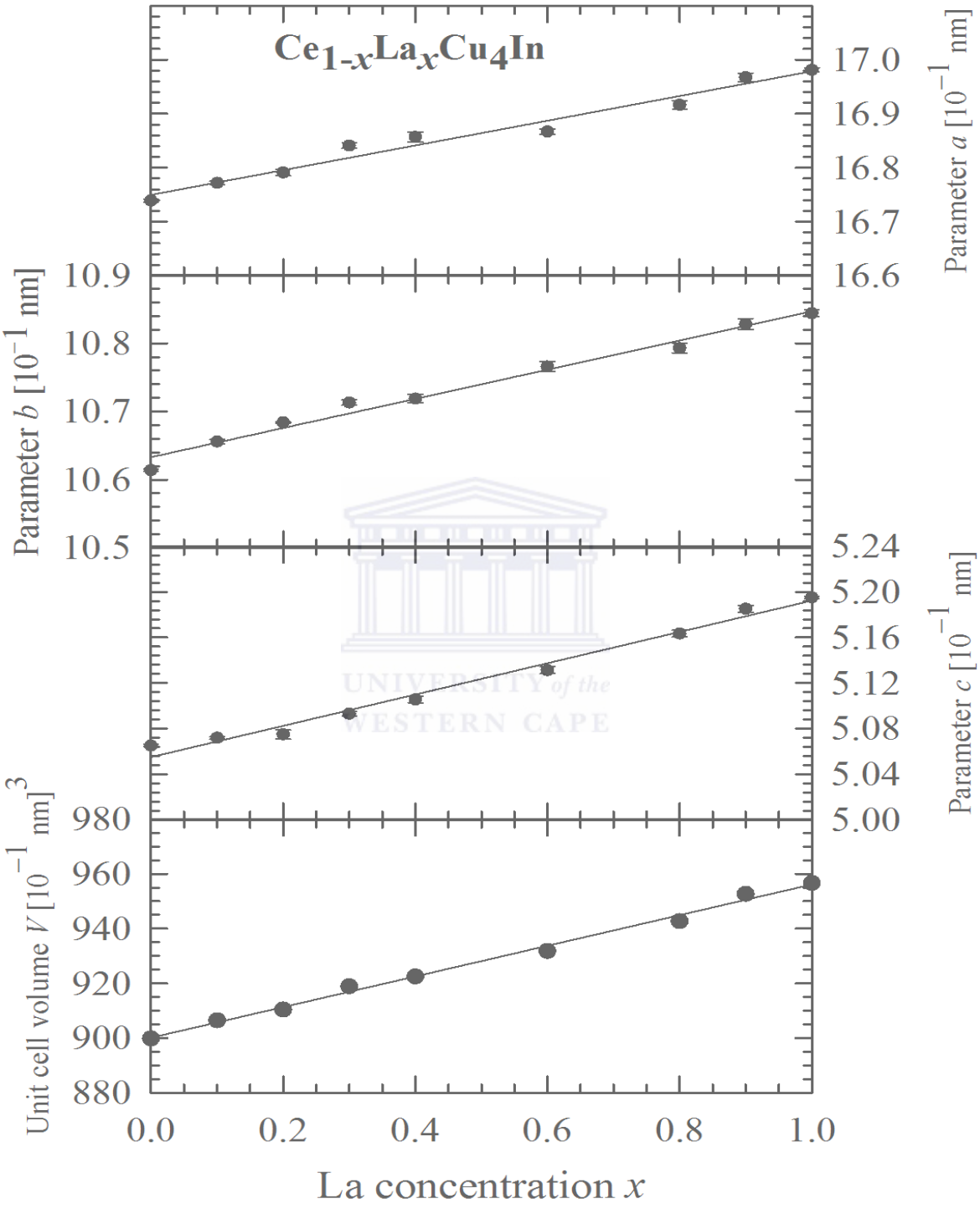

Figure 6.2: Lattice parameters a, b and c and unit cell volume V of the orthorhombic $Ce_{1-x}La_xCu_4In$ alloy system.

gives $\rho_0 = 5.59\mu\Omega$.cm.K^{-3}, $\kappa = 2000\mu\Omega$.cm.K, $\theta_R = 132K$ and $\alpha = 0.31\times10^{-8}\mu\Omega$.cm.K^{-3}. $\rho(T)$ for all compositions where incoherent Kondo scattering is observed are described by:

$$\rho_{ph}(T) = \rho_0^{\infty} + \rho_{BG} + \rho_{4f}, \tag{6.2}$$

where ρ_0^{∞} is the temperature independent resistivity as $T \to 0$. $\rho_{BG}(T)$ is the phonon contribution (second term in Eq. 6.1). ρ_{4f} is the $4f$-contribution which account for the Kondo effect given by [4]:

$$\rho_{4f}(T) = \rho_{spd}\left[1 + \alpha N(E_F)\Gamma_{sf} ln\left(\frac{T}{T_F}\right)\right], \tag{6.3}$$

with the Kondo temperature defined by:

$$T_K = D.exp\left[\frac{-1}{\Gamma_{sf}N(E_F)}\right]. \tag{6.4}$$

α is a constant which depends on the nature of the local moment, T_F is the Fermi temperature, $N(E_F)$ is the density of states at the Fermi level, D is the conduction electron bandwidth and Γ_{sf} is the direct exchange integral. For the LSQ fits Eq 6.2 to the experimental $\rho(T)$ data Eq 6.3 was approximate to $-CKln(T)$ with CK a measured of the strength of the Kondo interaction. It turns out that the temperature independent ρ_0^{∞} account not only for the scattering of electrons by lattice imperfections, dislocations, impurities, spin-disorder and the Nordhein-like contribution, but also for the strength of the Kondo interaction. The phonon contribution is taken as $\rho_{BG}(T) = bT$ which is approximately valid in the temperature region in which we fitted the data. It is observed that LSQ fits of $\rho(T)$ data to Eq 6.2 (solid curve Fig 6.3) for alloys with $x \leqslant 0.6$, the interband scattering that seems to be present for alloys with $x \geqslant 0.8$ is suppressed with 40% Ce doping. For this reason the Mott's term was included only for compositions with $x = 0.8$ and 0.9. LSQ fits of $\rho(T)$ to Eq 6.2 yield the resistivity parameters listed in Table 6.1 and α [$10^{-8}\mu\Omega$.cm.K^{-3}] = 4.3(3) and 23(2) for the $x = 0.8$ and 0.9 respectively. Fig 6.4 shows the $4f$ magnetic contribution to the total resistivity, $\rho_{4f}(T)$, presented in the

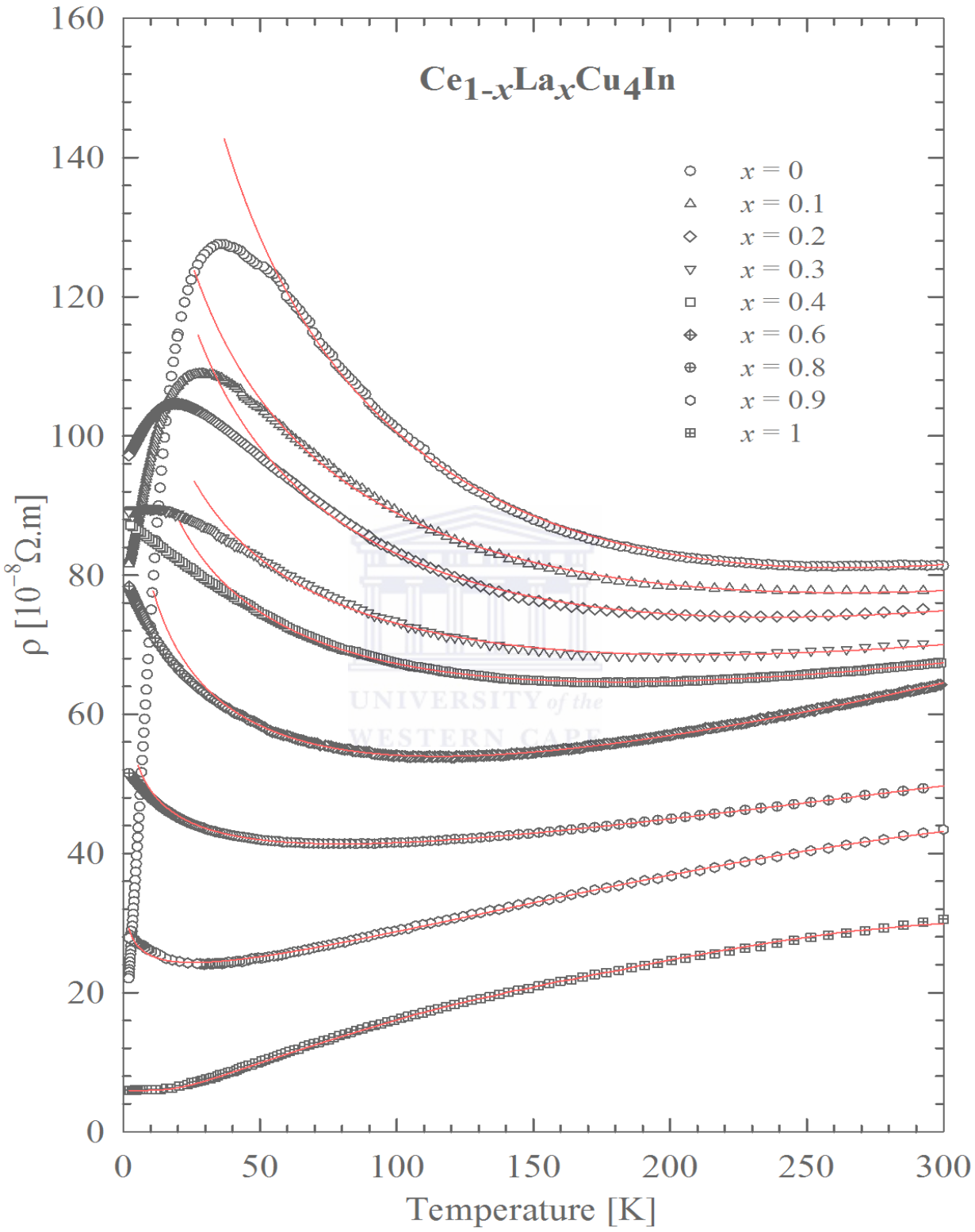

Figure 6.3: Temperature dependence of the electrical resistivity in the temperature range $2 \leq T \leq 300K$ for alloys the system $Ce_{1-x}La_xCu_4In$. The solid red lines are LSQ fits of Eq 6.1 and 6.2 to the measured data.

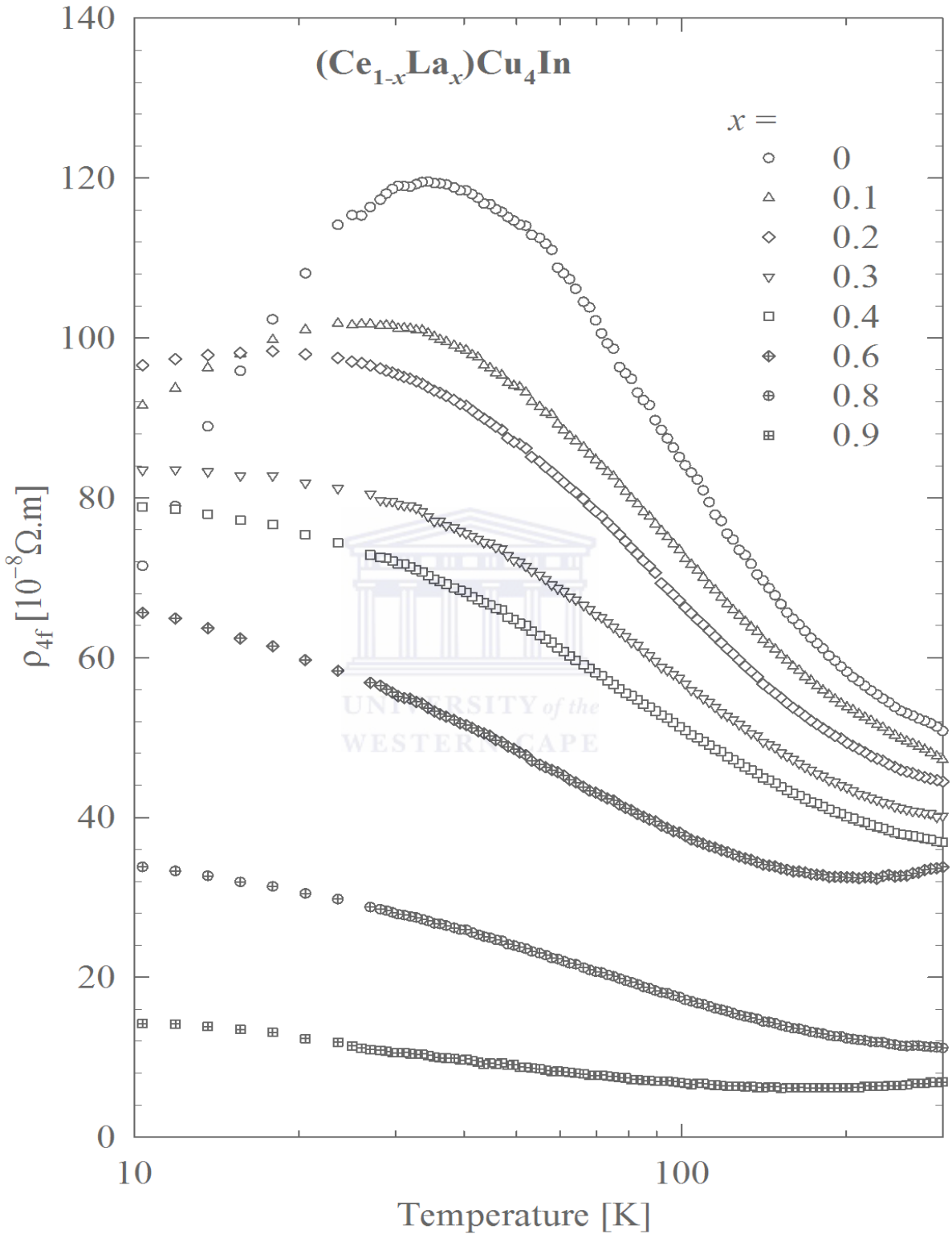

Figure 6.4: Temperature dependence of the magnetic resistivity $\rho_{4f}(T)$ of the $Ce_{1-x}La_xCu_4In$ system.

Table 6.1: Electrical resistivity parameters for the $(Ce_{1-x}La_x)Cu_4In$ alloy system. The values of ρ_0, b and C_K are obtained from Least square fits of Eq 6.2 to the measured data. The value of T_{max} for $0 \leqslant x \leqslant 0.3$ are obtained directly from the measured data.

x	ρ_0 [$\mu\Omega$.cm]	$b[10^{-3}$ $\mu\Omega$.cm/K]	$C_K[\mu\Omega$.cm]	T_{max}[K]
0	336(4)	210(8)	56(1)	34(1)
0.1	227(3)	124(7)	33(1)	27.9(1)
0.2	216(2)	133(3)	31.7(5)	17.8(1)
0.3	158(1)	98(3)	20.5(4)	13.4(1)
0.4	139.7(2)	99(4)	17.9(1)	
0.6	115.4(2)	142(3)	16.4(1)	
0.8	63.2(2)	82(7)	6.5(1)	
0.9	31.1(1)	118(2)	3.03(4)	

logarithmic scale. This magnetic resistivity was obtained by subtracting the $\rho(T)$ data of the non-magnetic counterpart $LaCu_4In$ from $\rho(T)$ data of each composition. It is observed that, for all compositions, $\rho_{4f}(T)$ shows a $-ln(T)$ increase with decreasing temperature as expected from the incoherent Kondo effect. At high temperatures near room temperature, deviation of a linear increase in $-ln(T)$ ocurrs which may be associated to the additional contribution of the $s-d$ interband scattering given by the Mott's term $-\alpha T^3$.

6.3.3 Magnetoresistivity (MR)

The isothermal MR was studied on a selected number of $Ce_{1-x}La_xCu_4In$ alloys for which their $\rho(T)$ curves are characteristic of incoherent Kondo scattering, for field up to 8 T, and at various temperatures between 1.5 and 28 K. The results of these studies are presented in Fig 6.5 for two representative compositions $Ce_{0.4}La_{0.6}Cu_4In$ and $Ce_{0.2}La_{0.8}Cu_4In$. For all the investigated alloys ($x = 0.3$, 0.4, 0.6 and 0.8), a negative MR has been observed at all temperatures as a result of suppression of the incoherent Kondo scattering in magnetic field. The experimental MR data were analyzed in terms of the Bethe-ansatz calculation of the Coqblin-Schrieffer model given by Andrei [82] and Schlottmann [27] for total angular momentum $J = 1/2$ in the integer valence limit:

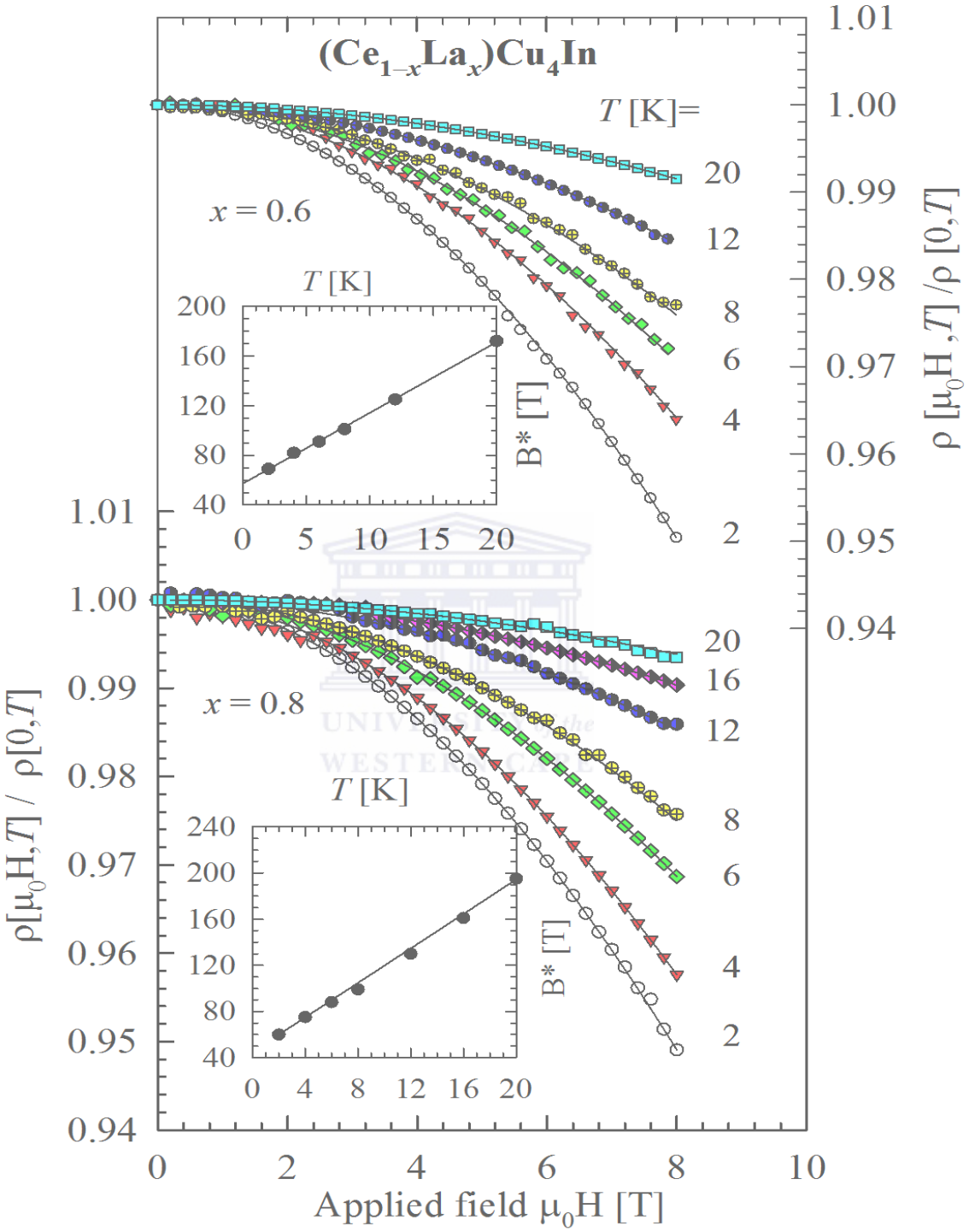

Figure 6.5: Magnetoresistivity isotherms at various temperatures of the $(Ce_{1-x}La_x)Cu_4In$, $x = 0.4$ and 0.8 compounds. The solid lines in the main panel are LSQ fits of Eq 6.5 to the measured data. The insets show the temperature variations of $B^*(T)$, and solid lines through the data points are the LSQ fits of Eq 6.6 to the $B^*(T)$ values.

$$\frac{\rho(B,T)}{\rho(B=0,T)} = \left[\frac{1}{2J+1} sin^2(\frac{\pi n_f}{2J+1}) \sum_{l=0}^{2J} sin^{-2}(\pi n_l)\right]^{-1}, \tag{6.5}$$

where n_f is the electron occupation number. Furthermore, the analysis of MR results at $T = 0$ depends universally on a single energy scale ($g_J \mu_K B^*$), related to the Kondo temperature T_K, where g_J is the landé factor, μ_K the magnetic moment of the Kondo ion and B^* the characteristic Kondo field. Following Batlogg *et al.* [83], the Kondo field depends linearly on temperature according to the equation:

$$B^* = B^*(0) + \frac{k_B T}{g\mu_K} = \frac{k_B(T_K + T)}{g\mu_K}. \tag{6.6}$$

The characteristic field $B^*(T)$ values are obtained from the LSQ fits to the experimental MR data to the Schlottmann's universal MR curve for $J = 1/2$ (solid lines in the main panel of Fig 6.5. The obtained values of B^* are plotted versus the temperature which yields a linear increase with the temperature (inset of Fig 6.5). A LSQ fit of B^* against Eq 6.5 (solid line in the inset of Fig 6.5) leads to a value of $B^*(0)$ and hence to the Kondo temperature T_K and Kondo moment μ_k. These calculated values of T_K and μ_K for alloys under investigation are listed in Table 6.2. Similarly to T_{max}, it is observed that values of T_K decrease monotonically with increase in La content x, which results from the increase in unit-cell volume which in turn weakens the on-site Kondo exchange interaction. Fig 6.5 illustrates for two compositions, the excellent scaling of the MR data

Table 6.2: Parameter values of the Kondo temperature T_K and the magnetic moment of Kondo ion μ_K obtained from the magnetoresistivity analysis using Eq 6.5 and 6.6.

x	T_K[K]	$\mu_K[\mu_B]$
0.3	20.1(3)	0.412(8)
0.4	11.3(8)	0.340(3)
0.6	10.1(2)	0.305(5)
0.8	6.0(4)	0.233(1)

in accordance with the Bethe-*ansatz* formulation of the single-ion magnetoresistivity by showing the collapse of MR data from all isotherms on a single curve in a plot of $\rho(\mu_0 H, T)/\rho(0,T)$ versus $\mu_0 H/B^*(T)$. Similar scaling of the MR was observed for all investigated compositions.

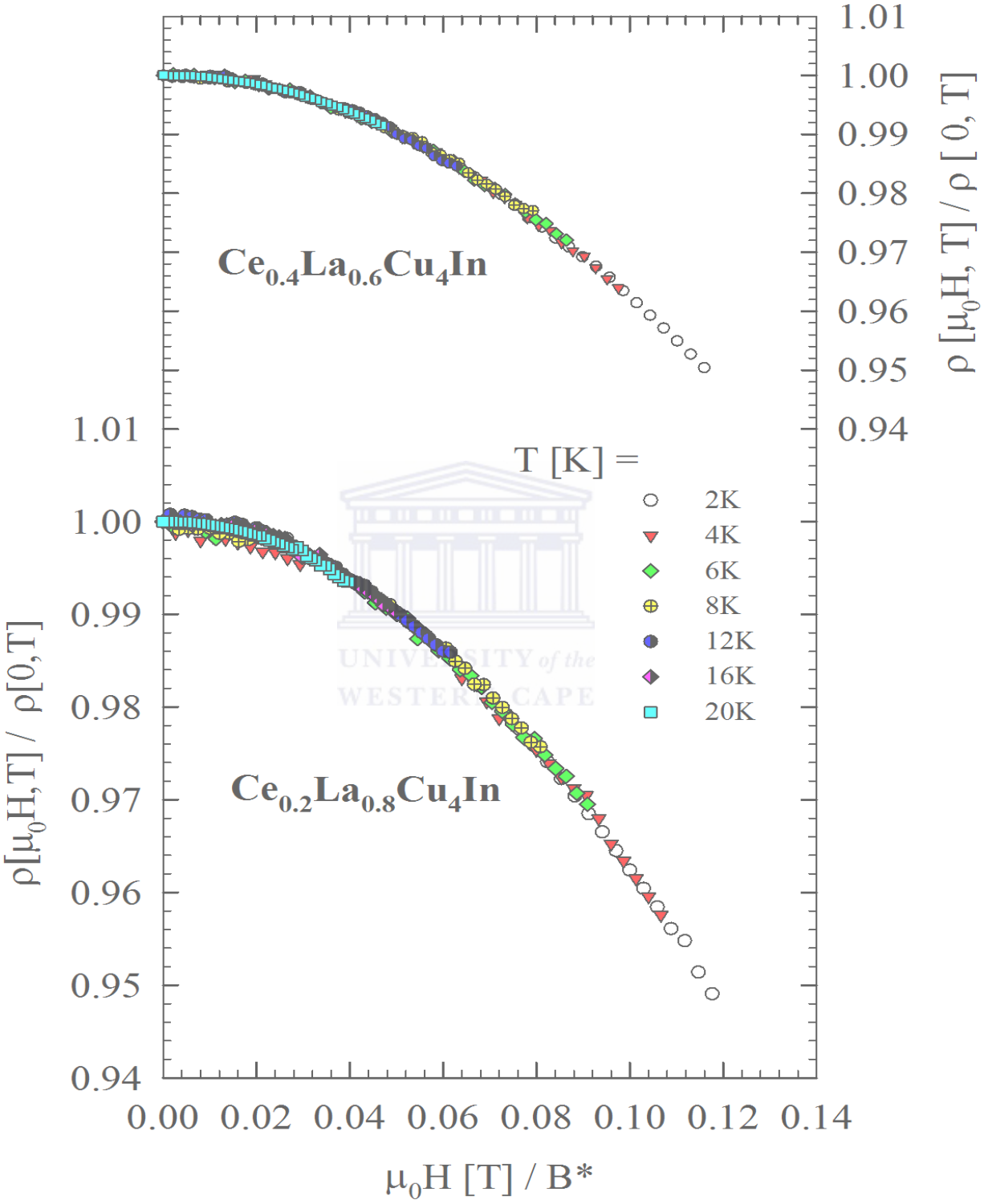

Figure 6.6: Scaling magnetoresistivity data for different isotherms as measured in field up to 8 T and at various temperatures between 2 K to 20 K.

6.3.4 The compressible Kondo lattice model

The temperature variation of the Kondo temperature T_K with hydrostatic or negative chemical pressure is usually described by the compressible Kondo lattice model. It was observed in many experimental results that pressure on a Kondo lattice compound does not affect the position of the $4f$ impurity level but rather acts on the degree of localization of this $4f$ state. Based on that the compressible Kondo lattice model, T_K is enhanced under the effect of pressure and given by [210]

$$T_K = \frac{D}{k_B} exp\left[- \frac{1}{JN(E_F)} \right], \tag{6.7}$$

where D is the conduction electron bandwidth, $N(E_F)$ is the density of state at the Fermi level and J the on-site exchange interaction given by the Coqblin-Schrieffer model [18] by:

$$J = \frac{\langle V_{kf} \rangle^2 U}{\varepsilon_f(\varepsilon_f + U)}. \tag{6.8}$$

In Eq 6.8, U represents the on-site Coulomb repulsion, ε_f is the position of the $4f$ level relative to the Fermi level and V_{kf} denotes the strength of the $4f$-electron and the conduction band hybridization. It is straightforward from Eq 6.8 that a change in T_K depends on a change in $N(E_F)$ or V_{kf}. For instance a decrease in either $N(E_F)$ or V_{kf} will result in a decrease of T_K. Based on the model suggested by Lacroix and Cyrot [211], Lavagna *et al* [210] introduced the effect of pressure on the Kondo lattice for which the volume dependence of $|JN(E_F)|$ is given by defined as

$$|JN(E_F)| = |JN(E_F)|_0 exp\left[\frac{-q(V - V_{0)}}{V_0} \right], \tag{6.9}$$

where $|JN(E_F)|_0$ represents the value of the quantity at initial volume V_0 and $|JN(E_F)|$ corresponds to a volume V. The constant q which can be approximated from Slater rules, is usually taken to be between 6 and 8. The linear expansion of the exponential term in Eq 6.9 for small change in volume ΔV and substitution in Eq 6.7 leads to the relation:

$$T_x(x) = T_x(0) exp\left[\frac{-q(V - V_{0)}}{V_0 |JN(E_F)|_0} \right]. \tag{6.10}$$

V and V_0 are the volume of the unit cell for La-doped alloy and the Ce parent compound, respectively. The initial effect of Ce substitution with La in $(Ce_{1-x}La_x)Cu_4In$ is that the system exhibits an increase in volume change, leading to a decrease in the values of T_K. Our results were interpreted in terms of Eq 6.10 by assuming that for dense Kondo alloys their maxima in $\rho(T)$ occurring at T_{max} are a fair indication of T_K. Eq 6.9 displays T_{max} obtained from the resistivity data and T_K obtained from the MR results as a function of the relative change in unit cell volume obtained from the XRD analysis. It is observed from this figure that T_{max} and T_K decrease monotonically with increase La content. An LSQ fit of Eq 6.10 to the combined data sets gives the solid line in Fig 6.7. The fit performed using $q = 6$ gives $|JN(E_F)|_0 = 0.082(3)$ for $CeCu_4In$, which may be compared to the values of 0.052, 0.09 and 0.065 obtained for heavy fermion $CeCu_5In$, $CeCu_6$ and $CePt_2Si_2$ compounds, respectively [212–214].

6.3.5 Thermoelectric power

The temperature dependence of the thermoelectric power, $S(T)$, of selected compositions in the alloy series $(Ce_{1-x}La_x)Cu_4In$ are displayed in Fig 6.8. Within the measured temperature range all these compositions exhibit positive values of $S(T)$ and a single maximum below room temperature typical of a heavy fermion compound and differ drastically to that of a normal metal. The maximum occurs roughly at the same temperature of 30 K. The observed maximum decreases in magnitude with increased La content x but is retained in all investigated compositions. Rather independent of x. In this respect the behaviour of $S(T)$ is different from that of $\rho(T)$ for this system in that the temperature maximum occurring in $\rho(T)$ diminishes significantly with La substitution as is evident in Table 6.3. These maxima occurring $S(T)$ are considered to originate from the combined effect of the crystalline electric field and Kondo behaviour [215]. The observed maximum value of S= 62 $\mu V/K$ at T_{max} = 32 K for the parent compound $CeCu_4In$ sample is compatible with that obtained for the same compound in Ref. [88]. The decreases $S(T)$ maximum with increasing La content was also observed in other alloys series such as $(Ce_{1-x}La_x)Al_3$ [216, 217], $(Ce_{1-x}La_x)In_3$ [218] and $(Ce_{1-x}La_x)Cu_3Al$ [219]. The analysis of the measured $S(T)$ data was carried out in terms of phenomenological resonance model [220], which describes the low temperature $S(T)$ data. This model assumes that the dominant contribution to $S(T)$ originates from the scattering of electrons from a wide conduction band into a narrow f-band approximate by a Lorentzian shape. According to the model, two parameters must be taken into account: the position of the f-electron band relative to the Fermi level $(E_f - E_F)$ and the width of the resonance peak W_f. Thus the temperature variation of $S(T)$ can be expressed in the form:

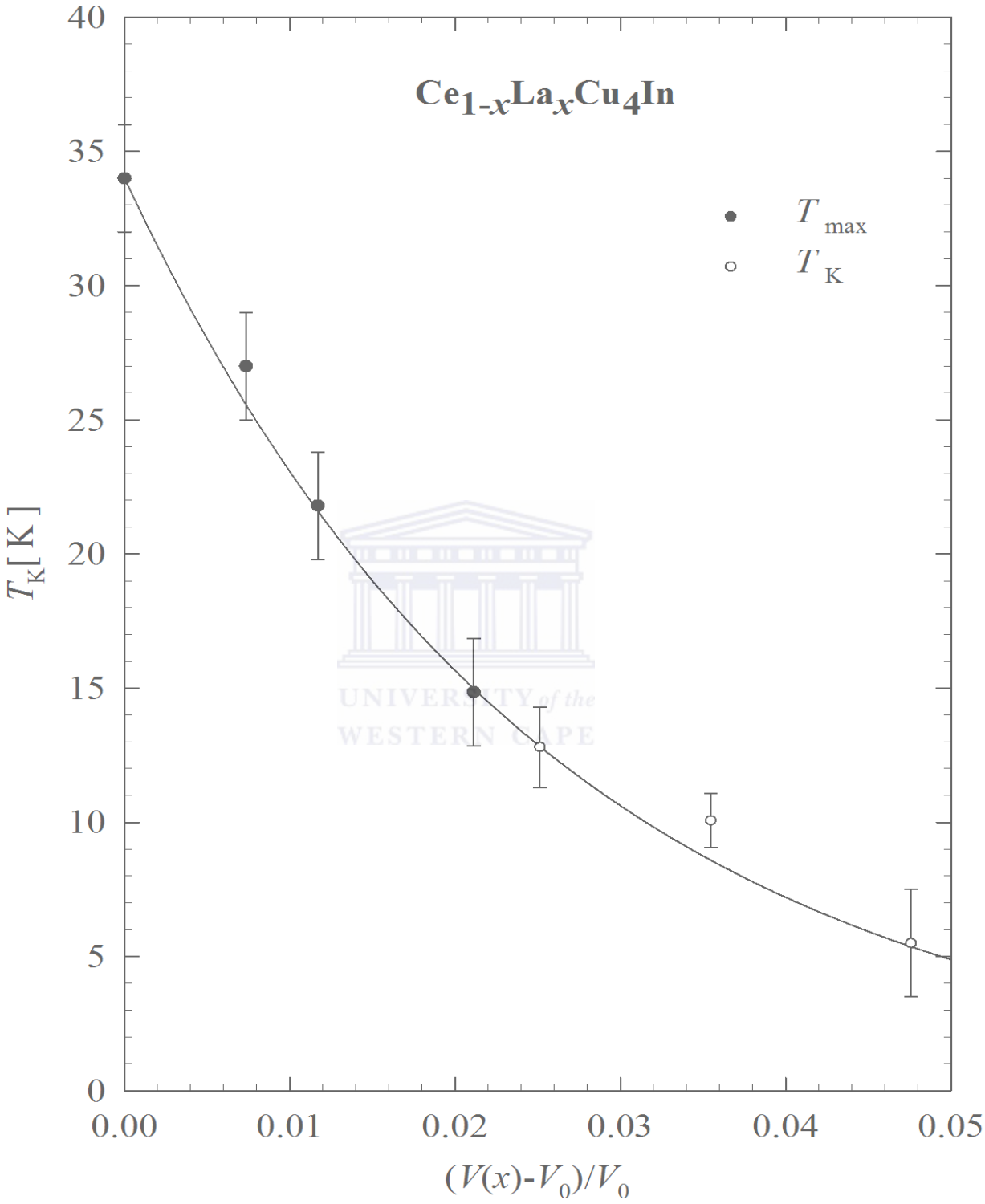

Figure 6.7: A plot of T_{max} and T_K values obtained from the resistivity and magnetoresistivity data versus the change in units cell volume of the alloys in the $(Ce_{1-x}La_x)Cu_4In$ system. The solid line is a LSQ fits of T_{max} together with T_K to the compressible Kondo model (Eq 6.10).

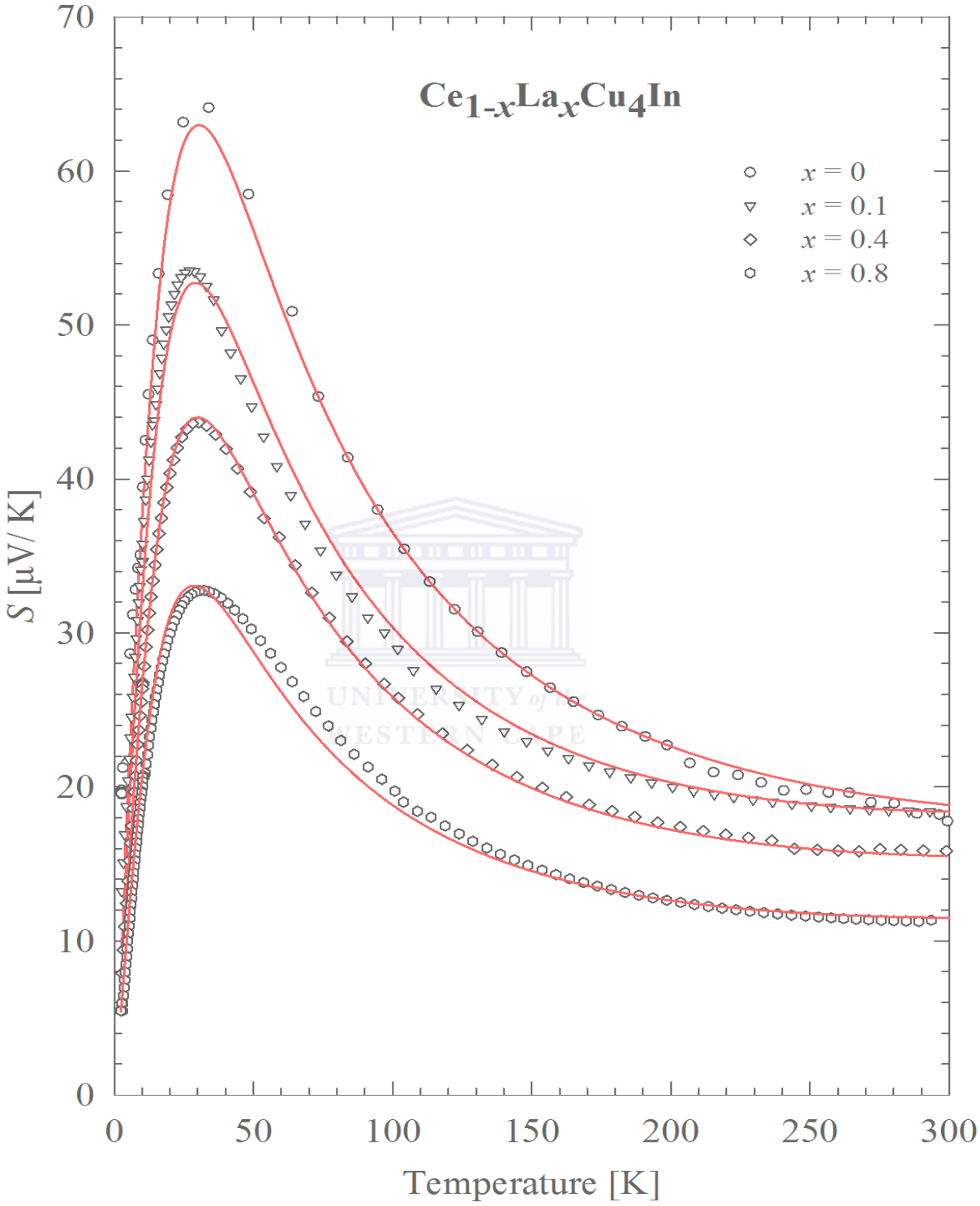

Figure 6.8: Temperature dependence of thermoelectric power $S(T)$ for alloys with $x = 0$, 0.1, 0.4 and 0.8 of the $(Ce_{1-x}La_x)Cu_4In$ alloys series, as measured from 2 K to 300 K. The solid red lines is a LSQ fit of the measured $S(T)$ data to the phenomenological model given in Eq 6.11.

$$S(T) = \frac{2}{3}\pi^2 \frac{k_B}{|e|} \frac{T.E_f}{(\pi^2/3)T^2 + E_f^2 + (\pi^2/N_f^2)W_f^2} + S_d(T), \tag{6.11}$$

where $S_d(T)$=aT is the Mott's contribution originating from the interband scattering, E_f and W_f have the unit of temperature (K). The first term in Eq 6.11 describes very well $S(T)$ of mixed valence system due to their high value of T_K. Therefore, to obtain a good fit shown by solid line in Fig 6.8 the Mott's term was included, and a similar assumption was taken as in reference [88], considering $E_f = T_K$ and $W_f = \pi T_{CEF}/N_f$, where N_f is the orbital degeneracy $2J+1$ and T_{CEF} is the characteristic temperature which is a measure of the CEF. LSQ fits of Eq 6.11 to the experimental $S(T)$ data give the parameters listed in Table 6.3. The resulting parameters obtained for our parent compound $CeCu_4In$ are in good agreement with previously reported results [88]. The behaviour of T_K obtained from $S(T)$ analysis with La content x is similar to that of T_{max} and T_K obtained from resistivity and MR analysis. The position of the DOS peak with respect to the Fermi level E_f is positive for $Ce_{1-x}La_xCu_4In$ and decreases with increasing La concentration. This means that there should be a DOS peak just above the Fermi level. It is also observed that the width of the narrow band W_f does not change significantly with La concentration and is almost of the same order of magnitude for all compounds. Since the W_f does not change with La concentration, one accepts that the values of T_{CEF} are similar for all compounds. The values of T_{CEF} were calculated by taking maximum orbital degeneracy for Ce $N_f = 2J+1 = 6$. These values are very close to those values of T_{CEF} obtained for $(Ce,La)Cu_4Al$ which are also independent of La concentration [134].

Table 6.3: Parameters values obtained from LSQ fits of $S(T)$ to the phenomenological model described in Eq 6.11.

x	E_f[meV]	W_f[meV]	$a[\mu V/K^2]$	T_{CEF} [K]	T_K [K]
0	20.1(3)	0.412(8)	0.022(2)	95	21.8
0.1	11.3(8)	0.340(3)	0.029(4)	94	17.3
0.4	10.1(2)	0.305(5)	0.024	98	14.9
0.2	6.0(4)	0.233(1)	0.018	96	10.7

6.3.6 Thermal conductivity

The temperature dependence of the total thermal conductivity, $\lambda_{tot}(T)$, together with electronic $\lambda_{elec}(T)$ and phonon $\lambda_{ph}(T)$ components for selected compositions of the alloys series $Ce_{1-x}La_xCu_4In$ are shows in Fig 6.9. The phonon contribution for which phonons are heat carriers, was obtained by subtracting the electronic contribution to $\lambda_{tot}(T)$) assuming that the two terms are independent of one another and that there are no other carriers of heat such magnons. It is further assumed that the electronic contribution is connected with resistivity through the Wiedemann-Franz law: $\lambda_{elec}(T) = L_0T/\rho_0$, where $L_0 = 2.45 \times^{-8}$ W Ω/K^2 is the Lorentz number. It is observed that $\lambda_{ph}(T)$ predominates $\lambda_{elec}(T)$ over wide temperature range of 2 K $\leqslant$ T $\leqslant$ 130 K, 50 K $\leqslant$ T $\leqslant$ 150 K, 2 K $\leqslant$ T $\leqslant$ 110 K and 2 K $\leqslant$ T $\leqslant$ 75 K for alloys with x = 0.8, 0.4 and 0 respectively. This dominance of $\lambda_{ph}(T)$ at low temperatures was observed in many Kondo lattice compounds such as $CeCu_4Ag$ [133], $CeCu_4Al$ [208] and $CeNiAl_4$ [135]. It is noted that the slope of the linear part of $\lambda_{tot}(T)$ in the temperature range is increased with decreasing La content x. At a temperature below 20 K, λ_{tot} is proportional to T, which is typical for scattering of electrons from lattice imperfections. At temperature above 150 K, $\lambda_{tot}(T)$ for dilute Ce alloys deviate from linearity, with a downward curvature and a tendency toward saturation above 300 K. Such a saturation of $\lambda_{tot}(T)$ follows the Willson's law which predicts a constant value of $\lambda_{tot}(T)$, typical for scattering electrons from thermally excited phonons only when the phonon excitation rate is constant in temperature [137]. The linear behaviour of $\lambda_{tot}(T)$ for the pure Ce compound is not predicted theoretically and was seen frequently in most heavy fermion compounds such as $CeCu_4Ag$ [133] and $CeCu_4Al$ [208]. It is also noted that the value of $\lambda_{tot}(T)$ decreases with La content x. Such was also observed in the alloy series $(Ce_{1-x}La_x)Cu_4Al$ and was attributed to the enhancement of mass and volume fluctuations in the alloys series [208].

Combining the results of $\lambda_{tot}(T)$ and $\rho(T)$, the plot of the Lorentz number $L(T) = \lambda_{tot}(T)\rho(T)/T$ normalized to the value of L_0 is shown in Fig 6.10 with the inset showing the reduced Lorentz number scaling to unity at room temperature. It is observed that the values of L/L_0 decrease rapidly with increasing La content x. The overall behaviour of L/L_0 for all investigated compositions is a rapid increase on cooling followed by a maximum at a temperature T_{max} which shifts slightly from 16 K to 9 K with increase La content x. This is followed by a sudden drop of L/L_0 be low T_{max}. The observed maximum decreases in magnitude with increase La content. The increase of L/L_0 at low temperature deviates from the Wiedemann-law which predict L/L_0= 1 at high temperature and at $T = 0$ if the lattice vibration can be neglected. This behaviour may be attributed to an additional lattice thermal conductivity or can also arise from the energy dependent Kondo scattering process. Such a tendency was observed for several Ce

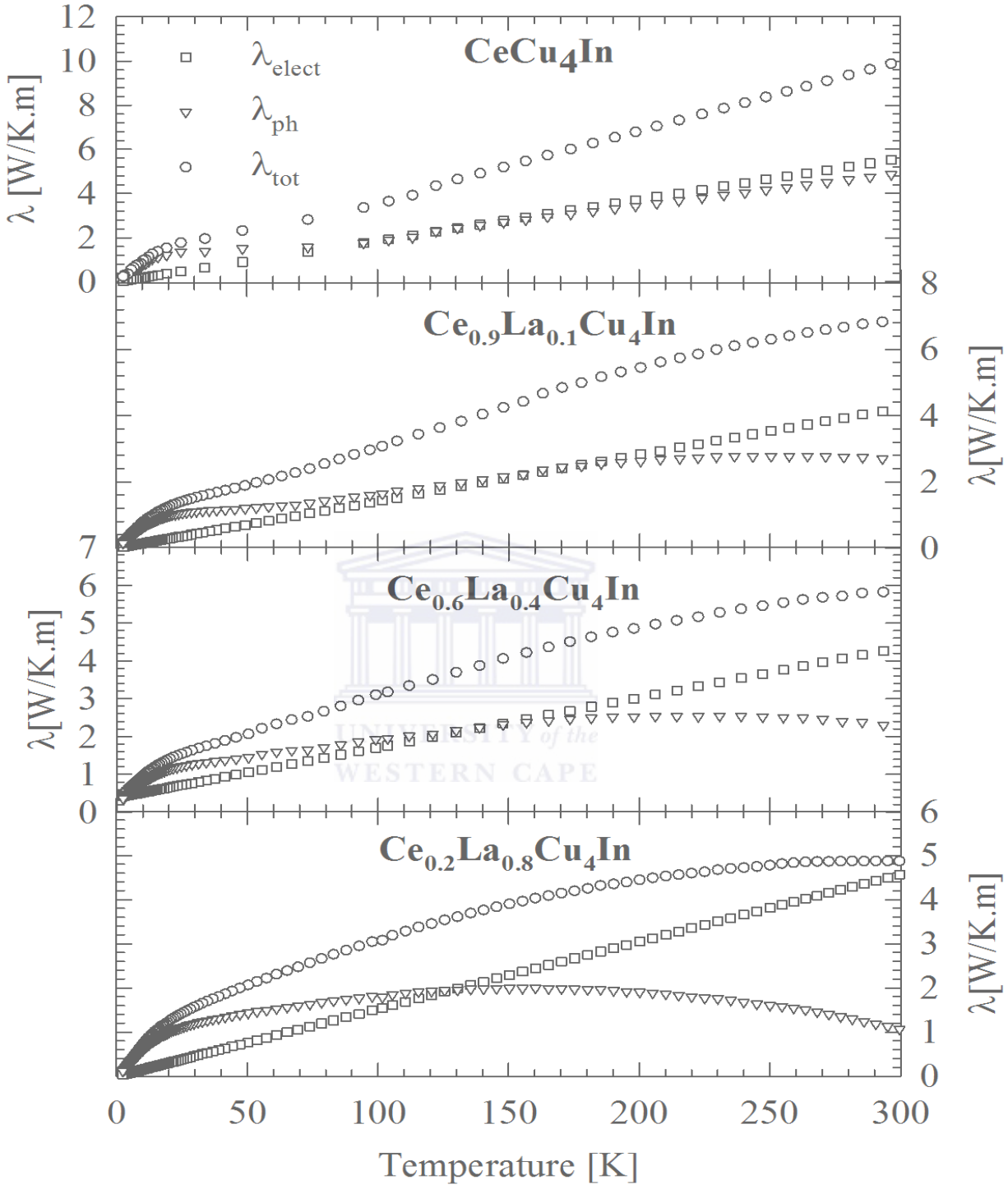

Figure 6.9: Temperature dependence of the total thermal conductivity, $\lambda(T)$ for $(Ce_{1-x}La_x)Cu_4In$ alloys with $x = 0$, 0.1, 0.4 and 0.8 together with the phonon, $\lambda_{ph}(T)$ and electronic contributions, $\lambda_{elec}(T)$.

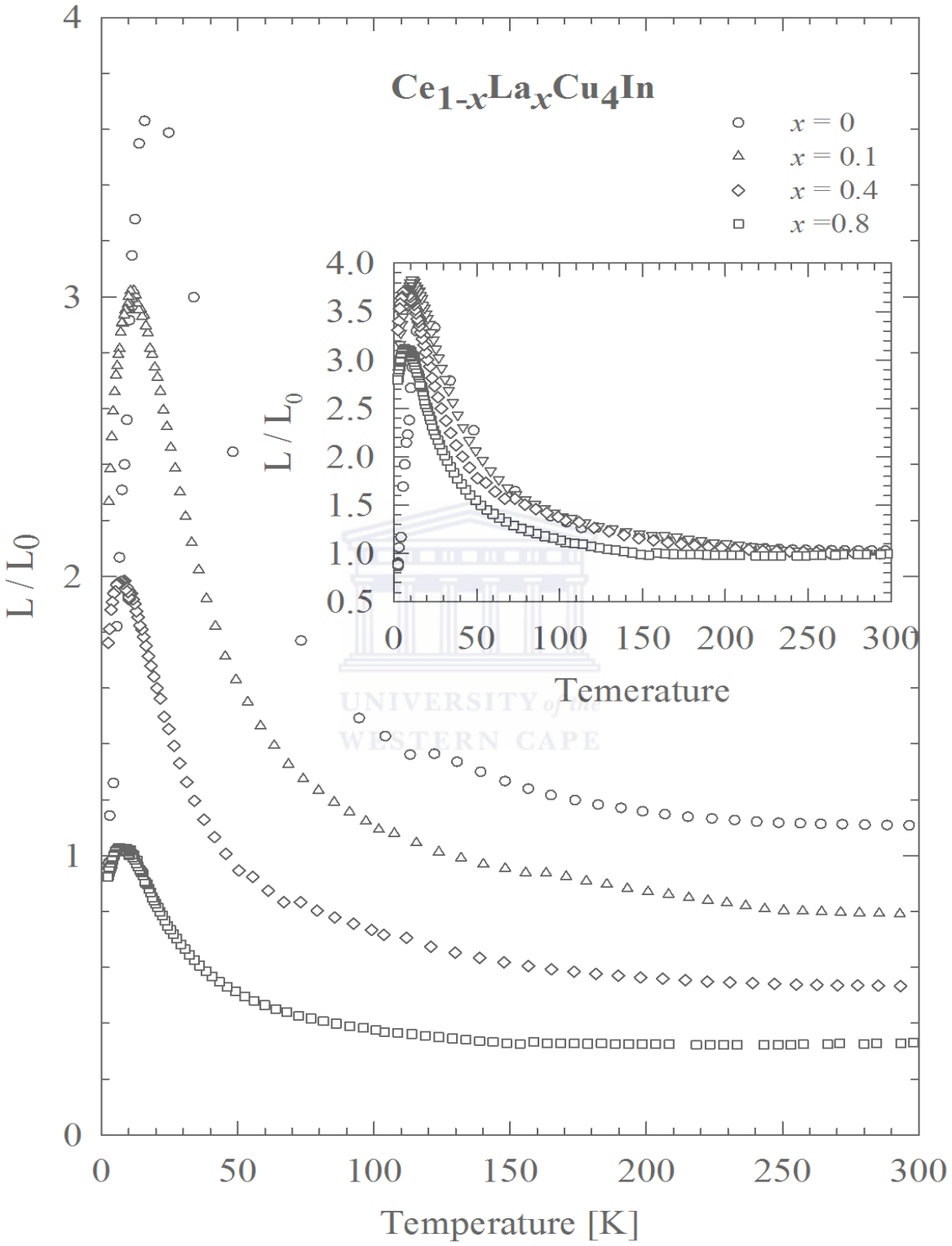

Figure 6.10: Temperature dependence of the reduced Lorentz number L/L_0 alloys with $x = 0$, 0.1, 0.4 and 0.8 in the $(Ce_{1-x}La_x)Cu_4In$ system, as measured from 2 K to 300 K. The inset shows the temperature dependence of the reduced Lorentz number L/L_0 scaled to unity.

compounds [133, 135, 208]. Finally for application point of view, it will be useful to compare the values of the dimensionless figure of merit:

$$ZT = S^2T/\lambda\rho, \tag{6.12}$$

which determines the efficiency of the thermoelectric material to that of the of the conventional thermoelectric materials Bi_2Te_3 and other heavy-fermion materials. Bi_2Te_3 is the common thermoelectric material in power generation or refrigeration with ZT between 0.8 and 1 [140]. The plot of ZT of the present system is shown in Fig 6.11. It is observed that ZT values for all the investigated compositions increase on cooling and exhibit a maximum at temperature between 42 and 48 K. The observed peak increases in magnitude with increasing La content, opposite to that of L/L_0. Our maximum value for $CeCu_4In$ is about 0.06 at T = 48 K and ZT takes the value of 12.5×10^{-3} at room temperature. These values are roughly twice larger than the values reported for the same compound in reference [136] at T= 50 K.

6.3.7 Magnetic susceptibility and magnetization

The temperature variation of the inverse magnetic susceptibility, $\chi^{-1}(T)$, measured in applied field of 0.01 T in the temperature range 2 to 300 K are depicted in Fig 6.12 for the $(Ce_{1-x}La_x)Cu_4In$ alloys with $0 \leqslant x \leqslant 1$. The field of 0.1 T was chosen since the field dependent magnetization was linear in this field range for all compositions at all temperatures. $\chi(T)$ data obtained for the parent compound $CeCu_4In$ are in good agreement with that reported in ref [204]. It is observed the reciprocal paramagnetic susceptibility follows a Curie-Weiss relation over an extended temperature range above 100 K

$$\chi^{-1}(T) = 3k_B(\theta_P - T)/N_A\mu_{eff}^2. \tag{6.13}$$

LSQ fits of the experimental data against Eq 6.13 in the temperature range 100 to 300 K are shown as solid line in Fig 6.12. Parameters obtained from the fits are gathered in Table 6.4 . The effective magnetic moment values obtained across the series are in fair agreement with the expected free-ion value of 2.54 μ_B that correspond to the free Ce^{3+} ion. Values of the paramagnetic Curie temperature constant vary in an irregular manner across the alloys series, whereas one would expect for Ce Kondo systems that $|\theta_p| \sim T_K$ should decrease monotonically with increase La content. This anomalous result is likely due to different degrees of preferred crystalline orientation in the different compositions

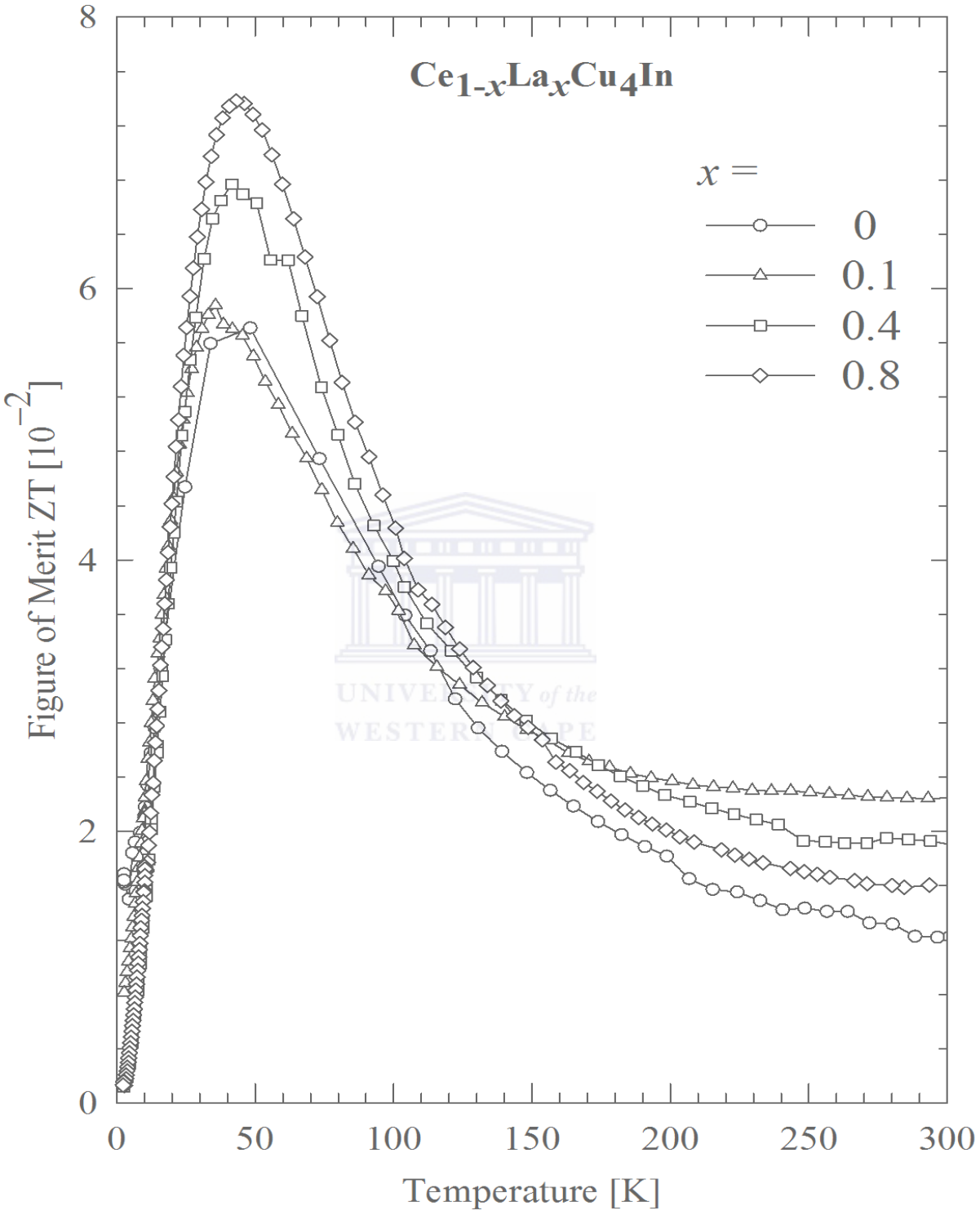

Figure 6.11: Figure of merits ZT of selected compositions in the alloy series $(Ce_{1-x}La_x)Cu_4In$. The solid red lines are guides for the eye.

also observed for $(Ce_{1-x}La_x)Cu_5In$ [212]. At low temperature $\chi^{-1}(T)$ deviate from the Curie-Weiss behaviour, which suggests a depopulation of the crystal-electric levels associated with $4f$ Ce ions. No evidence of magnetic ordering was found down to 2 K for $CeCu_4In$ as well as La substituted alloys from $\chi(T)$ measurements.

The field dependencies of magnetization $M(\mu_0 H)$ measured at 1.7 K in a field up to 5 T are depicted in Fig 6.13. It is observed that $M(\mu_0 H)$ shows no hysteresis effect with increasing and decreasing field as well as no metamagnetic behaviour for all compositions. The magnetization value at 5 T increases with La content ranging from 0.3 μ_B to 0.55 μ_B for $CeCu_4In$ and $(Ce_{0.1}La_{0.9})Cu_4In$ respectively.

Table 6.4: Values of paramagnetic Curie temperatures θ_P and the effective magnetic moment μ_{eff} of $(Ce_{1-x}La_x)Cu_4In$ series, resulting from LSQ of the inverse magnetic susceptibility χ^{-1} data to Curie-Weiss Law.

x	μ_{eff} $[\mu_B]$	$-\theta_P$[K]
0	2.50(3)	64.9(4)
0.1	2.52(3)	55.5(7)
0.2	2.56(2)	76.27(3)
0.3	2.59(5)	74.4(2)
0.4	2.48(2)	68.4(4)
0.6	2.65(5)	82(3)
0.8	2.51(2)	57(4)
0.9	2.63(1)	59(2)

6.4 Conclusion

XRD studies confirm the orthorhombic $CeCu_{4.38}In_{1.62}$-type crystal structure with space group $Pnnm$ (No. 58). The linear increase in unit cell volume values with increasing La content x obtained from the XRD analysis confirms the Vegard's rule. $\rho(T)$ measurements clearly illustrate the evolution from dense Kondo to incoherent single-ion Kondo scattering

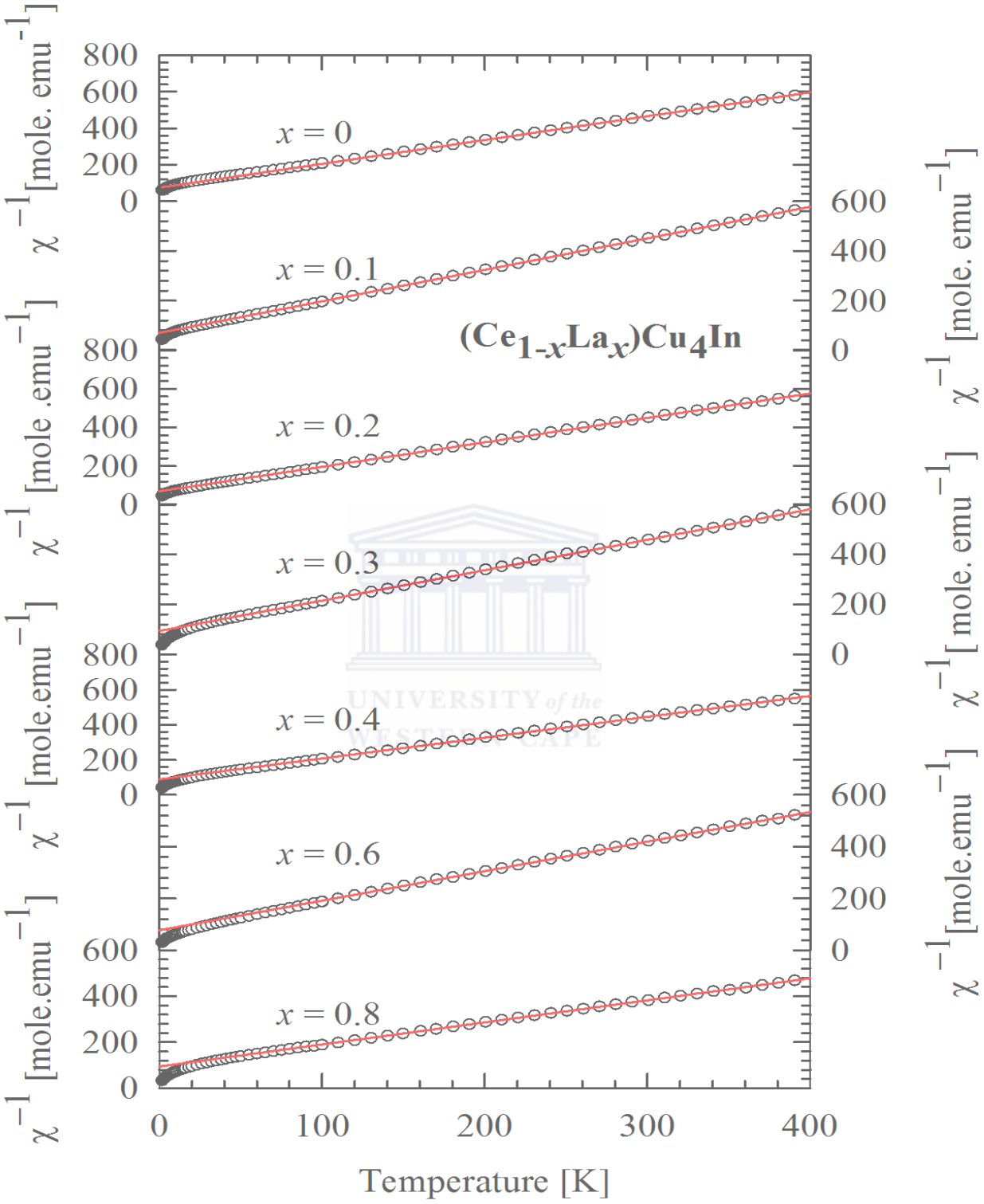

Figure 6.12: Temperature dependence of inverse magnetic susceptibility, $\chi^{-1}(T)$ of the $(Ce_{1-x}La_x)Cu_4In$ fitted to Curie-Weiss Law (red solid lines) at higher temperatures. The data of all compositions were measured in B = 0.01 T.

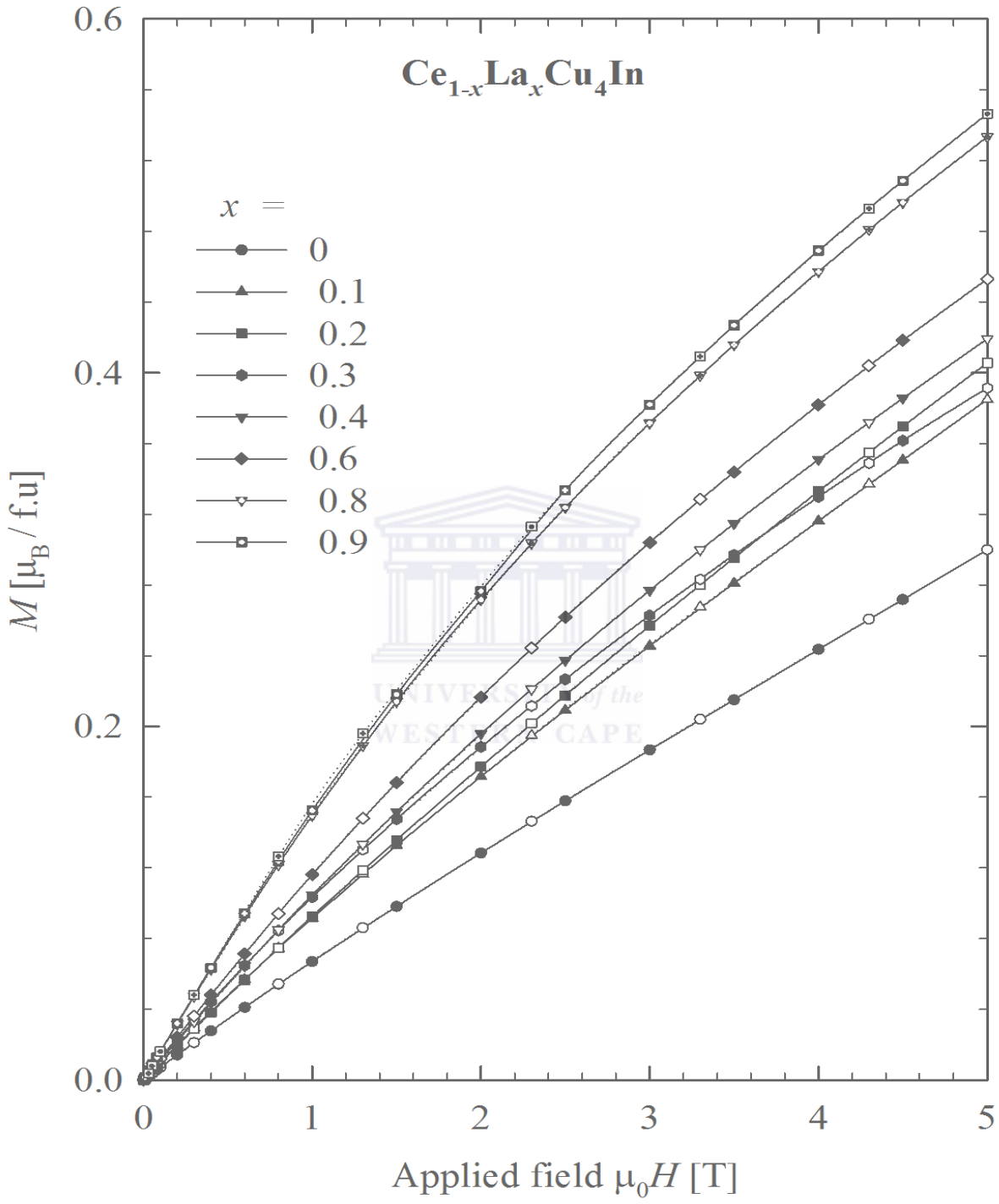

Figure 6.13: Field dependence of magnetization $M(\mu_0 H)$ for $(Ce_{1-x}La_x)Cu_4In$ alloys series, as measured up to 5 T and at a temperature $T = 1.7$ K.

with increase La content. A negative MR and positive $S(T)$ data are observed for all compositions. The positive $S(T)$ is likely to be understood in terms of the combined effects of the crystalline electric field and the Kondo behaviour. MR data are interpreted within the single-ion Bethe *ansatz* description of the Coblin-Schrieffer model. $S(T)$ data are described by the phenomenological resonance model. The resulting T_{max} values at which a maximum occurs for the coherent dense Kondo alloys together with the T_K values obtained from MR analysis are used in a compressible Kondo lattice description of the system. Susceptibility measurements at higher temperatures give effective magnetic moment in fair agreement with the Ce^{3+} value.

Chapter 7

Effect of La dilution and ligand substitution on the $Ce_8Pd_{24}Al$ antiferromagnetic Kondo lattice compound

7.1 Introduction

The $CePd_3$ alloy is well identified to be an archetypical intermediate valence (IV) compound at room temperature and atmospheric pressure [221]. This compound is found to form in cubic $AuCu_3$-type structure with space group $Pm\overline{3}m$ in which the Ce atoms are situated in the cubic corners and the Pd atoms in the cubic faces. Various studies [222, 223] on the magnetic susceptibility of this compound indicate a broad peak near 120-130 K. The study of thermoelectric power indicates that this compound possesses much larger value than normal metal and shows a maximum of approximately 125 μ V.K^{-1} at the same temperature as the resistivity maximum at 120 K [221, 224]. The heat capacity study reveals that the Summerfeld coefficient (γ) of this compound is about 39 mJ.mole^{-1}.K^{-2}, and X-ray photoemission spectra (XPS) results indicate the valence of Ce has a value of 3.3 at a temperature of 300 K [225].

The effect of dilution of Ce by Y as well as the substitution Pd by Rh or Ag are reported in several studies. For instance, the dilution of Ce by La [226] or Ce by Y [227] lead to a crossover from IV to a trivalent state. The substitution of Pd by Rh [228] show non-magnetic behaviour, whilst the substitution of Pd by Ag [229] reveals a Kondo-like behaviour. On other hand, several studies [230–237] on the effect of inserting other atoms (specially P block-atoms) into the structure of $CePd_3$ have been reported. The resulting

compounds $CePd_3M_x$, are thought to have the same cubic $AuCu_3$-type structure as the parent compound $CePd_3$, with the M atoms occupying the centre of the cube. However, the insertion of the M atoms considerably modify the chemical medium of the $4f$-electron states of the Ce atom, thus resulting in changing the IV state found in $CePd_3$ to a trivalent state in the new compounds. Therefore, the new compounds may manifest Kondo behaviour or magnetic ordering at low temperatures. For instance, the IV state of $CePd_3$ is changed to that of a magnetic Kondo state in $CePd_{24}Ga_{0.125}$ [237], while it is changed to single-ion Kondo behaviour in the case of inserting silicon [235].

The group of compounds $Ce_8Pd_{24}M$ which are closely related to $CePd_3M_x$ have been the subject of several experimental investigations due to the interesting magnetic ground state properties [238–241]. These compounds crystallize in a cubic superstructure closely related to the cubic $AuCu_3$-type structure of $CePd_3$ and is composed of a cube with eight unit cells of $CePd_3$ with an a axis double that of $CePd_3$. The M atoms are situated at the center of only certain palladium octahedrals [238–240], pushing the palladium atom outward from the faces of the cube. Most of these compounds order magnetically below 10 K. The existence of a magnetically ordered state in this group of compounds depends on a balance between the indirect RKKY exchange interaction and the on-site Kondo hybridization between the $4f$ electrons and the conduction electrons [242]. For compounds with M elements belonging to group 4A elements, e.g. Ge and Sn, the electrical resistivity behaviour is characteristic of electron-phonon scattering in the presence of crystal-electric field effect. The low-temperature magnetic susceptibility for these alloys show a typical antiferromagnetic peak at the Néel temperature. For instance, $Ce_8Pd_{24}Ge$ order at T_N = 5.3 K, while $Ce_8Pd_{24}Sn$ exhibits the highest magnetic ordering temperature of this series at T_N = 7.5 K [238, 239]. In the case of compounds with M belonging to group 3A elements, e.g; Ga, Al and In and transition elements like Mn and Zn, $\rho(T)$ shows strong Kondo interactions. For $Ce_8Pd_{24}Al$ in particular, $\rho(T)$ curve shows a strong Kondo interaction with a Kondo peak T_{max} = 14 K and a large region of negative temperature coefficient of resistivity from 14 to 300 K. Below T_{max}, $\rho(T)$ shows a sudden drop, suggesting coherence effect [238, 239]. Antiferromagnetic phase transition was observed at T_N = 4.6 or 4.7 K [241, 243]. FC and ZFC $\chi(T)$ indicate spin-glass behaviour for this compound below T_N.

The effect of changing Al concentration in $Ce_8Pd_{24}Al_x$ and the substitution of 50% Al with Zn in the parent dense Kondo lattice antiferromagnet $Ce_8Pd_{24}Al$ were reported [243, 244]. For $Ce_8Pd_{24}Al_x$, $\chi(T)$ data indicates AFM for compositions in the range $0.96 \leq x \leq 2$, while high temperature $\chi(T)$ follows the Curie-Weiss behaviour. $\rho(T)$ results indicate evolution from intermediate valence state in the Al-poor alloys to Kondo behaviour with

increasing Al concentration up to $x = 1.5$ [243]. Above this concentration, $\rho(T)$ behaviour is characteristic of electron-phonon scattering in the presence of crystal-electric effect. The intermediate valence state at Al-poor alloys are characterised by a strong-hybridization with a non-magnetic ground state. On the other hand, the substitution of Al with Zn by 50% expands the lattice marginally and $\rho(T)$ behaviour is characteristic of a coherent Kondo lattice scattering with a Kondo peak at 10 K. The Zn substitution increases T_N by 0.2 K [243]. In the case of $(CePd_3)_8Mn$, the Mn sublattice undergoes a ferromagnetic transition around 35 K, while the Ce ions form a dense Kondo lattice and are in a paramagnetic state down to 1.5 K [245]. The heat capacity study of $(CePd_3)_8Mn$ indicates a strongly correlated ground state arising from Kondo effect with a Summerfeld coefficient value $\gamma = 275$ mJ/mole.K^2 [245].

In view of this peculiar magnetic character of the family of compounds $Ce_8Pd_{24}Al$, we undertook to investigate the effect of Ce dilution with La as well as ligand substitution of Al with Sn on the magnetic and Kondo behaviour in $Ce_8Pd_{24}Al$, through measurements of $\rho(T)$, magnetoresistivity (MR), thermoelectric power ($S(T)$), thermal conductivity (λ(T)), magnetic susceptibility ($\chi(T)$) and magnetization ($M(\mu_0 H)$).

7.2 Effect of La dilution on $Ce_8Pd_{24}Al$ compound

7.2.1 Sample characterization

Polycrystalline samples of the alloy series $(Ce_{1-x}La_x)_8Pd_{24}Al$ were prepared by arc-melting using the same procedure described in section 3.1. Metals of the following purity in wt% were used: Ce, 99.98%; La, 99.98 %; Pd, 99.97%; Al, 99.9999%. For all samples a weight loss less than 1% were recorded. The quality of samples were checked by X-ray powder diffraction (XRD) at room temperature using a Bruker D8 Advance powder diffractometer with a CuKα radiation ($\lambda = 1.540598$ Å). The diffraction patterns were analysed using the cell and intensity least square (CAILS)-Pawely method from TOPAS ACADEMIC programme. All the samples investigated were found to be single phase materials. No evidence of parasitic phase or unreacted elements was found in the XRD patterns.

7.2.2 Results and discussions

XRD patterns confirm the superstructure closely related to the cubic $AuCu_3$-type structure with space group $Pm\overline{3}m$ of $CePd_3$. An example of a comparison of experimental and refinement X-ray diffractograms together with its difference curve (*i.e* difference between experimental and Rietveld calculated intensities) of the parent compounds $Ce_8Pd_{24}Al$ and

$La_8Pd_{24}Al$ are shown in Fig 7.1. The resultant parameters as a function of La content x are displayed in Fig 7.2 showing a linear increase with x consistent with Vegard's rule which suggests the stability of the Ce valence across the series as well as no change in the number of conduction electrons, which ensures metallic bonding of the alloy system. The lattice parameters of the two end compounds are in good agreement with previous reported results [243].

7.2.2.1 Electrical resistivity

The temperature dependencies of $\rho(T)$ data are shown in the main panel of Fig 7.3. It is observed that $\rho(T)$ at low temperatures evolves from coherent Kondo scattering for concentrated Ce alloys with a well defined Kondo peak at T_{max} (see Table 7.1) to incoherent single-ion Kondo behaviour for diluted Ce alloys. The observed resistivity maximum arises from the combined Kondo and crystalline-electric-field (CEF) effects as explained theoretically in refs.[246, 247]. At high temperatures $\rho(T)$ for all compositions are characteristic of a $-lnT$ increase upon cooling the samples, which could be attributed to the hallmark of Kondo-type interactions of the conduction electrons with the localized Ce magnetic moments. This behaviour of $\rho(T)$ at high temperature is expressed as:

$$\rho(T) = (\rho_0) + bT - C_K ln(T), \tag{7.1}$$

where ρ_0 includes, in addition to the electron-defect scattering component, a large temperature independent spin disorder component at $T = 0$ [246] and possibly a Nordheim like contribution resulting from atomic disorder due to the presence of two kinds of atoms (Ce, La) in the $Ce_8Pd_{24}Al$ Kondo lattice [248]. The second term is the high temperature approximation of the phonon contribution resulting from the Bloch-Grüneissen formula [209] with b a coefficient related to both the Debye resistivity temperature (θ_R) and κ a coefficient giving information about the strength of the electron-phonon interaction. The third term is the $4f$ magnetic contribution where the coefficient C_K gives information about the magnitude of the on-site interaction between the local Ce-$4f$ electrons and the conduction electrons and is proportional to the electronic density of states at the Fermi level, $N(E_F)$ [73]. Least-squares (LQS) fits of $\rho(T)$ data above 40 K for all compositions to Eq 7.1 (solid curves in Fig 7.3) yield values of $\rho(T)$ parameters gathered in Table 7.1. It is observed that C_K values decrease with increasing La content x which indicate

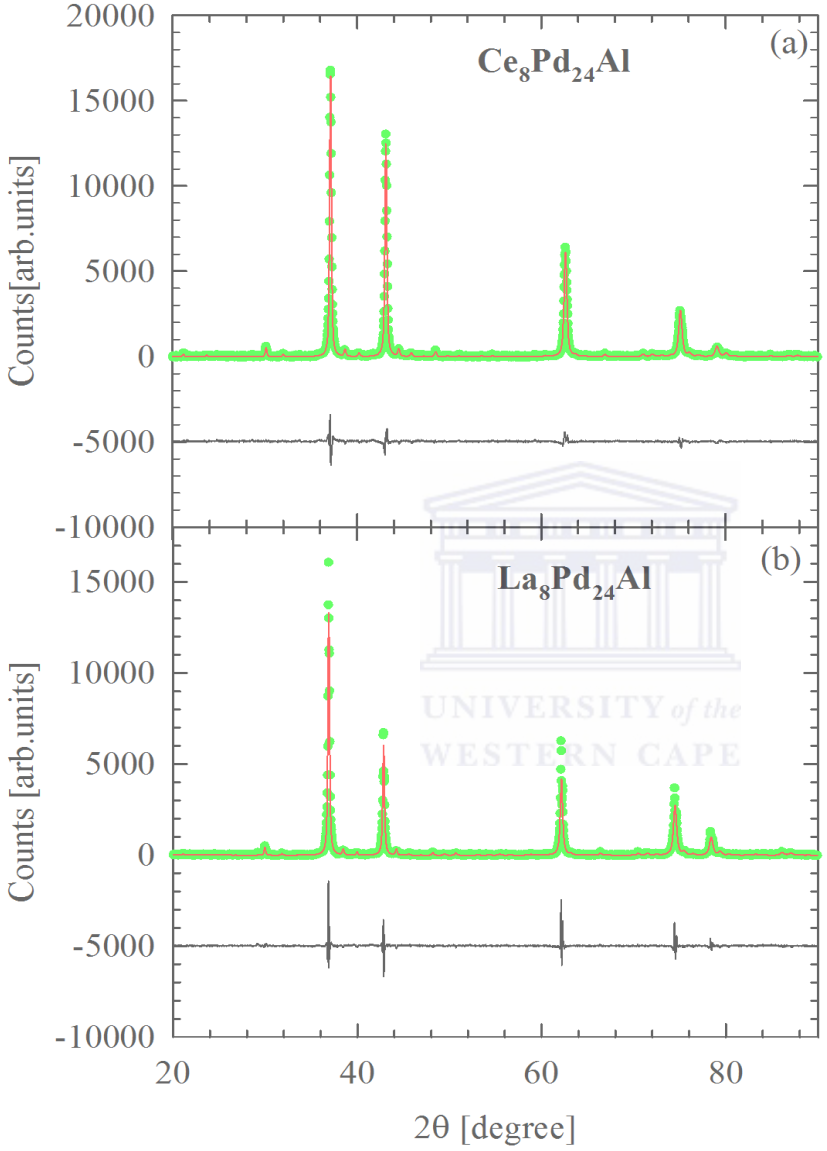

Figure 7.1: CAILS-Pawley (cell and intensity least squares) analyzed diffraction patterns for $Ce_8Pd_{24}Al$ and $La_8Pd_{24}Al$ alloys. The observed data are shown by green symbols and the solid black lines through the data represent the results of the CAILS-Pawley refinement. The lower red curves are the difference curves for the experimental data and the calculated curve.

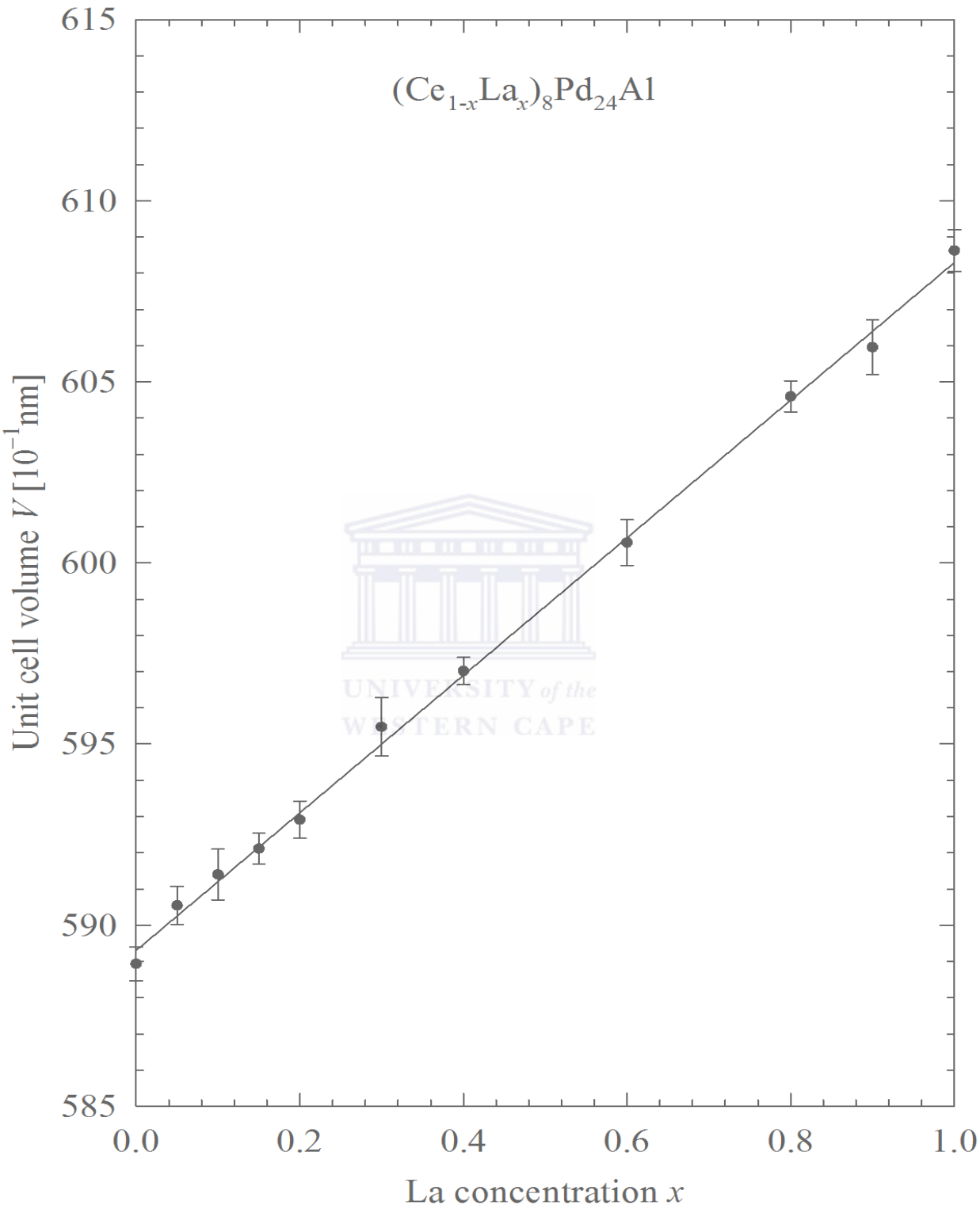

Figure 7.2: Unit cell volume V for the $(Ce_{1-x}\ la_x)_8Pd_{24}Al$ alloys as a function of La concentration x.

Table 7.1: $\rho(T)$ parameters resulting from the LSQ of Eq 7.1 to experimental data of the alloys series $(Ce_{1-x}La_x)_8Pd_{24}Al$.

x	ρ_0 [$\mu\Omega$.cm]	$b[10^{-8}$ Ω.cm/K]	$C_K[\mu\Omega$.cm]	T_{max}[K]
0	232(8)	210(8)	30.8(2)	9
0.1	175.9(6)	0.0378(3)	20.6(2)	7.5
0.2	161.7(4)	0.0293(2)	19.2(1)	6.5
0.3	115.8(4)	0.0184(5)	11.6(3)	5.1
0.8	58.1(1)	0.0443(3)	6.1(2)	
0.9	48.7(2)	0.0552(4)	5.7(1)	

a decrease in $N(E_F)$ and hence a suppression of Kondo effect. It is observed from Table 7.1 that ρ_0 decreases with increasing La content x. Such behaviour is in contrast with the behaviour of ρ_0 observed in $(Ce_{1-x}La_x)Cu_6$ [249], since increasing La content leads to an increased disorder only up to $x = 0.5$ according to the Nordheim's rule of residual resistivity of binary compounds. This deviation from the increase in ρ_0 with increase La content may originate from other factors we could not explain with the present data. Since the values of the atomic mass of Ce and La are nearly the same, the lattice vibrational spectra of these alloys and hence the Debye resistivity temperature (θ_R) are expected to be similar. It is noted from Table 7.1 that, the constant b values follow an irregular variation with increasing La content in contrast to the expected similar value. This deviation may originate from the difference in the electron-phonon interaction at high temperatures. Fig 7.4 represents the magnetic resistivity $\rho_{4f}(T)$ for the $(Ce_{1-x}La_x)_8Pd_{24}Al$ system. Due to the resistivity of the non-magnetic compound $La_8Pd_{24}Al$ was not measured along with the other compounds in this series, $\rho_{4f}(T)$ was calculated from the parameters that were obtained in Table 7.1 using the equation:

$$\rho_{4f}(T) = \rho(T) - bT - C_K ln(T). \tag{7.2}$$

It is observed at low temperature that $\rho_{4f}(T)$ shows a maximum only for alloys with $x \leqslant 0.3$, which illustrates the coherence of electrons scattering from the Kondo ions thus

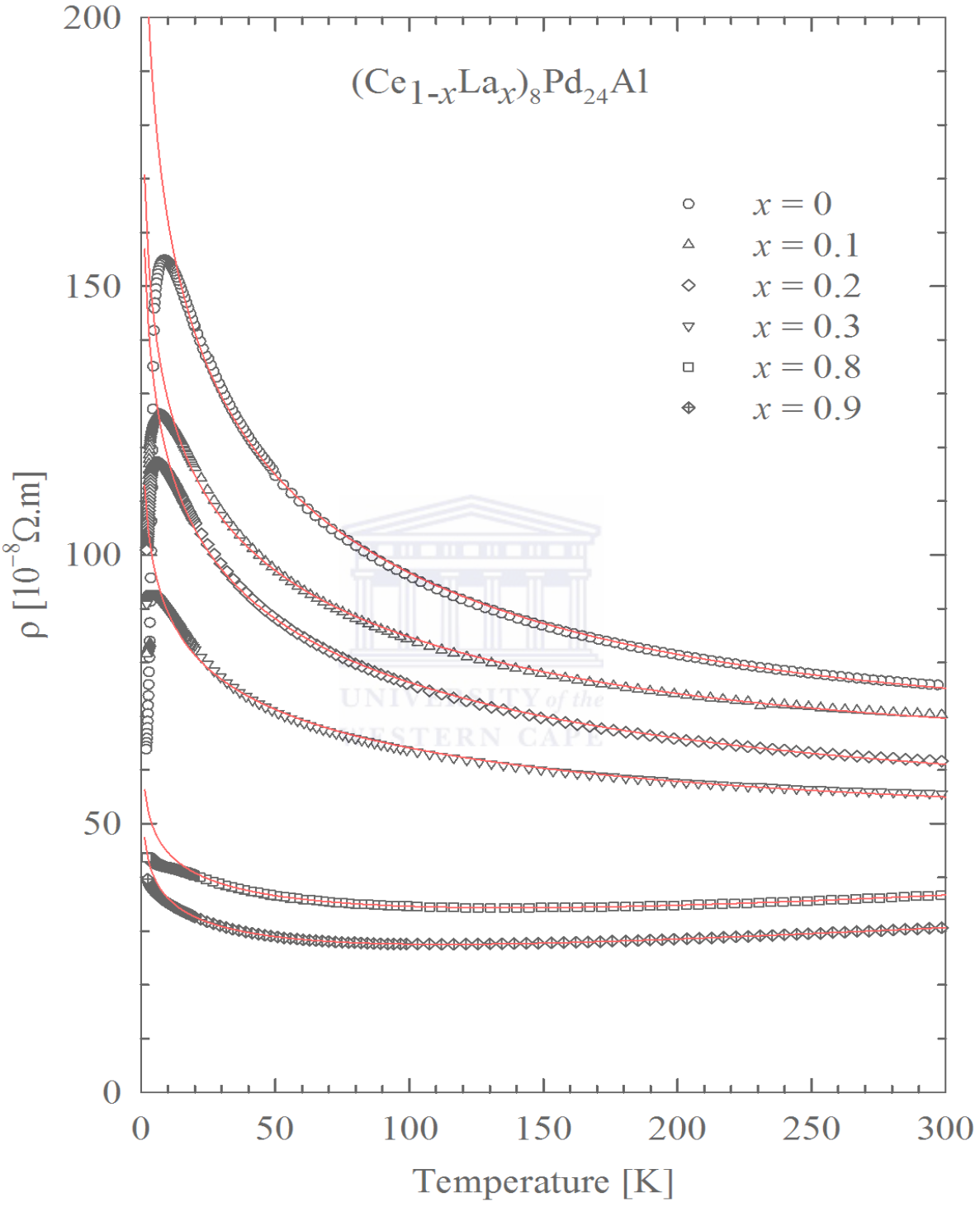

Figure 7.3: $\rho(T)$ data of the $(Ce_{1-x}\ la_x)_8Pd_{24}Al$ alloys with $0 \leqslant x \leqslant 0.9$. The solid red lines are LSQ fits of the measured data to Eq 7.1.

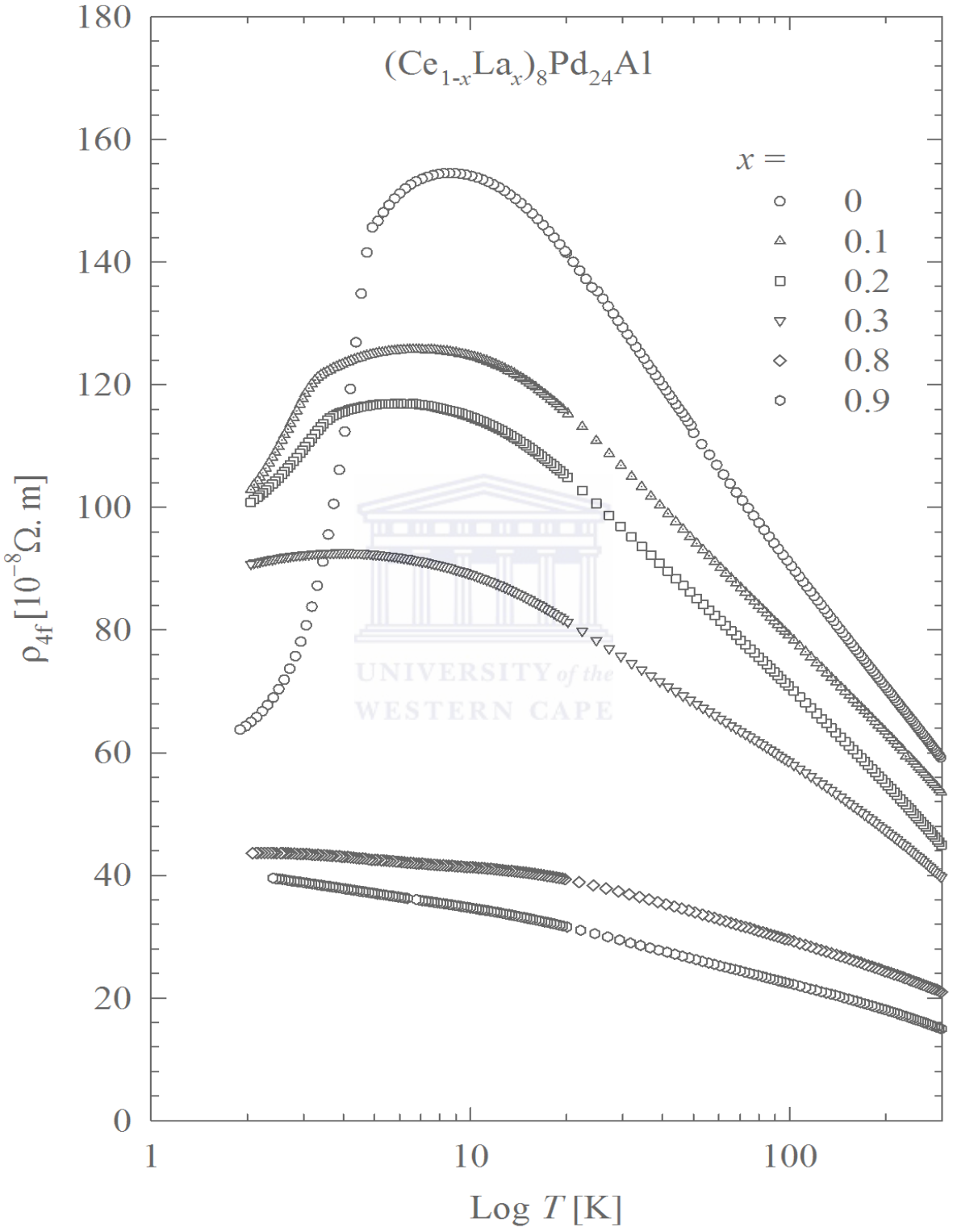

Figure 7.4: Magnetic resistivity $\rho_{4f}(T)$ of the $(Ce_{1-x}\ la_x)_8Pd_{24}Al$ alloys series.

leading to the formation of a Kondo lattice. A similar behaviour has been observed in $(Ce_{1-x}La_x)Cu_6$ [249] and $(Ce_{1-x}La_x)B_6$ [219]. For alloys with $x \geqslant 0.3$, ρ_{4f} tends to saturation as $T \rightarrow 0$.

7.2.2.2 Magnetoresistivity MR

MR measurements were performed for dilute Ce alloys for which $\rho(T)$ exhibits incoherent single-ion Kondo scattering $-lnT$ across the range of MR fitting ($x = 0.4$, 0.6 and 0.8). For all three compositions negative MR has been observed at all temperatures up to 20 K as a result of suppression of the incoherent Kondo scattering in a magnetic field as shown in Fig 7.5 for two representative compositions x= 0.4 and 0.6. The analysis of the MR results proceeded in terms of the Bethe-ansatz calculation of the Coqblin-Schrieffer model given by Andrei [25] and Schlottmann [27] for various values of the total angular momentum J of the Kondo impurity between $\frac{1}{2}$ and $\frac{5}{2}$:

$$\frac{\rho(B,T)}{\rho(B=0,T)} = \Big[\frac{1}{2J+1} sin^2(\frac{\pi n_f}{2J+1}) \sum_{l=0}^{2J} sin^{-2}(\pi n_l)\Big]^{-1}, \tag{7.3}$$

where n_f is the f-electron occupation number. An exact solution was obtained for the spin$\frac{1}{2}$ case notwithstanding that the Ce^{3+}-ion has $J = \frac{5}{2}$, since the CEF for cubic symmetry split the $J = \frac{5}{2}$ into a ground-doublet with an effective $J = \frac{1}{2}$ spin impurity at low temperatures and an excited quartet at high temperatures. This result corroborates the results of the thermoelectric power analysis (see section 7.2.2.4) where the dominant energy scale is the CEF leading to the quenching of the $4f$ hybridization which gives itinerant $4f$ character at low temperatures, which also produces heavy fermion state for which Ce behaves as spin$\frac{1}{2}$ as it does in many heavy fermion systems. LSQ fits of the Bethe-*ansatz* theory of MR (Eq 7.3) to the experimental isothermal MR data (solid curves main panel of Fig 7.5) yields values of the characteristic B^* related to T_K according to the relation [83]:

$$B^* = B^*(0) + \frac{k_B T}{g\mu_K} = \frac{k_B(T_K^{MR} + T)}{g\mu_K}, \tag{7.4}$$

where k_B is the Boltzmann constant, g_J is the Landé factor and μ_K is the effective magnetic moment of the Kondo ion. LSQ fits of B^* values obtained at the isotherms in Fig 7.3 to 7.4 are shown by solid lines in the insets of Fig 7.5. The resulting values of T_K and μ_K are gathered in Table 7.2. Similar to C_K, it is observed that T_K values decrease

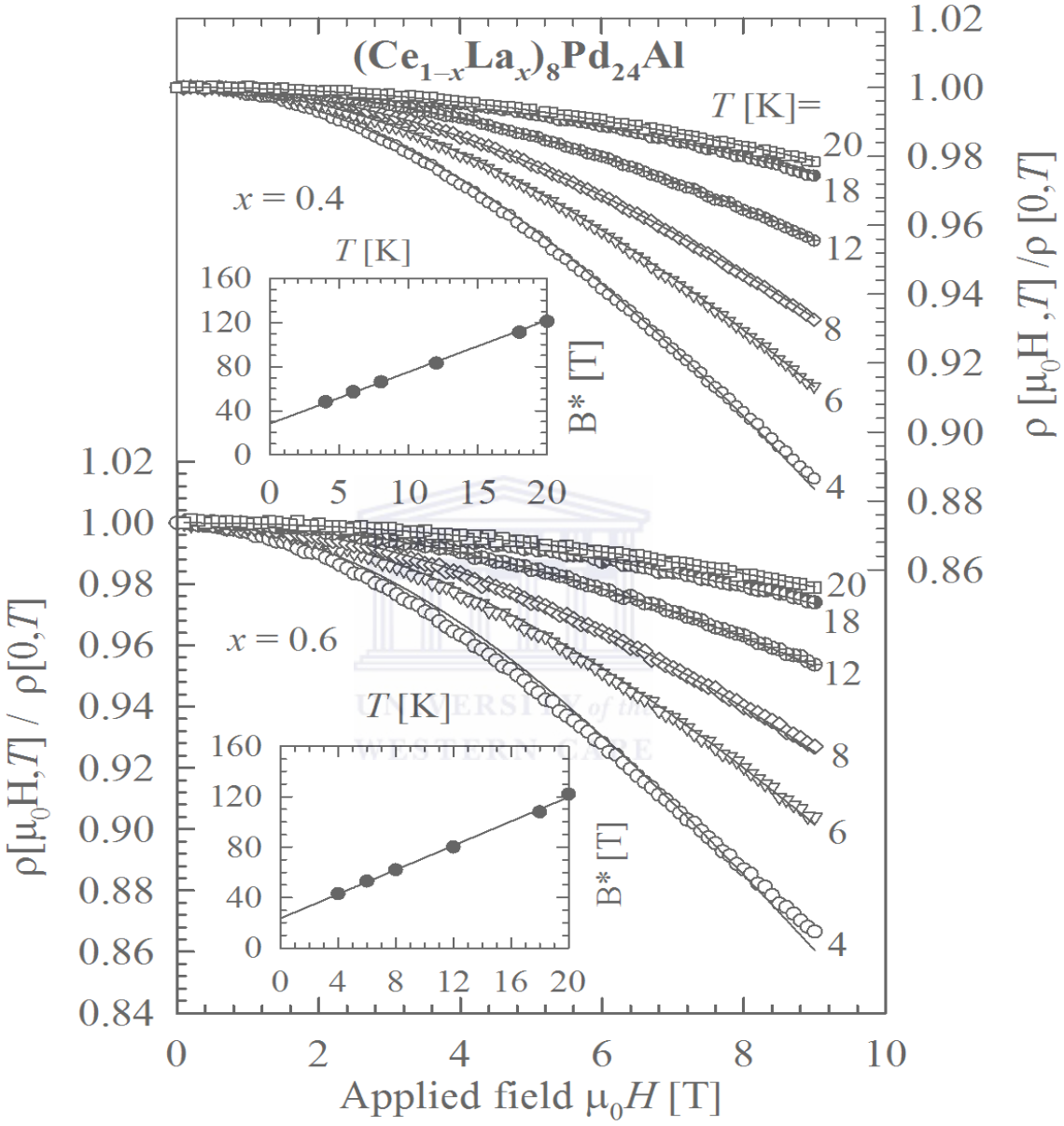

Figure 7.5: Magnetic field variation of $\rho(T)$ at a number of sample temperature for the alloys $(Ce_{1-x}\ la_x)_8Pd_{24}Al$ with $x = 0.4$ and 0.6. The solid red lines are LSQ fits of the Bethe-*ansatz* theory of MR, Eq 7.3, to the measured data. The inset shows the temperature variation of the characteristic field $B^*(T)$ and the solid line through the data points is a LSQ fit of Eq 7.4 to the B^* values.

with increasing La content x. This results from the increase in unit-cell volume which in turn weakens the on-site Kondo exchange interaction according to the compressible Kondo lattice model [210]. Fig 7.6 illustrates the excellent scaling of the Schlottmann models for $J = \frac{1}{2}$. The MR data at various temperatures have been scaled to the theoretical curve by adjusting the temperature dependence of $B^*(T)$ at each temperature. The scaling behaviour is excellent in the temperature range $4 \leqslant T \leqslant 20$ K for the three compositions.

Table 7.2: MR parameters resulting from the LSQ fits of Eqs 7.3 and 7.4 (Fig 7.5) of the alloy series $(Ce_{1-x}La_x)_8Pd_{24}Al$ with x= 0.4, 0.6 and 0.8.

x	T_K[K]	$\mu_K[\mu_B]$
0.4	5.6(6)	0.159(5)
0.6	4.3(4)	0.154(3)
0.8	3.1(2)	0.114(7)

7.2.2.3 The volume dependence of T_K

The variation of T_K with La concentration, $T_K(x)$ is often described in terms of the compressible Kondo lattice model [210] where

$$T_x(x) = T_x(0)exp\left[\frac{-q(V - V_{0)}}{V_0|JN(E_F)|_0}\right]. \tag{7.5}$$

V(x) and V_0 are the volumes of the unit cell for the La-doped alloy and the $Ce_8Pd_{24}Al$ parent compound respectively. γ is the on-site Kondo interaction, $N(E_F)$ is the electronic density of states at the Fermi level and q is a constant taking values between 6 and 8 [210]. Our results were interpreted in terms of the compressible Kondo lattice model (Eq 7.5) by assuming that for the dense Kondo systems, T_{max} the temperatures of $\rho(T)$ maxima are a fair indication of the Kondo temperature T_K. A similar decrease in T_{max} and T_K with increase in La content x or the relative change in unit cell volume is observed (see Fig 7.7). It should be noted that, the decrease of T_{max} and T_K with increasing La content x may also be due partly to spin dynamics, owing to intersite exchange interaction usually observed in magnetic Kondo systems [250, 251]. A plot of T_{max} and T_K values against $(V(x) - V_0/V_0)$ as obtained from our XRD measurements is depicted in Fig 7.7. Both data sets show a smooth decrease with volume increase. LSQ fit of Eq 7.5 to the combined

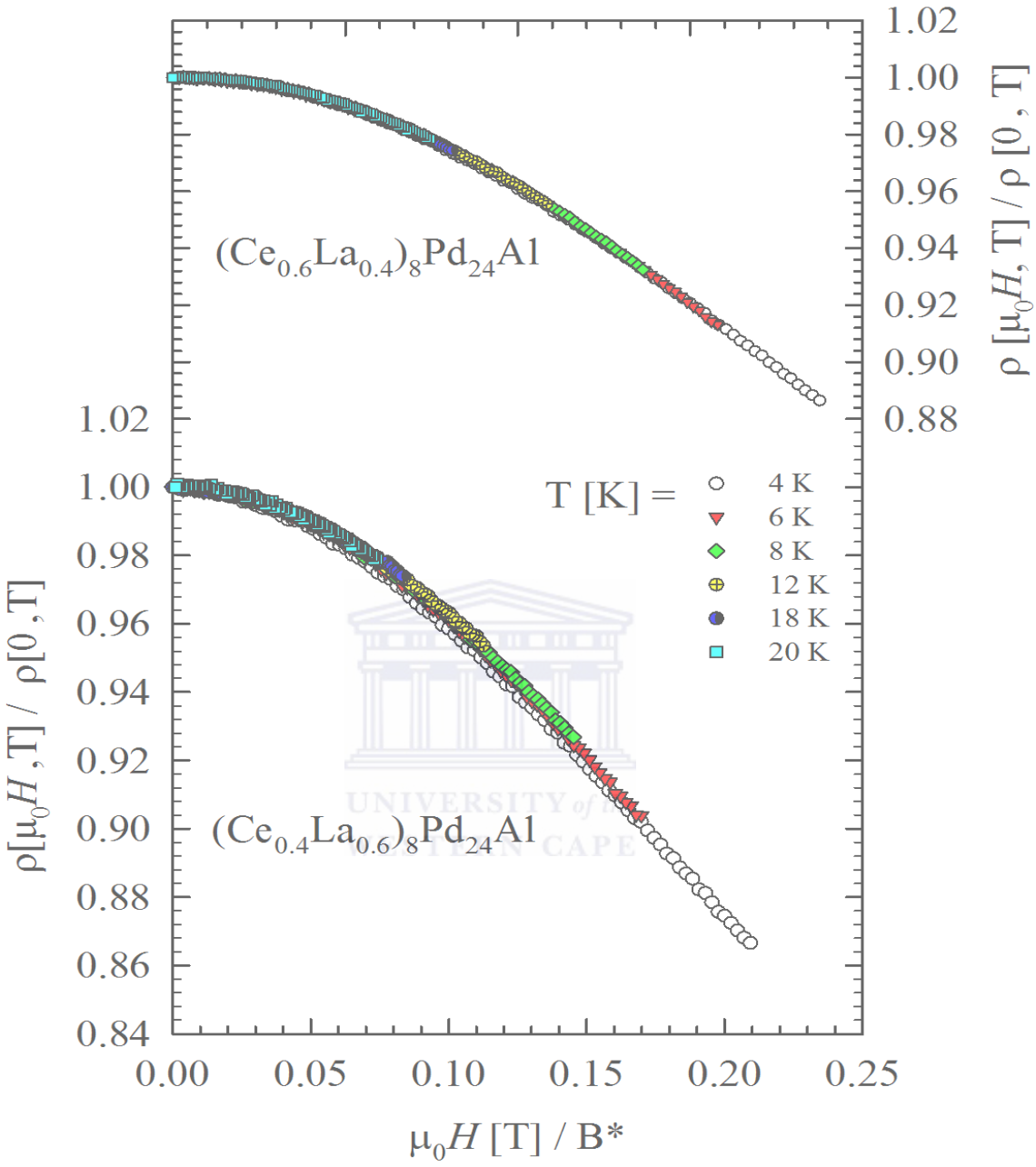

Figure 7.6: Magnetoresistivity data for different isotherms of the $(Ce_{1-x}\ la_x)_8Pd_{24}Al$ alloys with x = 0.4 and 0.6 as measured in field up to 9 T and at various temperatures between 4 and 20 K are shown to scale well with the Bethe-*ansatz* formulation of the single-ion Kondo magnetoresistivity.

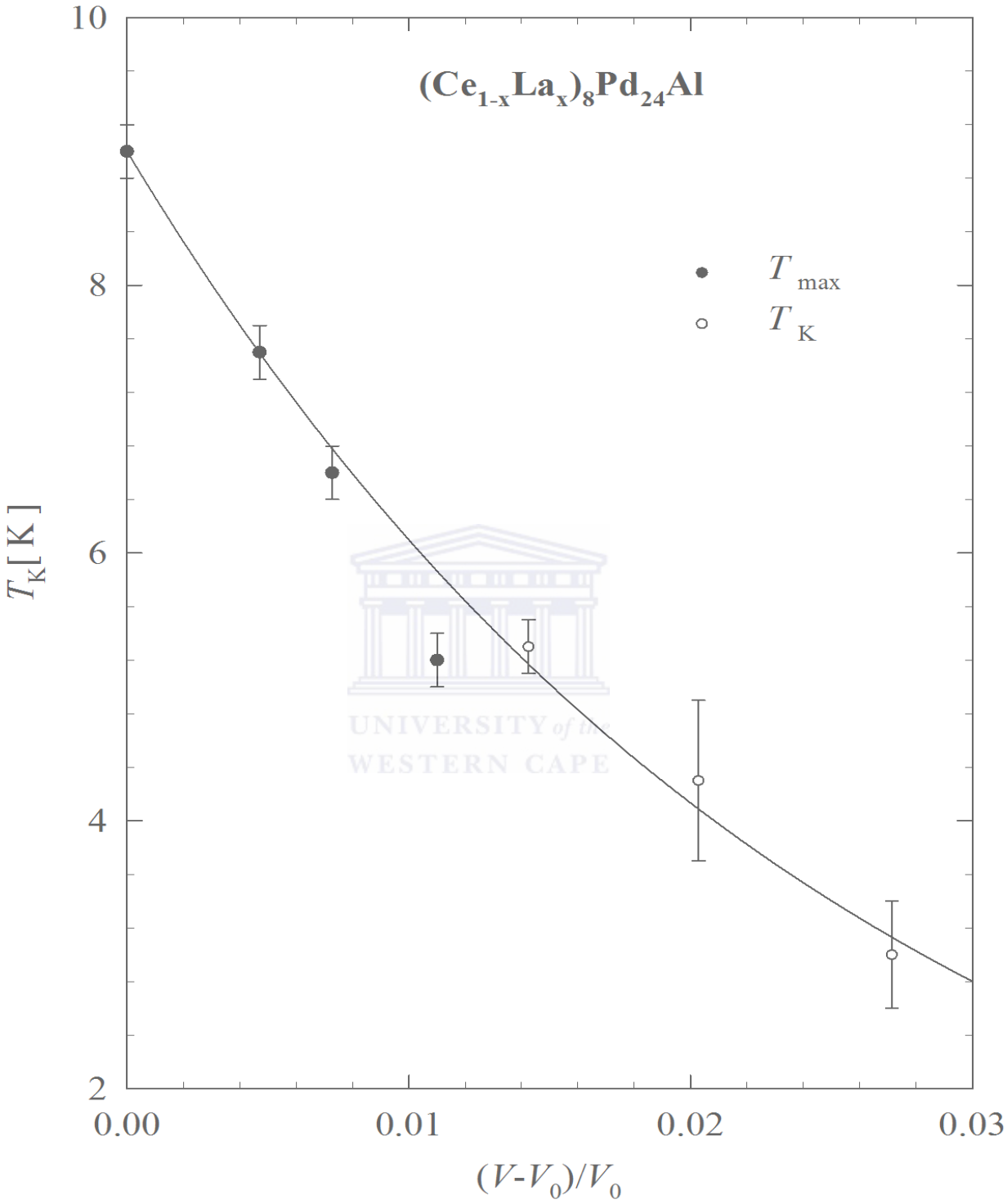

Figure 7.7: A plot of T_{max} (closed symbols) and T_K (opened symbols) values obtained from the resistivity and magnetoresistivity respectively as a function of the relative change in unit cell volume $(V - V_0)/V_0$ as obtained from our X-ray diffraction measurements. The solid curve is an LSQ fit of Eq 7.5 to the T_{max} and T_K values.

data sets gives the solid line through the data points in Fig 7.7). Using the constant q = 6, the analysis gives $|\Gamma.N(E_F)|_0 = 0.077(2)$ for $Ce_8Pd_{24}Al$ which may be compared to the values obtained for many Kondo and heavy-fermion systems such as 0.053 and 0.09 obtained for $CeCu_5In$ [212] and $CeCu_6$ [213] respectively.

7.2.2.4 Thermoelectric power

The thermoelectric power (TEP) versus temperature, $S(T)$, measurements on selected compositions are shown in Fig 7.8. Except for the parent compound $Ce_8Pd_{24}Al$, $S(T)$ data show a crossover from positive to negative values over the whole measured temperature range. The overall behaviour of $S(T)$ data is similar for all measured compositions, showing a pronounced minimum at low temperature. This pronounced minimum and a cross-over to positive $S(T)$ values is typical for magnetically ordered Kondo compounds [137]. The high temperatures $S(T)$ data is dominated by a broad maximum which may be due to the competition between crystal electric field (CEF) and Kondo effect and possibly due to phonon drag effect and / or the inelastic scattering of charge carriers by acoustic phonons also observed in many Ce compounds [88, 133]. However, $S(T)$ data of the measured compositions were analysed using phenomenological resonance model [89]. In this model, the dominant contribution to the thermoelectric power is caused by the scattering of electrons from the wide s-band into a narrow f-band approximated by the Lorentzian shape. According to this model, $S(T)$ can be expressed by:

$$S(T) = \frac{2}{3}\pi^2 \frac{k_B}{|e|} \frac{T.E_f}{(\pi^2/3)T^2 + E_f^2 + W_f^2} \tag{7.6}$$

where E_f and W_f taken in units of Kelvin, are the position of the f-band peak relative to the Fermi level E_F and its width, respectively. It was observed that, Eq 7.6 satisfactorily described $S(T)$ data of a large number of Ce based intermediate valence compounds characterized by large values of T_K. Similar to the heavy fermion-compounds $CeCu_4In$ and $CeCu_4Ga$ [203, 204], $Ce_8Pd_{24}Al$ is a moderate heavy fermion compound with low T_K value, therefore Eq 7.6 describes the scattering of conduction electrons on an ensemble of incoherent impurities than on a narrow f-band [88]. Accordingly, in our case W_f in Eq 7.6 can be related mainly to temperature of CEF (T_{CEF}) according to the assumption given in Ref [88], (*i.e* $W_f = \frac{\pi T_{CEF}}{N_f}$, where $N_f = 2J + 1$ is the orbital degeneracy with J being the angular momentum quantum number). In order to obtain a good fit for our $S(T)$ data, Mott's term ($S_d = \frac{\pi^2 k_B^2 T}{3eE_F}$) is included to Eq 7.6, which accounts for the usual nonmagnetic Mott-type scattering of electrons in a broad $5d - 6s$ conduction band which

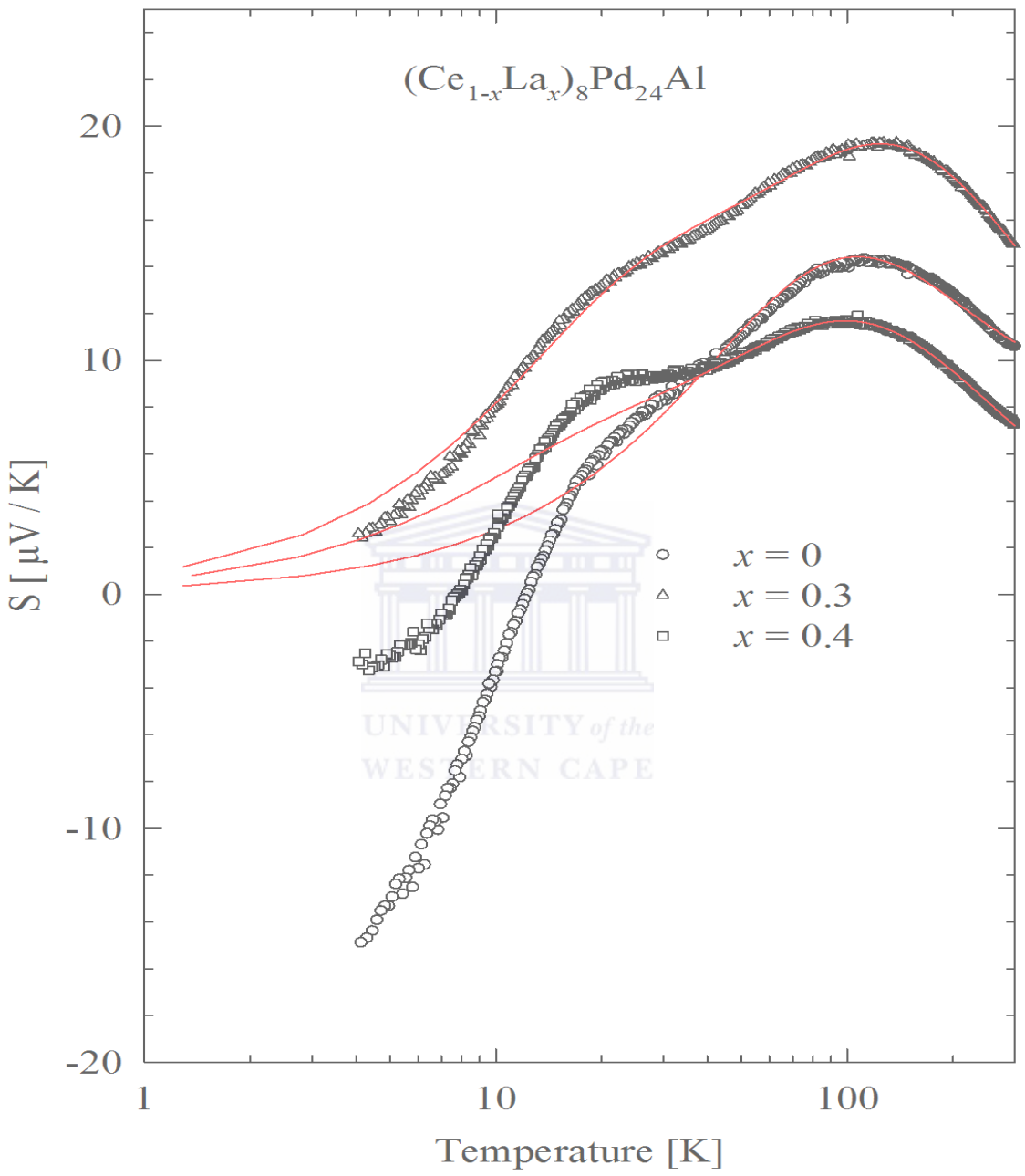

Figure 7.8: The thermoelectric power versus temperature, $S(T)$, data of the $(Ce_{1-x}\,la_x)_8Pd_{24}Al$ alloys with $x = 0$, 0.3 and 0.4. The red solid curves are the fits of $S(T)$ data to the phenomenological resonance model.

Table 7.3: Thermoelectric data of the alloys series(Ce_{1-x} $la_x)_8Pd_{24}Al$ with $x = 0, 0.3$ and 0.4.

x	0	0.1	0.3
E_f[meV]	1.39(2)	2.4(1)	1.038(8)
W_f[meV]	12.4(1)	11.0(1)	13.92(7)
$a[\mu$ V/K$^2]$	21.7(5)	10.2(4)	3.7(2)
E_F [eV]	1.13(3)	2.4(1)	6.6(4)
T_{CEF} [T]	274	333	308

is determined by Fermi energy [252, 253]. LSQ fits of the measured $S(T)$ to Eq 7.6 plus the Mott's term above 50 K for the alloys with x= 0, 0.3 and 0.4 gives $S(T)$ parameters gathered in Table 7.3. The values of T_{CEF} were obtained by using a degeneracy $N_f = 6$ and the values of the Fermi energy were calculated using Mott's term. It has been reported that the temperature dependence of thermoelectric power in the Kondo lattice system arises from two contributions: the Kondo scattering from the ground state which gives rise to a maximum at low temperature around T_K and the incoherent scattering at excited CEF levels which gives rise to a broad high temperature anomaly at $T_{max} \approx (\frac{1}{3} - \frac{1}{6})T_{CEF}$ [215]. The shoulder observed in $S(T)$ data at low temperatures presumably may originates from the Kondo scattering scattering at the ground state while the broad maximum at high temperature originate from incoherent scattering at the excited CEF levels with $T_{max} \approx \frac{1}{3}T_{CEF}$. The obtained Fermi energy values are typical of a normal metal. Our values of W_f are three times larger in magnitude compared to the values obtained for many Ce compounds such as $CeCu_4Al$ [208]. CeT_4M (T=Cu, Ni; M=In, Ga) [88], $CeNi_4Cr$ [136]. $Ce_{1-x}La_xCu_4Al$ [134]. Similar to other Ce-based compounds [88, 133, 136], the positive values of E_f obtained for our alloys system indicate that the density of state peaks are just below the Fermi energy.

7.2.2.5 Thermal conductivity

The temperature dependencies of the thermal conductivity $\lambda(T)$ on selected alloys in $Ce_{1-x}La_xPd_{24}Al$ system with $x = 0$, 0.3 and 0.4 are shown in Fig 7.9. It is seen that $\lambda(T)$ data for the three compositions decrease almost linearly upon cooling the samples. Furthermore, the slope of the linear decrease in $\lambda(T)$ decreases with an increase in La

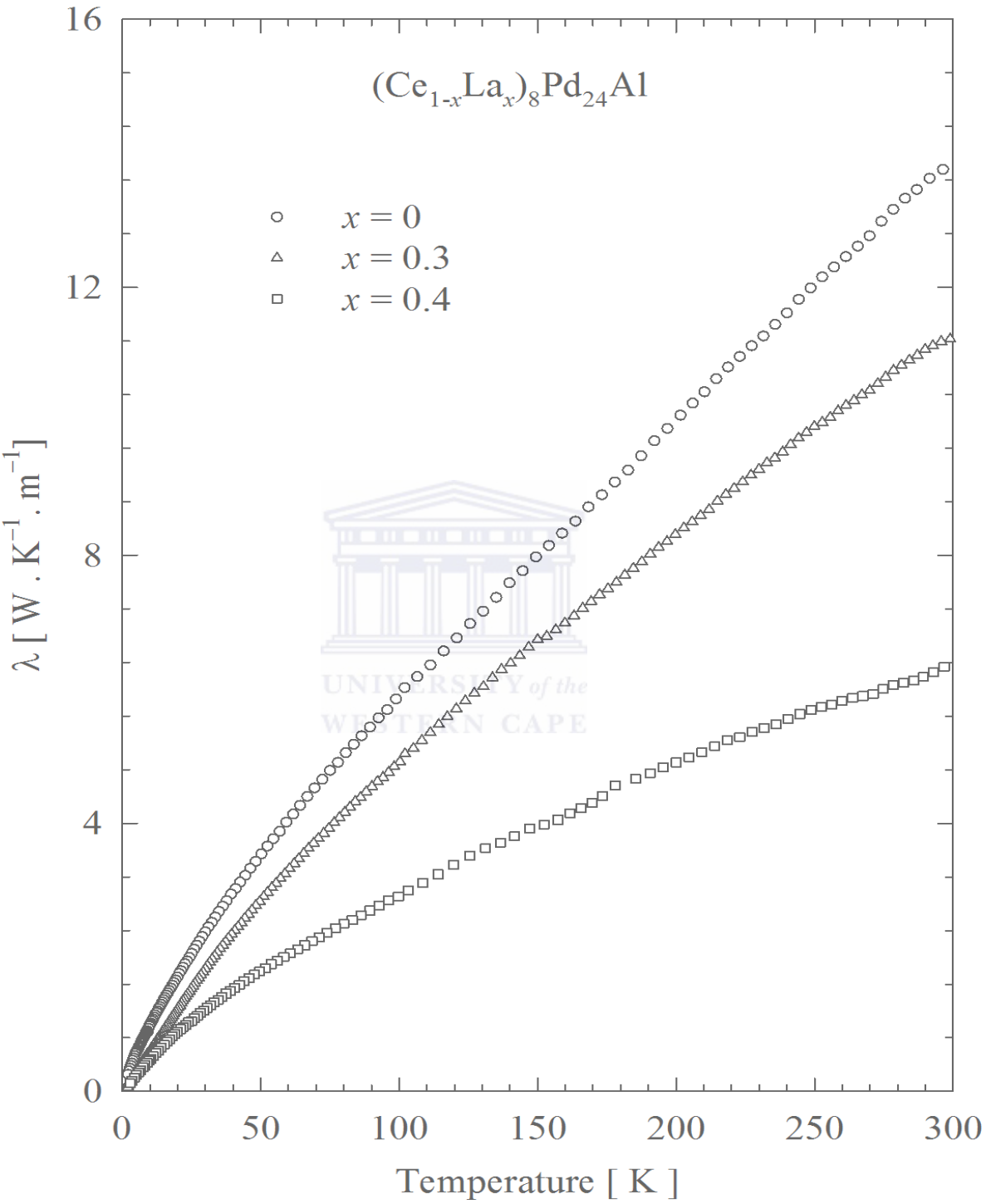

Figure 7.9: Temperature dependence of the total thermal conductivity, λ(T), for $(Ce_{1-x}la_x)_8Pd_{24}Al$ alloys with $x = 0$, 0.3 and 0.4.

concentration x. It should be noted that the linear decrease of $\lambda(T)$ from room temperature down to 2 K is in contradiction with Wilson's law which predicts a constant value of $\lambda(T)$, typical for scattering electrons on thermally excited phonons [137]. Fig 7.10 shows the temperature dependencies of $\lambda(T)$ of two alloy compositions $x = 0$ and 0.4, together with the separated phonon ($\lambda_{ph}(T)$) and electronic contribution ($\lambda_e(T)$). The phonon contribution is obtained by subtracting the electronic contribution from the total $\lambda(T)$ and assuming that the two terms are independent of one another and that there are no other carriers of heat (such as magnons). We further assume that $\lambda_e(T)$ the electronic contribution is connected with resistivity through the Wiedemann-Franz Law: $\lambda_e = L_0T/\rho_0$ where $L_0 = 2.45 \times^{-8}$ W.Ω.K^{-2} is the Lorentz number. It is observed that $\lambda_{ph}(T)$ for both alloys predominates λ_e over a wide range of temperatures (2 K $\leqslant$ T $\leqslant$ 150 K).

7.2.2.6 Lorentz number and Figure of Merit

The Lorentz number, L/L_0 scaled to unity at room temperature is shown in Fig 7.11 for x= 0 and 0.3 alloys. L/L_0 increases gradually below 300 K and reaches a peak around 6 K followed by a sudden drop below 6 K. The growth of L/L_0 on cooling the samples confirms the predominance of the phonon contribution ($\lambda_e(T)$) to the total thermal conductivity λ_{tot} as shown in Fig 7.10. Similar behaviour was observed in many other compounds [88, 134, 136]. Furthermore, the slope of the linear decrease in $\lambda(T)$ as well as the magnitudes of L/L_0 maximum decrease with increasing La content x. According to the Wiedemann-Franz Law L/L_0 should aim at unity in the whole temperature range if the lattice vibration can be neglected. Therefore, the decrease observed in L/L_0 maximum in our system indicates the suppression of the lattice vibration with increase in La content x.

For application point of view, it will be useful to compare the values of figure of merit $ZT = \dfrac{S^2T}{\lambda\rho}$ with that conventional thermoelectric material Bi_2 Te_3 and the other heavy-fermion compounds. ZT as well as the thermoelectric power factor ($PF = \dfrac{S^2}{\rho}$) provide information about the efficiency of the thermoelectric materials. It should be noted that to obtain a good thermoelectric material, one has to minimize both the thermal conductivity and the electrical resistivity. Fig 7.12 shows ZT of the parent compound and one selected composition $x = 0.3$. It is observed that ZT value of the parent compound at room temperature (10.7×10^{-3}) is much larger compared to the alloys composition $x = 0.3$ with a value of 4×10^{-3}. Both compounds exhibit a maximum at high temperature at 17 K with peak value of 13.7 for the parent compound at 140 K with a peak value of 8.3 for x = 0.3. A similar behaviour was also observed for other heavy fermion compounds such

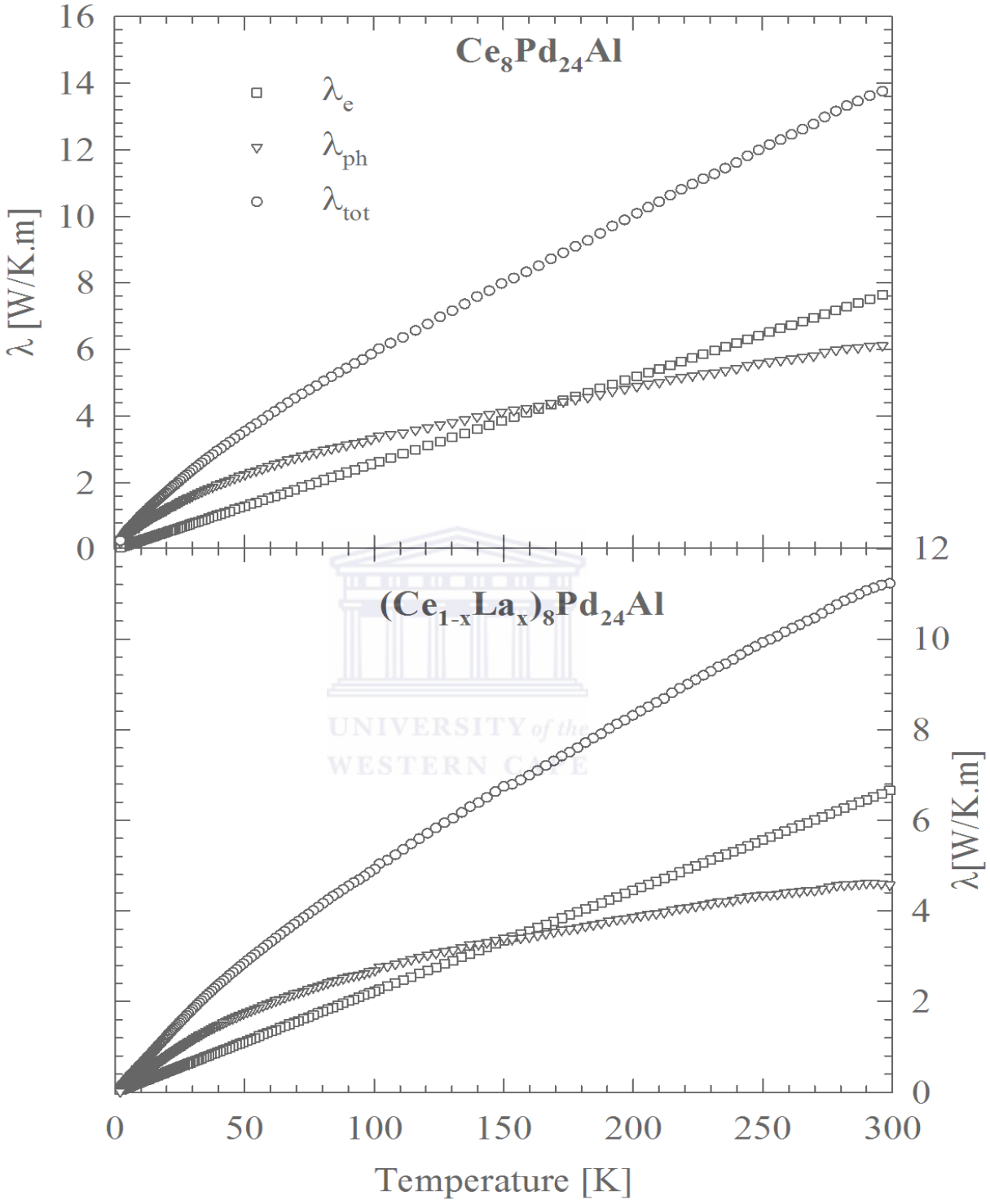

Figure 7.10: Temperature dependence of the total thermal conductivity, $\lambda(T)$, for $(Ce_{1-x}$ $la_x)_8Pd_{24}Al$ alloys with $x = 0$ and 0.4 together with the phonon, $\lambda_{ph}(T)$ and electronic contributions, $\lambda_e(T)$.

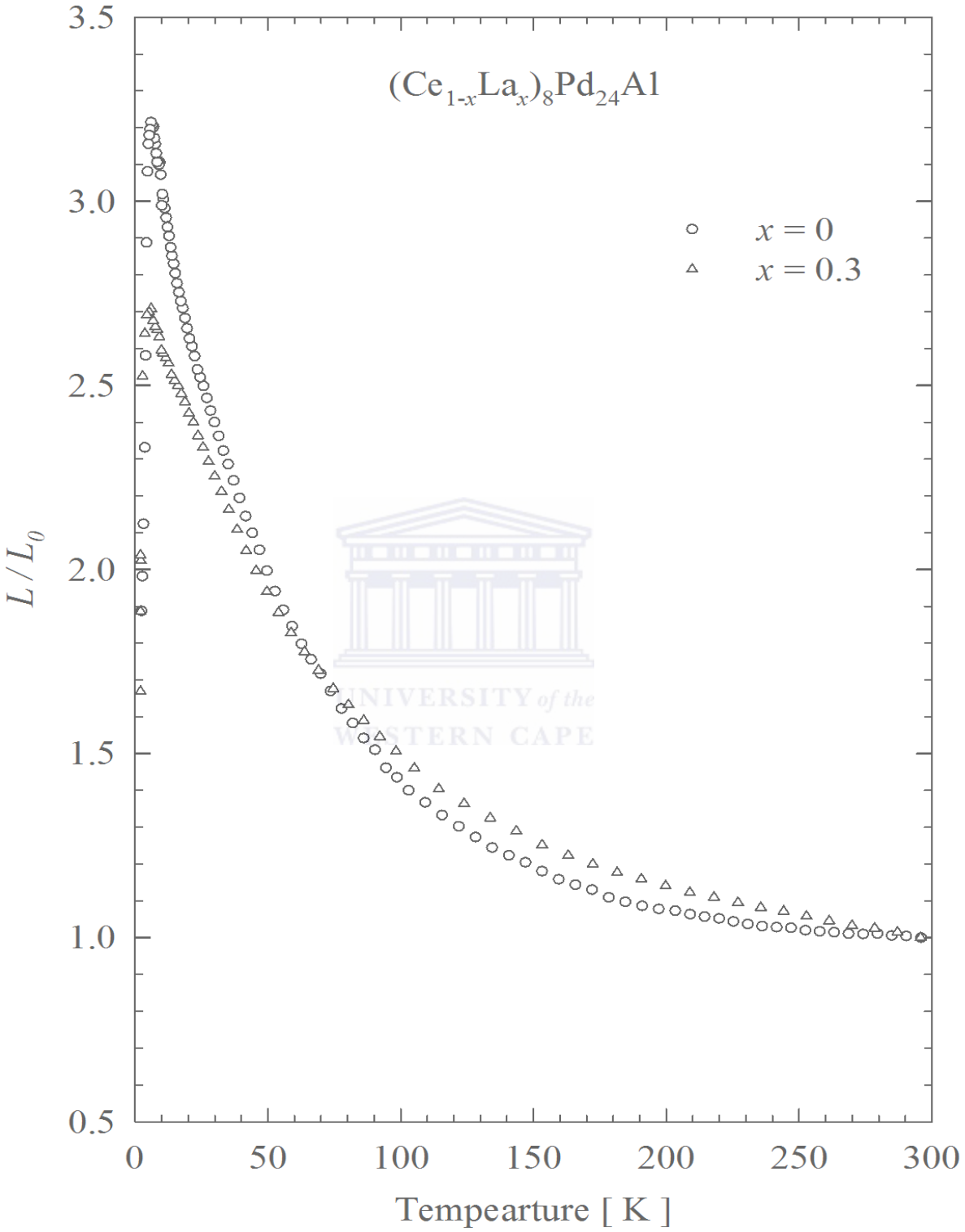

Figure 7.11: Lorentz number, L/L_0 scale to unity, for $(Ce_{1-x}\ la_x)_8Pd_{24}Al$ alloys with $x = 0$ and 0.4.

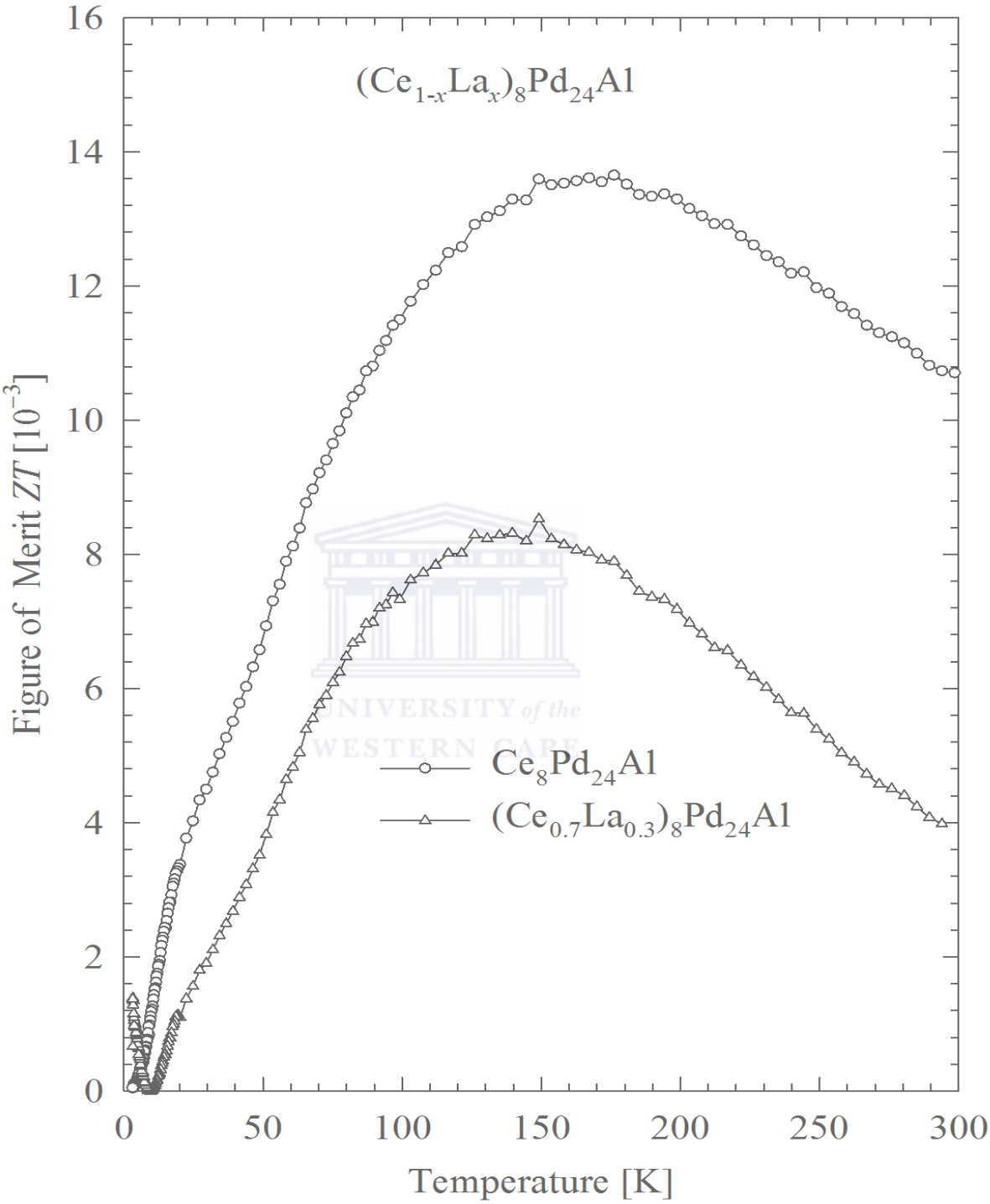

Figure 7.12: Temperature dependencies of the thermoelectric figure of merit (ZT) of the $(Ce_{1-x}la_x)_8Pd_{24}Al$ alloys with $x = 0$ and 0.3.

as $CeCu_4In$ and $CeCu_4Ga$ with a peak at $T_{max} = 50$ K [136]. The thermoelectric power factor reach the maximum values of 4.4μ W/cm.K^2 at $T = 147$ K and 3.3 μ W/cm.K^2 at $T = 140$ K for $x = 0$ and 0.3, respectively. These values of ZT and PF are tiny compared to that of the conventional thermoelectric material Bi_2 Te_3 with the values of $ZT = 1$ and $PF = 40$ μ W/(cm.K^2) at room temperature.

7.2.2.7 Magnetic susceptibility and magnetization

The inverse magnetic susceptibility,$\chi^{-1}(T)$ data are shown in Fig 7.13. It is observed that $\chi^{-1}(T)$ data convey a Curie-Weiss (CW) magnetic behaviour for all compositions above 50 K, giving an effective magnetic moment, μ_{eff} and a paramagnetic Weiss constant θ_P value listed in Table 7.4, when fitted to the CW relation:

$$\chi^{-1} = \frac{3k_B(T - \theta_P)}{N_A \mu_{eff}^2} \tag{7.7}$$

where N_A is the Avogadro's number and k_B is the Boltzmann constant. The obtained μ_{eff} values for all compositions are in close agreement to the value of 2.54 μ_B expected for the free Ce^{3+}-ion. Deviation at low temperature may be attributed to magnetocrystalline anisotropy. Values of θ_P change in irregular manner which may be ascribed to different degrees of preferred crystalline orientation in the different alloy samples. Also they show negative but somewhat smaller values which are consistent with the observed antiferromagnetic interactions. The low temperature $\chi(T)$ data for compositions showing magnetic order are displayed in the Fig 7.14. $\chi(T)$ data show an AFM anomaly associated with T_N listed in Table 7.4. The observed T_N values decrease linearly with increasing La content x (see top inset of Fig 7.14) and extrapolation to $T_N = 0$ give a critical concentration value $x_c = 0.35$. The value of $T_N = 4.3$ K observed for the parent compound $Ce_8Pd_{24}Al$ is slightly smaller from $T_N = 4.7$ K obtained for the same compound in Ref [243].

$M(\mu_0 H)$ for $(Ce_{1-x}La_x)_8Pd_{24}Al$ series measured at 1.8 K in fields up to 5 T is shown Fig 7.15. It is observed that $M(\mu_0 H)$ increases linearly with field up to 5 T for the compositions in the range $0 \leqslant x \leqslant 0.2$ and deviate from linearity with a downward curvature for $x \geq 0.25$. $M(\mu_0 H)$ values at 5 T increase with increasing x across the series and take values ranging between $0.44\mu_B$ and $1.10\mu_B$ for compositions in the concentration range $0 \leqslant x \leqslant 0.9$. This increase of μ_B is probably symptomatic of the more positive θ_P values we observe with increasing La content. The maximum values 1.10 μ_B for $x = 0.9$

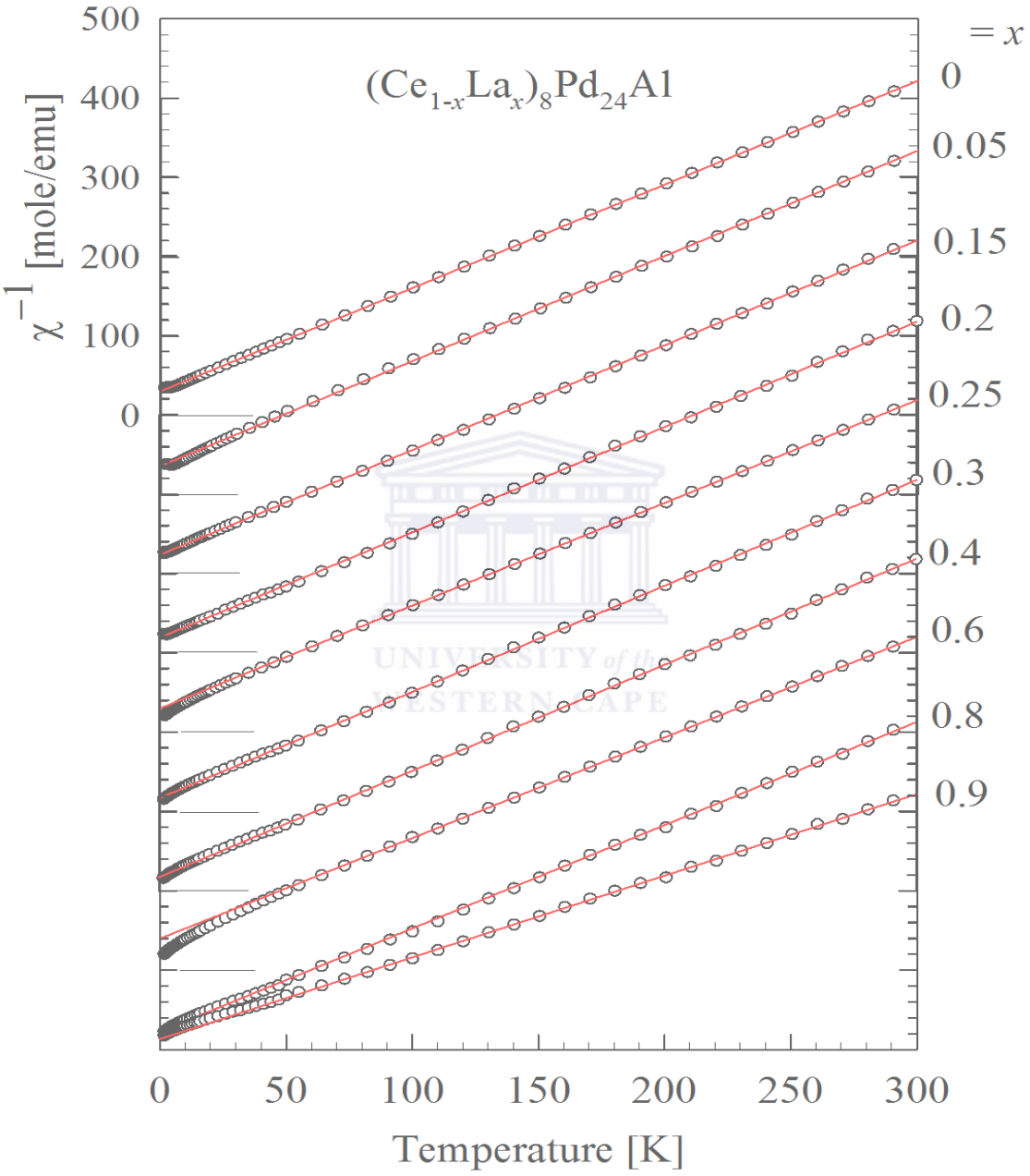

Figure 7.13: $\chi^{-1}(T)$ data of the $(Ce_{1-x}\ la_x)_8Pd_{24}Al$ alloys with the Curie-Weiss fit (red solid lines) according to the experimental data 50 K.

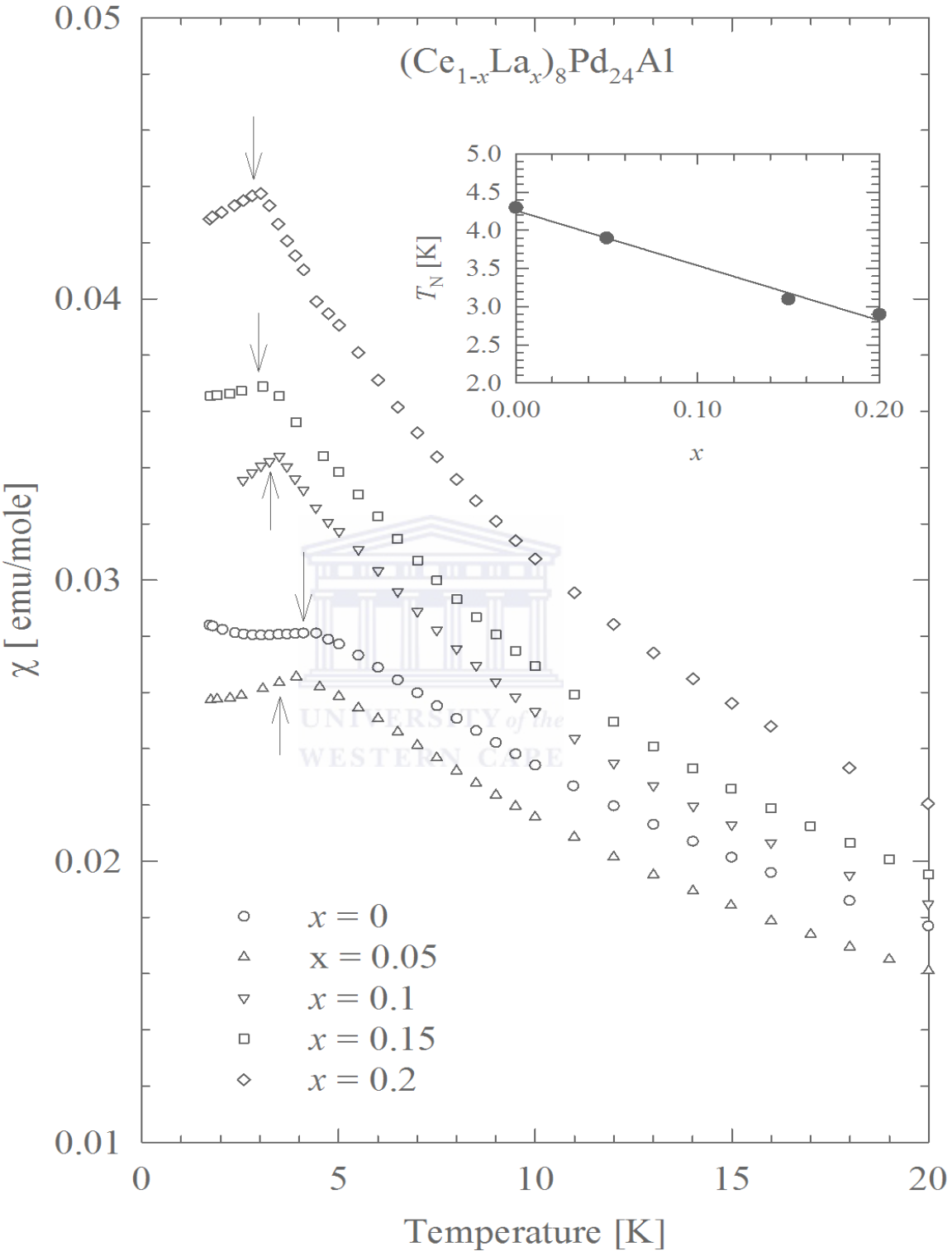

Figure 7.14: Low temperature $\chi(T)$ data of $(Ce_{1-x}\ la_x)_8Pd_{24}Al$ alloys, with the arrows indicating the magnetic phase transition temperature. The top inset shows the variation of T_N as a function of La content x.

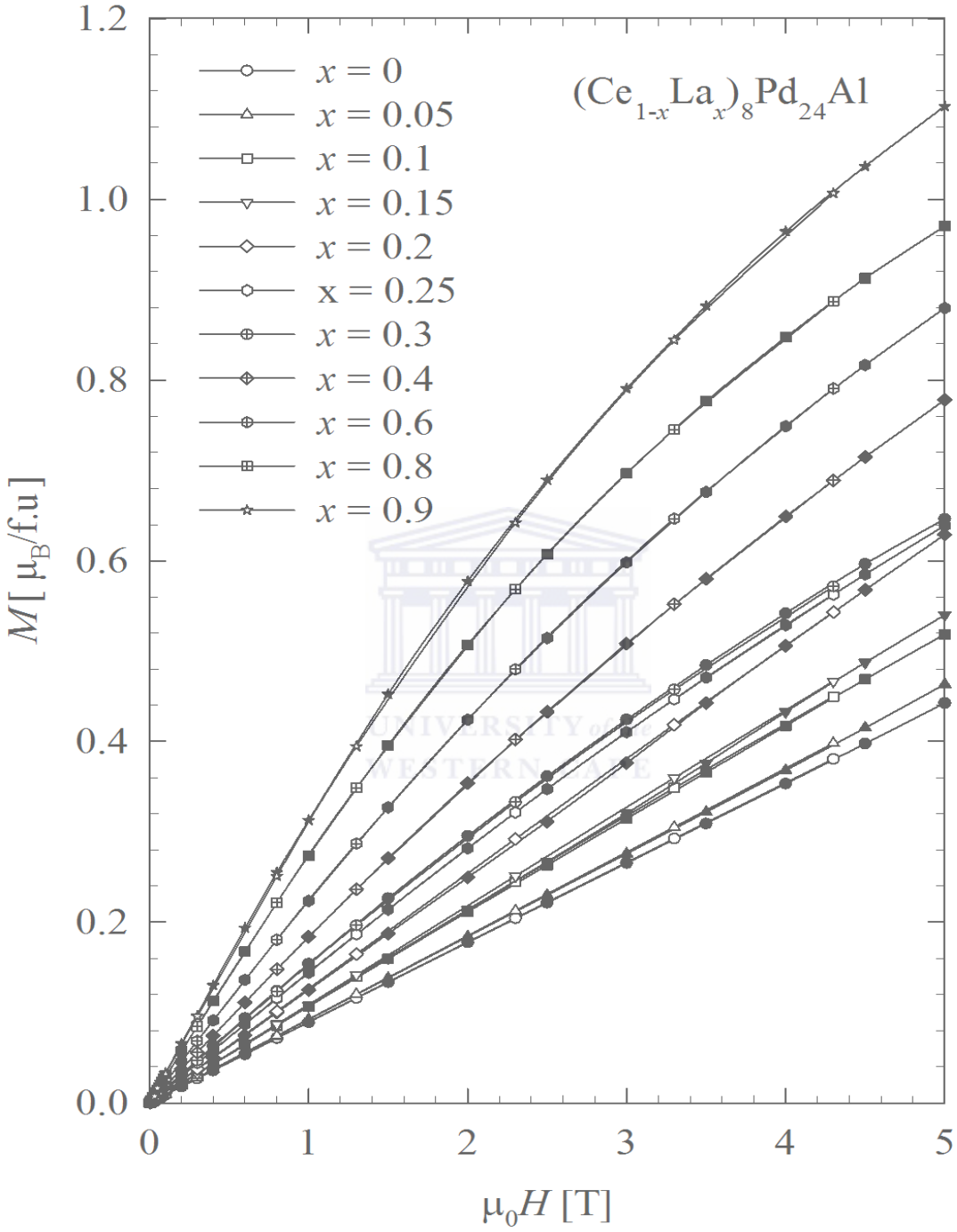

Figure 7.15: $M(\mu_0 H)$ data of the $(Ce_{1-x}\ la_x)_8Pd_{24}Al$ alloys measured in increasing (closed symbols) and decreasing (opened symbols) field.

Table 7.4: Magnetic susceptibility parameters of the alloys series $(Ce_{1-x}\ la_x)_8Pd_{24}Al$.

x	μ_{eff} $[\mu_B]$	$-\theta_P$[K]	T_N [K]
0	2.47(1)	23.5(1)	4.3
0.05	2.52(3)	19.2(4)	3.9
0.1	2.46(5)	20.1(2)	3.5
0.15	2.40(2)	15.3(6)	3.1
0.2	2.45(2)	14.2(4)	2.9
0.25	2.41(5)	16.2(3)	
0.3	2.48(3)	31.1(4)	
0.5	2.51(4)	13.5(2)	
0.7	2.44(2)	12.7(5)	
0.8	2.48(4)	17.4(3)	
0.9	2.43(3)	12.1(4)	

is approximately half the theoretical saturation magnetization of full $g_J J = 2.14\ \mu_B$ free C^{3+} ion moment. This shortfall may be associated with a magnetocrystalline anisotropy for polycrystalline samples. No evidence of hysteresis was observed in all compositions in the process of increasing and decreasing field.

7.2.3 Conclusion

The present study confirms the interplay of AFM and Kondo effect in $(Ce_{1-x}La_x)_8Pd_{24}Al$. The AFM state is observed from the low temperature $\chi(T)$ for Ce rich alloys while the Kondo effect and dynamics are observed for all compositions. $\rho(T)$ evolves from coherent to incoherent single-ion Kondo scattering. Results of MR measurements on selected $(Ce_{1-x}La_x)_8Pd_{24}Al$ alloys conform with the Bethe-ansatz description of single-ion formulation and are used to obtain $T_K(x)$ values. The variations of $T_{max}(x)$ and $T_K(x)$ are interpreted in terms of the compressible Kondo lattice model. In diluted alloys, $S(T)$ data show a crossover from positive to negative values. $S(T)$ data at high temperatures

are well described in terms of the phenomenological resonance model in the high temperature region to give the values T_{CEF} , E_f, and the Mott's constant a which was used to obtain E_F. $\lambda(T)$ deviates from Wilson's law, which predicts a saturation of $\lambda(T)$ at 300 K. L/L_0 increases gradually below 300 K and reaches a peak at around 6 K. $\chi(T)$ data at high temperatures (50 to 300 K) give effective magnetic moments in fair agreement with the Ce^{3+} value. The low temperature $\chi(T)$ data indicate AFM-like anomalies associated with T_N while $M(\mu_0 H)$ show no evidence of metamagnetic behaviour.

7.3 Ligand substitution on $Ce_8Pd_{24}Al$

In the present work, the study of Kondo and crystal-eletcric field effects and magnetic behaviour in $Ce_8Pd_{24}Al_{1-x}Sn_x$ is reported, by substitution of Al with Sn up to 100%. This study was done by means of XRD, electrical resistivity, thermoelectric power, thermal conductivity, magnetic susceptibility and magnetization measurements.

7.4 Experimental details

Polycrystalline samples of the alloy series $Ce_8Pd_{24}Al_{1-x}Sn_x$ were prepared as indicated in chapter 3. Metals of the following purity in wt% were used: Ce, 99.98%; Pd, 99.97%; Al and Sn, 99.9999%. The buttons were turned over and remelted several times to ensure good homogeneity of the samples. Weight losses after melting were always less than 1%. The quality of the samples were checked by X-ray powder diffraction (XRD) at room temperature using a Bruker D8 Advance powder diffractometer with a CuK_α radiation (λ = 1.540598 Å). The diffraction patterns were analyzed using the cell and intensity least square (CAILS)-Pawley method from TOPAS ACADEMIC programme. All the samples investigated were single-phase materials. No evidence of parasitic phase or unreacted elements was found in the XRD patterns.

7.5 Results and discussion

7.5.1 X-ray diffraction and lattice parameter

XRD patterns obtained for some $Ce_8Pd_{24}Al_{1-x}Sn_x$ compounds with $x = 0.5$, 0.8 and 1, as a representative examples, together with the CAILS refinement fits to the data, are shown in Fig 7.16. XRD patterns for all compositions reveal single-phase character. The space group used in the CAILS-Pawley refinement was $Pm\overline{3}m$ cubic AuCu3-type structure. The resulting unit cell volume (V) as a function of Sn content x are shown in Fig 7.17.

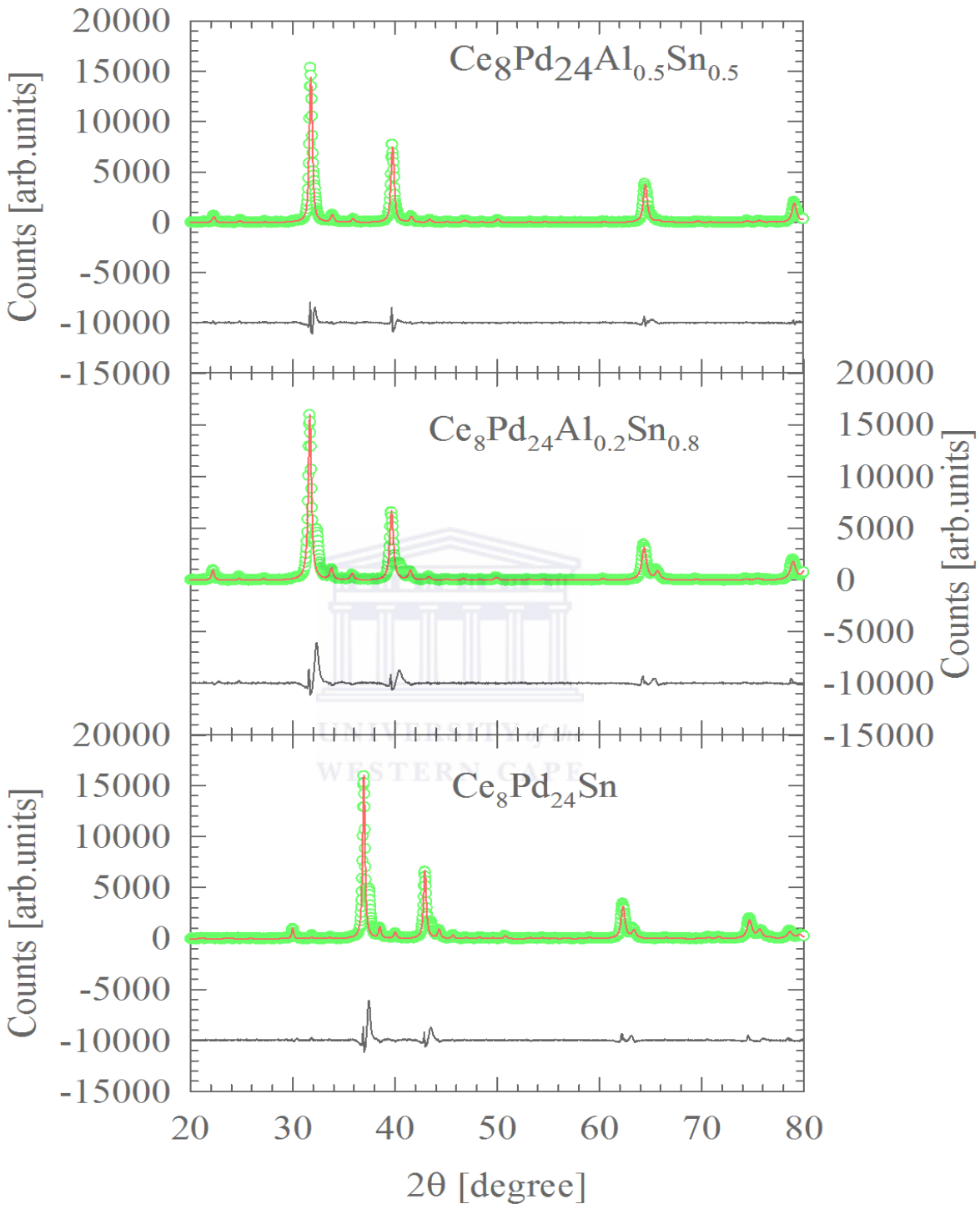

Figure 7.16: CAILS-Pawley (cell and intensity least-squares) analysed diffraction patterns for $Ce_8Pd_{24}(Al_{1-x}Sn_x)$ with $x = 0.5$, 0.8 and 1. The observed data are shown by green symbols and the solid red lines through the data represent the results of the CAILS-Pawley refinement. The lower black curves are the difference curves for the experimental data and the calculated curve.

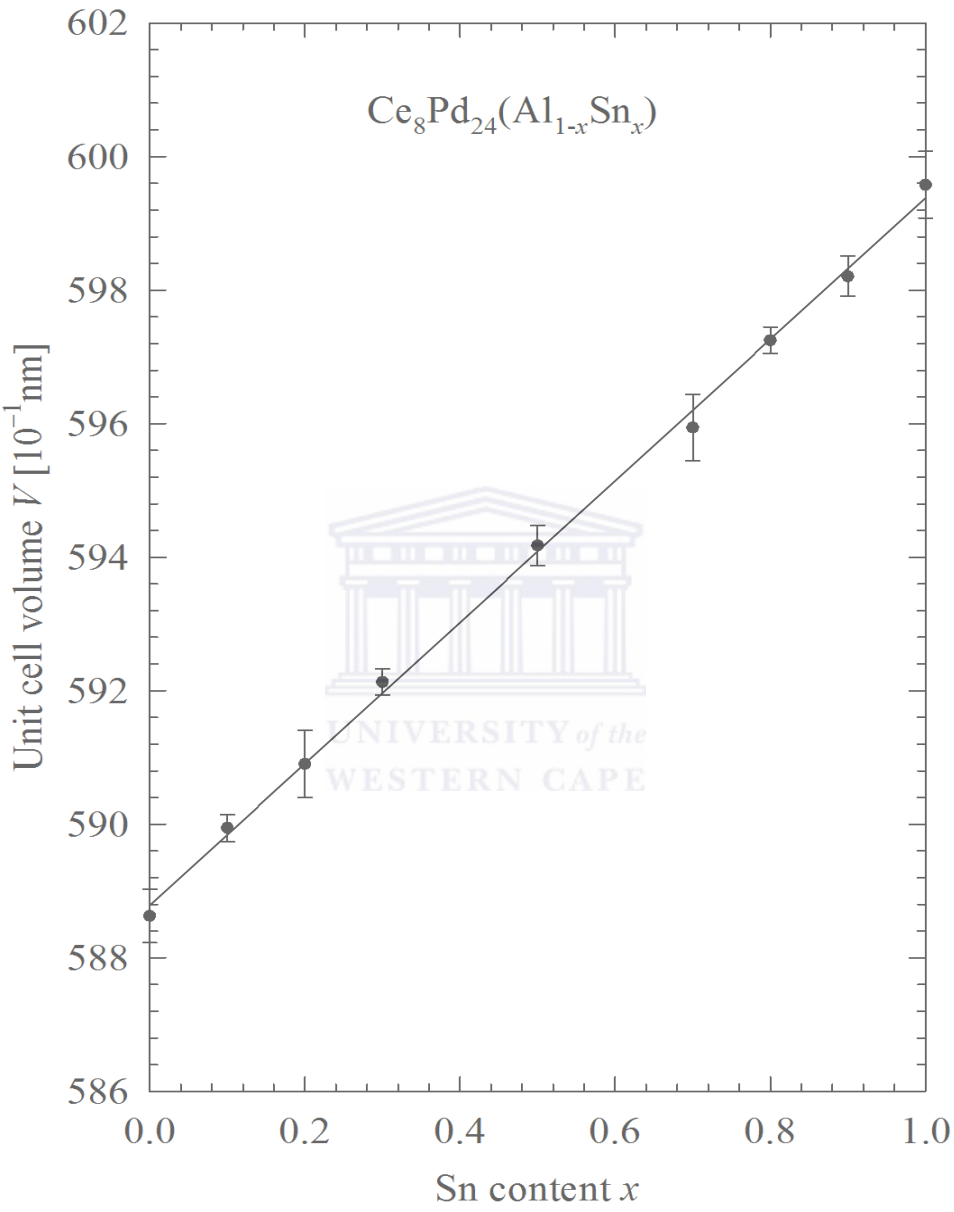

Figure 7.17: The cubic unit-cell volume V as a function Sn content x of the alloys system $Ce_8Pd_{24}(Al_{1-x}Sn$, obtained from the CAILS-Pawley refinement method. The solid line through the data points is a linear fit in accordance with the Vegard's rule.

It is observed that $V(x)$ increases linearly with x in accordance with Vegard's rule which suggests the stability of the Ce valence across the series. Sn substitution of Al expands the unit volume up to 1.87% between the two end compounds. The obtained values of the lattice parameter a of 8.382 Å and 8.432 Å for the $Ce_8Pd_{24}Al$ and $Ce_8Pd_{24}Sn$ compounds are in good agreement with previous reported values [239, 243, 254].

7.5.2 Electrical resistivity

The temperature dependence of $\rho(T)$ data are shown in Fig 7.18. At high temperatures, $\rho(T)$ data for compositions in the concentration range of $0 \leqslant x \leqslant 0.7$ are characteristic of a $-lnT$ increase upon cooling the samples. This behaviour is due to incoherent Kondo scattering of conduction electrons by the localized $4f$ moments of Ce atom. Following to the $-lnT$ increase, $\rho(T)$ at low temperatures reaches a maximum which arises from the combined presence of Kondo and CEF effects. These combined effect on $\rho(T)$ behaviour have been explained theoretically by Cornut and Coqblin [246] and later by Fisher [247]. The observed temperature of the resistivity maximum (T_{max}) are gathered in Table 7.5. It is observed from Table 7.5 that, T_{max} increases with increase Sn content x or with unit cell volume V. The increase of V with increase Sn content brings some qualitative changes in the thermal variation of the total resistivity, also observed in Zn substitution of Al up to 50% [245]. The increase of T_{max} in this system is in contradiction with the compressible Kondo lattice model which predict a decrease in T_K / T_{max} with increase unit cell volume for the dense Kondo systems [210]. This observation may suggest that the observed resistivity maximum is mainly due to CEF effect which indicates the robustness of CEF against Kondo effect. The high temperature $\rho(T)$ behaviour is described by;

$$\rho(T) = \rho_0 + \rho_{ph}(T) + \rho_{4f}(T), \tag{7.8}$$

with $\rho(T)_{ph}$ being the phonon contribution given by [70]:

$$\rho_{ph}(T) = \rho_0 + \frac{4\kappa}{\Theta_R}\left(\frac{T}{\Theta_R}\right)^5 \int_0^{\Theta_R/T} \frac{x^5 dx}{(e^x - 1)(1 - e^x)} - \alpha T^3, \tag{7.9}$$

and $\rho_{4f}(T)$ is the $4f$ magnetic contribution which account for the Kondo effect given by [4]:

$$\rho_{4f} = \rho_{spd}\left[1 + \alpha N(E_F)\Gamma_{sf} ln\left(\frac{T_F}{T}\right)\right]. \tag{7.10}$$

α is a constant which depends on the nature of the local moment, T_F is the Fermi

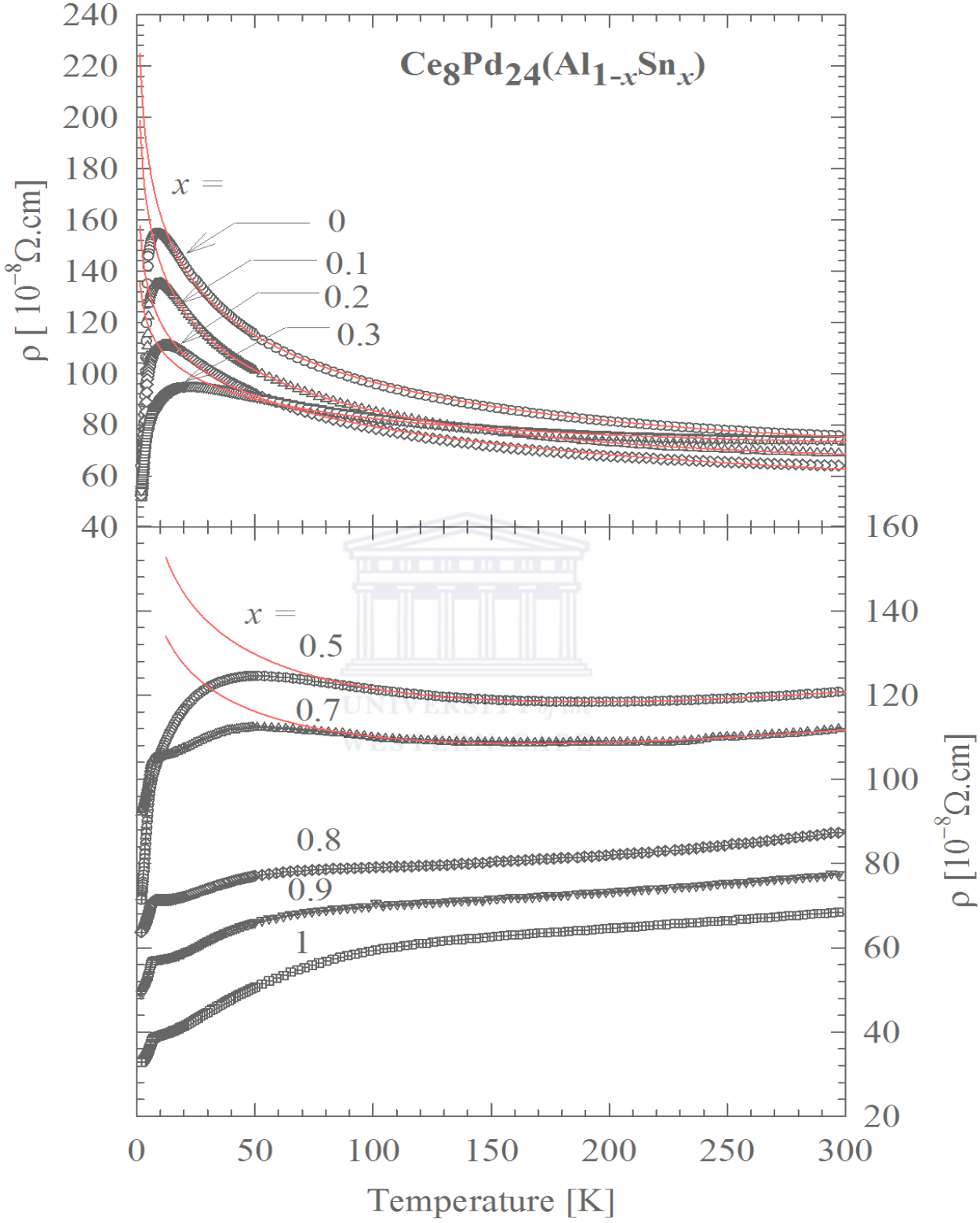

Figure 7.18: Temperature variations of the electrical resistivity $\rho(T)$ of $Ce_8Pd_{24}(Al_{1-x}Sn_x)$ alloys with $0 \leqslant x \leqslant 1$. The solid curves are the LSQ fits of the measured data to Eq 7.8.

Table 7.5: Electrical resistivity data of $Ce_8Pd_{24}(Al_{1-x}Sn_x)$ alloys. The values of ρ_0, b and CK were obtained from the high temperature LSQ fits of the measured data to Eq 7.8. The values of T_N^ρ were obtained from the position of the divergence of $d\rho/dT$.

x	ρ_0 [$\mu\Omega$.cm]	$b[10^{-3}$ $\mu\Omega$.cm/K]	$C_K[\mu\Omega$.cm]	T_{max}[K]	T_N[K]
0	232.5(8)	6.2(3)	30.8(2)	9	4.2
0.1	205.6(5)	0.66(2)	27.5(2)	10.4	4.6
0.2	162(1)	1.7	18.3(3)	12.7	4.7
0.3	129(1)	7.2(3)	10.3(4)	21	5.2
0.5	199(1)	10.1(1)	19.1(2)	51	5.5
0.7	171(2)	9.1(3)	15.2(6)	54	5.9
0.8			6.5(1)		6.4
0.9			3.03(4)		6.6
1			3.03(4)		7

temperature , $N(E_F)$ is the density of states at the Fermi level and Γ_{sf} is the direct exchange integral. ρ_0 is the temperature-independent residual resistivity due to the sample-defects scattering of the conduction electrons, also includes a large temperature-independent spin-disorder component at $T = 0$ [246]. For the high temperatures least square (LSQ) fits of $\rho(T)$ to Eq 7.8, $\rho_{ph}(T)$ was approximated to bT which is approximately valid in the high temperature region for which we fit the data, with b a coefficient giving information about the strength of the electron-phonon interaction. The $4f$ magnetic contribution was also approximated to $-C_K ln(T)$ where the coefficient C_K gives information about the magnitude of the on-site interaction between the local Ce-$4f$ electrons and the conduction electrons and it is proportional to the density of states at the Fermi level, $N(E_F)$ [3]. It turns out that the temperature-independent ρ_0 also accounts for the strength of the Kondo interaction. LSQ fits of $\rho(T)$ data for compositions in the concentration range $0 \leqslant x \leqslant 0.7$ (solid curves Fig 7.18) gives the resistivity parameters listed in Table 7.5. For compositions in the concentration range of $0.8 \leqslant x \leqslant 1$, $\rho(T)$ data is characteristic of electron-phonon scattering in the presence of CEF effect, characterized by a gradual increasing slope on cooling the sample between 30 K and 100 K which

results from thermal depopulation of the crystal field splitting of the $4f$ states. Such behaviour was also observed from the same compound $Ce_8Pd_{24}Sn$ by Gordon *et al.* [254]. It is observed from Table 7.5 that the values of C_K decrease gradually with increasing Sn content x, suggesting the decrease of the Kondo effect and the increase of CEF effect. Fig 7.19 displays the low temperature $\rho(T)$ data for all measured compositions. One can see that, $\rho(T)$ data show a sudden drop at a temperature T_N due to the freezing of spin disorder from the alloys and the resultant decrease in the magnetic scattering of charge carriers. The resulting values of T_N were obtained from the position of the divergence in $d\rho/dT$ and listed in Table 7.6 . It is observed that T_N increases gradually with increased Sn content x. The observed values of T_N for the two end compounds 4.2 K for $Ce_8Pd_{24}Al$ and 7.0 K for $Ce_8Pd_{24}Sn$ are in good agreement with previous reported values of 4.7 K [243], 4.3 K [241] for $Ce_8Pd_{24}Al$ and 7.5 K for $Ce_8Pd_{24}Sn$ [239, 254]. Below T_N, $\rho(T)$ is well described by the spin-wave dispersion relation with energy gap Δ_ρ given in the form [74]:

Table 7.6: Low temperature electrical resistivity data of $Ce_8Pd_{24}(Al_{1-x}Sn)$alloys. The prefactor A, the energy gap Δ and the residual resistivity ρ_0 were obtained from LSQ fits of the spin-wave dispersion relation (Eq 7.11) to the measured data in Fig 7.19.

x	ρ_0 [$10^{-8}\Omega$.m]	$A[10^{-8}\ \Omega.\mathrm{m/K^{-2}}]$	Δ [K]
0	64.5(4)	8.0(3)	9.3(3)
0.1	62.6(1)	6.97(9)	10.9(1)
0.2	59.6(3)	5.11(4)	6.9(1)
0.3	46(2)	2.1(3)	3.5(7)
0.5	70.0(4)	1.48(2)	5.0(5)
0.7	68.56(8)	0.389(4)	5.0(3)
0.8	63.15(8)	0.292(6)	4.3(4)
0.9	48.22(6)	0.351(3)	1.3(2)
1	32.29(2)	0.228(4)	0.73(6)

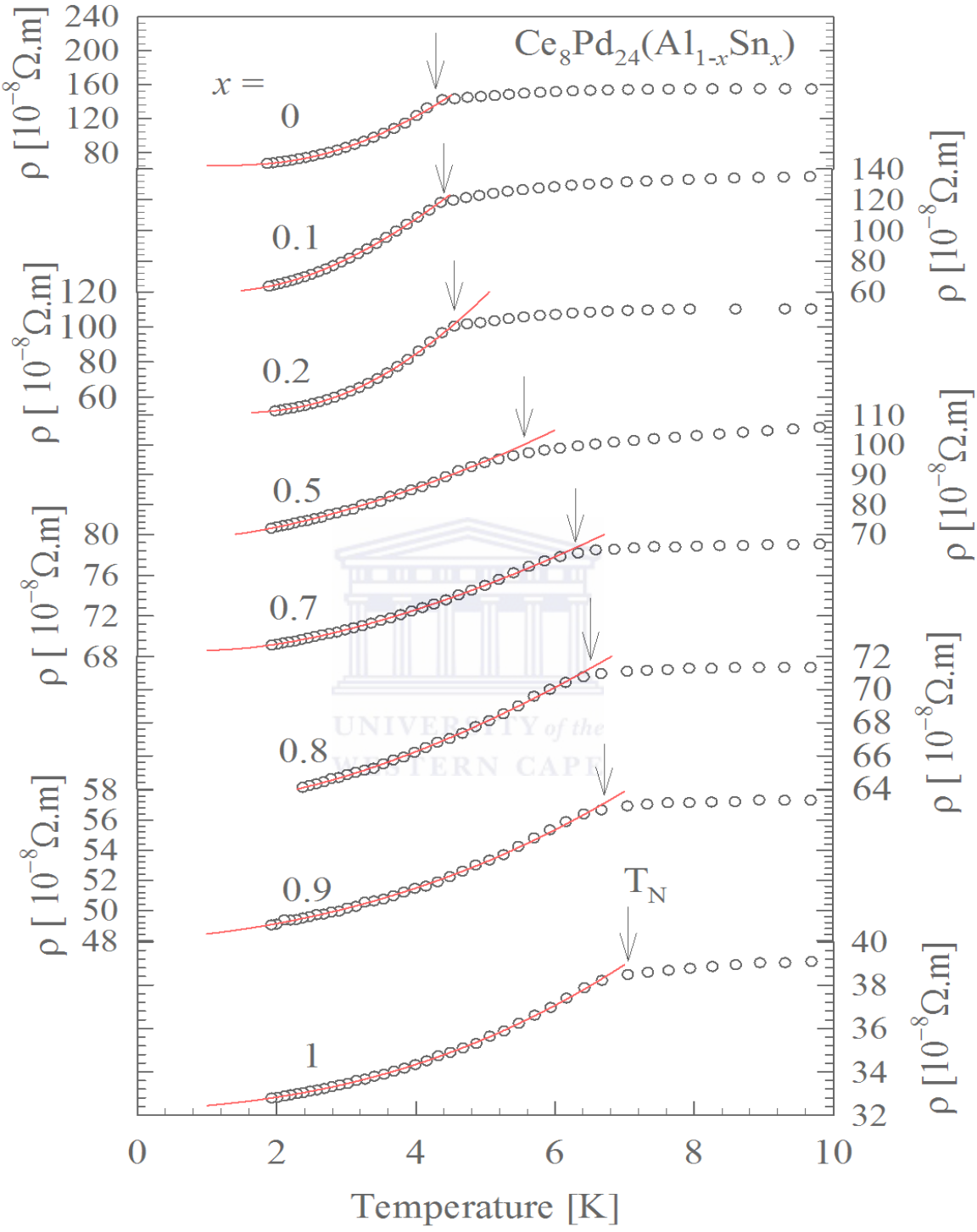

Figure 7.19: The low temperature $\rho(T)$ of $Ce_8Pd_{24}(Al_{1-x}Sn)$ alloys with $0 \leqslant x \leqslant 1$. The solid curves are LSQ fits of the measured data to the spin-wave spectrum (Eq 7.11). The vertical arrows indicate the position of the magnetic phase transition temperature T_N.

$$\rho(T) = \rho(0) + A_{\rho,AFM}\Delta^{3/2}_{\rho,AFM}T^{1/2}exp(-\Delta_{\rho,AFM}/T) \times \left[1 + \frac{2}{3}\frac{T}{\Delta_\rho} + \frac{2}{5}\left(\frac{T}{\Delta_\rho}\right)^2\right], \quad (7.11)$$

where $\rho(0)$ is the residual resistivity and A is a prefactor. LSQ fits of $\rho(T)$ data below T_N to Eq 7.11 (see Fig 7.19) yields values of the parameters gathered in Table 7.6. The value of Δ_ρ obtained for $Ce_8Pd_{24}Al$ is in good agreement with the value of 8.9(6) K obtained in Ref.[243] for the annealed sample.

7.5.3 Thermoelectric power

Fig 7.20 shows the thermoelectric power as a function of temperature, $S(T)$ for three selected compositions in the Kondo regime ($x = 0$, 0.1 and 0.3). Except for the $x = 0$ compound, $S(T)$ data show a crossover from positive to negative values over the whole measured temperature range. At low temperatures, $S(T)$ data show a minimum at temperatures of 3.8, 4.3 and 5.1 K for the $x = 0$, 0.1 and 0.3 alloys respectively close to their respective T_N values (see inset Fig 7.20) observed in $\rho(T)$ and $\chi(T)$ results. This minimum and a crossover from negative to positive $S(T)$ values is typical for magnetically ordered Kondo compounds [137]. The high temperatures $S(T)$ data is dominated by a broad maximum which may originate from the competition between Kondo and CEF effects and possibly from the phonon drag effect and / or the inelastic scattering of charge carriers by acoustic phonons similar to many rare-earth compounds [88, 133]. This high temperature $S(T)$ behaviour was interpreted using the solid curves in Fig 7.20, which represent LSQ fits of an expression [89] for the temperature dependence of scattering of electrons from the wide s-band into a narrow f-band approximation by the Lorentzian shape:

$$S(T) = \frac{2}{3}\pi^2\frac{k_B}{|e|}\frac{T.E_f}{(\pi^2/3)T^2 + E_f^2 + W_f^2} - S_d(T). \quad (7.12)$$

In this equation, E_f and W_f are the position of the f-band peak relative to the Fermi energy E_F and its width respectively, both in unit of Kelvins. The last term represents the Mott's term $S_d(T) = aT = \frac{\pi^2 k_B^2 T}{3q_e E_F}$, ($q_e$ being the charge of an electron) which accounts for usual non-magnetic Mott-type scattering of electrons in a broad $5d-6s$ conduction band and determined by the Fermi energy [252, 253]. For moderate heavy-fermion compounds as in the present case, Eq 7.12 describes a scattering of conduction electrons from an ensemble of incoherent impurities with a narrow f-band [133]. Therefore, in the case of

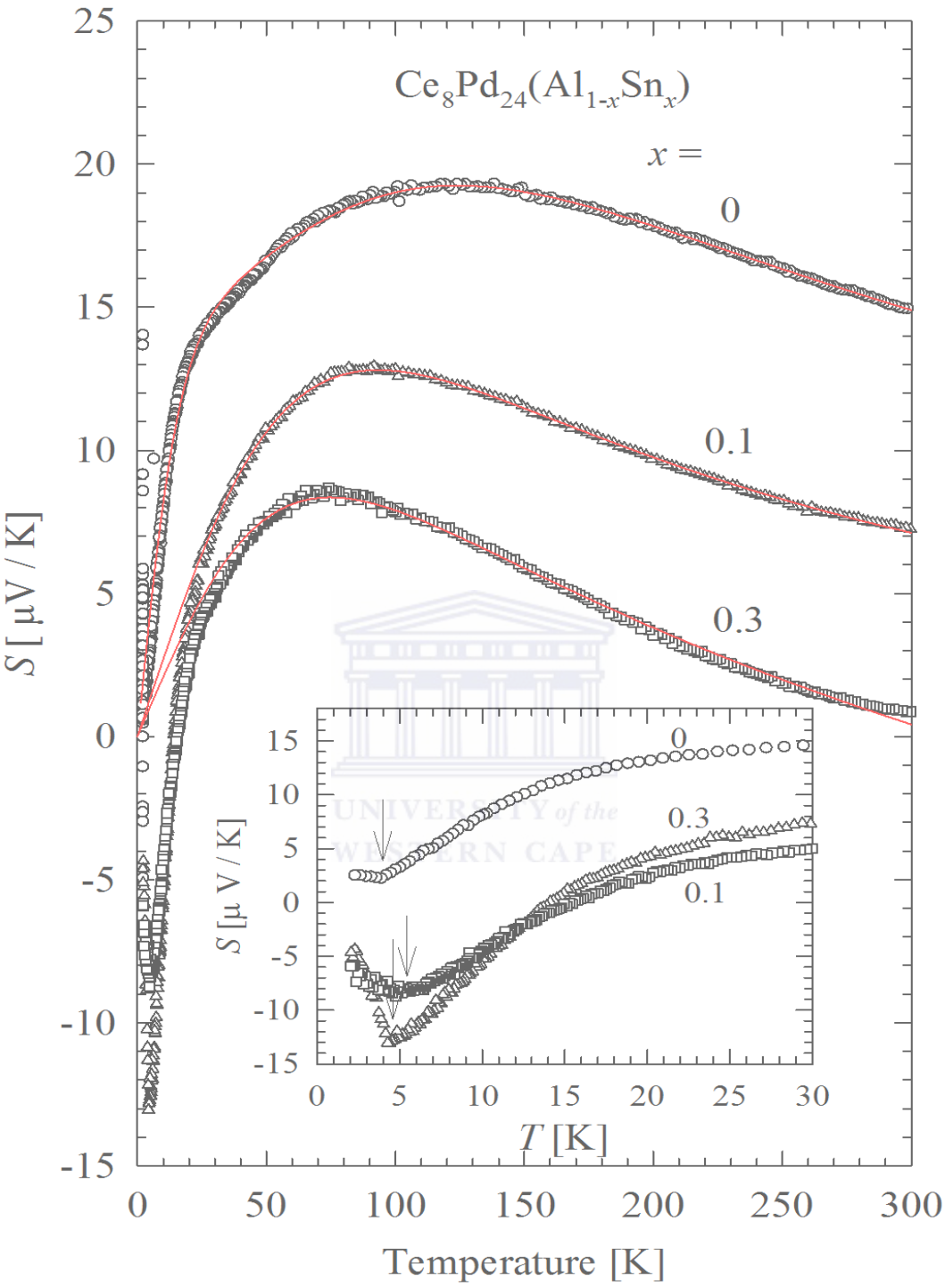

Figure 7.20: The thermoelectric power as a function of temperature, $S(T)$, of selected compositions in the alloys $Ce_8Pd_{24}(Al_{1-x}Sn_x)$. The solid curves are the fits of $S(T)$ data to the phenomenological resonance model Eq 7.12 . The inset shows an expanded view of the low temperature $S(T)$ data with the arrows indicating the position of the magnetic phase transition temperature at T_N.

Table 7.7: Thermoelectric power data of $Ce_8Pd_{24}(Al_{1-x}Sn_x)$ alloys with x= 0, 0.1 and 0.3. These data were obtained from LSQ fits of the measured data to the phenomenological resonance model Eq 7.12 .

Sn content x	0	0.1	0.3
E_f[meV]	16.1(2)	14.6(2)	16.8(1)
W_f[K]	144(1)	175(1)	187(1)
$a[\mu$ V/K$^2]$	21.7(5)	18.2(4)	16.0(3)
E_F [eV]	1.13(3)	1.34(3)	1.52(3)
T_{CEF} [K]	275	334	357

energy scale dominated by CEF, as in the present system, W_f is related mainly to the temperature of the CEF (T_{CEF}): $Wf = \frac{\pi T_{CEF}}{N_f}$ for $T \leqslant T_K$, where $N_f = 2J + 1$ is the degeneracy, with J being the total angular momentum. The obtained LSQ fit parameters are listed in Table 7.7. The values of T_{CEF} and E_F were obtained using the degeneracy $N_f = 6$ and the Mott's term respectively. The obtained Fermi energy values are typical of normal metals. The values of T_{CEF} increase with Sn content x, which suggest that the CEF effect becomes more important as one moves to the Sn-rich alloys. This behaviour corroborates with the resistivity results where C_K decreases with increasing Sn content x, suggesting the decrease of the Kondo effect in favour of the increase of the CEF in the alloy system.

7.5.4 Thermal conductivity and the Lorentz number

The temperature variation of the total thermal conductivity, λ_{tot} of the three selected compositions are displayed in Fig 7.21. For the three compositions, λ_{tot} decreases linearly with decreasing temperature, typical for scattering of electrons by lattice imperfections, also observed in many Ce compounds [134–137]. This linear behaviour is in contradiction to Wilson's law which predicts a constant value of λ_{tot}, typical for scattering electrons by thermally excited phonons only when the phonon excitation rate is constant in temperature [137]. The linear behaviour for pure Ce compounds is not predicted theoretically. It is also observed that the slope of this linear behaviour, decreases with increasing Sn content x. No evidence of a maximum was observed down to lowest temperatures similar

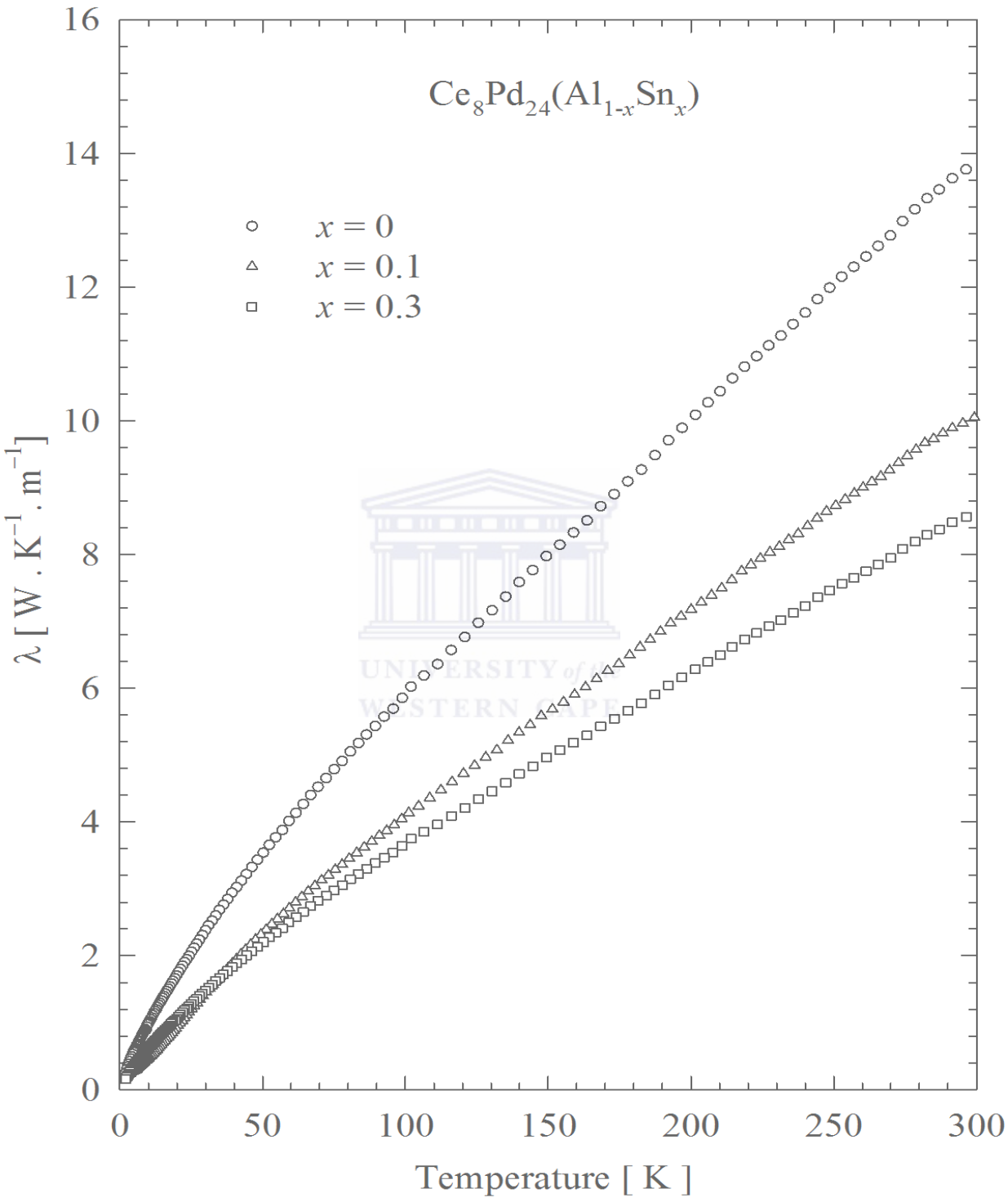

Figure 7.21: Temperature dependence of the total thermal conductivity, $\lambda_{tot}(T)$ for selected compositions in the alloys $Ce_8Pd_{24}(Al_{1-x}Sn_x)$.

to many rare earth compounds, which imply a short electron mean free path related to the larger contribution of residual scattering processes in favour of the weak coupling of electrons with phonons [135]. The interpretation of λ_{tot} is based on two components: an electronic component (λ_{ele}) for which the electrons act as heat carriers and the lattice or phonon component (λ_{ph}) for which the thermal vibrations act as heat carriers (Fig 7.22). It follows that λ_{tot} is given as a sum of the two components:

$$\lambda_{tot}(T) = \lambda_{ele}(T) + \lambda_{ph}(T). \tag{7.13}$$

The electronic component originates from the scattering of conduction electrons from lattice imperfections, phonon and magnetic moments. This component depends on both the temperature and the carrier concentration and it is given by the Weidemann-Franz law:

$$\lambda_{ele}(T) = \frac{L_0 T}{\rho}, \tag{7.14}$$

where $L_0 = 2.54 \times 10^{-8}$ W/K^2 is the Lorentz number. The lattice component originates from collisions of phonons from lattice impurities and / or defects and conduction electrons. This contribution is obtained by subtracting $\lambda_{ele}(T)$ from $\lambda_{tot}(T)$. The dominant scattering of electrons and phonons is due to lattice imperfections. Fig 7.22 shows the temperature dependence of $\lambda_{tot}(T)$ together with separated electronic and lattice components. It appears that for the three compositions, the lattice contribution predominates below 170 K, 150 K and 120 K for $x = 0$, 0.1 and 0.3 respectively. This also indicates the suppression of the lattice contribution in favour of the electronic component with increase in Sn content x. This predominance of lattice contribution corroborates with the result of the reduced Lorentz number (L/L_0) which increase with a reduction of temperature (see Fig 7.23). Similar behaviour has been reported for many rare-earth compounds [88, 136, 137].

Combining the results of λ_{tot} and $\rho(T)$, we have plotted in Fig 7.23 the Lorentz number $L(T) = \dfrac{\lambda\rho}{T}$ normalized to L/L_0. It is observed that L/L_0 for the three compositions increase upon cooling and reaches maximum values of 3.2 at 7 K, 3 at 5.2 K and 2.7 at 4.8 K for $x = 0$, 0.1 and 0.3 alloys respectively (see inset Fig 7.23). Below these temperature maximum L/L_0 shows a sudden decrease with further decrease in temperature. A similar behaviour of L/L_0 was observed in many rare-earth compounds and was attributed to an additional thermal conductivity or can be caused by energy dependence Kondo scattering processes [135]. Similar to $CeCu_4Al$, it should be noted that, the large L/L_0 values

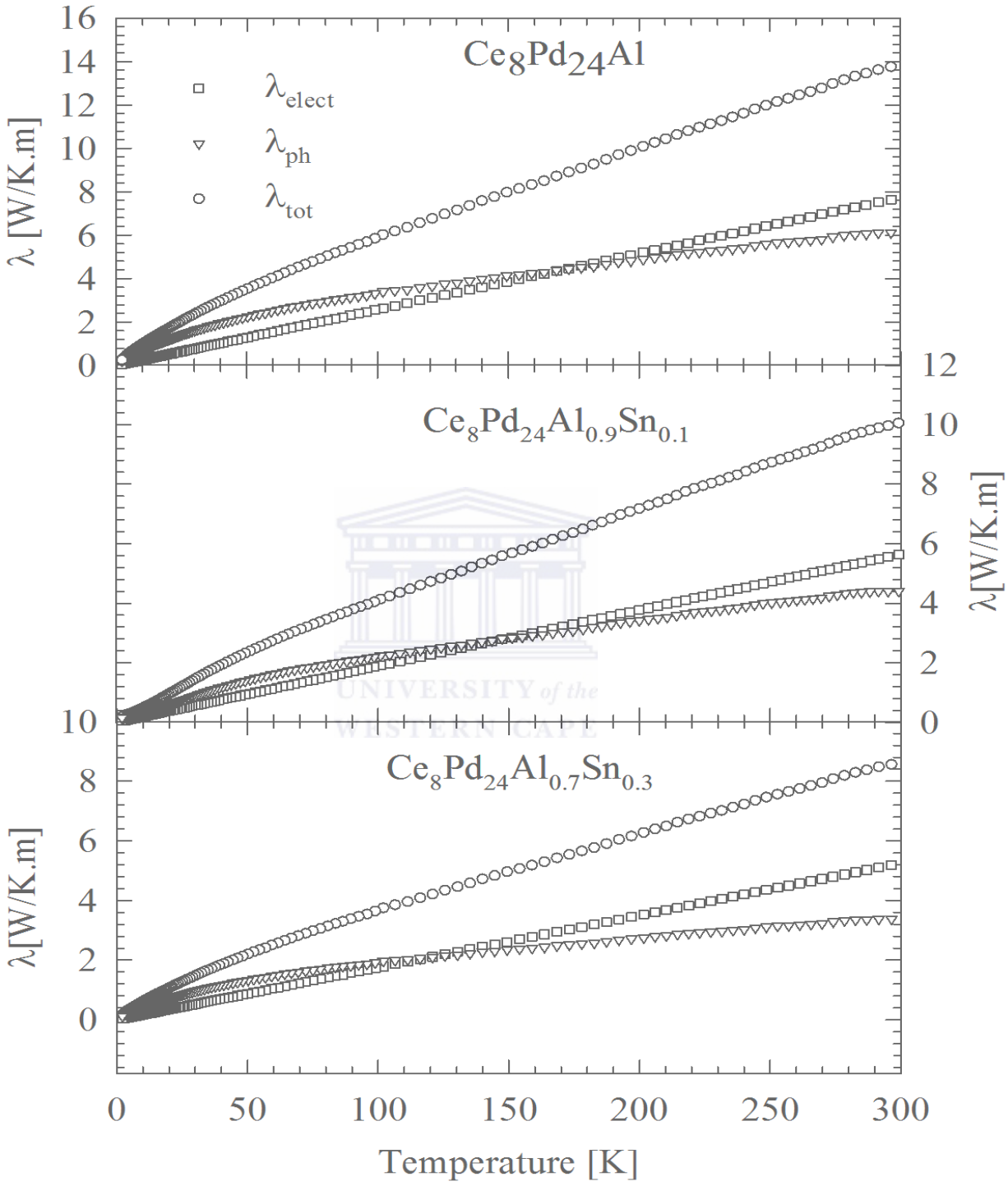

Figure 7.22: Temperature dependence of the total thermal conductivity, $\lambda_{tot}(T)$, together with electronic and phonon components.

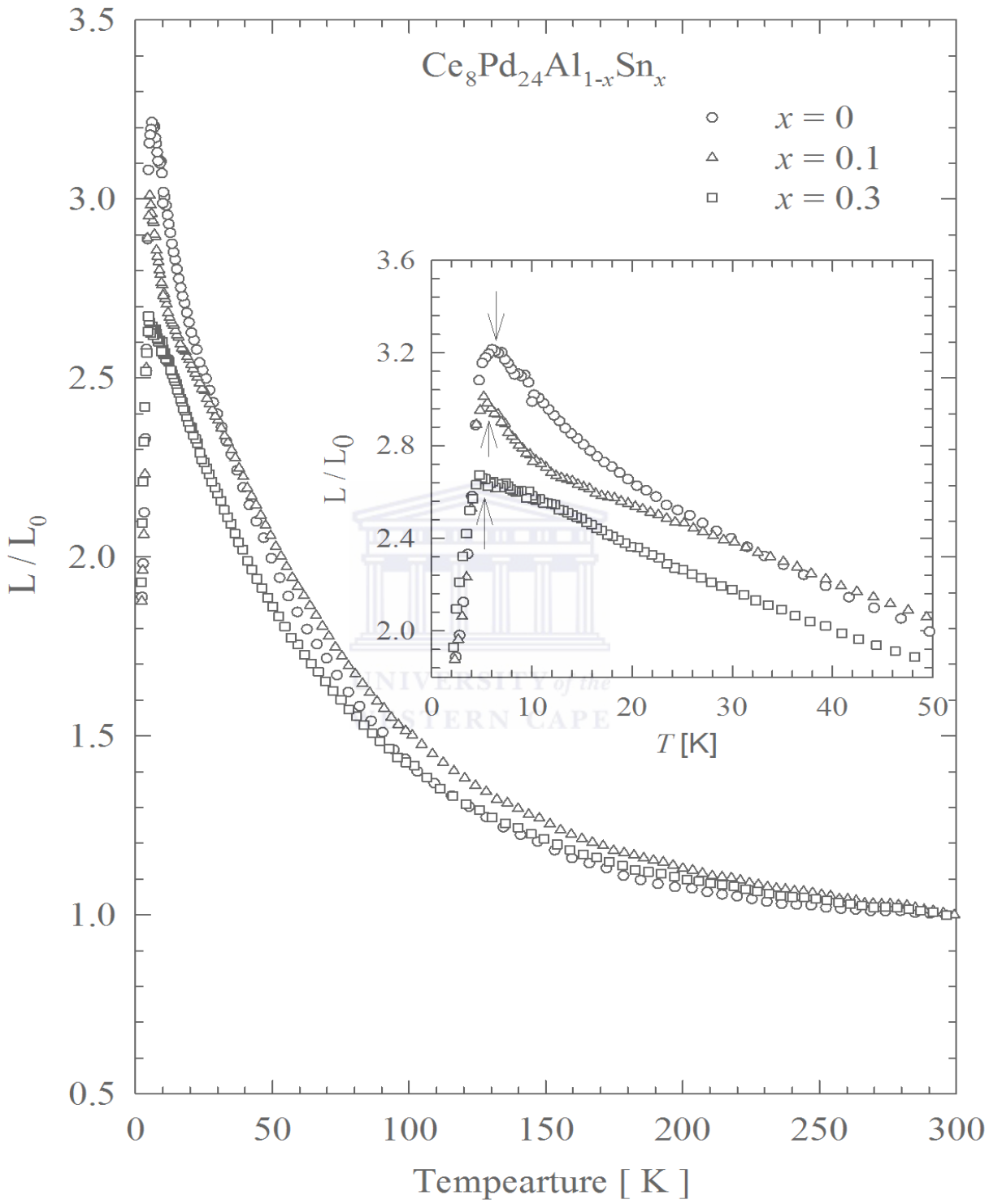

Figure 7.23: The normalized Lorentz number L/L_0 scale to 1 at 300 K of selected compositions in the alloys $Ce_8Pd_{24}(Al_{1-x}Sn_x)$. The inset shows the expanded view of the low temperature behaviour of L/L_0 with the arrows indicating the position of the temperature maximum.

indicate that the dominant heat carriers are phonons and the spin scattering of charge carriers does not play an important role [135]. Our maximum value of L/L_0 for alloy with $x = 0$ is relatively smaller compared to the values usually obtained for typical heavy fermion compounds such as $CeCu_4Al$ [134] which confirm the assumption made of moderate heavy fermion character of our system in the analysis of $S(T)$. For comparison to typical thermoelectrical materials, we have plotted in Fig 7.24 the dimensionaless figure of merit, ZT which is a measure of the efficiency of the thermoelectric materials given by: $ZT = \frac{S^2T}{\rho\lambda}$. From this relation it is clear, that to obtain a good efficiency one has to minimize both the thermal conductivity and the electrical resistivity. A commonly used thermoelectric material in power generation or refrigeration is Bi_2Te_3 with ZT between 0.8 and 1 [140]. It is observed from Fig 7.24 that, ZT data for all three compositions increase with a decrease in temperature and exhibit a broad maximum between 100 and 200 K similar to the many heavy fermion compounds such as $CeCu_4M$ (M = In and Ga) [136] and $(Ce_{1-x}La_x)Cu_4In$ [255, ref therein]. The room temperature ZT amount to 11.5×10^{-3}, 3.8×10^{-3} and 0.7×10^{-3} for x= 0, 0.1 and 0.3 respectively. These values are very small compared to the commonly used thermoelectric material Bi_2Te_3.

7.5.5 Magnetic susceptibility and magnetization

Fig 7.25 shows the inverse magnetic susceptibility, $\chi^{-1}(T)$ data, which show a Curie-Weiss (CW) magnetic behaviour above 50 K for all measured compositions. LSQ fits of the CW relationship:

$$\chi^{-1} = \frac{3k_B(T - \theta_P)}{N_A\mu_{eff}^2} \tag{7.15}$$

gives an effective magnetic moment (μ_{eff}) and paramagnetic Weiss temperature constant (θ_p) values listed in Table 7.8. The obtained μ_{eff} values for all compositions are in close agreement to the value of 2.54 μ_B expected for the free Ce^{3+}-ion. Negative θ_p values were obtained for all compositions indicating the dominance of the AFM interactions which may include the RKKY as well as the on-site Kondo interaction between conduction electrons and the Ce $4f$ spins in the case of compositions ($0 \leqslant x \leqslant 0.7$) showing Kondo effect. Deviation of the CW relation at low temperatures may be attributed to magnetocrystalline anisotropy. $\chi(T)$ data at low temperatures (Fig 7.26) rises into an anomaly at T_N which is associated to AFM phase transition. The values of T_N were estimated at the peak of $\chi(T)$ curve as indicated by the arrows in Fig 7.26 and listed in Table 7.8. The observed values of T_N corroborates the values of T_N obtained from $\rho(T)$ data. Fig 7.27 shows the Sn content x dependence of T_N as obtained from $\chi(T)$ data. One can see that T_N values increase linearly with increase in Sn content x as indicated by the linear fit in Fig 7.27.

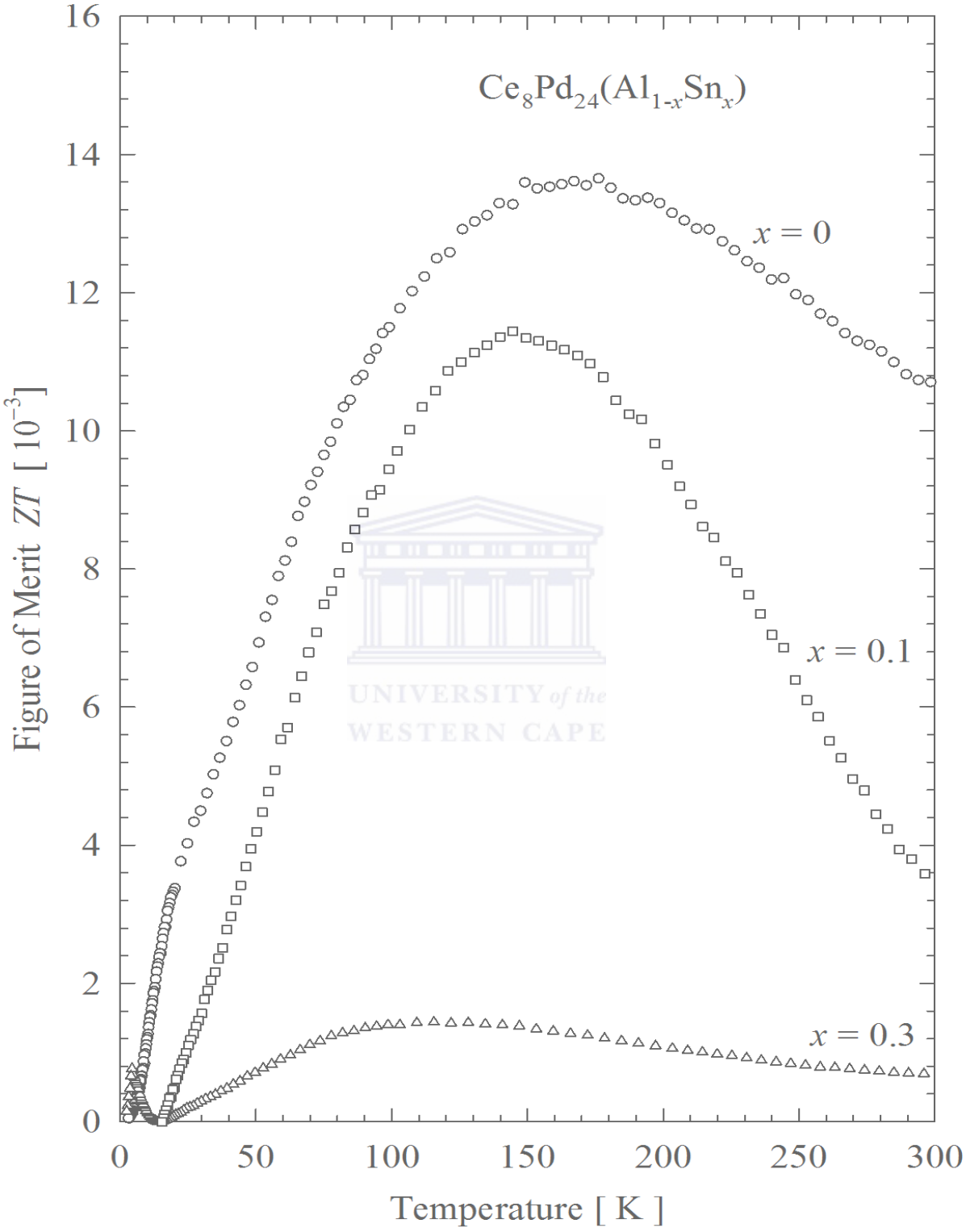

Figure 7.24: Temperature variation of the thermoelectric figure of merit (ZT) of selected compositions in the alloys $Ce_8Pd_{24}(Al_{1-x}Sn_x.)$

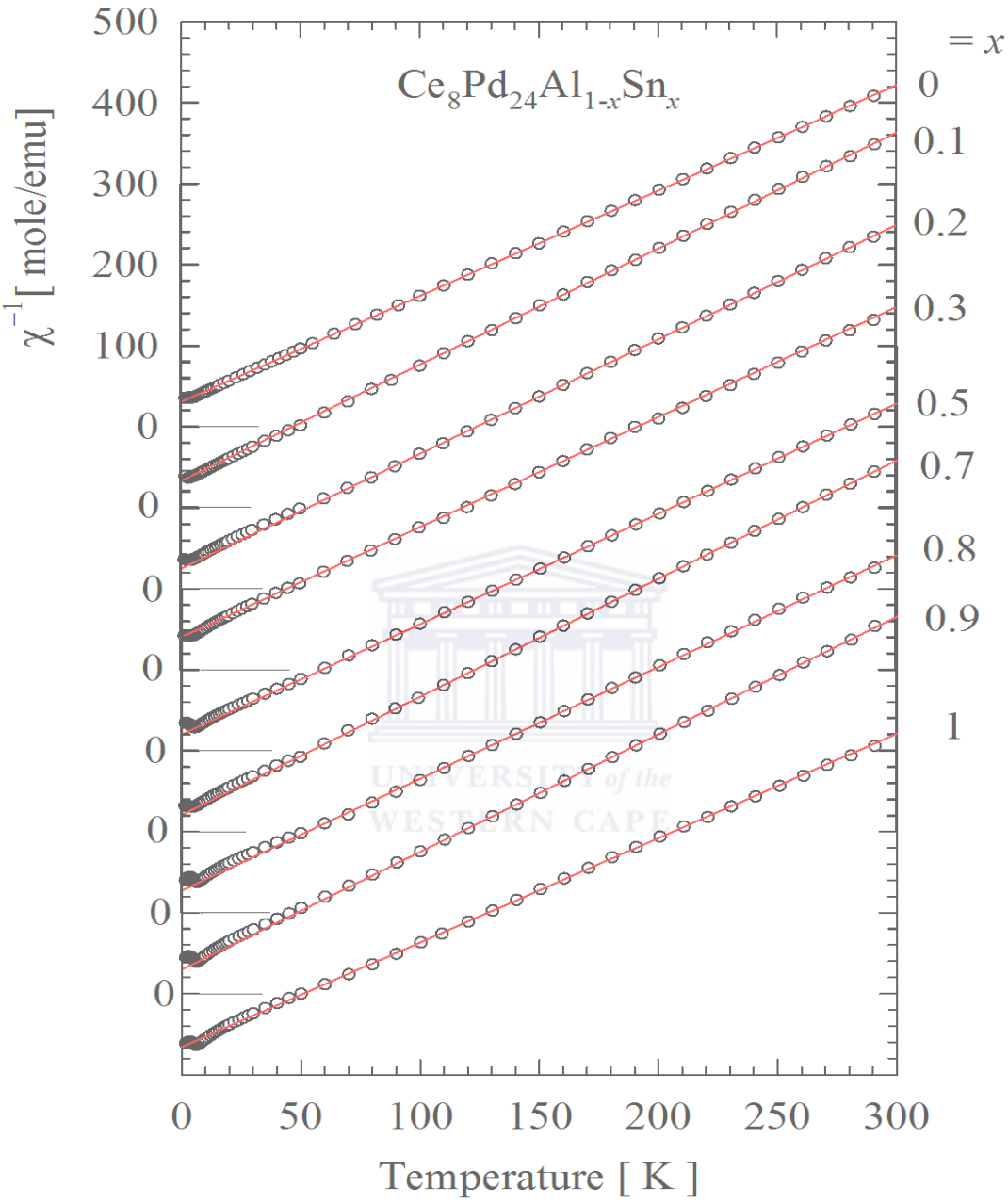

Figure 7.25: The inverse magnetic susceptibility, $\chi^{-1}(T)$ data of the $Ce_8Pd_{24}(Al_{1-x}Sn_x)$ alloys with the Curie-Weiss fit (red solid lines) according to the experimental data above 50 K.

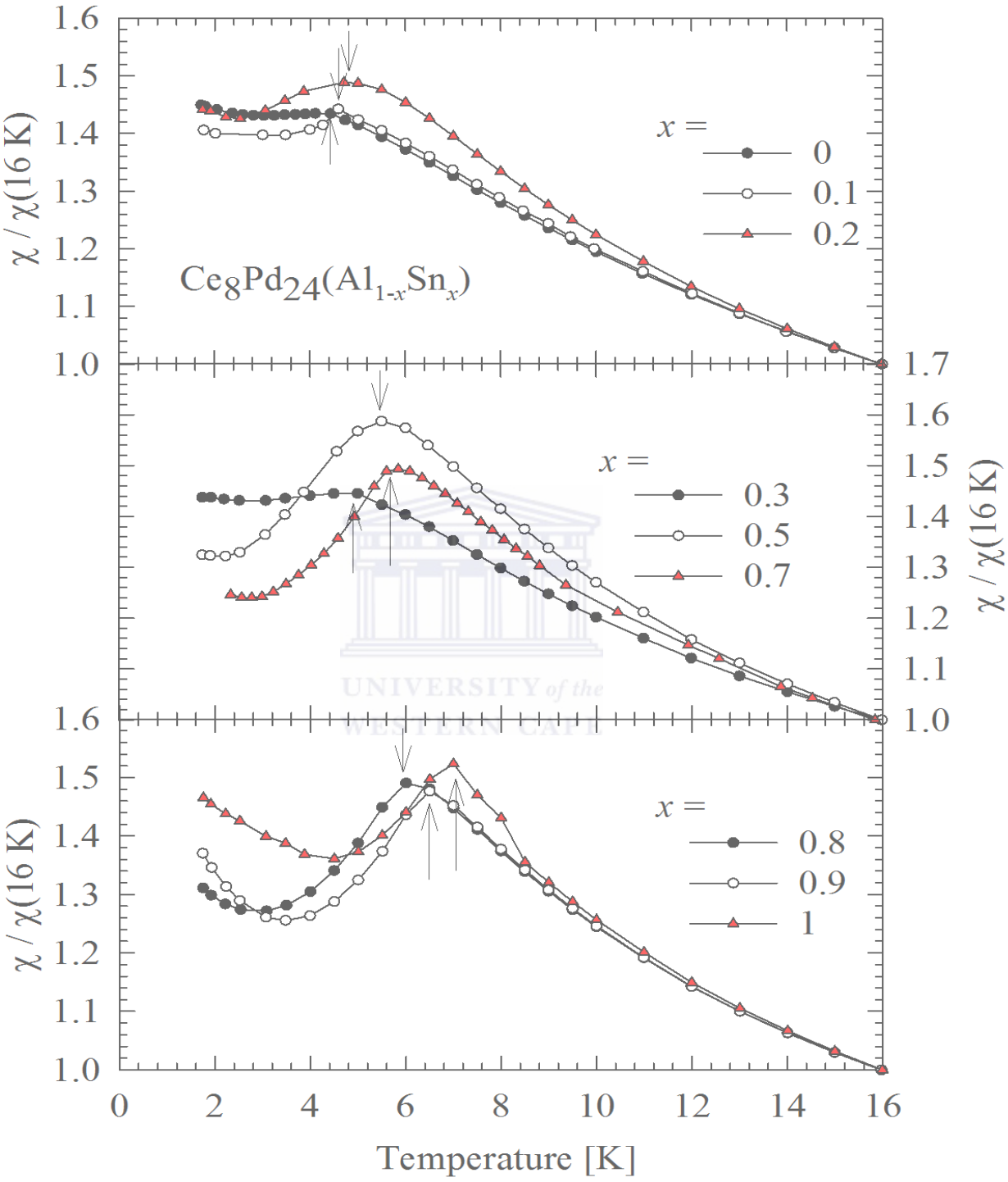

Figure 7.26: The low temperatures $\chi(T)$ data of the $Ce_8Pd_{24}(Al_{1-x}Sn_x)$ alloys showing their magnetic phase transition temperature T_N at the maximum as indicated by the arrows.

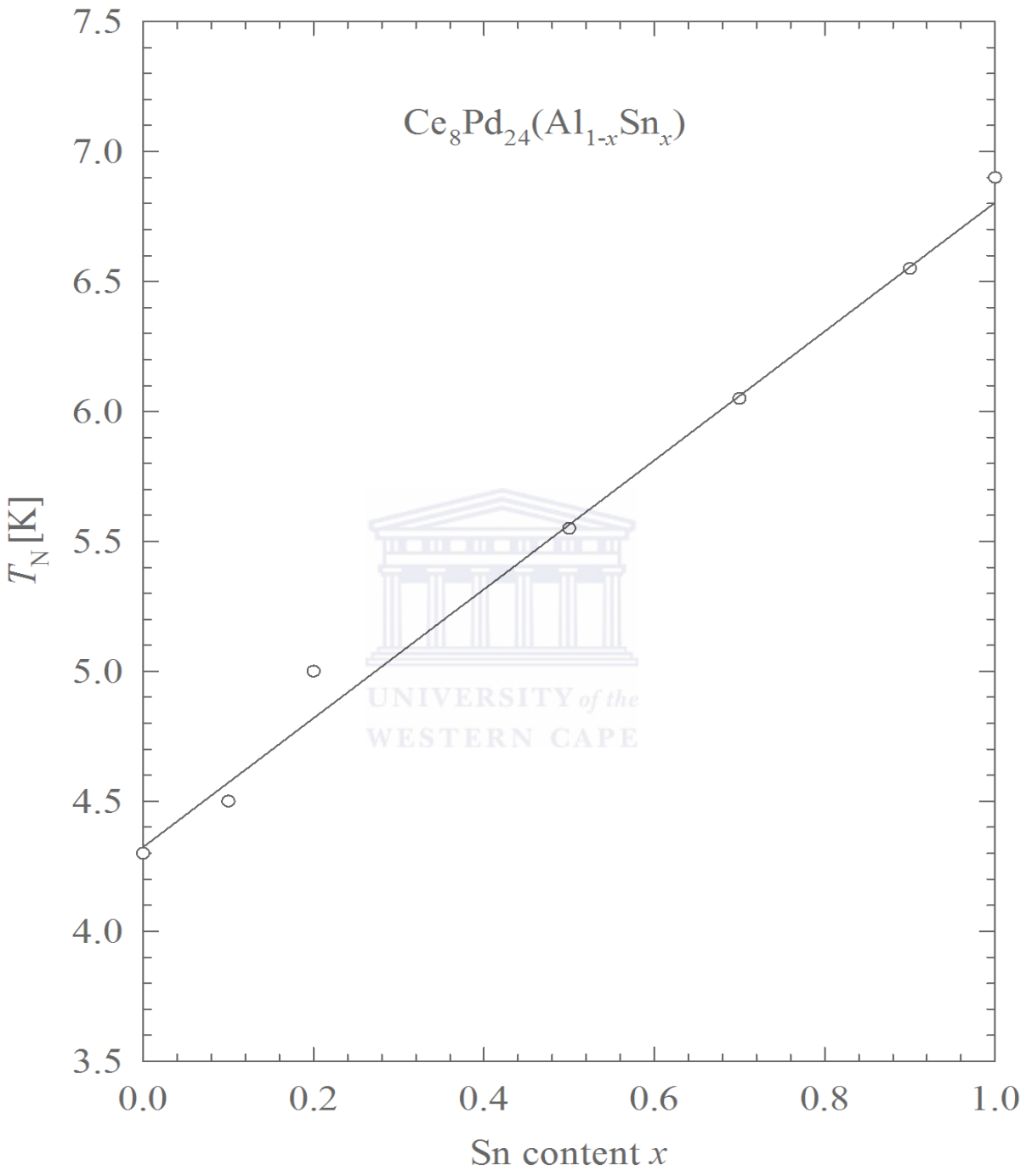

Figure 7.27: Sn content x dependence of T_N obtained from $\chi(T)$. The solid line is the linear fit of T_N obtained from $\chi(T)$.

Table 7.8: Magnetic susceptibility data of $Ce_8Pd_{24}(Al_{1-x}Sn_x)$ alloys. The effective magnetic moment, μ_{eff} , the paramagnetic Weiss temperature constant, θ_P were obtained from LSQ fits of the Curie-Weiss relation Eq 7.12 to the measured data in Fig 7.20. Values of T_N were inferred from the position of the maximum value of $\chi(T)$ as indicate by arrows in Figs 7.21.

x	μ_{eff} [μ_B]	$-\theta_P$[K]	T_N [K]
0	2.47(1)	23.5(1)	4.1
0.1	2.36(2)	22.5(6)	4.6
0.2	2.38(6)	17.2(4)	4.7
0.3	2.45(1)	29.1(8)	5.0
0.5	2.44(3)	14.6(2)	5.5
0.7	2.35(5)	13.5(2)	5.8
0.8	2.41(6)	19.7(9)	6.0
0.9	2.42(5)	19.9(9)	6.5
1	2.49(3)	26.2(4)	7.0

Fig 7.28 shows the low temperature field-cooled (FC) and zero-field-cooled (ZFC) $\chi(T)$ data of three selected compositions. It is observed that the FC and ZFC $\chi(T)$ data taken in a field of 0.1 T split into two branches below T_s as indicated by arrows for compositions up to 50% Al substitution. Such a bifurcation may originate from an inhomogeneous magnetic ground state in these compositions. This behaviour was also observed in some rare earth compounds such as NdAuGe [256, ref therein].

The magnetization, $M(\mu_0 H)$ measured at 1.7 K in field up to 5 T in Fig 7.29 increase linearly with field with no evidence of metamagnetic transition. Such linear increase illustrates the dominance of AFM interaction at low temperatures. No evidence of hysteresis effect was observed during the process of increasing and the decreasing field. The observed values of $M(\mu_0 H)$ at 5 T increases gradually with increase Sn content x, ranging from 0.42 μ_B to 0.78 μ_B.

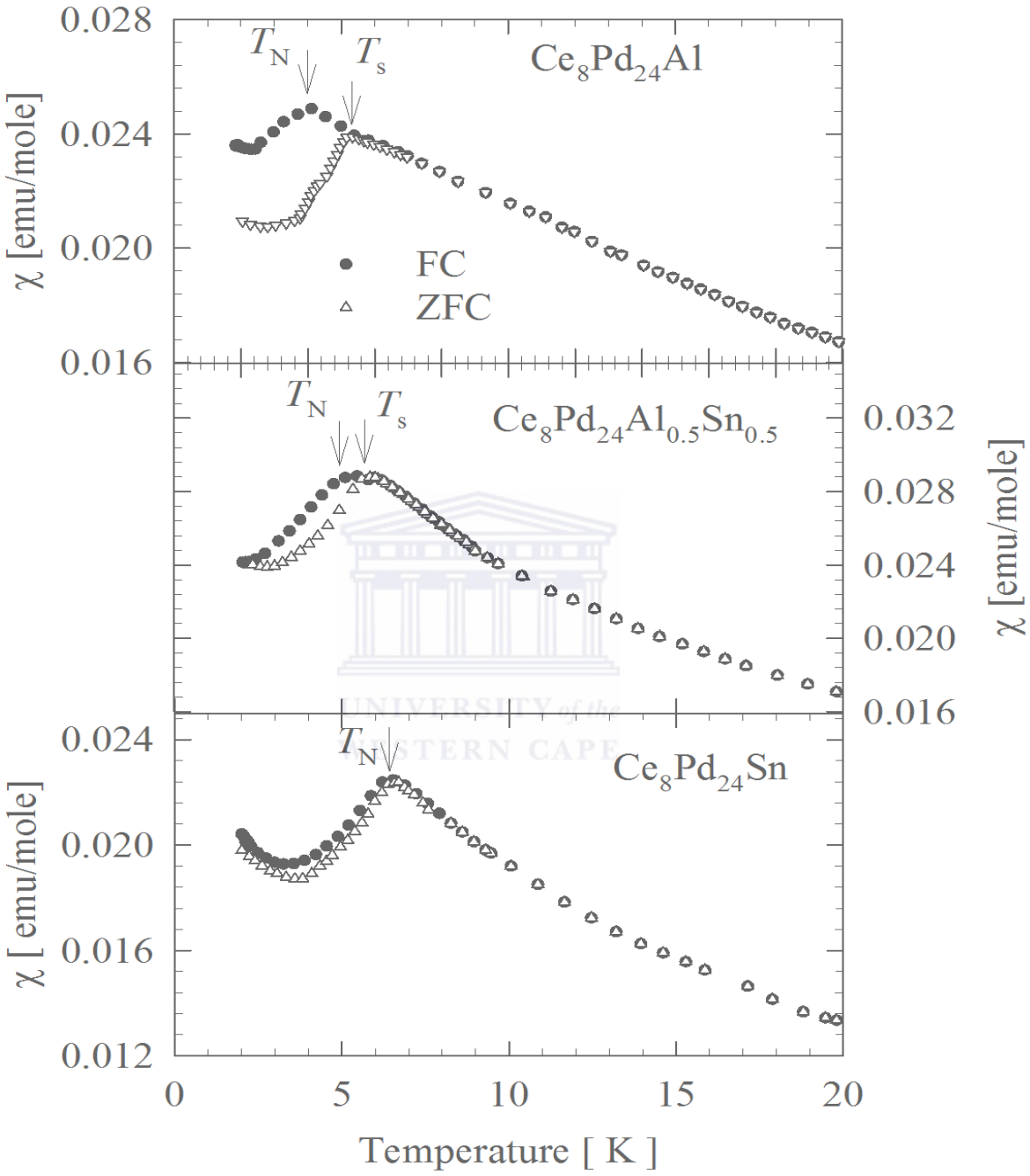

Figure 7.28: The low temperatures $\chi(T)$ data measured in Zero-field-cooled (ZFC) and in Field-cooled (FC) runs. The arrows indicate the magnetic phase transition temperature T_N and the temperature at which the splitting occurs, T_s between ZFC and FC runs.

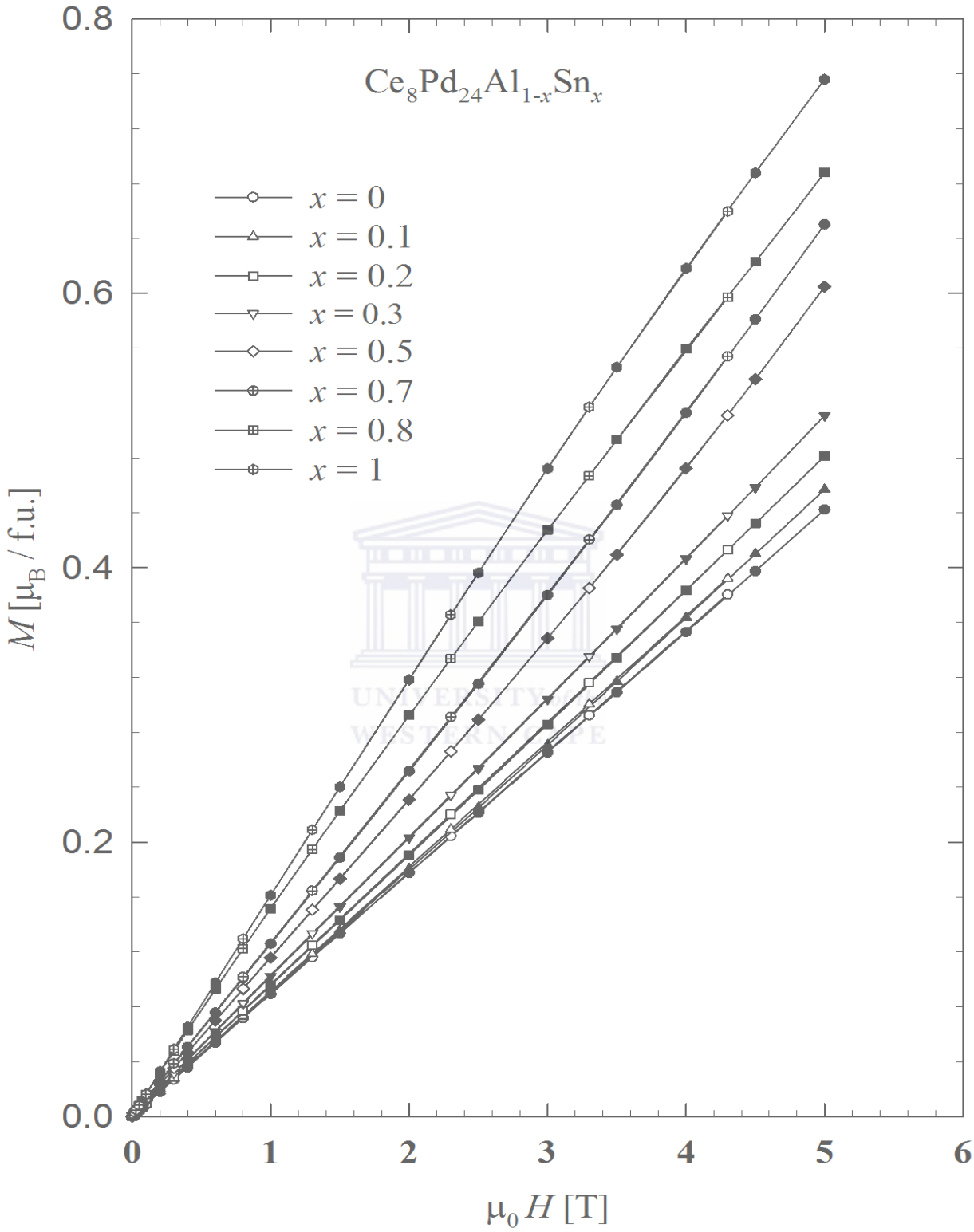

Figure 7.29: The field variation of the magnetization $M(\mu_0 H)$ data of the $Ce_8Pd_{24}(Al_{1-x}Sn_x)$ alloys measured in increasing (closed symbols) and decreasing (opened symbols) field.

7.5.6 Conclusion

The present study of $Ce_8Pd_{24}(Al_{1-x}Sn_x)$ indicates that the dominant $\rho(T)$ behaviour is that of the combined CEF and Kondo effect for compositions in the range $0 \leqslant x \leqslant 0.7$ and only of CEF at Sn-rich alloys. For all compositions, the low temperature $\rho(T)$ data is described by spin-wave dispersion below T_N with an energy gap Δ. $S(T)$ results are described by the phenomenological resonance model. The low temperature $S(T)$ shows a minimum at T_N which corroborate with the results of $\rho(T)$ and $\chi(T)$. The resulting T_N values increase linearly with increased Sn content x. $\chi(T)$ data indicate spin-glass behaviour up to 50% Al substitution for Sn. No evidence of metamagnetic behaviour and hysteresis were observed from the magnetization results. The total $\lambda(T)$ study reveals a dominant contribution of the phonon component compared to the electronic component at low temperatures.

Chapter 8

Conclusion and future work

Beside the conclusions given in each chapter, this chapter summarises all the results obtained in the thesis using different experimental techniques described in chapter 3.

8.1 Conclusion

The low temperature physical properties of a number of rare-earth intermetallic compounds and alloys as well as their characterization are studied in the thesis. We have reported XRD diffraction for the structural characterization and single-phase purity as well SEM measurements. The properties investigated, include: the electrical and thermal transport such as: the electrical resistivity, the magnetoresistivity, the thermoelectric power and the thermal conductivity. The thermodynamic properties studied include: the magnetic susceptibility, the magnetization, the heat capacity and the magnetocaloric effect. XRD spectra analysis confirm the crystal structure of each rare earth compound and system viz. the cubic $MgCu_4Sn$-type crystal structure for the two compounds $RECu_4Au$ (RE = Nd and Gd): the $CeCu_2$-type orthorhombic crystal structure for NdAuGa; the LiGaGe-type structure for NdAuGe; the $CeCu_{4.38}In_{1.62}$-type crystal structure for the alloys series $(Ce_{1-x}La_x)Cu_4In$ and the cubic $AuCu_3$-type structure for both alloys systems $(Ce_{1-x}La_x)_8Pd_{24}Al$ and $Ce_8Pd_{24}(Al_{1-x}S_x)$. The unified observation of the La dilution with Ce based rare earth compounds and alloys is that resistivity data clearly indicate the evolution from coherent Kondo lattice to incoherent single-ion Kondo scattering with increase La concentration. Results of the magnetoresistivity measurements for the La dilute alloys confirm the Bethe *ansatz* description of this property and are used to obtain the Kondo temperature T_k values. These values of T_k together with values of the temperature maximum T_{max} at which a maximum occurs for the coherent dense Kondo alloys, are used in a compressible Kondo lattice description of the following systems $(Ce_{1-x}La_x)Cu_4In$ and $(Ce_{1-x}La_x)_8Pd_{24}Al$. The low temperature resistivity data indicate anomalies associated

to the antiferromagnetic phase transition at T_N for the NdAuGe, NdAuGa, $NdCu_4Au$, $GdCu_4Au$, Ce-rich alloys in $(Ce_{1-x}L_x)_8Pd_{24}Al$ and for all compositions in the alloys series $Ce_8Pd_{24}(Al_{1-x}S_x)$. The high temperature resistivity data of the rare compound NdAuGe show normal metallic behaviour. The results of the thermoelectric power measurements for some investigated alloys in this thesis are interpreted in terms of the phenomenological resonance model at high temperature to gives the values of the temperature scale of the crystalline-electric field, the energy of the $4f$-electron and the Mott's constant which were used to obtain the Fermi energy. The study of $(Ce_{1-x}L_x)_8Pd_{24}Al$ in particular confirms the interplay of antiferromagnetic and Kondo effect. The thermal conductivity data studies for some compounds and alloys in this thesis deviate from Wilson's law except for the Ce dilute alloys for the system $(Ce_{1-x}La_x)Cu_4In$ near room temperature. The reduced Lorentz number results for compositions investigated increase gradually from room temperature and reach a peak at low temperatures. The figure of merit for the alloys systems $(Ce_{1-x}La_x)Cu_4In$, $(Ce_{1-x}L_x)_8Pd_{24}Al$ and $Ce_8Pd_{24}(Al_{1-x}S_x)$ increase with rapidly upon cooling the sample followed by a maximum at low temperature. The inverse magnetic susceptibility data at high temperatures for all investigated compounds and alloys follow the Curie-Weiss behaviour except for the compound $NdCu_4Au$ which follows the modified Curie-Weiss behaviour. The resulting effective magnetic moments are in fair agreement with the RE^{3+} Hund's rule expectation. Except for the alloys series $(Ce_{1-x}La_x)Cu_4In$, the low temperatures of the magnetic susceptibility for all the compounds and alloys in the system $Ce_8Pd_{24}(Al_{1-x}S_x)$ and for Ce-rich alloys show antiferromagnetic-like anomaly associated with Neél temperature T_N. The zero-field-cooling and field- cooling magnetic susceptibility for NdAuGe, GdCu4Au compounds and Al-rich alloys in $Ce_8Pd_{24}(Al_{1-x}S_x)$ indicate spin-glass behaviour. The magnetization studies indicate the occurrence of metamagnetic behaviour for the $GdCu_4Au$, NdAuGe and NdAuGa compounds. The low temperature heat capacity data for selected compounds confirm the phase transition of a putative antiferromagnetic character at T_N, also observed in the resistivity and magnetic susceptibility. For the NdAuGa, a second anomaly is observed below T_N associated to spin reorientation transition. Above T_N magnetic contribution to the total heat capacity for the NdAuGe and $NdCu_4Au$ exhibit broad centred peaks around 16.5 K and 20 K respectively, characteristic of Schottky-type anomalies with energy splitting of the Nd^{3+} ($J = 9/2$) multiplet due to crystal-electric-field effect. In the case of $NdCu_4Au$, the $4f$-electron derived entropy indicates long-range correlation above T_N. The magnetocaloric effect studied for NdAuGa compound is fairly modest, weaker than in other representative of RETX family, while the Arrott-plot indicates that the magnetic phase transition is found to be second in nature.

8.2 Future work

Future investigations within the rare earth compounds and alloys showing magnetic transition at low temperature by, neutron diffraction experiment is foreseen in order to study their magnetic structure.

Future investigations for compounds and alloys for which the CEF have been estimated, inelastic neutron scattering studies are foreseen in order to estimate their CEF for comparison with values with different experimental techniques in this thesis.

The study of the magnetocaloric effect and critical behaviour around the transition temperature of other compounds in the RETX family is currently under investigation.

The study of Ce dilution in $Ce_8Pd_{24}Al$ revealed the occurrence of a quantum critical point at a critical La concentration. This will be extended by the application of a magnetic field and hydrostatic pressure on resistivity and heat capacity measurements.

The work on NdAuGa for which the heat capacity result shows spin orientation below T_N has been reported and published. Further study will be conducted at very low temperature and high magnetic field.

References

[1] H. Szymczak and R. Szymczak. *Materials Science-Poland,*, Vol. **26**, No. 4, (2008) 807.

[2] K.H.J. Buschow. *Prog.Phys*, **40**, (1977)1179-1256.

[3] J. Kondo. *Solid State Phys*, **23**, (1969) 183.

[4] E. Bauer. *Adv. Phys.*, **40**, (1991)417.

[5] P. Coleman. "condensed matter, strongly correlated electron physics". *Physics world Issue*, **12**, (1995) 29.

[6] A.C.Hewson. *"The Kondo Problem to Heavy-Fermion"*. (Cambridge,Cambridge University press), (1993).

[7] F. Steglich, J. Aarts, C.D Bredl, W. Lieke, D. Meschedle, W. Franz, and J. Schafer. *Phys. Rev. lett*, **43**, (1979)1892.

[8] G.R Stewart. *Rev.Mod.Phys*, **56**, (1984) 755.

[9] K. Andres, J. E Graebner, and H. R Ott. *Phys. Rev. Lett.*, **35**,(1975) 1179.

[10] C. Kittel. *Introduction to Solid State Physics.* (John Wiley & Sons, Inc., New York, 1986).

[11] S. Doniach. *Physica B*, **91**, (1977)231.

[12] K.H.J. Buschow, editor. *Concise Encyclopedia of Magnetic and Superconducting Materials.* Elsevier Ltd, second edition, 2005.

[13] C.M Varma. *Rev.Mod.Phys*, **48**, (1976)183.

[14] K.A.Jr Gschneidner and A.H Daane. *Handbook on the Physics and Chemistry of Rare Earths*, volume 11. eds. Gschneidner and Eyring,(North-Holland: Amesterdam), (1988).

[15] J. Jenesn and A.R. Mackintosh. *Rare Earth Magnetism, Structures and Excitations.* CLARENDON PRESS.OXFORD, (1991).

[16] K. Fischer. *Phys.stat.sol.(b)*, **46**, (1971)11.

[17] P.W. Anderson. *Phys.Rev*, **124**, (1961)41.

[18] B. Coqblin and J.R Schrieffer. *Phy.Rev.*, **185**, (1969)847.

[19] J.R. Schrieffer and P.A. Wolff. *Phy.Rev.*, **149**, (1975)491.

[20] K.G Wilson. *Rev. Mod. Phys*, **47**,(1975) 773.

[21] L.N Oliveria and J.W Wilkins. *Phys.Rev.Lett*, **47**, (1981)1553.

[22] H.R Krishna-Murthy, J.W, and K.G Wilson. *Phys.Re.Lett* ***35****(1975)1011;Phys.Rev.B* ***21****(1980)1003;Phys.Rev.B* ***21****(1980)1044.*

[23] A.M. Tsvelick and P.B Wiegmann. *J.Phy.C: Solid state*, **15**, (1982)1707.

[24] PB. Wiegmann. *Sov.Phys.JETP lett*, **45**, (1980)379.

[25] N Andrei. *Phy.Rev.Lett*, **45**, (1980)379.

[26] H. Bethe. *Z.Physik*, **71**, (1931)205.

[27] P. Schlottmann. *Z. Phys B*, **51**, (1983)223.

[28] C. Kittel. *Indirect exchange interactions in metals,*. (Academic Press Inc., NY, 1968), Vol. 22.

[29] M. Ocko, D. Drobac, B. Buschinger, C. Geibel, and F. Steglich. *Phys.Rev.B*, **64**, (2001)195106.

[30] N.D. Mermin N.W. Aschcroft. *Solid State Physics.* (1981) Holt-Saunders.

[31] L.D. Landau. *Sov.Phys.JETP*, **3**, (1957)920.

[32] L.D. Landau. *Sov.Phys.JETP*, **5**, (1957)101.

[33] L.D. Landau. *Sov.Phys.JETP*, **8**, (1959)70.

[34] H.V. Löhneysen, A. Roch, M.Vojta, and P.Wolfle. *Rev.Mod.Phys*, **79**, (2007)1015.

[35] C.M. Varma, Z. Nussinov, and W.V. Saarloos. *Phys.Reports*, **361**, (2002)267-417.

[36] G.R Stewart. *Rev.Mod.Phys*, **73**, (2001)797.

[37] D.L. Cox and A. Zawadowski. *Adv. phys.*, **47**, (1998)599.

[38] Ph. Noziéres and A. Blandin. *J.physique*, **41**, (1980)193-211.

[39] D.L. Cox. *Phy.Rev.Lett*, **59**, (1987)1240.

[40] A.H. Castro Neto, G. Castilla, and B.A. Jones. *Phy.Rev.Lett*, **81**, (1998)3531.

[41] R.B. Griffiths. *Phy.Rev.Lett*, **23**, (1969)17.

[42] P. Coleman. *arxiv.org/abs/cond-mat/0612006v3*, (2007).

[43] J. A. Hertz. *Phys. Rev. B*, **14**, (1976)1165.

[44] A. J. Millis. *Phys. Rev. B*, **48**, (1993)7183.

[45] U. Zülicke and A. J.Millis. *Phys. Rev. B*, **51**, (1995)8996.

[46] A.Tari. *The specific heat of Matter at low temperatures.* (Imperial College Press, London 2003).

[47] F.J Blatt. *Physics of electronic Conduction in solids.* (McGraw-Hill: New York), 1968.

[48] A. Amaro, D. Jaccard, J. Flouquet, F. Lapierre, J.L. Tholence, R.A. Fisher, S.E. Lacy, J.A. Olsen, and N.E. Phillips. *J. Low Temp.Phys*, **68**, (1987)371.

[49] J.van Kronendonk and J.H. van Vleck. *Rev*, **30**, (1958)1.

[50] C. Kittel. *Quantum Theory of solids.* 2nd ed.,(Wiley,1987),Chapter 4.

[51] E.S.R Gopal. *Specific heat at low Temperature.* (Plenum Press: New York)(1966).

[52] Weigmann. *Phys.Lett*, **80A**, (1980)163.

[53] V.T Rajan. *Phys.Rev.Lett*, **47**, (1983)308.

[54] N. Andrei and J. H. Lowenstein. *Phys. Rev. Lett.*, **46**, (1981) 356.

[55] W. Pauli. *Z.Physik*, **41**, 81(1926).

[56] A.H.Morrish. *The physical principles of Magnetism.* (John Wiley & Sons,Inc.,New York)(1965).

[57] J. Becquerel and J. van den Handel. *J.phys.radium*, **10**, (1939)10.

[58] J.A.Mdosh. *Spin glasses: An experimental introduction.* (London.Washington,DC), (1993).

[59] N. Andrei and J.H. lowenstein. *Phy.Rev.Lett*, **46**, (1981) 356.

[60] F. Steglich. *J.Magn. Magn. Matter*, **100**, 186(1991).

[61] J. Sok and B.K. Cho. *J. Korean Phys.Soc*, **47**, (2005)318-320.

[62] B.K. Cho, B.N. Harmon, D.C. Johnston, and P.C Canfield. *Phys.Rev .B*, **53**, (1996)2217.

[63] K.W.H. Stevens. *Proc Phys.Soc*, **A65**, (1952)209.

[64] K. A. Jr. Gschneider, V. K. Pecharsky, and A. O. Tsokl. *Rep. Prog. Phys*, **68**, (2005) 1479.

[65] M.H Phan and S. C. Yu. *J. Magn. Magn. Mater*, **306**, (2007) 325.

[66] A M Tishin and Y I Spichkin. *The Magnetocaloric Effect and its Applications.* Institute of Physics Publishing Bristol and Philadelphia 2003.

[67] Kohler. *M.Ann.Physik*, **40**, (1942)602.

[68] P.L. Rossiter. *The electrical resistivity of metals and alloys.* Cambrige University Press, (1987).

[69] Meaden G.T. *Electrical Resistance of Metals.* (Plenum press: NewYork) (1965).

[70] J. M. Ziman. *Electrons and Phonons.* Oxford University Press, London, 1965.

[71] E. GRATZ. *J.Magn. Magn. Matter*, **24**, (1981) 1-6.

[72] P.G de Gennes and J.Friedel. *J.Phys.Chem.Solids*, **4**, (1958) 71.

[73] J. Kondo. *Prog.Theor.Phys*, **32**, (1964) 37.

[74] M. B. Fontes, J. C. Trochez, B. Giordanengo, S. L. Bud'ko, D. R. Sanchez, E. M. Baggio-Soitovich, and M. A. Continentino. *Phys. Rev. B .*, **60**, (1999) 6781.

[75] H. Yamada and S. Takada. *Pro.Theor Phys*, **48**, (1972)6A.

[76] K. Yoshida. *Phys.Rev*, **107**, (1957) 397.

[77] G. Williams. *Solid State Comm*, **8**, (1970)1451.

[78] J. Flouquet, P. Haen, F. Lapierre, C. Fierz, A. Amato, and D. Jaccard. *J.Magn. Magn. Matter*, **76**, (1988)285.

[79] Grewe.N and Steglich. *Handbook on the physics and chemsitry of Rare Earths*, volume Vol 14. (North-Holland: Amsterdam), (1991).

[80] A. de Visser, A. Menovsky, and J.M Franse. *Physica B*, **147**, (1987)81.

[81] V.I. Belitskií and A.V Gol' tsev. *Sov.Phys.JETP*, **69**, (1989)1026.

[82] N.Andrei. *Phys. Lett. A*, **87**, (1982) 299.

[83] B. Batlogg, D. J. Bishop, E. Bucher, B. Golding, Jr., A. P. Ramirez, Z. Fisk, and J. L. Smith. *J. Magn. Magn. Mater.*, **63**, (1987)441.

[84] E. Gratz and H. Nowotny. *Physica*, **130B**, (1985)75-80.

[85] F.J. Blatt, P.A. Schroeder, C.A. Foiles, and D. Greig. *Thermoelectric power of Metals.*

[86] A.M. Guenault. *J.Phys*, **F1**, (1971)373.

[87] V.Zlatić and R.Monnier. *Phys.Rev .B*, **71**, (2005)165109.

[88] T. Toliński, V. Zlatić, and A. Kowalczyk. *J.Alloy.comp*, **490**, (2010)15-18.

[89] M.D Koterlyn, O.I. Babych, and G.M. Koterlyn. *J.Alloy*, **325**, (2001)6-11.

[90] N.E. Bickers, D.L. Cox, and J.W Wilkins. *Phys.Rev .B*, **36**, (1987)2036.

[91] I.A Campbell and A.Fert. *Ferromagnetic Materials.* ed.Wohlfarth E.P.,(North-Holland: Amesterdam), Vol 3, Chap 9(1982).

[92] J.E. Parrott and A.D. Stuckes. *Thermal Conductivity of Solids.* (Methuem, New York)(1975).

[93] J. Shang Hwang, K. Jan Lin, and C. Tien. *Rev. Sci. Instrum.*, **68**, (1997)94.

[94] K. H. J. Buschow and A. S. van der Goot. *Acta Cryst. (1971). B27, 1085-1088*, **B27**, (1971) 1085-1088.

[95] K.H.J. Buschow, A.S. Van Der Goot, and J. Birkhan. *J. Less Common Metals*, **19**, (1969) 433-436.

[96] A.E Dwight. *Trans. Amer. Soc. Metals*, **53**, (1961) 479.

[97] J.H Wernick and S.Geller. *Acta Cryst.*, **12**, (1959)662.

[98] S.E Haszko. *Trans. A.I.M.E. 218 763; 1962 International Tables for X-ray crystallography III , Birmingham: Kynoch Press.*

[99] K.V. Shah, P. Bonville, P. Manfrinetti, A. Provino, and S.K. Dhar. *J. Magn and Magn Mater*, **321**, (2009) 3164-3170.

[100] L.D. Tunga, K.H.J. Buschow, J.J.M. Franse, P.E. Brommer, H.G.M. Duijin, E. Br uck, and N.P. Thuy. *J.Alloys and Comp*, **269**, (1998) 17-24.

[101] T.Takeshita, S.K.Malik, A.A El-Attar A A, and W.E Wallace. *AIP conf. Proc.*, **34**, (1976) 230.

[102] T. Kaneko, S. Arai, S. Abe, and K. Kamigaki. *J. Phys. Soc. Jpn*, **55**, (1986)4441.

[103] T. Takeshita, S.K. Malik, and W.E. Wallace. *J.Solid State Chem*, **23**, (1978)(225-229).

[104] S. Abe, Y. Atsumi, T. Kambo, and H. Yshida. *J. Magn. Magn. Mater.*, **104-107**, (1992) 1397.

[105] H. Nakamura, K. It0, A. Uenishi, H. Wada, and M. Shiga. *J. Phys. Soc. Jpn*, **62**, (1993) 1446.

[106] S. Abe, H. Nakazawa, T. Kaneko, H. Yoshida, K. Kamigaki, Y. Nakagawa, and S. Miura. *J. Phys. Soc. Jpn*, **58**, (1989) 3328-3333.

[107] S. Abe, H. Nakazawa, T. Kaneko, H. Yoshida, and K. Kamigaki. *J. Phys. Colloques*, **49**, (1988) C8.

[108] D. Kaczorowski, M.B. Tchoula Tchokonte, A.M. Strydom, and P. de V. du Plessis. *J. Magn.Magn Mater*, **218**, (2000) 238.

[109] K. Andres, E. Bucher, P. H. Schmidt, J. P. Maita, and S. Darack. *Phys. Rev. B*, **11**, (1975) 4364.

[110] E. Bauer, E. Gratz, and Ch. Schmitzer. *J.Magn. Magn. Matter*, **63-64**, (1987) 37.

[111] E. Bauer, K. Payer, R. Hauser, E. Gratz, D. Gignoux, D. Schmitt, N. Pillmayr, and G. Schaudy. *J. Magn. Magn. Mater.*, **104-107**, (1992)651.

[112] J.M. Barandiaran, D. Gignoux, and J. Rodriguez-Fernandez. *Physica B*, **154**, (1989)293.

[113] H. Nakamura, A. Uenishi, K. Ito, M. Shiga, T. Kuwai, and J. Sakurai. *J. Magn. Magn. Mater.*, **140-144**, (1995)923.

[114] H. Nakamura, K. Ito, and M. Shiga. *J. Phys: Conden Matter,*, **6**, (1994)6801.

[115] H. Nakamura, N. Kim, M. Shiga, R. Kmiec, K. Tomala, E. Ressouche, J.P. Sanchez, and B.Malaman. *J.Phys: Conden Matter*, **11**, (1999)1095.

[116] J.L. Sarrao. *Physica B*, **259-261**, (1999) 128.

[117] E.Figueroa, J.M Lawrence, J.L Sarrao, Z.Fisk, M.F Hundley, and J.D Thompson. *Solid State Commun.*, **106**, (1998)347.

[118] S. K. Dhar, R. Kulkarni, P. Manfrinetti, M. L. Fornasini, and C. Bernini. *Phys. Rev.B*, **27**, (2008)054424.

[119] M. Diviš, E.A. Goremychkin, P. Svoboda, V. Nekvasil, J. Bischof, and R. Osborn. *Physica B: Condensed Matter*, **168**, (1991) 251-256.

[120] V.M.T.S. Barthem, D. Gignoux, A. Nait-Saada, D. Schmitt, and A.Y. Takeuchi. *J. Magn. Magn. Mater*, **80**, (1989) 142.

[121] S. Zhang, T. Kitai, Y. Yamaguchi, K. Koyama, H. Yoshida, and T. Kaneko. *J. Phys. Soc. Jpn.*, **79**, (2010) 043704.

[122] T. Tayama, Y. Takayama, Y. Miura, S. Zhang, and Y. Isikawa. *J. Phys. Soc. Jpn.*, **80**, (2011), p. SA074.

[123] K. Koyama, R. Sakakura, and K. Wanatebe. *J.Phys.: Conf. Ser. 156 (2009) 012019.*, **156**, (2009) 012019.

[124] P. Alessia, N. Kumar, P. Manfrinetti, and S.K. Dhar. *J. Appl. Phys.*, **109**, (2011), p. 07E134.

[125] Y. Adashi and K. Koyama. N. Kobayashi (Ed.), 2006 Annual Report, High field Laboratory for Superconducting Materials, Institute for Materials Research, Tohoku University, Sendai, 2007, p. 86.

[126] B.H. Toby. *Powder Diffraction*, **21**, March 2006.

[127] M. Falkowski, B. Andrzejewski, and A. Kowalczyk. *J. Alloys Compd.*, **155**, (2007)442.

[128] Podgornykh S M and Kourov N I 2007. 2007 bulletin of the russian academy of sciences: Physics. 71 1079.

[129] S. Abe, T. Kaneko, H. Yamauchi, H. Yoshida, H. Nakazawa, and K. Kamigaki. *J. Magn. Magn. Mater.*, **70**, (1987) 289.

[130] V.K Anand and D.C Johnston. *J. Phys. Condens. Matter*, **26**, (2014), p. 286002.

[131] V.K. Anand, D.T. Adroja, and A.D. Hillier. *J. Phys. Condens. Matter*, **25**, (2013), p. 196003.

[132] S. Zhang, T. Tayama, T. Mizushima, T. Kuwai, and Y. Isikawa. *J. Phys. Soc. Jpn*, **80**, (2011), p. SA076.

[133] A. Kowalczyk, T. ToliŃSKi, M. Falkowski, and M. Timko. *ACTA PHYSICA POLONICA A*, **118**, (2010) 936.

[134] M. Falkowski and A. Kowalczyk. *Intermetallics*, **20**, (2012) 173-175.

[135] M.Falkowski and A.Kowalczyk. *Intermetallics*, **37**, (2013) 65-68.

[136] T.Toliński. *Eur. Phys. J B*, **84**, (2011)177-181.

[137] E. Bauer, E. Gratz, G. Hutflesz, and H. Muller. *J. Phys : Condens. Matter*, **3**, (1991) 7641.

[138] P.G. Klemens. *Solid State Phy*, **7**, (1958) 1-98.

[139] K. KAWASAKI. *Prog.Theor.Phys*, **29**, (1963)801.

[140] H.J. Goldsmid. *Thermoelectric Refrigeration.* (Plenum, New York, 1964).

[141] S. Baran, A. Szytuła, J. Leciejewicz, N. Stüsser, A. Zygmunt, Z. Tomkowicz, and M. Guillot. *J.Alloys Comp.*, **243**, (1996)112.

[142] A. Iandelli. *J. Alloys Comp*, **198**, (1993) 141.

[143] A. Iandelli. *J.Less-Common Met.*, **90**, (1983)121.

[144] W. Rieger and E. Parthé. *Monatsh.Chem.*, **100**, (1969)439.

[145] A. Oleś, R. Duraj, M. Kolenda, B. Penc, and A. Szytuła. *J.Alloys Comp*, **363**, (2004)63.

[146] A. Iandelli. *J.Alloys Comp.*, **198**, 141(1993).

[147] P. Spatz, K. Gross, A. Züttel, F. Fauth, P. Fischer, and L. Schlapbach. *J. Alloys Comp.*, **261**, (1997)263.

[148] M. Oboz and E. Talik. *J. Alloys Comp.*, **509**, (2011)5441.

[149] S.K. Dhar, C. Mitra, P. Manfrinetti, R. Palenzona, and A. Palenzona. *J. Phase Equilibria*, **23**, (2002)79.

[150] R. Marazza, D. Rossi, and R. Ferro. *J. Less Common Met.*, **75**, 25 (1980).

[151] E. Hovestreydt, N. Engel, K. Klepp, B. Chabot, and E. Parthé. *J. Less-Common. Met.*, **85**, (1982)247.

[152] F. Hulliger. *J. Alloys Comp*, **239**, (1996)131.

[153] B. Penc, A. Szytuła, J.H. Velasco, and A. Zygmunt. *J. Magn. Magn. Mater.*, **256**, (2003)373.

[154] B. Chevalier, A. Cole, P. Lejay, M. Vlasse, J. Etourneau, and P. Hagenmuller. *Mat. Res. Bull.*, **17**, (1982)251.

[155] K. Katoh, Y. Mano, K. Nakano, G. Terui, Y. Niide, and A. Ochiai. *J. Magn. Magn. Mater.*, **268**, (2004)212.

[156] S.K. Malik, H. Takeya, and K.A. Gschneidner Jr. *J. Alloys Comp.*, **207**, (1994)237.

[157] M.G. Haase, T. Schmidt, C.G. Richter, H. Block, and W. Jeitschko. *J. Solid State Chem.*, **168**, 18 (2002).

[158] D. Rossi and R. Ferro. *J. Alloys Comp.*, **317**, (2001)521.

[159] I. Karla, J. Pierre, and R.V. Skolozdra. *J. Alloys Comp.*, **265**, (1998)42.

[160] H. Oesterreicher. *J. Less-Common Met.*, **30**, (1973)225.

[161] P. Javorský, L. Havela, V. Sechovský, H. Michor, and K. Jurek. *J.Alloys Comp.*, **264**, (1998)38.

[162] M. Kurisu, R. Hara, G. Nakamoto, Y. Andoh, S. Kawano, and D. Schmitt. *Phys.B*, **312**, (2002)861.

[163] Ch. Routsi, J.K. Yakinthos, and E. G-Seale. *J. Magn. Magn. Mater.*, **98**, (1991)257.

[164] Ch. Routsi, J.K. Yakinthos, and H. G-Seale. *J. Magn. Magn. Mater.*, **117**, (1992)79.

[165] M. Kurisu, H. Hori, M. Furusawa, M. Miyanke, Y. Andoh, I. Oguro, K. Kindo, T. Takeuchi, and A. Yamagishi. *Phys.B,*, **201**, (1994)201.

[166] S. Gupta, K.G. Suresh, A.K. Nigam, Yu.V. Knyazev, Yu.I . Kuz'min, and A.V. Lukoyanov. *J.Phys.D: Appl.Phys.*, **47**, (2014)365002.

[167] L. Menon and S.K. Malik. *Phys. Rev. B*, **51**, (1995)51.

[168] M. Kasaya, H. Suzuki, T. Yamaguchi, and K. Katoh. *J. Phys. Soc. Jpn.*, **61**, (1992)4187.

[169] N.H. Kumar and S.K. Malik. *Solid State Commun.*, **114**, 223(2000).

[170] P. Rogl, B. Chevalier, M.J. Besnus, and J. Etourneau. *J.Magn.Magn.Mater.*, **80**, (1989)305.

[171] Y. Kawasaki, Y. Kishimoto, N. Imai, T. Ohno, H. Kubo, S. Yoshii, and M. Kasaya. *J.Phys.Soc.Jpn.*, **73**, (2004)694.

[172] B.J. Gibson, W. Schnelle, R. Pöttgen, K. Bartkowski, and R.K. Kremer. In : Proc. of Int. Conf. on Low Temp. Phys. Prague, August 8-14, 1996.

[173] B. Chevalier, M. Pasturel, J. L. Bobet, F. Weill, R. Decourt, and J. Etourneau. *J. Solid State Chem.*, **177**, (2004)752.

[174] D. Gignoux, D. Schmitt, and M. Zerguine. *Solid State Commun.*, **58**, (1986)559.

[175] H. Oesterreicher. *Phys. Stat. Sol. (a)*, **34**, (1976)723.

[176] A.M strydom. *Eur.Phys.J.B*, **74**, (2010) 9-18.

[177] F.M. Mulder, R.C. Thiel, and K.H.J Buschow. *J.AlloysComp*, **205**, (1994)169.

[178] A. Szytuła W. Baźela and J. Leciejewicz. *Solid State Commun.*, **56**, (1985)1043.

[179] S. Baran, J. Leciejewicz, N. Stüsser, A.Szytuła, Z. Tomkowicz, and A. Zygmunt. *Acta Phys.Pol.,A*, **56**, (1997)271.

[180] B.J. Gibson, R. Pöttgen, and R.K. Kremer. *Phys.B*, **276**, (2000)p.734.

[181] W. Schnelle, R. Pöttgeny, R.K. Kremer, E. Gmelin, and O. Jepsen. *J.Phys: Condens.Matter*, **9**, (1997)1435-1450.

[182] B. Penc, S. Baran, M. Ślaski, and A. Szytuła. *J. Alloys Comp.*, **282**, (1999)p. L6J.

[183] S. Baran, M. Hofmann, B. Penc, M. Ślaski, A. Szytua, and A. Zygmunt. *Phys.B*, **276**, (2000)p.656.

[184] S. Baran, M. Hofmann, G. Lampert, N. Stüsser, A. Szytuła, D. Többens, P. Smeibidl, and S. Kausche. *J. Magn. Magn. Mater.*, **236**, (2001)p.293.

[185] B.M. Sondezi and A.M. Strydom. *Acta phys polon A*, **127**, (2015)288.

[186] V. Goruganti, K. D. D. Rathnayaka, Jr. Joseph H. Ross, Y. Öner, C. S. Lue, and Y. K. Kuo. *J. App.Phys*, **103**, (2008) 073919.

[187] N. Sato, N. Aso, K. Hirota, T. Komatsubara, Y. Endoh, S. M. Shapiro, G. H. Lander, and K. Kakurai. *Phys. Rev. B*, **53**, (1996)14043.

[188] A.I. Akhiezer, V.G. Baryakhtar, and M.I. Kazanov. *Uspechi Fiz. Nauk*, **12**, (1960) 533.

[189] S.K. Banerjee. *Phys.lett*, **12**, (1964) 16.

[190] S.Gupta and K.G. Suresh. *J.Magn. Magn. Matter*, **391**, (2015) 151-155.

[191] S.Gupta, K. G. Suresh, and A. V. Lukoyanov. *J Mater Sci*, **50**, (2015) 5723.

[192] Q. Y. Dong, H. W. Zhang, J. L. Shen, J. R. Sun, and B. G. Shen. *J. Magn. Magn. Mater.*, **319**, (2007) 56.

[193] J. Shen, L.Q. Yan, J. Zhang, F.W. Wang, J.R. Sun, F.X. Hu, C.B. Rong, and Y.X. Li. *J. Appl. Phys*, **103**, (2008) (07B315).

[194] S. Gupta, K.G. Suresh, and A.K. Nigam. *arXiv:*, **1305**, (2013) 1124.

[195] S. Gupta, K.G. Suresh, and A.K. Nigam. *J.App.phys*, **112**, (2012) 103909.

[196] J.O Willis, R.H Aiken, Z.Fisk, E.Zimgibl, J.D Thompson, H.R Ott, and B.Batlogg. *Theoritcal and Experimental Aspects of valance Fluctuations and Heavy Fermions.* eds L C Gupta and S K Malik (New York : Plenum) p 57, 1987.

[197] E.A Goremychkin, I. Natkanie, E. Mühler, H. Müller, and P. Frach. *Solid State Communications*, **64**, (1987) 1437.

[198] H. Armbruster and F. Steglich. *Solid State Communications*, **27**, (1987) 873.

[199] Y. Onuki, Y. Machii, Y. Shimizu, T. Komatsubara, and T. Fujita. *J.Phys.Soc.Japan*, **54**, (1985) 3562.

[200] E. Bauer, G. Amoretti, L.C Andreani, B. Delley, M. Ellerby, K. McEwen, R. Monnier, E. Pavarini, and P. Santini. *J.Phys: Condens. Matter*, **10**, (1998) 4465-4475.

[201] K.V. Shah, S.K Dhar, A. Provino, and P. Manfrinetti. *Solid State Communications*, **148**, (2008) 155-158.

[202] A. Kowalczyk, T. ToliŃSKi, M. Reiffer, M. Pugaczowa-Michalska, G. Chełkowska, and E. Gažo. *J. Phys.: Condens. Matter*, **20**, (2008) 255252 (7pp).

[203] E. Bauer, N. Pillmayr, E. Gratz, D. Gignoux, D. Schmitt, K. Winzer, and J. Kohlmann. *J.Magn. Magn. Matter*, **17**, (1988) 311-317.

[204] A. Kowalczyk, T. Toliński, M. Falkowski, B. Andrzejewski, A. Szewczyk, and M. Reiffers. *J.Alloy and comp*, **481**, (2009) 40.

[205] M. Falkowski, A. Kowalczyk, and T. Toliński. *J.Solid state communications*, **150**, (2010) 1548.

[206] M. Falkowski, A. Kowalczyk, T. Toliński, and D. Krychowski. *Interme*, **19**, (2011) 433.

[207] M. Falkowski, A. Kowalczyk, and T. Toliński. *J.Alloys comp*, **509**, (2011) 6135.

[208] M. Falkowski and A. Kowalczyk. *J.App.Phys*, **111**, (2012) 093725.

[209] N.F Mott and H.Jones. *The theory of the properties of metals and alloys.* (Oxford: Oxford university Press), (1958).

[210] M. Lavagna, C. Lacroix, and M. Cyrot. *J.Phys F: Met. Phys.*, **13**, (1983) 1007.

[211] C. Lacroix and M. Cyrot. *Phys.Rev.B*, **20**, (1979) 1969.

[212] M B Tchoula Tchokonté, P de V du Plessis, A M Strydom, D Kaczorowski, A Czopnik, and Z Kletowski. *J.Phys: Condens. Matter*, **16**, (2004) 1981-1994.

[213] T.Kagayama and G.Oomi. *Transport and Thermal Properties of f-electrons Systems.* eds. G.Oomi *et al* (Plenum Press: New York), (1993) 155.

[214] P. de V. du Plessis and V.H Tran. *J.Phys: Condens. Matter*, **9**, (1997) 8527.

[215] A.K. Bhattacharjee and B. Coqblin. *Phy.Rev.B*, **13**, (1976)3441.

[216] P.B Aken, H.J Daal, and K.H.J Buschow. *Phys Lett A 1974*, **49**, (1974) 201.

[217] R. Cibin, D. Jaccard, and J.J Sierro. *J.Magn Magn Mater*, **108**, (1992) 107.

[218] J. Sakurai, T. Ohyama, and Y. Komura. *J.Magn Magn Mater 1985;52:320.*, **52**, (1985) 320.

[219] H. Sato, I. Sakamoto, K. Yonemitsu, Y. Onuki, T. Komatsbura, and Y. Kabwuragi et al. *J.Magn Magn Mater*, **52**, (1985) 357.

[220] U. Gottwick, K. Gloss, S. Horn, F. Steglich, and N. Grewe. *J.Magn. Magn. Mater.*, **47**, (1985) 536.

[221] P. Scoboria, J.E Crow, and T. Mihalisin. *J.Appl.Phys*, **50**, (1979)1895.

[222] J.R. Thompson, S.T. Sekula, C.K loong, and C. Stassis. *J.Appl.Phys*, **53**, (1982)7893.

[223] W.E. Gardner, J. Penfod, T.F. Smith, and I.R Harris. *J.Phys. F: Met. Phys.*, **2**, (1972)133.

[224] R.J. Gambino, W.D. Grobman, and A.M. Toxen. *J.ApplJ.App.lett*, **22**, (1973)506.

[225] G. krill, L. Abadli, M.F. Ravent, J.P. Kapler, A. Meyer, and J.de. *Physique*, **41**, (1980)1211.

[226] U.V.S Rao, R.D Hutchens, and J.E Greedan. *J.Phys. Chem. Solid*, **32**, (1971)2755.

[227] M.J. Besnus, J.P. Kapler, J.P. Krill, M.F, N. Hamdaoui, and A.Meyer. *Valance instablities.* ed.P. Wachter , and H.Boppart.,(North-Holland; Amesterdam)(1982)165.

[228] E. Beaurepaire, G. Krill, J.P. Kapler, and J. Röhler. *Solid State Commun*, **49**, (1983)65.

[229] T. Mihalisin, P. Scoboria, and J.A. Ward. *Phy.Rev.Lett*, **46**, (1981)862.

[230] S.K. Malik, R. Vijayaraghavan, E.B. Boltich, R.S. Craig, W.E Wallace, and S.K. Dhar. *Solid State Commun*, **43**, (1982)243.

[231] R. Kuentzler, S.K. Dhar, S.K Malik, R. Vijayaraghavan, and B. Coqblin. *Solid State Commun*, **50**, (1984)145.

[232] J.P Kappler, M.J Besnus, E.Beaurepaire, A.Meyer, J.Sereni, and G.Nieva. *J.Magn. Magn. Matter*, **47& 48**, (1985)111.

[233] J.P Kappler, M.J Besnus, P.Lehmann, A.Meyer, and J.Sereni. *J.Less-Common Metals*, **111**, (1985)261.

[234] J. Sereni, G. Nieva, J.P Kappler, M.J Besnus, and A. Meyer. *J.Phys. F: Met. Phys.*, **16**, (1986)435.

[235] D.T Adroja, B.D Rainford, and A.G.M Jansen. *J.Magn. Magn. Matter*, **140-144**, (1995)1217.

[236] M. Houshiar, D.T Adroja, and B.D Rainford. *Physica B*, **223 & 224**, (1996)268.

[237] D. KaczorowsKi, M. Koźlik, and L. Kepiński. *J.Phys.Chem of Solids*, **60**, (1999)521.

[238] C.D.W Jones, R.A. Gordon, B.K. Cho, F.J. DiSalvo, S.J. Kim, and G.R Stewart. *Physica B*, **262**, (1999)248.

[239] R.A. Gordon, C.D.W Jones, M.G Alexander, and F.J. DiSalvo. *J.Physica B*, **225**, (1996)23.

[240] R.A. Gordon and F.J. DiSalvo. *Z.für Naturforschung*, **51b**, (1996)52.

[241] B.K. Cho, R.A. Gordon, C.D.W Jones, F.J. DiSalvo, J.S. Kim, and G.R Stewart. *Phys. Rev. B*, **57**, (1998)15191.

[242] S.Donicah. *Valance instablities and related narrow-band phenomena.* ed R.D.Park(New York Plenum) p 169.

[243] M.B. Tchoula Tchokonte, P.de V du Plessis, A.M. Strydom, and D.Kaczorowaski. *J.Alloys and Comp*, **681**, (2016)359-366.

[244] S. Singh and S. Dhar. *J.Phys.Condens.Matter*, **14**, (2002)11795.

[245] S. Singh and S. Dhar. *J.Phys.Rev B*, **68**, (2003)144433.

[246] B. Cornut and B. Coqblin. *Phys. Rev. B*, **5**, (1972) 4541.

[247] K. H. Fisher. *Z. Phys. B*, **74**, (1989) 475.

[248] A. Sumiyama, Y. Oda, H. Nagano, Y. Ónuki, K. Shibutani, and T. Komatsubara. *J. Phys. Soc. Jpn .*, **55**, (1986) 1294.

[249] Y. Ónuki, Y.Shimizu, M.Nishihara, Y.Machii, and T. Komatsubara. *J.Phys.Soc.Jpn*, **55**, (1985)1964.

[250] V. Yu Irkhin and M.I Katsnelson. *Z.Phys B*, **75**, (1989)67.

[251] V. Yu Irkhin and M.I Katsnelson. *Z.Phys B*, **82**, (1991) 77.

[252] A. Freimuth. *J.Magn. Magn. Matter*, **68**, (1987)28.

[253] C.S. Grade and J. Ray. *Phy.Rev.B*, **51**, (1995)2960.

[254] R. A. Gordon and F. J. DiSalvo. *J. Alloys Comp.*, **238**, (1996) 57.

[255] A. K. Bashir, M. B. Tchoula Tchokonte, B. M. Sondezi D. Britz, A. M. Strydom, and D. Kaczorowski. *J. Phys.: Conf. Series*, **529**, (2015) 012004.

[256] A. K. H. Bashir, M. B. Tchoula Tchokonte, J. L. Snyman, B. M. Sondezi, and A. M. Strydom. *J. Appl. Phys.*, **115**, (2014) 17E134.